On-Chip Plasmonic Nanosurface for Molecular Profiling of Single Extracellular Vesicles in Cancer Liquid Biopsy

Mahsa Jalali

Department of Bioengineering

McGill University

May 2023

A thesis presented to McGill University as partial fulfilment requirement for the degree of Doctor of Philosophy in Biological and Biomedical

©2023 Mahsa Jalali

Abstract

Extracellular vesicles (EVs) continually released from cancer cells into biofluids, carry actionable molecular fingerprints of the underlying disease with considerable diagnostic and therapeutic potential that could overcome barriers in real time monitoring of hard to access tumors such as brain tumors. The scarcity, heterogeneity, and intrinsic complexity of tumour EVs from brain tumors in plasma due to the brain-blood barrier present a major technological challenge.

With existing technologies, we are subjected to use bioassays that comprise the core components of today's diagnostic armamentaria. While bioassay's complexity, delicacy, and error-prone quantification of the target concentration together with a finite number of available receptors and fluorophores with non-overlapping spectra are limiting their use. We hypothesize that a label-free molecular profiling analysis technique such as surface-enhanced Raman spectroscopy (SERS) could potentially improve diagnostic accuracy necessary to distinguish cancer EVs amongst a large background of host EVs without need for immunoaffinity based capture. Development of portable on-chip devices for molecular profiling of the heterogeneous EVs as circulating cancer biomarkers and monitoring of their molecular transformational can significantly improve understanding of the complexity of cancer and monitoring its development.

The vision of this research involves the integration of optimized nanosurface on-chip detection platforms in translational diagnosis of molecular alteration traits in the heterogeneous circulating EVs as an alternative liquid biopsy approach. To that end, this thesis initially aims to develop portable platforms capable of differentiating the molecular profiles of cancer-derived extracellular vesicles (EVs) from various tumor cell lines under controlled conditions, in comparison to non-cancer EVs. To achieve this, multifunctional plasmonic nanostructured materials integrated with functional mono- or few-layer 2D materials (Graphene and MoS_2) are

utilized within ordered confined spaces (nanoarrays). This integration allows for the exploration of how surface morphology, lattice geometry, and electronic properties of the materials contribute to the highly sensitive surface-enhanced optical molecular profiling of EVs. By investigating these factors, the thesis seeks to enhance our understanding of EVs and enable accurate characterization of cancer EVs for diagnostic and research purposes.

Next, the thesis aims to employ customizable on-chip plasmonic nanoarrays, enhanced by 2D nanomaterials, to enable label-free single EV investigation of molecular alterations with the vision is to distinguish the signatures of Glioblastoma (GBM) brain cancer paradigmatic molecular subtypes, including the mutant oncogenic variant of epidermal growth factor receptor (EGFR), known as EGFRvIII, as well as O^6-Methylguanine-DNA Methyltransferase (MGMT), a marker of resistance to chemotherapy.

Ultimately, this research envisions identifying the SERS fingerprint molecular profile of single EV underlying the chemotherapy resistance in GBM. To that end, the hybrid plasmonic nanocavity array interface with a machine learning algorithm as a tool was used for classifying the expression of the molecular traits stratifying the identification of EVs as derived from drug susceptible or resistant cells and estimated their probabilities of detection in human CSF and plasma of GBM patients.

This thesis transitions from an overview of the technologies integrating plasmonic nanostructured arrays, monolayer 2D materials and surface-enhanced optical sensing into a more comprehensive nanosurface microchip design for translational study of cancer (GBM) patients via single extracellular vesicles as liquid biopsy biomarkers (provisional patent: US63/253,605). We conclude this investigation with an overview of the future outlook in three areas: diagnostics, therapeutics, and materials science and engineering.

Abstraite

Les vésicules extracellulaires (EV) continuellement libérées des cellules cancéreuses dans les biofluides, portent des empreintes moléculaires exploitables de la maladie sous-jacente avec un potentiel diagnostique et thérapeutique considérable qui pourrait surmonter les obstacles dans la surveillance en temps réel des tumeurs difficiles d'accès telles que les tumeurs cérébrales. La rareté, l'hétérogénéité et la complexité intrinsèque des EV tumoraux des tumeurs cérébrales dans le plasma en raison de la barrière hémato-encéphalique présentent un défi technologique majeur.

Les technologies existantes reposent souvent sur des essais biologiques, essentiels au diagnostic actuel. Cependant, l'aspect complexe, délicat et la quantification sujette aux erreurs du bioessai, ainsi que le nombre limité de récepteurs et de fluorophores avec des spectres non chevauchants, en restreignent l'utilisation. Nous émettons l'hypothèse qu'une technique d'analyse de profilage moléculaire sans étiquette telle que la spectroscopie Raman améliorée en surface (SERS) pourrait potentiellement améliorer la précision diagnostique nécessaire pour distinguer les véhicules électriques du cancer parmi un large éventail de véhicules électriques hôtes sans avoir besoin d'une capture basée sur l'immunoaffinité. Le développement de dispositifs portables pour le profilage moléculaire des EV hétérogènes en tant que biomarqueurs circulants et la surveillance de leurs transformations moléculaires pourraient grandement améliorer la compréhension de la complexité du cancer et son évolution.

Cette recherche envisage l'intégration de plateformes optimisées de nanosurface dans le diagnostic translationnel des altérations moléculaires dans les EV circulants, comme alternative à la biopsie liquide. À cette fin, cette thèse vise dans un premier temps à développer des plateformes portables capables de différencier les profils moléculaires des vésicules extracellulaires (VE) dérivées du cancer de diverses lignées cellulaires tumorales dans des conditions contrôlées, par

rapport aux VE non cancéreuses. Des matériaux nanostructurés plasmoniques intégrés à des matériaux 2D (graphène, MoS_2) sont utilisés dans des nanoarrays pour explorer comment la morphologie, la géométrie du réseau et les propriétés électroniques contribuent au profilage moléculaire amélioré des EV.

Ensuite, la thèse vise à utiliser des nanoréseaux plasmoniques personnalisables sur puce, améliorés par des nanomatériaux 2D, pour permettre une étude EV unique sans étiquette des altérations moléculaires avec la vision est de distinguer les signatures des sous-types moléculaires paradigmatiques du cancer du cerveau du glioblastome (GBM), y compris le variant oncogénique mutant du récepteur du facteur de croissance épidermique (EGFR), connu sous le nom d'EGFRvIII, ainsi que la O6-Methylguanine-DNA Methyltransferase (MGMT), un marqueur de résistance à la chimiothérapie.

Enfin, cette recherche aspire à identifier le profil moléculaire de l'empreinte SERS d'un EV lié à la résistance à la chimiothérapie dans le GBM. Un réseau de nanocavités plasmoniques hybrides avec un algorithme d'apprentissage automatique est utilisé pour classer l'expression des traits moléculaires et estimer leurs probabilités de détection dans le liquide céphalorachidien et le plasma des patients atteints de GBM.

Cette thèse passe d'un aperçu des technologies intégrant des réseaux nanostructurés plasmoniques, des matériaux monocouches et à quelques couches et une détection optique améliorée en surface à une conception plus complète de micropuces à nanosurface pour l'étude translationnelle des patients atteints de cancer (GBM) via des vésicules extracellulaires comme biomarqueurs de biopsie liquide (provisoire brevet : États-Unis 63/253 605). Enfin, nous concluons cette enquête par un aperçu des perspectives d'avenir dans trois domaines : le diagnostic, la thérapeutique et la science et l'ingénierie des matériaux.

Acknowledgement

The past years at McGill University have been an amazing journey, made all the more meaningful because of the incredible individuals I have met. I am profoundly grateful for their impact on my studies and their encouragement throughout this transformative chapter of my life.

First and foremost, I would like to thank my advisor, Prof. Sara Mahshid, for her contagious enthusiasm and inspiration. I started off as the first PhD student in her lab and we have since then traversed more than a PhD and countless hours of interactions. Infusing me with confidence and guiding me to shape my ideas into practical solutions for unmet needs, she inspired me to step fearlessly into the unknown and challenge myself to improve.

I am grateful to have had the chance to interact with Prof. Janusz Rak, at RI-MUHC for the majority of my PhD duration. His enthusiasm for a dazzling array of topics in the world of cancer liquid biopsy and his ability to decompose any problem or idea into its key principles – and his passion for guiding students to do so – is quite simply, inspiring.

I was brought up to speed by dozens of outstanding and collaborative people to all of whom I am thankful. My PhD committee at McGill University, Prof. S. Wachssman-Hogiu, Prof. A. Ehrlicher, and Prof. S. Omanovic for their technical and inspirational guidance and enthusiasm for this work. Prof. K. Petrecca from Montreal Neurological Institute (MNI) for his critical role in this project providing us with rare Glioblastoma patient samples. Prof. W. Reisner for taking the time out of a busy schedule to mentor me on critical writing. Dr. Roozbeh Siavash Moakhar for his mentorship in analytical chemistry, Dr. Sahar Mahshid, for sharing her experience in the field of biosensing and Laura Montermini, who taught me a great deal in cell biology.

I would like to thank the scholarships and fellowships that unburdened my mind financially and allowed me to focus primarily on my research, McGill Engineering Doctoral Award (MEDA)

and Fonds de recherche du Québec Nature et technologies (FRQNT), and MedTech Talent Accelerator internship.

I was fortunate to work directly with many different researchers and staff, all of whom shared experience and expertise that enhanced my time at McGill. Biological and Biomedical Engineering staff Pina Sorrini, Xavier Elisseff, and Aimee Jabour for always being there to help students. In nanofabrication and characterization, I thank the NFF, GCM and FEMR center staff, Dr. Zhao, Dr. Bernier and Dr. Sears who facilitated the procedures with their technical insights. All professors, staff, and students at the Bioengineering Department of McGill University for creating such a rich and collaborative environment to prosper. Especially staff and students at Nano-Bio Medical Devices Lab, Roozbeh, Tamer, Carolina, Yao, and Imman, with whom we grew together with the kind of discourse you dream graduate school will involve.

My cohort at McGill has been a great group of people to spend time with. I thank all the friends I've met through the shared office spaces, collaborations, Graduate Engineering Equity Committee (GEEC), and Thompson House clubs. Having passions outside of grad school is all but essential for survival, and the fantastic people I've met have helped keep me sane through it all.

Finally, I would like to express my sincerest gratitude to my family for their constant and unlimited love and support. To my parents, the best teachers I've ever known, for their never-ending encouragement and their solid belief in me. To my sister Melika and my brother Amirhossein for always being a huge inspiration. To my husband, Roozbeh, who has been with me and encouraging me through this process literally every step of the way. I could not possibly express the gratitude here that is commensurate with the support you have provided.

Table of Content

List of Figures and Tables

1 Introduction

1.1 Contribution to Original Knowledge

The on-chip optical interrogation of single EV strategy developed by the candidate is a novel and innovative approach to molecular profiling of EVs in complex biological samples (tissue cells, CSF, and blood plasma) to stratify and identify the underlying molecular traits that represents development of the resistant genes in the tumor. This work has the potential to lead to new molecular profiling tools for monitoring the evolution of hard to access cancers, such as glioblastoma (GBM). Overall, this thesis represents a significant contribution to the field of biosensing and has the potential to drive further research and development in this area.

This thesis presented a significant contribution to the field of cancer research by developing portable platforms that can distinguish molecular profiling of cancer EVs from different tumor cell lines grown under controlled conditions against non-cancer EVs. The thesis aimed to distinguish the signatures of brain cancer paradigmatic molecular subtypes, including EGFRvIII and MGMT, a marker of resistance to chemotherapy. The research used multifunctional plasmonic nanostructured materials in the ordered confined spaces integrated with surface chemistry of functional mono- or few-layer 2D materials such as graphene and MoS_2.

The study developed customizable on-chip plasmonic nanoarrays promoted with 2D nanomaterials for label-free investigation of molecular alteration traits in heterogeneous circulating EVs in translational research settings as an alternative liquid biopsy technique. The research involved the design, fabrication, and optimization of the plasmonic nanoarrays with enhanced optical and electrical properties to improve Raman spectroscopy and optical signal distinction. The thesis reported on the potential of single EV SERS for differentiation of the EVs

derived from molecularly altered cancer cell lines (GBM) and compiled their spectra as a reference library.

The thesis demonstrated the potential of single EV SERS fingerprinting in monitoring the transformational events in tumor-derived cells that cause resistance to therapy (temozolomide chemotherapy). The thesis transitioned from an overview of the technologies integrating plasmonic nanostructured arrays, monolayer and few-layer materials, and surface-enhanced optical sensing into a more comprehensive nanosurface microchip design for translational study of cancer (GBM) patients via extracellular vesicles as liquid biopsy biomarkers.

The thesis's ultimate vision involves the integration of optimized nanosurface on-chip detection platforms connected to advanced signal analysis methods in translational diagnosis of molecular alteration traits in the heterogeneous circulating EVs as an alternative liquid biopsy approach. This doctoral project presents a promising approach for the early diagnosis of cancer and monitoring of treatment efficacy using non-invasive liquid biopsy biomarkers. The results of this research have the potential to significantly impact cancer diagnosis, treatment, and patient care.

Publication List:

1. Mahsa Jalali, Carolina del Real Mata, Olivia Jeanne, Laura Montermini, Imman I. Hosseini, Zonglin Gu, Cristiana Spinelli, Yao Lu, Marie-Christine Guiot, Zhi He, Sebastian Wachsmann Hogiu, Ruhong Zhou, Kevin Petrecca, Walter Reisner, Janusz Rak, Sara Mahshid, MoS_2 -Plasmonic Nanocavities for Raman Spectra of Single Extracellular Vesicles Reveal Molecular Progression in Glioblastoma, ***ACS Nano***, 2023, DOI: 10.1021/acsnano.2c09222, Featured cover art.
2. Mahsa Jalali, Iman Isac Hosseini, Tamer AbdelFatah, Laura Montermini, Sebastian Wachsmann Hogiu, Janusz Rak, Sara Mahshid, Plasmonic Nanobowtiefluidic Device for Sensitive Detection of Glioma Extracellular Vesicles by Raman Spectrometry, ***Lab on Chip*** 2020, DOI: 10.1039/D0LC00957A. Featured inside cover art.

3. Tamer AbdelFatah[†], Mahsa Jalali [†], Sripadh Guptha Yedire, Imman I. Hosseini, Carolina del Real Mata, Haleema Khan, Seyed Vahid Hamidi, Olivia Jeanne, Roozbeh Siavash Moakhar, Myles McLean, Dhanesh Patel, Zhen Wang, Geoffrey McKay, Mitra Yousefi, Dao Nguyen, Silvia M. Vidal, Chen Liang, Sara Mahshid, Nanoplasmonic amplification in microfluidics enables accelerated colorimetric quantification of nucleic acid biomarkers from pathogens. ***Nature Nanotechnology***, 2023, DOI: 10.1038/s41565-023-01384-5, [†]These authors equally contributed to this work.

4. Mahsa Jalali, Roozbeh Siavash Moakhar, Tamer Abdelfattah, Elizabeth Filine, Sahar Sadat Mahshid, and Sara Mahshid, Nanopattern-Assisted Direct Growth of Peony-like 3D MoS_2/Au Composite for Nonenzymatic Photoelectrochemical Sensing, ***ACS Applied Materials & Interfaces*** 2020, 7411-7422, DOI: 10.1021/acsami.9b17449.
5. Mahsa Jalali, Elizabeth Filine, Samantha Dalfen, Sara Mahshid, Microscale Reactor Embedded with Integrated Graphene/ Hierarchical Gold Nano/ Microstructures for Electrochemical Sensing, ***Microchimica Acta***, DOI: 10.1007/s00604-019-4059-4.
6. Mahsa Jalali, Tamer AbdelFatah, Sahar Sadat Mahshid, Mahmoud Labib, Ayyappasamy Sudalaiyadum Perumal, Sara Mahshid, A Hierarchical 3D

Nanostructured Microfluidic Device for Sensitive Detection of Pathogenic Bacteria, ***Small***, 2018, DOI: 10.1002/smll.201801893.

7. Roozbeh Siavash Moakhar, Carolina del Real Mata, Mahsa Jalali, Houda Shafique, Alireza Sanati, Justin de Vries, J. Strauss, Tamer AbdElFatah, Fatemeh Ghasemi, M. McLean, Imman Hosseini, Sahar S. Mahshid, M. A. Tabatabaiefar, C. Liang, Sara Mahshid, A Versatile Biomimic Nanotemplating Fluidic Assay for Multiplex Quantitative Monitoring of Viral Respiratory Infections and Immune Responses in Saliva and Blood, ***Advanced Science***, 2022, DOI: 10.1002/advs.202204246.
8. Carolina del Real Mata, Roozbeh Siavash Moakhar, Iman Hosseini, Mahsa Jalali, Sara Mahshid, A nanostructured microfluidic device for plasmonic-assisted electrochemical detection of hydrogen peroxide released from cancer cells, ***Nanoscale,*** 2021, DOI: 10.1039/D0NR07608B.
9. Tamer AbdelFatah, Mahsa Jalali, Sara Mahshid, Multifunctional nanofilter for fluidic devices by pillar-assisted self-assembly microparticles, ***Biomicrofluidics***, 2018, DOI: 10.1063/1.50486.

1.3 Contribution of Authors

This thesis is presented as a collection of manuscripts written by the candidate with the assistance, collaboration and supervision of the co-authors. The candidate has played a significant role in the creation of the design, fabrication (ebeam lithography, fab-less self-assembly nanoparticle lift-off) and development of nanosurface on-chip biosensing strategy and its associated methods. The candidate was responsible to conduct majority of the surface characterizations (including electron microscopy, atomic force microscopy and others), optical interrogation of extracellular vesicles (EVs) experiments via fluorescent microscopy and surface - enhanced Raman spectroscopy (SERS). The candidate was responsible for theoretical studies via finite difference time-domain (FDTD) for feasibility characterizations of the structures for effective optical properties. The candidate has taken an active role in the design of the experiments with supervisory oversight of Prof. Mahshid, acquired data and ran the analysis for the research presented in this thesis. The contribution of the candidate alongside the other co-authors are described in detail I the following section:

Project (1)

Plasmonic Nanobowtiefluidic Device for Sensitive Detection of Glioma Extracellular Vesicles by Raman Spectrometry

Mahsa Jalali,[a] Sayed Imman Isac Hosseini,[a] Tamer AbdelFatah,[a] Laura Montermini,[b] Sebastian Wachsmann Hogiu,[a] Janusz Rak,[b] Sara Mahshid*[a]

[a]Department of Bioengineering, McGill University, Montreal, QC H3A 0E9, Canada

[b]Research Institute of the McGill University Health Centre (RIMUHC), Montreal, Quebec, Canada

M.J. initiated the idea, design and fabrication protocols, performed the physical characterizations including SEM, and fluorescent microscopy; performed FDTD modelling, assisted in EV isolation and purification, performed SERS data collection and multivariate analysis, performed data analysis and contributed to writing the manuscript. S.I.I.H. performed the theoretical studies of the fluid flow and pressure inside the microfluidic device to optimize the design parameters and contributed to the COMSOL studies of the fluid flow. T.A. designed and fabricated the microfluidic device and contributed to the COMSOL studies of the fluid flow. L.M. contributed in EVs sample preparation, purification, and running the standard tests. J.R. provided the EVs and samples from GBM cell lines for the entire project, advice on the EV's biological and contributed to the writing of the manuscript. S. M. supervised the project from the idea to development, contributed to the design of the figure sets and writing of the manuscript.

Project (2)

MoS_2- Plasmonic Nanocavities for Raman Spectra of Single Extracellular Vesicles Reveal Molecular Progression in Glioblastoma

Mahsa Jalali[1], Carolina del Real Mata[1], Laura Montermini[2], Olivia Jeanne[1], Imman I. Hosseini[1,3], Zonglin Gu[4], Cristiana Spinelli[2], Yao Lu[1], Nadim Tawil[2], Marie Christine Guiot[5], Zhi He[6], Sebastian Wachsmann-Hogiu[1], Ruhong Zhou[6], Kevin Petrecca[5], Walter W. Reisner[3], Janusz Rak[2], Sara Mahshid[1,7*]

[1] Department of Bioengineering, McGill University, Montreal, QC, H3A 0E9 Canada

[2] Research Institute of the McGill University Health Centre (RIMUHC), Montreal, Quebec, H4A 3J1 Canada

[3] Department of Physics, McGill University, Montreal, QC, H3A 2T8 Canada

[4] College of Physical Science and Technology, Yangzhou University, Jiangsu, 225009 China

[5]Department of Neuropathology, Montreal Neurological Institute-Hospital, McGill University, Montreal, Quebec, H3A 2B4 Canada

[6] Institute of Quantitative Biology, College of Life Sciences, Zhejiang University, Hangzhou, 310058 China

[7] Division of Experimental Medicine, McGill University, Montreal, QC, H4A 3J1 Canada

M.J. initiated the idea, design, and fabrication protocols, performed the physical characterizations, sample preparation, SERS data collection, FDTD modelling, data processing and analysis as well as writing the manuscript. C.D.R.M. contributed to the SERS data collection, running machine learning algorithm and writing the manuscript. O.J. contributed with the machine learning algorithms and data analysis. L.M. and N.T. contributed in EVs sample preparation, purification, and running the standard tests. I.I.H. contributed to the fabrication of the fluidic device and theoretical studies with MD. Z.G. and Z.H. contributed to the MD simulations and data collection. C.S. contributed to providing CAS-9 gene altered glioma stem cell lines. Y.L. contributed to the SERS experiments. K.P. provided patient samples and clinical annotations. M.C.G contributed to patient samples phenotyping and pathological tests. R.Z. provided the design and analyses on the theoretical studies with MD. S.W.H. provided advice on SERS optimization and functionality of the platform. W.R. provided advice on single EVs confinement and contributed to writing of the manuscript. J.R. provided the EV samples from GBM cell lines for the entire project, advice on the EV's biological and contributed to the writing of the manuscript. S.M. supervised the project

from the idea to development, contributed to the design of the figure sets and writing of the manuscript.

Project (3)

Biomarker-Free Single Extracellular Vesicle SERS for Molecular Profiling of Resistance in Glioblastoma

Mahsa Jalali[1], Yao Lu[1], Laura Montermini[2], Janusz Rak[2], Sara Mahshid[1,3*]

[1] Department of Bioengineering, McGill University, Montreal, QC, Canada

[2] Research Institute of the McGill University Health Centre (RIMUHC), Montreal, QC, Canada

[3]Department of Medicine, Division of Experimental Medicine, McGill University, Montreal, QC, Canada

M.J. initiated the idea, design, and fabrication protocols, performed the physical characterizations, sample preparation, SERS data collection, FDTD modelling, data processing and analysis, designing the library for machine learning as well as writing the manuscript. Y.L. contributed to the SERS data collection, running machine learning algorithm and writing the supporting information. L.M. contributed in EVs sample preparation, purification, and NTA tests. J.R. provided the EV samples from GBM cell lines for the entire project, advice on the EV's biological and contributed to the writing of the manuscript. S.M. supervised the project from the idea to development, contributed to the design of the figure sets and writing of the manuscript.

1.4 Scope of Thesis

1.4.1 Objectives and Aims

The primary vision of this research is to develop portable platforms based on multifunctional plasmonic nanostructured materials in ordered confined spaces to distinguish the molecular profiling of cancer EVs from different tumor cell lines against non-cancer EVs. This research will study the contribution of surface morphology, lattice geometry and electronic properties of materials in the highly sensitive surface-enhanced optical molecular profiling of biological analytes. Next, the aim is to distinguish the signatures of brain cancer paradigmatic molecular subtypes. The focus of this dissertation is to identify the underlying principles for translational molecular profiling of circulating EVs from Glioblastoma cancer patients via single EV SERS fingerprinting. Then, the thesis aims to demonstrate the successful incorporation of the single EV SERS in the translational investigation of the molecular alteration hallmark in specific patients diagnosed with the most common and aggressive primary astrocytic brain tumor, Glioblastoma (GBM). This dissertation covers a broad range of technological developments in the field of nanosurface on-chip biological detection based on customizable plasmonic nanoarrays promoted with 2D nanomaterials, that is used for detection and diagnosis of heterogeneous extracellular vesicles as circulating EVs with high sensitivity, throughput, and rapidity in the absence of a bioassay via surface-enhanced optical microscopy and spectroscopy. Finally, the ultimate goal of this study is to differentiate the mutational epigenetic molecular traits in the patient samples and to determine the molecular traits that participate in resistance to the chemotherapy using a label-free and minimally invasive single EV SERS method, as a potential tool for monitoring tumor transformation via liquid biopsy.

Objective 1: Develop a robust and reliable platform for single EV entrapment for surface-enhanced optical interrogation. Over the course of understanding the nanostructured materials properties in confined geometrical spaces for detection of bioanalytes with nanoscale geometrical magnitude, the objective is to seek an approach to convey biorecognition element-free identification and monitoring of heterogeneous EVs as a potential cancer liquid biopsy marker.

Ob1.1 Design and fabricate microchips based on confined hybrid plasmonic nanosurfaces: The aim is to develop a microchip based on a hybrid nanocavity plasmonic surface for capturing the Raman spectra of single extracellular vesicles (EVs). This aim is to study hybrid plasmonic nanoarrays (convex and concave) promoted with monolayer materials to fabricate an efficient platform to enhance the electromagnetic field efficiency and consecutively improve the resolution of the SERS spectra in low concentrations down to single EV resolution. By combining bottom-up and top-down fabrication techniques we aim to fabricate the following building blocks of the platforms: (I) a top-down lithography technique (photolithography) will be used to pattern sample delivery system and the micro/nanoscale windows on the substrates followed by (II) patterning of nanostructured materials that can support surface plasmon resonance (such as gold, silver and aluminium) via colloidal self-assembly patterning or ebeam lithography. As part of the characterization, the surface morphology (SEM, TEM, AFM), physical light-matter interaction (FDTD simulation, UV-visible) and material properties (Raman spectroscopy, EDS) of the on-chip nanostructured platforms.

Ob1.2 Optimize the platform to achieve high-resolution molecular profiling of individual EVs, ensuring accurate single EV entrapment and sustained EVs during SERS experiments: The aim is to establish a robust and reliable platform capable of capturing and characterizing individual EVs at high resolution. Validate the platform using control bilayer lipid liposomes and EVs derived

from cells, focusing on single EV entrapment and the system's ability to sustain EVs during SERS experiments. By establishing a robust and reliable platform and validating it using control samples and cell derived EVs, this project aims to assess the platform's capability for single EV entrapment, ensuring that it can accurately isolate and analyze single EVs. To address this, we aim to experimentally study the interaction of bilayer lipids and active materials and establish characterized EVs entrapped in the plasmonic concave (nanocavity-like) platform via SEM, EDS, fluorescent microscopy and other methods.

Ob1.3 Validate the sensitivity of the platform using control Raman markers, bilayer lipid liposomes and cell derived EVs: The aim is to establish the parameters to optimize the Raman spectroscopy molecular profiling of EVs based on their SERS fingerprinting to differentiate EVs derived from different origins. To address this, we aimed to theoretically and experimentally investigate the performance of the on-chip hybrid plasmonic nanoarrays for surface-enhanced optical readout methods (i.e. surface-enhanced Raman spectroscopy and validate by surface-enhanced fluorescent microscopy) using well characterized SERS markers such as Rhodamin6G, controlled bilayer lipid liposomes and EVs derived from well characterized cell lines (cancerous and non-cancerous) in controlled environment.

Objective 2: Investigate the potential of single EV SERS interrogation in enhancing the differentiation of glioblastoma-specific variants. The aim is to investigate the potential of single EV SERS interrogation in enhancing the differentiation of glioblastoma-specific variants in characterized cell-derived EVs. In this section, the project aims to delve into the potential of single EV SERS fingerprinting for improving the differentiation of glioblastoma-specific variants present in well-characterized cell-derived EVs. This investigation will provide valuable insights into the

molecular heterogeneity of glioblastoma and contribute to a deeper understanding of the molecular diversity within glioblastoma tumors.

Ob2.1 Perform SERS fingerprinting on characterized cell-derived EVs from glioblastoma-specific variants: The aim is to investigate the potential of single EV SERS interrogation in enhancing the differentiation of glioblastoma-specific variants in characterized cell-derived EVs. In this section, the project aims to delve into the potential of single EV SERS fingerprinting for improving the differentiation of glioblastoma-specific variants present in well-characterized cell-derived EVs. This investigation will provide valuable insights into the molecular heterogeneity of glioblastoma and contribute to a deeper understanding of the molecular diversity within glioblastoma tumors.

Ob2.2 Analyze and compare the SERS spectra to identify molecular changes associated with glioblastoma subtypes. The aim is isolate EVs at the single level to differentiate EVs derived from cancer cell lines bearing molecular alteration traits representative of the GBM cancer hallmark (EGFR amplification, EGFRvIII, PTEN and MGMT) using their SERS molecular profiling by developing and customizing an on-chip, nanoarray assay for surface-enhanced optical readout methods (i.e. surface-enhanced Raman spectroscopy and validate by surface-enhanced fluorescent microscopy) while building a library of 70-100 spectra from each set of cell lines (12 cell lines).

Ob2.3 Study the differentiation of drug-resistant glioblastoma-specific variants through the application of single EV SERS interrogation technique in cell derived EVs. The aim is to explore the ability of single EV SERS fingerprinting to detect and analyze molecular changes associated with temozolomide (TMZ) resistance in glioma stem cell lines, providing valuable insights into treatment response on these stem cells. This section focuses on exploring the capability of single

extracellular vesicle EV SERS fingerprinting to identify and analyze molecular changes associated with resistance to TMZ in glioma stem cell lines. By investigating the single EV fingerprint alterations underlying TMZ resistance, this project aims to provide valuable insights into liquid biopsy monitoring treatment response and potential therapeutic strategies targeting resistance in GBM.

Objective 3: Quantify and analyze single EV SERS fingerprint results from circulating EVs in glioblastoma patients for clinical evaluation and explore detection of molecular changes associated with TMZ resistance. The objective is to investigate the potential of single EV SERS interrogation in enhancing the differentiation of glioblastoma-specific variants in characterized cell-derived EVs and circulating EVs found in the plasma samples of patients. The aim is to evaluate the single EV SERS differentiation in categorizing the circulating EVs according to the probability of expressing certain GBM-specific molecular alterations.

Ob3.1 Perform single EV SERS analysis on circulating EVs to obtain single SERS fingerprint results: The aim is to quantify and analyze the single EV SERS fingerprint results obtained from circulating EVs in the cerebrospinal fluid (CSF) and plasma of glioblastoma patients for differentiation between the positive and negative state. To quantify and analyze the SERS results obtained from circulating EVs in the samples of glioblastoma patients. The aim is to evaluate the diagnostic value and clinical potential of single EV SERS analysis as a non-invasive method for assessing treatment responses, monitoring disease progression, and informing clinical decision-making.

Ob3.2 Quantify and analyze the SERS fingerprint results to differentiate between positive and negative states. The *third* aim is to stratify these molecular traits in circulating plasma EVs of cancer patients (diagnosed with GBM) using their SERS molecular profiling, thus distinguishing

between patients who carry these molecular traits, by customizing an on-chip nanoarray assay for sensitive single EV SERS molecular profiling.

Ob3.3 Study the differentiation of glioblastoma-specific variants in circulating EVs through the application of single EV SERS interrogation techniques. The molecular profiling of the healthy- and patient- derived circulating EVs is tested and compared with the library of the SERS fingerprint from controlled cell line EVs bearing (EGFR amplification, EGFRvIII, and MGMT) mutations. The human EV samples are then stratified according to the similarity of their SERS spectra to that of the cell lines grown in controlled condition. In addition, it is in interest of this objective that the underlying molecular profile representing drug resistance in the hallmark of GBM is highlighted via single EV SERS to understand the extent of its potential in therapeutic roadmap. This dissertation, is focused not only on developing and evaluating technologies based on developing confined plasmonic frameworks promoted with 2D nanomaterials for quantifiable detection of biomarkers, but also on testing the underlying principles for translational molecular profiling of circulating EVs from GBM cancer patients via liquid biopsy of EVs.

Ob3.4 Identify and analyze the alterations in the single EV SERS fingerprints associated with TMZ resistance. Assess the diagnostic value and clinical potential of SERS analysis as a non-invasive method for evaluating the resistant towards treatment, with future potential in aiding in clinical decision-making. To explore the molecular changes reflected in the SERS spectra that contribute to cellular responses to temozolomide (TMZ) chemotherapy, a cornerstone of standard care in glioblastoma patients. This aim involves investigating specific molecular mechanisms, such as the expression of O^6-methylguanine DNA methyltransferase (MGMT) or the presence of a hypermutant phenotype, which influence the response to TMZ and contribute to drug resistance.

1.4.2 Rationales

For cancers with low survival rates technologies enabling non-invasive monitoring and diagnostic accessibility are key to improving care. Current cancer diagnostics consists of imaging and tissue sampling (at surgery or biopsy) that are costly and fail to give a rapid, safe and frequent access to the information regarding disease progression and therapeutic responses.(Reifenberger et al., 2017a) Liquid biopsy represents an emerging paradigm in cancer with the potential to assess cancer status rapidly, continually with minimal invasiveness and in a clinically actionable manner.(S Rickard et al., 2020) Extracellular vesicles (EVs) are a promising platform for liquid biopsy applications in cancer (Pan et al., 2021; Shao et al., 2012b, 2015).

EVs are heterogeneous lipid-bilayer based vesicular structures shed into biofluids from most cells including cancer cells. Circulating EVs are an attractive option for liquid biopsy of hard-to-access tumors such as glioblastoma (GBM) because they contain a wide-range of molecular cargo, such as proteins and nucleic acids, that may serve as cancer-specific markers.(Boriachek et al., 2018; Im et al., 2014a; Mollaei et al., 2017; C.-Y. Wu et al., 2017; Y. G. Zhou et al., 2016) Critically, as each EV represents a specific cell, the cancer markers contained in the tumor derived EV landscape relate to the properties of a given cellular population reflecting its diversity.(Zachariah et al., 2018) Consequently, the information contained in a population of individual EVs can capture the remarkable and clinically important traits reflective of cellular heterogeneity in cancer (Al-Nedawi et al., 2008a; Ramirez et al., 2018a). The development of a microchip based on a hybrid nanocavity plasmonic surface for capturing and characterizing single extracellular vesicles (EVs) is crucial. Current methods for EV analysis lack the resolution and sensitivity required for studying individual EVs and their molecular content. By developing a robust and reliable platform for single EV entrapment and surface-enhanced Raman spectroscopy

(SERS), we can overcome these limitations and achieve high-resolution molecular profiling of EVs. This technology will enable us to study EVs derived from different tumor cell lines, including cancer and non-cancer EVs, and distinguish their molecular profiles. By validating the platform using control bilayer lipid liposomes and cell derived EVs, we can ensure its accuracy and reliability in capturing and sustaining EVs during SERS experiments.

In addition, mutational and epigenetic driver events profoundly alter the release, molecular composition, and biological activity of EVs, which, therefore, may contain signatures of these diagnostically crucial influences.(Boriachek et al., 2018; Im et al., 2014a; Mollaei et al., 2017; C.-Y. Wu et al., 2017) Notably, EVs carry signatures of cancer molecular subtypes, which are essential for proper stratification of patients included in clinical studies.(Lane et al., 2019) Among the paradigmatic molecular characteristics of GBM cells that can be revealed through EV analysis are the mutant oncogenic variant of epidermal growth factor receptor (EGFR), known as EGFRvIII(Al-Nedawi et al., 2008a), as well as O^6-Methylguanine-DNA Methyltransferase (MGMT), a marker of resistance to chemotherapy. By utilizing single EV SERS fingerprinting, we can delve deeper into the molecular characteristics of glioblastoma-specific variants and improve their differentiation. This preclinical validation will provide valuable insights into the molecular changes associated with temozolomide (TMZ) resistance in glioma stem cell lines. Understanding the treatment response and mechanisms underlying resistance in these stem cells is crucial for developing effective therapeutic strategies.

The quantification and analysis of single EV SERS fingerprint results obtained from circulating EVs in glioblastoma patients can offer a non-invasive method for assessing treatment responses and monitoring disease progression. Traditional diagnostic methods for glioblastoma are invasive, costly, and time-consuming. By evaluating the diagnostic value and clinical potential of

single EV SERS analysis, we aim to provide a non-invasive alternative that can aid in clinical decision-making. Additionally, investigating the potential of single EV SERS interrogation in enhancing the differentiation of glioblastoma-specific variants in characterized cell-derived EVs and circulating EVs found in plasma samples can provide valuable information for categorizing and characterizing the molecular alterations associated with glioblastoma. This knowledge can contribute to personalized treatment approaches and improve patient outcomes. Moreover, assessing the molecular changes reflected in the SERS spectra that contribute to cellular responses to temozolomide (TMZ) chemotherapy is crucial for understanding drug resistance mechanisms and developing targeted therapies. By exploring specific molecular mechanisms such as the expression of O^6-methylguanine DNA methyltransferase (MGMT) or the presence of a hypermutant phenotype, we aim to uncover insights that can aid in monitoring drug resistance in glioblastoma patients.

With existing technologies, we are subjected to use bioassays that comprise the core components of today's diagnostic armamentaria. While bioassay's complexity, delicacy and error-prone quantification of the target concentration together with finite number of available receptors and fluorophores with non-overlapping spectra are limiting their use. Development of portable on-chip devices for molecular profiling of the heterogeneous EVs as circulating cancer biomarkers and monitoring of their molecular transformational events can exceptionally improve understanding of the complexity of the cancer and monitoring its development.

1.4.3 Hypothesis

We hypothesize that a label-free molecular profiling analysis technique such as surface-enhanced Raman spectroscopy (SERS) could potentially improve diagnostic accuracy necessary to distinguish cancer EVs amongst a large background of host EVs without need for

immunoaffinity based capture. Development of portable on-chip devices for molecular profiling of the heterogeneous EVs as circulating cancer biomarkers and monitoring of their molecular transformational events can exceptionally improve understanding of the complexity of the cancer and monitoring its development.

Initially we concentrated on the hypothesis that the fabless plasmonic nanobowtie array with advanced characteristics of plasmonic gaps combined with a high throughput sample-delivery system for concentration of the EVs at the vicinity of the detection site has the potential for label-free and non-immunological SERS detection of EVs to distinguish between different cancer cell lines.

In addition, approaches that can yield molecular level information usually average over multiple EVs, which hamper access the diagnostically and therapeutically significant information contained inside encapsulated EV cargo. In particular, the lack of single EV level resolution is a fundamental consequence of the large, exposed capture area of existing EV sensing technology.

We hypothesized that single EV molecular profiling analysis via SERS could potentially distinguish the fingerprint spectra of EVs derived from mutated cells compared to their parental counterparts. We presumed that the on-chip plasmonic nanocavities promoted with single crystalline monolayer MoS_2 has the potential to achieve single EV resolved SERS spectrum due to three main factors. Firstly, our optimized photonic design achieves sufficiently strong in-cavity field enhancement to produce sufficient signal to obtain SERS spectra from single EVs. Secondly, relying on attractive interactions between the EV lipid membrane and the MoS_2 monolayer, we obtain EV entrapment in nanocavities without requiring biological recognition elements. Thirdly, as the cavities are made sufficiently small to accommodate only a single EV, we ensure that the spectrum obtained from a single cavity in fact corresponds to the spectrum of a single EV.

In conclusion, we hypothesized that developing portable platforms based on multifunctional plasmonic nanostructured materials in ordered confined spaces promoted with the surface chemistry characterizations of 2D nanomaterials have the potential to (1) distinguish the molecular profiling of cancer EVs from different tumor cell lines against non-cancer EVs, (2) distinguish the signatures of brain cancer paradigmatic molecular subtypes against their parental counterparts, (3) stratify the molecular alteration hallmark in patients diagnosed with the most common and aggressive primary astrocytic brain tumor, GBM, in a translational investigation.

1.4.4 Chapter Summary

In this thesis, we illustrated the attempts that led to on-chip plasmonic nanostructured platforms with enhanced light-matter interaction properties suitable for surface-enhanced optical investigation of EVs. In the following chapters, manuscripts on successful attempts in designing on-chip plasmonic nanoarray platforms for molecular interrogation of EVs are discussed.

During my PhD, I worked on developing novel technologies for the real-time monitoring of complex cancers such as glioblastoma (GBM) using extracellular vesicles (EVs). These EVs are continually released from cancer cells into biofluids and carry actionable molecular fingerprints of the underlying disease. However, their scarcity, heterogeneity, and intrinsic complexity present a major technological challenge.

In my first project, I reported on a nanostructured microfluidic device that employs surface-enhanced Raman spectroscopy (SERS) for unambiguous identification of EVs from different GBM cell populations. The device features fabless plasmonic nanobowties for label-free and non-immunological SERS detection of EVs. The optimized fabless nanobowtie structures with an average electric field enhancement factor of 9×10^5 achieved distinguishable and high-intensity SERS signals. Using the nanobowtie fluidic and a micro-Raman equipment, we were able to

distinguish a library of peaks expressed in GBM EVs subpopulations from two distinct Glioblastomas cell lines (U373, U87) and compare to that of non-cancerous glial EVs (NHA) and artificial homogenous vesicles. The cost-effective and easy-to-fabricate SERS platform and a portable sample-delivery system for discerning the sub-population GBM EVs and non-cancerous glial EVs may have broader applications to different types of cancer and their molecular/oncogenic signature.

In my second project, I developed a multiplex fluidic device with embedded arrayed nanocavity microchips (MoSERS microchip) that achieves 97% confinement of single EVs in a minute amount of fluid (<10 μl) and enables molecular profiling of single EVs with SERS. The nanocavity arrays combine two featuring characteristics: (1) An embedded MoS_2 monolayer that enables label-free isolation and nanoconfinement of single EVs due to physical interaction (Coulomb and van der Waals) between the MoS_2 edge sites and lipid bilayer; and (2) A layered plasmonic cavity that enables sufficient electromagnetic field enhancement inside the cavities to obtain single EV level signal resolution for stratifying the molecular alterations. We used the GBM paradigm to demonstrate the diagnostic potential of the SERS single EV molecular profiling approach. MoSERS multiplexing fluidic achieves parallel signal acquisition of glioma molecular variants (EGFRvIII oncogenic mutation and MGMT expression) in GBM cells. When interfaced with a convolutional neural network (CNN), MoSERS improved diagnostic accuracy (87%) with which GBM mutations were detected in 12 patient blood samples, on par with clinical pathology tests. Thus, MoSERS demonstrates the potential for molecular stratification of cancer patients using circulating EVs.

In my third project, I explored the molecular changes that contribute to the cellular evolution of TMZ-naïve and -resistance xenograft models in a series of human glioma stem cells

(GSCs) with mesenchymal molecular characteristics using single EV SERS technology. GSC 1123 parental and genetically modified cells to express representation of O^6-methylguanine DNA methyltransferase (MGMT) upregulation were used to identify the correlated molecular traits compared with the parental cells. The presence of these characteristic molecular traits was monitored in the presence of TMZ after 24 and 72 hours. This observation demonstrated the set of molecular traits responsible for the acquisition of TMZ resistance in GBM. The findings showed that SERS technology can be used to monitor molecular changes underlying the EVs and detect resistance development. This study provides a basis for a more comprehensive understanding of the molecular mechanism.

1.5 Motivation and Background

Motivation- Although the conventional clinical modalities are cornerstones of diagnosis, there is an urgent need for fast, sensitive, low-cost, and easy-to-operate portable devices. The development of on-Chip diagnostic methods that are central to a minimally invasive diagnosis based on blood circulating biomarkers have the potential to revolutionize diagnosis in particular cancer liquid biopsy. The main challenge of using blood as the reservoir of tumour biomarkers lies in considerably lower concentrations of them requiring exceptionally higher sensitivity (Arraud et al., 2014). The common and widely established clinical tests for cancer biopsy as clinical diagnostic tools which have been used for over a century and are now the gold standard cancer diagnosing (Robersona et al., 2010; K. S. Yang et al., 2017a), are not only costly, but also fail to give a rapid, safe and frequent access to the information regarding disease progression and therapeutic responses. One-time biopsy, consisting of either a piece of a surgical specimen or a needle aspirate, may not fully represent a tumor's genomic landscape and may introduce bias in evaluation because of the heterogeneity. For personalized cancer management, an alternative to

tissue-based biopsy that provides multiple and serial specimens enables integral and dynamic monitoring of cancer progression and treatment response(Biswas et al., 2020). In particular, for cancers with low survival rates, technologies enabling non-invasive monitoring and diagnostic accessibility are key to improving care.

EVs represent a promising platform for liquid biopsy applications in GBM. EVs are heterogeneous structures shed into the biofluids by all cells thereby exteriorizing their unique fingerprints.(Im et al., 2014b; Mollaei et al., 2017; C.-Y. Wu et al., 2017) For this reason, EVs are attractive liquid biopsy analytes in cancer, given the molecular information contained in their delimiting lipid membrane bilayer, as wells as luminal cargo. These constituents are physically integrated into highly complex structures the analysis of which may overcome the limitations associated with soluble analytes including proteins and nucleic acids (Boriachek et al., 2018; Im et al., 2014a; Mollaei et al., 2017; C.-Y. Wu et al., 2017). Indeed, EV populations contain molecular signatures of donor cells, their identity, state, diversity, and degree of transformation including cancer-driving mutations.(Zachariah et al., 2018) EVs also carry distinguishing features of cancer cells from which they originated, and therefore unlike any other liquid biopsy analyte, their composition can capture the remarkable and clinically important traits reflective of cellular heterogeneity in cancer (Al-Nedawi et al., 2008b; Ramirez et al., 2018b). While a number of technologies have been developed for translational detection of EVs derived from blood, these approaches so far either average over multiple EVs, loosing critical information related to cell-to-cell variability or depend on the biorecognition elements.

Surface-enhanced approaches based on the plasmonic effect of the ordered array of nanostructured surface and signal enhancement have been used in this project to investigate the traits of molecular alterations in heterogeneous circulating EVs as alternative cancer biomarkers.

Approaches based on surface-enhanced Raman spectroscopy (SERS) offer considerable advantages due to the high sensitivity of SERS and potential for providing biochemical information on a label-free basis. SERS can already differentiate between biological samples collected from healthy and diseased donors.(S. Feng et al., 2017; Jaena Park et al., 2017; Shin, Oh, Hong, Kang, Kang, Ji, Choi, Kang, et al., 2020a; Jing Wang et al., 2019) However, SERS approaches have the potential to distinguish signals specific to certain molecular traits in the EVs pertaining the mutational epigenetic information on the releasing cells.

Brief Background- Over the past decade, sensitive detection platforms based on the application of nanomaterials(L. Liu et al., 2018; Mustafa et al., 2017) (*e.g.* gold,(Juhong Chen et al., 2016; Du et al., 2011; Saha et al., 2012) Zinc oxide,(X. Yu et al., 2017)) and advanced instrumentation(Váradi et al., 2017; Kaiqiang Wang et al., 2018) (*e.g.* micro-Hall chips,(Issadore et al., 2013; So et al., 2008) microfluidic lab-on-chips,(Dittrich & Manz, 2006; Foudeh et al., 2012; Kim et al., 2017; McClain et al., 2001; Pereiro et al., 2017; Yeo et al., 2011; M. Yu et al., 2018)) for target recognition and signal transduction have been developed in research labs. Amongst, the concept of using portable nanostructured materials platform was coined as a sensitive and durable sensing platform with less fabrication process complexity while enabling integration with any type of fluidic, electrophoretic and field effect devices.

Conductive three-dimensional (3D) nanostructured materials found many applications in the fields of electronic, optics and biological applications(Gittens et al., 2013; Potyrailo & Naik, n.d.; Rose et al., 2011; The et al., 2002; Joseph Wang, 2005). Importantly the 3D nanostructures were found to be promising candidates for probe-free and non-enzymatic detection of different biological analytes based on their surface roughness,(Harris et al., 2007; Pengchao Zhang et al., 2013)morphology(Elbourne et al., 2017; Tripathy et al., 2017; P. Yu et al., 2016) and

physiochemical properties of their interfaces. (X. Fan et al., 2008; Hu et al., 2006; Runrun Wu et al., 2018a; J. Yang et al., 2016) Previous studies demonstrated the contribution of the nanostructured materials in sensitive capturing and detection of biological analytes based on the effects of functionalized carbon nanotube(Ye Yang et al., 2018), photoluminescent gold nanodots(W. Y. Chen et al., 2015), SiO_2 (Massad-Ivanir et al., 2010), Graphene oxide (Runrun Wu et al., 2018b) and prickly zinc-doped cupric oxide (Runrun Wu et al., 2016, 2018b).

Furthermore, 2D materials (Graphene and MoS_2) are layered materials that are sensitive to changes corresponded to binding of biomolecules, proteins and other biological analytes at their interface due to the applied changes in their electrical properties.(Gao et al., 2013) The high sensitivity, low-cost, easy patternability and integrability of graphene and MoS_2 raised attentions in past few years on integrating and decorating them with other materials to enhance their properties in sensing applications (Jing Chen et al., 2016; S. J. Li et al., 2013; C. Zhao et al., 2017; Y. Zhu et al., 2010).

In addition, the surface plasmon resonance platforms have been widely studied over the past decades for biological and chemical sensing applications(Anker et al., 2008; Lodewijks et al., 2013). Both propagating Surface Plasmon Polaritons (SPPs) and Localized Surface Plasmon Resonances (LSPRs) exhibit very interesting properties for sensing applications due to their high degree of tunability and their susceptibility to the dielectric properties of the surrounding environment. (Svedendahl et al., 2009) Moreover, the dimensions of many structures that support (localized) plasmon resonances are very similar to the scales of biological analytes, which makes them an ideal interface to profile the analytes.

Optical read-out systems such as fluorescent microscopy and micro-Raman spectroscopy has been widely studied for detection of biological analytes to visualize and profile them either based on their geometry or fluorescent labels. There are two major parameters affecting the quality of optical microscopy: *first,* bleaching of the fluorophores and *second* reflectivity of the surface. The degree of overcoming these challenges determines the capacity of optical microscopy. (Toma et al., 2013; Kaikai Wang & He, 2018) In addition, sensitive out-of-plane resonance mode of material which is submissive towards surface binding to the material, (C. Lee et al., 2017; Plowman et al., 2014; Premasiri et al., 2005) *and* localized surface plasmon resonance of the substrate, (Biagioni et al., 2013; Link & El-Sayed, 1999b) to enhance optical gain and surface anti-reflectivity.

2 Literature Review

2.1 Introduction

The use of biopsy has been a diagnostic cornerstone for over a century and it remains the gold standard in many fields including cancer (Robersona et al., 2010; K. S. Yang et al., 2017a). With introduction and development of new technologies, biopsy in recent decades was able to provide not only the histological information, but also molecular characteristics of the affected tissue including the expression of relevant genes and proteins, as well as genetic mutations of significance to specific types of cancer, all of which contributed to remarkable changes in disease management(Chaffer & Weinberg, 2011). Despite progress achieved in the use of conventional tissue biopsy techniques and their impact on targeted therapies in cancer, multiple challenges do remain. Indeed, several types and molecular subtypes of cancer are still associated with high rates of morbidity, treatment failure, metastasis, and ultimately mortality aftermaths of the inability of traditional diagnostics to capture and therapeutically respond to the dynamic evolution of the disease. Current gold standard diagnostics based on one time tissue biopsy that are not only costly, but also fail to give a rapid, safe and frequent access to the information regarding disease progression and changing therapeutic responses.[5] Indeed, the absence of alternative non-invasive diagnostic methods is among the major impediments in exploring new therapies. One of the major obstacles in enacting necessary progress is that the traditional biopsy assessments are typically based on tumor tissue obtained from surgery or fine-needle aspiration, which are usually done after the detection of a lesion either clinically or by medical imaging, often at relatively advanced stages in the disease process. Moreover, invasive techniques to obtain tissue specimens limit the use of tissue-based biopsy for routine and recurrent disease screening; thus, patients may be deprived of early treatment opportunities(Piccart-Gebhart et al., 2005). While

recurrent biopsy programs are in place in some clinical settings and in larger centres, in the standard practice obtaining multiple and serial biopsies is challenging and risky, often impossible. Therefore, targeted therapies are normally based on the initial assessments of the primary tumor, while it may no longer be effective during the recurrence and metastasis. In other words, the assessment of molecular markers and targets in primary tumor tissues may not represent their status in real time given the change occurring during tumor evolution and following initial cancer treatment. Likewise, the temporal and spatial tumor heterogeneity may lead to inaccurate determination of the salient molecular characteristics, which may affect the efficacy of conventional and targeted therapies(Mateo et al., 2020). One-time biopsy, consisting of either a piece of a surgical specimen or a needle aspirate, may not fully represent a tumor's genomic landscape and may introduce a bias in the disease evaluation. For personalized cancer management, an alternative to tissue-based biopsy that provides multiple and serial specimens enables integral and dynamic monitoring of cancer progression and treatment response including multiple regions and sites of the malignant growth(Biswas et al., 2020). In particular, for cancers with low survival rates, technologies enabling non-invasive monitoring and diagnostic accessibility of the molecular profile of the disease are key to improving care.

2.1.1 Extracellular Vesicles as Liquid Biopsy Biomarkers

Liquid biopsy represents an emerging paradigm in the space of non-invasive cancer monitoring with the potential to assess cancer status rapidly and continually with minimal invasiveness and in a clinically actionable manner(S Rickard et al., 2020). In recent years, advances in liquid biopsy have enabled the extraction of useful information from tumor-derived material released into biofluids, less invasively and with relatively low cost.(“Liquid Biopsy,”

2021) Circulating blood delivers cells, nutrients, oxygen, and other biochemical components throughout the body and along with them are the circulating carriers of cancer biomarkers, such as circulating tumor cells (CTCs), circulating tumor DNA (ctDNA), and RNA (ctRNA), as well as cancer cell-derived extracellular vesicles (EVs). While all these materials constitute potential platforms for cancer diagnosis(Bardelli & Pantel, 2017; Mader & Pantel, 2017; Pantel & Alix-Panabières, 2016), EVs present unique and significant numerical and biological disadvantages, due to their high numbers in the circulating blood and intrinsic molecular complexity harbouring wealth of biological information about originating cells (Figure 2-1a). As progress in precision oncology is increasingly based on advances in molecular profiling and tumor biomarker analysis of tissues (e.g. through next generation and single cell sequencing of traditional biopsy material), its natural extension into biofluids emerges as the next promising frontier(Choi, Montermini, et al., 2019). However, one obstacle that limits the use of molecular profiling of liquid biopsy analytes is the requirement for higher sensitivity creating pressure on the related technologies and assays. In this regard, great hopes lie with the use of nanotechnology, which offers new analytical opportunities but has yet to impact routine cancer care(Siravegna et al., 2017; Zachariah et al., 2018).

EVs have been shown to represent a promising platform for liquid biopsy applications in cancer diagnostics and monitoring for several compelling reasons related to their biology and structure(Im et al., 2014b; Mollaei et al., 2017; C.-Y. Wu et al., 2017). Thus, the term “EVs” comprises a heterogeneous mixture of lipid bilayer-encased vesicular structures that are shed into biofluids from all cells including cancer cells. Traditionally, liquid biopsy assays targeted circulating tumor cells themselves which may have offered an advantage of size (10–30 μm diameter) and amount of material, which was however off set by relatively low numbers of CTCs

that impeded their harvesting and may not fully reflect the cellular heterogeneity of the underlying cancer. In contrast, EVs represent a relatively new target with unique physical properties, such as markedly smaller size (typically 50–200 nm in diameter), but considerably greater numbers (on the order of 10^{10}/mL of blood) and substantial intrinsic and inter-EV complexity that may better reflect the phenotype of their donor cells and capture the composition of heterogenous cancer cell populations (Yáñez-Mó et al., 2015).

The advent of EV analysis has been slow in coming. Reports on 'particles' detected in various biological systems date back to 1967(Wolf, 1967) and have emerged throughout the intervening years in the context of diverse biological processes, such as hemostasis, bone calcification, cellular secretion and in pathology, such as clotting disorders, immunity and cancer(Couch et al., 2021). A more systematic description of the role of EVs in specific biological processes such as cellular protein export, occurred in early 1980s(Johnstone, 1983; Stahl, 1977; Trams et al., 1981). In 1990s, the function of EVs in immunoregulation was revealed through studies on B lymphocytes and dendritic cells to where EVs are involved in antigen presentation and immune response(Raposo et al., 1996; Zitvogel et al., 1998). Later, the function of EVs was extended to intercellular communication and other processes in cancer and beyond, as recently reviewed(Broekman et al., 2018). Over the past two decades, the astounding diversity of EV subtypes and biogenetic processes have been described in increasing detail(van Niel et al., 2022) and membrane-less extracellular particles (EPs) have entered the scene as yet another aspects of the informative insoluble cellular secretome(Q. Zhang et al., 2021). Regardless of their nature and functions, EVs are now considered one of the most promising sources of circulating cancer biomarkers (Figure 2-1b)(Shao et al., 2018a; Yokoi & Ochiya, 2021).

EVs contain a wide-range of molecular cargo, such as lipids, metabolites, proteins and nucleic acids that may be altered during the malignant process and thereby serve as cancer-specific biomarkers. For example, EV membranes harbor cellular receptors, membrane bound ligands, adhesion molecules and major histocompatibility complex molecules, as well as molecular hubs for various molecular complexes such as sythenin, tetraspanins (CD9, CD63, CD81, CD82), integrins, and other molecules. These constituents are physically integrated into highly complex structures of EVs and the co-expression of which reflects the corresponding features of the originating cell. Because some of these molecules may define the identity, state and function of such donor cells, EVs carrying them may provide essential information as to their cellular sources, or contexts in which a given molecular trait is expressed. Therefore, the analysis of the EV composition may overcome some of the limitations associated with the analysis of single soluble analytes including proteins and nucleic acids, as to which such molecular contexts is not accessible. For these and other reasons, EVs are an attractive and unique option for liquid biopsy(Boriachek et al., 2018; Im et al., 2014a; Mollaei et al., 2017; C.-Y. Wu et al., 2017).

As mentioned earlier, EVs are also highly heterogenous. Thus the information contained in a population of individual EVs can capture the remarkable and clinically important traits reflective of cellular heterogeneity associated with the underlying disease state, such as cancer.(Al-Nedawi et al., 2008b; Ramirez et al., 2018b) This also includes the mutational and epigenetic landscapes of cellular populations, repertoires of driver events, cellular phenotypes and other aspects of cancer (Boriachek et al., 2018; Im et al., 2014b; Mollaei et al., 2017; C.-Y. Wu et al., 2017).

Functionally, EVs are mostly described as protumorigenic in cancer settings, but their subsets may also carry and transfer tumour suppressor genes(Putz et al., 2012) or anti-metastatic

molecules(Plebanek et al., 2017). It has been proposed that certain host cells, such as macrophages in the lymph nodes, may eliminate EVs from the tumour microenvironment and circulation, thereby slowing down tumour growth (Pucci et al., 2016). However, EVs also play a role in many processes indirectly related to cancer progression such as angiogenesis, immunoregulation, coagulation, stroma formation and others, such that establishing their exact biological roles require further studies.

Mutational and epigenetic driver events profoundly alter the release, molecular composition, and biological activity of EVs(Boriachek et al., 2018; Im et al., 2014a; Mollaei et al., 2017; C.-Y. Wu et al., 2017). In addition, EVs become carriers of mutant drivers and functionally important macromolecules unique to specific cancer types and subtypes(Rak, 2013)..

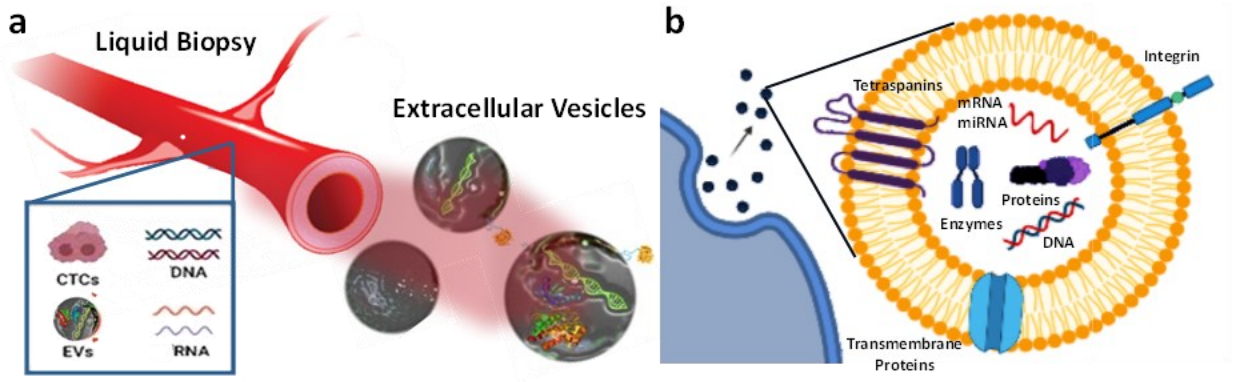

Figure 2.1-1. Liquid Biopsy of EVs. (a) Liquid biopsy markers in blood. (b) The EVs secretion and content reflecting on the important set of information it carries that could give rise to the EVs heterogeneity.

With the promise and advantages of EVs as biomarker platform in cancer, one daunting challenge is the aforementioned barrier of detection, sensitivity and capturing EV complexity. In this regard bulk biochemical analysis methods encounter numerous limitations, so as the emerging single EV detection technologies (e.g. flow cytometry) based on optical analysis of markers {refs}. This technological gap represents a window of opportunity for nanotechnology-based approaches and

ultrasensitive detection using unconventional physical principles. Among them of special interest is the rapidly developing field of plasmonic nanoarrays.

2.1.2 Fundamentals of Plasmonic Nanoarrays for Enhanced Optical Detection

Nanostructured materials have long been used in biosensing with the purpose of enhancing the interaction interface and amplifying the readout signals(W. Li et al., 2019). This is especially relevant when exploiting effective light-matter interaction in the metallic and semi-metallic nanoscale structures leading to phenomena called surface plasmon resonances. It is through these effects that the nanostructures have become widely adopted in optical sensing(Rojalin et al., 2019). A large variety of nanosurfaces including nanoparticle aggregations, nanorough thin films and nanostructured arrays found their way to platforms designed for the isolation and detection of the EVs for the cancer-related liquid biopsy applications(Min et al., 2021). Amongst those approaches the nanostructured arrays became a large domain of exploration due to remarkable advantages such as reproducibility, stability, and consistency, while being able to offer more sensitive signal transduction(Giannini et al., 2011).

With a given incident electromagnetic (EM) field and the shape, size, and relative dielectric function, ε, of the scatterer, the nanostructured surface give rise to a determined EM field enhancement which must satisfy the Maxwell's equations. Surface plasmon polaritons are transverse magnetic waves propagating along a metal-dielectric interface and decay evanescently in the perpendicular direction(Raether, 1988). Surface Plasmon polaritons are a mixture of EM waves and surface-charges created by the interaction between light and the collective oscillation of conduction electrons within the metal. The dispersion relation (frequency vs parallel wavevector) in an infinite flat metallic surface, which is the simplest system supporting these confined EM modes, is derived by Maxwell's equations(Giannini et al., 2011):

$$k_{||} = k_0 \sqrt{\frac{\varepsilon(\omega)\varepsilon_d}{\varepsilon(\omega) + \varepsilon_d}}$$

where $k_0 = \omega/c$ and $\varepsilon(\omega)$ and ε_d are the metal and dielectric permittivity, respectively. For metallic surfaces, the permittivity decreases and approaches ε_d in the visible wavelengths. Once an EM field enters a dielectric material, it experiences a rapid decay along the normal direction. Thus, EM energy can be concentrated into subwavelength areas at the surface of the metal, and this circumvents one of the principal constraints of classical optics, diffraction.

Other than flat surfaces, plasmonic EM modes arise in other geometries such as in the polarizability of a spherical metallic nanoparticle. The polarizability, α_p, of a spherical metallic nanoparticle is defined as the ratio of the induced dipole moment by an incidence wave and the amplitude of the incident displacement field(Maier, 2004):

$$\alpha_p = 4\pi r^3 \frac{\varepsilon(\omega) - \varepsilon_d}{\varepsilon(\omega) + 2\varepsilon_d}$$

Similar to the flat geometry, the polarizability in nanoparticles grows for smaller metal permittivity. However, unlike the flat geometry, when the incidence wavelength matching those plasmonic modes, the nanoscale particles give rise to resonances called localized surface plasmon resonances (LSPR). The formation of LSPR in metallic nanoparticles with different shapes and sizes is calculated through the Optical Theorem based on the extinction cross section normalized to the physical cross-section(Bohren, 1983):

$$q_{ext} = \frac{\sigma_{ext}}{A}, \quad \sigma_{ext} = \sqrt{\varepsilon_d} k_0 Im\{\alpha_p\}$$

Thus, other than the type of metal, shape affects the properties of LSPR supported by metal nanoparticles, including the height and width of the cross-section maxima. For example, Elongated nanoparticles, nanotriangles, and nanocubes further tailor the optical properties of the plasmonic

system as they can sustain plasmonic resonances with varying symmetry properties, however the substantial radiative property of dipolar charge oscillations is what mainly controls the interaction of single nanostructure with free space radiation. These plasmonic modes, which are the lowest in energy, are termed bright modes. Metallic structures with larger dimensions support more multipole resonances, which are weakly coupled to radiation. These LSPRs are referred to as dark modes. Retardation effects within the nanoantenna are the only mechanism that permits the optical excitation of multipole resonances. There is a phase mismatch between the incident fields and the effective charge oscillations within the nanoantenna because of the slow response with respect to the incoming frequency of the metal's conduction electrons to the external EM excitation.

The LSPRs sustained by individual nanostructures interact when a number of them are placed in close proximity, which leads to the formation of hybrid plasmonic modes supported by the resulting structure as a whole. When we have a two-dimensional array of plasmonic nanostructures, the incident light is scattered by a variety of elements in the nanoarray comprising the presence of order in the system and leads to the appearance of coherent scattering waves that is explained by Bloch's theorem(Ashcroft, N. W.; Mermin, 1968). By calculating the effective polarizability of a spherical nanoparticle in a harmonized array using the coupled dipole approximation, it is possible to find out how array resonances affect the optical properties of individual structures(De Abajo, 2007):

$$\alpha_p' = \frac{\alpha_p}{1 - S\alpha_p}$$

where α_p is the polarizability of the single isolated structure (simplified as a spherical nanoparticle) and S is the array factor ensemble the dipole induced in each nanostructure by the EM fields scattered by the rest in the array(Zou & Schatz, 2004). As a result, the array resonances improve the intensity of the plasmonic resonances in the individual nanoparticles. The periodic

arrangement of metallic nanoparticles allows one to tune their optical properties and modify their contribution to optical signal amplification sensing.

The advances in understanding the underlying principles of tailoring nanostructures properties into nanoarrays with their geometries and materials, as well as in nanofabrication techniques, led to a considerable surge in attempts to control their properties through configuring the shape, size, and/or spacing of the nanostructures to enhance the optimal signal transduction(Fort & Grésillon, 2008a; W. B. Stiles et al., 2008).

In the context of EV analysis, the nanostructured arrays can be divided into two types pertaining to the functional motif characteristics: i) the convex nanostructured arrays where the motif is a nanoscale structure fabricated on top of the substrate and is able to differ with the substrate in type and ii) the concave nanostructured arrays that are carved out of the substrate enabling available sites for isolation and enrichment of EVs (Figure 2-2). Bringing the nanostructures into a two-dimensional array not only assisted the isolation of spots for optical immunocapturing and probe-free entrapment of EVs, but also provided different detection systems with unique and enhanced properties in signal transduction that was not possible with random nanorough surfaces. In particular, the surfaced enhanced optical readout systems were substantially affected by the improvements in fabrication techniques.

Fluorescent signals and spectral signals are the two main types of optical signals recorded in EV detection(Min et al., 2021). Several generation modes of nanostructures have been adopted to improve the limit of detection of EVs, including direct detection of fluorescent signals by microscopy and quantification of the results, and spectral signal sensing entailing surface plasmon resonance (SPR), and surface-enhanced Raman spectroscopy (SERS) techniques, which are alternative label-free methods for detecting EVs.

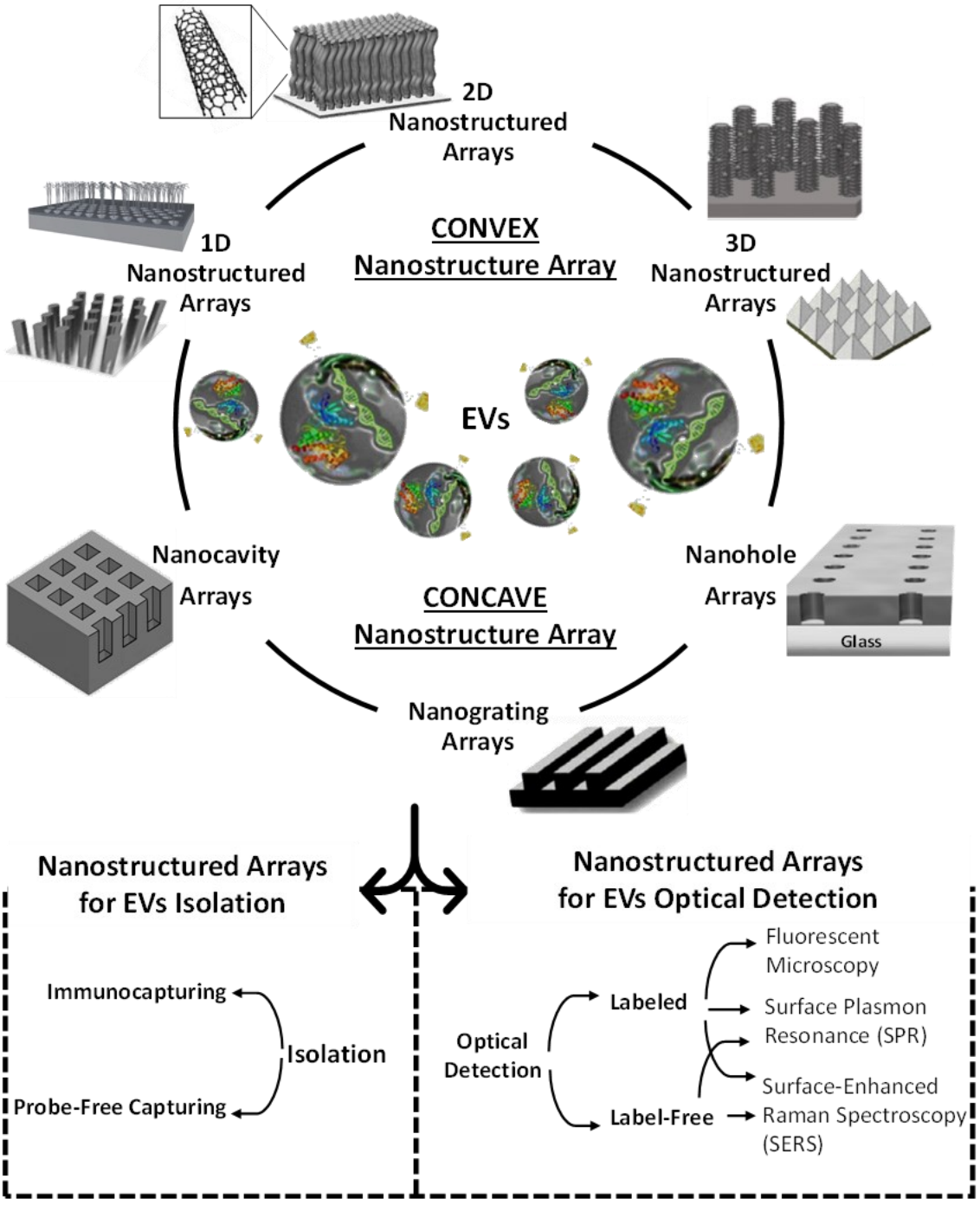

Figure 2.1-2. Nanostructured arrays for EVs Detection. (a) Nanostructured arrays used for isolation and detection of cancer EVs. (b) The role of nanostructured arrays in enhancement of isolation and optical detection of EVs.

2.2 Role of Plasmonic Nanoarrays in EVs Detection

The main challenge in studying the molecular constituent of EVs is in achieving a high enough sensitivity of the assay to recognize and transduce meaningful signals, which is generally hindered by the EVs low concentration, heterogeneity, their diffusion limits in the solution(Tantussi, Messina, Capozza, Dipalo, & Lovato, 2018), and the statistical forces(Ruggeri & Krishnan, 2018). The liquid biopsy involving EVs is especially amenable to nanotechnology, which consists of using materials, structures, and devices whose size and function are in the range of ≤ 1 μm at least in one dimension (Whitesides, 2003; Wong et al., 2013). Nanostructures were extensively interrogated for their ability to enhance the sensitivity of the methods designed to analyse EVs, including super-resolution microscopy, biological marker detection, microfluidic devices(Peng Zhang et al., 2016a), localized surface plasmon resonance (LSPR)(Im et al., 2014a), and surface enhance Raman spectroscopy (SERS)(C R Bagshaw & Cherny, 2006; Clive R Bagshaw et al., 2000; Schuster et al., 2005; Uno et al., 2014; Vietmeyer et al., 2011; Yeow et al., 2006). Nanostructures have a large surface area to volume ratio, which can lead to more interactions between the assay and biomarkers, increasing the chances of capturing the EVs for signal transduction(Soleymani et al., 2009). In addition, the small dimension of nanostructures aids in capturing and enriching nanoscale biomarkers, such as EVs, and can enhance localized signals from EVs, particularly when they are densely organized(Peng Zhang, Zhou, He, et al., 2019a).

2.2.1 Plasmonic Nanoarrays Assisting Isolation and Enrichment

Isolation of EVs for analysis remains a labor-intensive and time-consuming challenge given their nanoscale dimensions (30–200 nm), low buoyant density, and their high heterogeneity. Therefore

a variety of nanostructured arrays including different types of convex and concave structural surfaces have been used alone(Min et al., 2021) and integrated with microfluidic sample delivery systems(Xie et al., 2020) to venture higher isolation efficiency in minute size EV samples in order to facilitate and enhance the capture efficiency (Figure 2-3a).

A ciliated micropilar array was first integrated with a microfluidic device to compensate the EVs isolation efficiency among cells, debris and circulating proteins (Figure 2-3b)(Zongxing Wang et al., 2013). The ciliated micropillar array formed a porous silicon nanowire-on-micropillar structure that assisted preferential entrapment of EVs, while simultaneously filtering out proteins and cell debris. In this isolation scenario, the cells were depleted before entering the micropillar region, while cellular debris as well as proteins and other small objects flew through, bypassing the micropillars. EVs on the other hand highly enriched by trapping within the nanowires. Trapped lipid vesicles were recovered intact as evidence by dissolving the porous nanowires in PBS buffer. Using scanning electrom microscopy different stages of fabrication of ciliated micropillars were captured. Starting by a uniform silver deposition using the pulse reverse plating method, porous silicon nanowires were formed on the sidewalls of the micropillars via an electroless etch.

Similarly, a simple, size-based EV separation technology that integrates 1024 nanoscale deterministic lateral displacement (nanoDLD) arrays on a single chip(Zongxing Wang et al., 2013) was developed that was capable of parallel processing sample fluids at rates of up to 900 $\mu L\ h^{-1}$. Benchmarking the nanoDLD chip against commonly used EV isolation technologies, including ultracentrifugation, ultracentrifugation plus density gradient, qEV size-exclusion chromatography (Izon Science), and the exoEasy Maxi Kit (QIAGEN), they demonstrated a superior yield of ~50% for both serum and urine samples for the nanorod-based displacement array, representing the

ability to use smaller input volumes to achieve the same number of isolated EVs. The convex nanostructured arrays were also used to enhance the immunoaffinity isolation of the EVs. Immunoaffinity based EV isolation technologies use antibodies targeting surface markers on EVs to provide higher isolation specificity and purity. A radial flow device based on bean-shape microposts functionalized with biotin-conjugated anti-epithelial cell adhesion molecule (EpCAM) antibody through biotin–avidin link chemistry was developed to excel the affinity interaction of the EVs with functional bio-probes on the bean-shaped micropost array(Lo et al., 2020). This chip was applied for EVs isolation with antibodies against common EV surface markers, CD9, CD63, and CD81, to achieve high throughput EV isolation.

A high-throughput platform consisting of 3D carbon nanotube arrays that rapidly capture different EVs based on their sizes, without any bio-probes was reported (Figure 2-3c)(Lo et al., 2020). The material characteristics of this nanotube array enabled maintenance of the integrity of the EVs when they were excreted from a host cell, thus allowing comprehensive downstream analyses using conventional approaches. A stamping technique was acquired to construct a gradient of nanotube herringbone arrays and integrate them into a microdevice that allowed processing of a wide range of sample volumes, microliters to milliliters, in several minutes through a syringe via manual hand pushing and without any sample preparation with higher efficiency towards smaller EVs compared to larger EVs.

Concave nanostructured arrays patterned inside the substrate have been widely used to fully harness the diagnostic potential of EVs for liquid biopsy application. The concave nanostructured arrays embodied nanocavity arrays, allow profiling EV populations without sacrificing single EV level detail by averaging over multiple EVs. In a probe-free EV isolation attempt, nanocavity arrays have been integrated with a tunable confinement system to trap EVs in a free-energy

landscape that modulates vesicle dynamics in a manner dependent on EV size and charge (Figure 2-3d)(Hosseini et al., 2021). A lattice of circular nanocavities patterned in silicon nitride substrate were bonded to a flexible membrane lid and a pneumatic pressure was applied to deflect the lid downward to control the degree of vertical confinement experienced by the EVs. The efficacy of the nanocavity arrays integrated with a tunable confinement system was validated via glioblastoma cancer EV populations.

Similar to the convex nanostructured arrays, the concave nanostructured arrays were also used to enhance the immunoaffinity isolation of the EVs for higher isolation specificity and purity. An antibody-conjugated signaling nanocavity array was developed by molecular imprinting-based dynamic molding chemical nanoprocessing for sensing intact EVs fabricated (Figure 2-3e)(Takeuchi et al., 2020). A molecular imprinting-based dynamic molding approach was used to fabricate antibody-conjugated signaling nanocavity array capable of size recognition. This enabled the establishment of an easy-to-use, rapid, sensitive, pretreatment-free, and noninvasive EV detection platform for efficient EV detection-based cancer diagnosis. The dissociation constant was estimated to be 1000 times higher than that of commercial immunoassays upon validation test via EVs derived from tears, clearly differentiating between healthy donors and breast cancer patients, as well as between samples collected before and after total mastectomy.

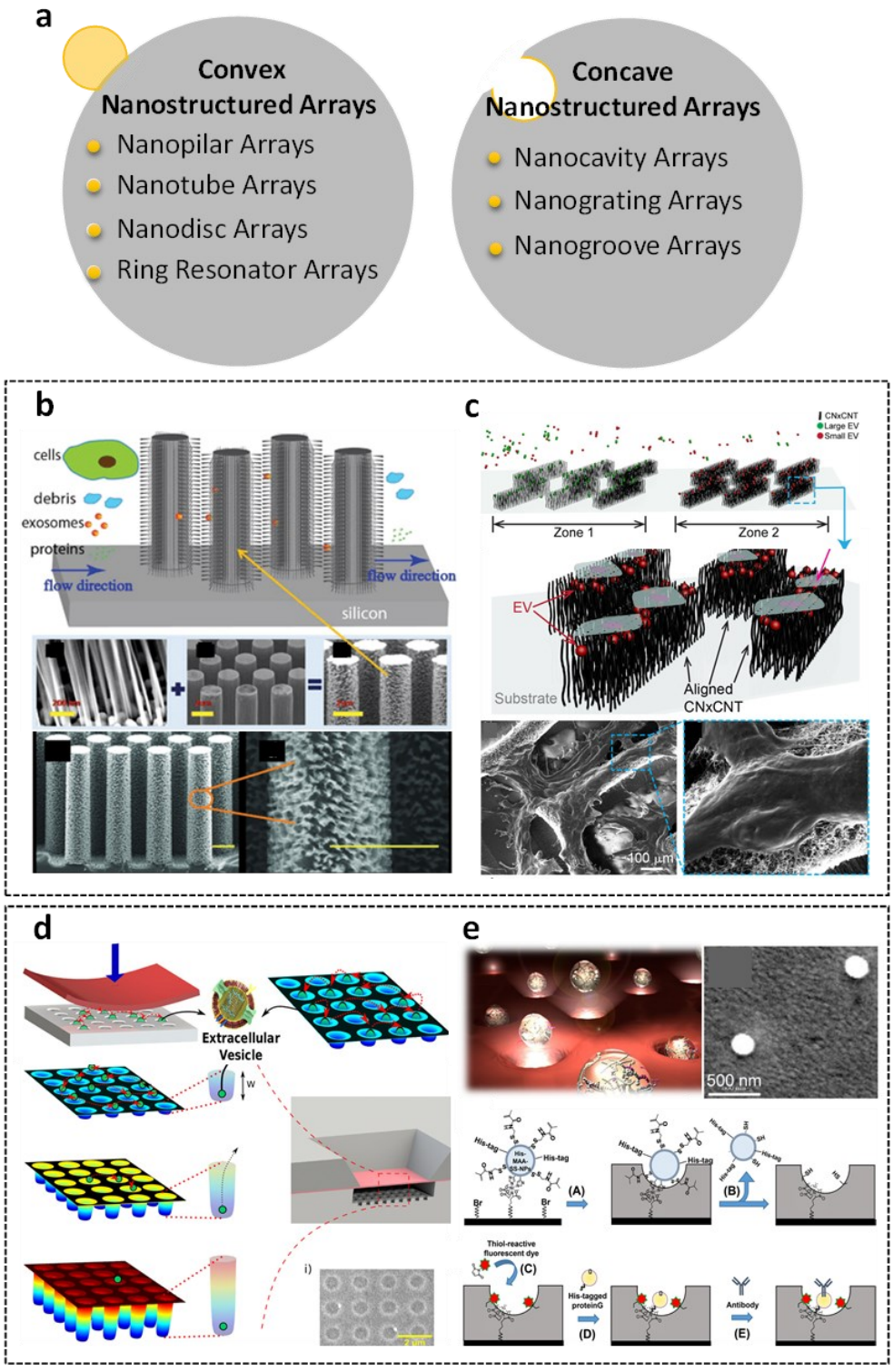

Figure 2.1-3. Nanostructured Arrays for whole EVs isolation. (a) Two types of nanostructured arrays that are used to enhance EVs isolation categorizing them into nanostructured arrays fabricated on the surface as convex nanostructures and nanostructured arrays patterned inside the substrate as concave nanostructures.

(b) A ciliated micropillar array for EVs isolation. The cells are depleted before entering the micropillar region, while cellular debris as well as proteins and other small objects flow through, bypassing the micropillars. Exosomes are highly enriched by trapping within the nanowires. The representative porous silicon nanowire forest, and representative ciliated micropillars. Reproduced with permission (Zongxing Wang et al., 2013). Copyright 2013, The Royal Society of Chemistry. (c) A high-throughput 3D carbon nanotube arrays for rapid capture of whole EVs based on their sizes. Reproduced with permission(Lo et al., 2020). Copyright 2020, The Royal Society of Chemistry. (d) A lattice of circular nanocavities patterned in silicon nitride substrate were bonded to a flexible membrane lid and a pneumatic pressure was applied to deflect the lid downward to control the degree of vertical confinement experienced by the EVs. Reproduced with permission(Hosseini et al., 2021). Copyright 2021, American Chemical Society. (e) An antibody-conjugated signaling nanocavity array for sensing intact EVs fabricated by molecular imprinting-based dynamic molding chemical nanoprocessing. Reproduced with permission(Takeuchi et al., 2020). Copyright 2020, American Chemical Society.

2.2.2 Plasmonic Nanoarrays Assisting Optical Signal Transduction

. There are two main types of optical sensors used in EV detection: fluorescent signals and spectral signals(Min et al., 2021). By combining fluorescent probes with antibodies or aptamers, fluorescent signals can be detected to visualize and quantify EVs or their surface biomarkers. Several generation modes of fluorescent signals have been adopted to improve the limit of detection of EVs, including fluorescence quenching, molecular beacons, quantum dots, and fluorescence polarization. Aside from the direct detection of fluorescent signals, spectral signal sensing is an alternative method for detecting EVs, including surface plasmon resonance (SPR), and surface-enhanced Raman spectroscopy (SERS).

The ability to tailor the optical properties of nanomaterials has played a crucial role to a wide variety of optical detection systems, ranging from microscopy(Fort & Grésillon, 2008b) to spectroscopy(P. L. Stiles et al., 2008). Fluorescent optical microscopy, plasmon resonance spectroscopy, and micro-Raman/ photoluminescent spectroscopy have been excelled over surface enhancement via nano-structuring for quantitative detection of nanoscale biomarkers such as EVs. Nanostructured array patterning techniques have often been integrated into surface-enhanced fluorescent microscopy (SEF), surface plasmon resonance spectroscopy (SPR), and surface-enhanced Raman spectroscopy (SERS) so as to enhance their reproducibility. In addition, the sensitive out-of-plane resonance mode of material which is submissive towards surface binding to the material, (C. Lee et al., 2017; Plowman et al., 2014; Premasiri et al., 2005) is the essence of optical micro-Raman spectroscopy. The surface plasmon resonance platforms used for biological and chemical sensing applications(Anker et al., 2008; Lodewijks et al., 2013), exhibited a very high degree of tunability and susceptibility to the dielectric properties of the surrounding environment. (Svedendahl et al., 2009) This determines the ability to adjust the localized surface plasmon resonance of the substrate, (Biagioni et al., 2013; Link & El-Sayed, 1999b) to enhance Raman scattering and optical gain.

The ability of nanostructured arrays to concentrate light into small volumes enables the enhancement of the local density of states and thereby the decay rate of an emitter. In addition, when light is concentrated into subdiffraction volumes, the electric field in the small volumes becomes very intense, causing the formation of hot spots which leads to enhancement of the incident field intensity by a factor of 10^3. Therefore, the hot spot improves the efficiency of the optical excitation process when placing a molecule there(Giannini et al., 2011).

The major enhancement in optical readout of EVs based on nanostructured arrays is pertained by the light iridescence in the array that is majorly amplified in the plasmonic nanostructured arrays. As light passes through a two-dimensional array of metal particles, it is scattered by various elements in the structure. The presence of order in the system leads to coherent effects among the scattered waves. The Blach's theorem shows the relationship between the in-plane wavevectors, and the geometry of a structure, which implies that when the wavelength of the incident light is similar to the pitch of the array, at the normal light incidence, the lowest order coherent superposition of the incoming and scattered fields happens(De Abajo, 2007). This gives rise to collective electromagnetic (EM) resonances of the plasmonic nanostructures in the array, which are spectrally very narrow due to their extended spatial character. These phenomena are similar to the Rayleigh's and Wood's anomalies observed when light is diffracted by metallic gratings and implies that all the momentum of the scattered radiation is parallel to the plane of the array that is in favor of enhancing SPR and SERS sensitivity.

2.2.2.1 Surface Enhanced Fluorescent Microscopy

Fluorescence is one type of luminescence - a phenomenon characterized by the emission of light from a substance due to radiant relaxation following an electronic excitation. As a consequence, fluorescence appears when a material absorbs light at a particular wavelength and emits light of a longer wavelength. Jablonski diagrams are used to illustrate the relationship between absorption and emission of light.

Fluorescence is widely used in optical devices, microscopy imaging, biology, medical research and diagnosis. The conventional microscope uses visible light (400-700 nm) to illuminate and produce a magnified image of a sample. A fluorescence microscope uses a much higher intensity light source which excites a fluorescent marker attached to the sample of interest. These

fluorescent markers in turn emits a lower energy light of a longer wavelength that produces the magnified image instead of the original light source.(Bradbury, S. and Evennett, P., 1996) The modern fluorescence microscopy techniques combine the power of high performance optical components with computerized control of the instrument, and digital image acquisition, to achieve a level of sophistication that far exceeds that of simple observation by the human eye. However, the bleaching of the fluorophores and reflectivity of the surface have destructive effects on the output when imaging nanoscale objects such as EVs. The degree of overcoming these challenges determines the capacity of optical microscopy. (Toma et al., 2013; Kaikai Wang & He, 2018) Nanostructured surfaces, in particular plasmonically active nanostructures, allow for engineering the spectroscopic properties of molecules/fluorophores positioned in its vicinity, via the surface plasmon resonance (SPR) coupling allowing for collective oscillation of their conduction electrons upon excitation by light.(Lakowicz, 2006) When the frequency of the incident light matches with the collective oscillation of the plasmonic nanoarray, a strong electromagnetic field is generated at the interface which allows the nanostructures in the array to act as an antenna for molecules positioned in its near field. Fluorophores will benefit from this electromagnetic field interaction to enhance both excitation and emission pathways (Figure 2-4a)(Fontaine et al., 2020). A number of substrates have been fabricated to date to facilitate plasmonic coupling including 1D and 2D grating structures (Figure 2-4b)(Yuting Yang et al., 2018). The optical configuration of the plasmon-coupled nanostructured surface measurements is proven to be robust and not require cumbersome optics and allow the substrate to be easily incorporated with the existing sample delivery systems. In these approaches, with the use of nanostructured surfaces involving nanorough interfaces, 3D structures and nanocavities/ gratings researchers have sought to partially overcome the fundamental limits in fluorescent biosensing of EVs as nanoscale and heterogeneous

biomarkers(Peng Zhang, Zhou, He, et al., 2019a) to address mass transfer, surface reaction and boundary effects, that presents a major conceptual constraint in leveraging the biosensing performance based on fluorescent microscopy.

2.2.2.2 Surface Plasmon Resonance

Even though fluorescent microscopy is proven to be an effective technique for liquid biopsy of EVs, as discussed above, it relies on fluorescent labels and antibodies to conjugate them to the captured EVs(Y. Liang et al., 2021). While this probe-based technique offers simple experimental implementation and direct visualization using basic microscopes, fluorescent markers are also inherently restricted by multiplexed measurement, instability of photobleaching, and false-positive results due to unspecific binding(Kaizhe Wang et al., 2020). Therefore, subsequent washing steps are required to remove unbounded EVs prior to readout for correct quantification(Hartjes et al., 2019). With the progression in development of nanostructured arrays to substitute metal nanoparticle aggregation, surface plasmon based detection became a potential substitute to recognize the specifically captured EVs in the absence of fluorescent tags(Chin et al., 2020).

Surface plasmon resonance (SPR) is a physically optical phenomenon caused by total reflection of light at the metal film/liquid level interface to analyze molecular interactions. SPR is a probe-free techniques that offers an alternative for non-invasive biomolecule sensing with larger operational freedom and high sensitivity(Juanjuan Liu et al., 2020a). First discovered in the 1960s, SPR can be defined as the collective resonance between the polarized incident light and the free electrons in the thin metal layer where the light is being reflected(M. Li et al., 2015). Rather than an arbitrary event, SPR can only be observed at specific incident angles with the reflected light reaching minimum intensity (Figure 2-4c). A common setup is known as the Kretschmann

configuration, where the sensing platform deposited with a metal outer layer is directly placed over the base of a dielectric prism(Menon et al., 2019). Any mass addition due to biomolecule capturing can change the local refractive index of the metal layer(Ferhan et al., 2018), and this change in plasmon propagation leads to shift or even disappearance of the SPR angle. Thus, tracking the dynamic change of this angle can bring valuable information of target EVs, even measuring concentration based on binding kinetics(Rojalin et al., 2019). More detailed working principles have been discussed thoroughly in previous works and are out of the scope of this review(Imanbekova et al., 2022; Miyazaki et al., 2017).

Nanoparticle aggregates(Sina et al., 2019) and Self-assembled metal nanoparticles(Thakur et al., 2017) are a type of relatively simple nanostructure but least reproducible since it forms randomly generated patterns. Although its inherently high sensitivity and versatile nature have made SPR and LSPR methods one of the gold standards in measuring real-time molecular interactions, the incorporation of nanostructured arrays was the potent asset that further pushed its measuring boundaries by removing the inconsistencies raised from nanoparticle agglomeration and unpredicted gaps on the surfaces(Chin et al., 2020). The relatively narrow effective range of SPR (around 300 nm) matches well with the small size of EVs in the vicinity of the metal surface layer(W. Chen et al., 2020; Nguyen et al., 2015). The mass displacement of EVs over fluidic channel assisted placement of gold nanorods led to distinguished signal between conjugated EVs on the nanorods (Figure 2-4d)(Ferhan et al., 2018). Some of the first few studies that incorporated SPR for EV characterization were carried out by Weissleder's(Im et al., 2014b; K. S. Yang et al., 2017b), and Höök's(Rupert et al., 2014) groups in 2014.. The former developed the well-established nanostructured array platform while the latter functionalized the sensor surface with anti-CD63 Abs for easier EV quantification. In the following sections, we will discuss in more

details the nanostructured arrays in the form of convex nanoarray fabricated on top of the substrates and concave nanoarrays engraved in the substrates that have been produced to excel the SPR readout in EV studies based on the different morphological characteristics of the nanostructures.

2.2.2.3 Surface Enhanced Raman Spectroscopy

C. V. Raman first reported the scattering phenomenon in 1928, which now bears his name, Raman scattering.(Raman & Krishnan, 1928) It has since become a powerful analytical technique for molecular profiling in biomedical applications, with which label-free detection and identification of bioanalytes became possible.(Diem et al., 2004) The Raman spectroscopy process involves irradiating a sample with laser light and detecting the resulting inelastically scattered photons. Photons with such energies correspond precisely to chemical bonds and structures in the sample. Thus, Raman spectra are based on the relative wavenumbers on the ordinate and intensity of scattering on the abscissa.

Knowing that only 1 in 10^7 photons undergo inelastic (Raman) scattering while the rest experience elastic (Rayleigh) scattering, it is known as a rather insensitive detection method.(Butler et al., 2016) In 1974, a signal enhancement approach was discovered based on the influence of the roughened metal surface that later on been named as surface-enhanced Raman scattering (SERS), and the term SERS was coined for the physical phenomenon(Laing et al., 2017). It affords high chemical specificity, minimal to no sample processing, and is inherently non-destructive, and relatively inert to aqueous background. SERS can enhance the Raman signal of EVs attached to the rough metal surfaces or nanopatterned surfaces through electromagnetic enhancement and chemical mechanisms. SERS became one of the most powerful techniques in analytical chemistry, with potential of single-molecule detection with noble-metal nanopatterns (Figure 2-4e).

Nanostructures are widely employed to enhance the sensitivity of SERS(Jiangang Liu et al., 2020; Shin, Oh, Kang, et al., 2020; Xi et al., 2009) to advance detection of EVs. SERS enables recovery of molecular fingerprints of the bioanalytes. The vibrational and rotational modes of chemical bonding structures reflect as spectral peaks based on the electromagnetic field (EM-field) generated in plasmonic nanopatterns(Juanjuan Liu et al., 2020b; Shin et al., 2018a). In general, SERS-based bio detection applications are employed in two major forms namely the indirect detection via SERS tags and the label-free detection. SERS is a comparative method that not only offers immunoaffinity detection of EVs but also when connected to powerful analytical methods offers probe-free (no immune-capturing of bioanalytes) identification and stratification of EVs. Recent advances in amplifying the SERS spectrum using a variety of plasmonic nanostructures(Knudson et al., 2015; Shin et al., 2018a; Stremersch, Marro, Pinchasik, Baatsen, Hendrix, De Smedt, Loza-alvarez, et al., 2016; Tantussi, Messina, Capozza, Dipalo, & Lovato, 2018), shed light on the potential of this technique for the probe-free identification of EVs (Henkel et al., 2010).

Comparing the EM-field sustained by individual nanostructures with collective EM-field enhancement from the interaction of the plasmonic motifs that are placed in close proximity, demonstrated the formation of hybrid plasmonic modes supporting by the nanoarray. A variety of nanostructured surfaces tailoring nanorough interfaces, 3D nanostructures and nanocavities/ gratings including nanosphere array (Figure 2-4f)(Shin et al., 2018b) have been extensively used to enhance the sensitivity of this approach in parallel to the advancement of the analytical methods to facilitate the immune capturing and probe-free SERS approach for stratifying cancer EVs in the pool of non-cancerous EVs.

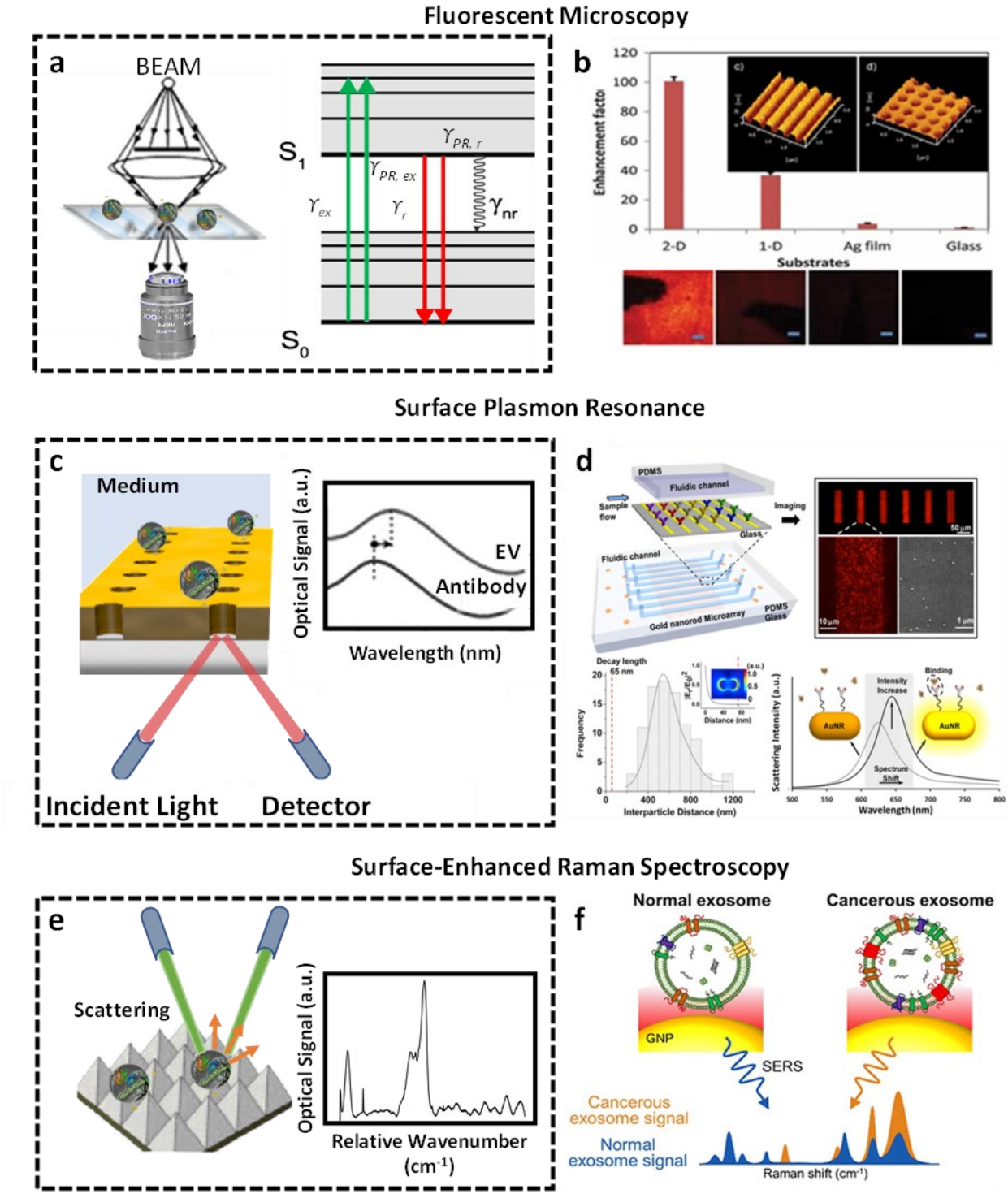

Figure 2.1-4.Surface-enhanced optical microscopy and spectroscopy of EVs: the perks of nanostructured array platforms. (a) The surface -enhanced fluorescent microscopy of EVs via nanostructured arrays. (b) Enhanced fluorescent microscopy: a comparison between glass, plasmonic thin-film, 1D plasmonic

nanoarray and 2D plasmonic nanoarray. Reproduced with permission(Y. Yang et al., 2018). Copyright 2018, National Academy of Sciences. (c) The surface plasmon spectroscopy of EVs via nanostructured arrays. (d) The mass displacement of EVs over fluidic channel assisted placement of gold nanorods led to distinguished signal between conjugated EVs on the nanorods. Reproduced with permission(Ferhan et al., 2018). Copyright 2018, Elsevier. (e) The surface -enhanced Raman spectroscopy of EVs via nanostructured arrays. (f) Spherical particle array to distinguish cancer EVs from non-cancer EVs via SERS. Reproduced with permission(Shin et al., 2018b). Copyright 2018, American Society of Chemistry.

Table 2.1-1. Technologies developed for cancer liquid biopsy of EVs via surface-enhanced optical detection

Technology	Cancer	Biomarker	Body Fluid	Readout	Ref
Single EV analysis (sEVA) of mutated proteins	Pancreatic	Extracellular vesicles	Blood plasma	FL Microscopy	2021(Ferguson et al., 2022) SEP
Thermophoretic aptasensor	Breast	Extracellular vesicles	Blood serum	FL Microscopy	2021(Tian et al., 2021)
Microfluidic chip for EVs multiplex phenotyping based on Raman reporters barcoding	Melanoma	Extracellular vesicles	Serum	SERS	2021(Jing Wang et al., 2021)
Microscale biosilicate nanofilter doped with AgNPs	Ovarian, Endometrial	Extracellular vesicles	Serum	SERS	2020(Rojalin et al., 2020a)

SERS nanotags EVs profiling via sandwich immunoassay	Colorectal, Bladder, Pancreatic	Extracellular vesicles	Serum	SERS	2020(W. Zhang et al., 2020)
Aggregated spherical AuNP substrate on APTES-coated glass.	Lung	Extracellular vesicles	Serum	SERS	2020(Shin, Oh, Hong, Kang, Kang, Ji, Choi, Kang, et al., 2020b)
Microfluidic chip based on herringbone nanopatterns	Ovarian	Extracellular vesicles	Blood plasma	FL Microscopy	2019(Peng Zhang, Zhou, He, et al., 2019b)
Sequential detection of EVs via DNA-PAINT on PEI modified glass	Breast, ovarian, liver	Extracellular vesicles	Blood plasma	TIRF microscopy	2019(C. Chen et al., 2019a)
Multiplex immunostaining and imaging chip for EVs profiling	Glioblastoma	Extracellular vesicles	Blood plasma	Fluorescence microscopy	2018(K. Lee et al., 2018a)
Biotinated EVs immobilization on streptavidin-coated coverslip	Glioblastoma	Microvesicles	Blood plasma	Fluorescence microscopy	2018(Fraser et al., 2019a)
n-PLEX Chip microfluidic based on periodic nanohole arrays	Ovarian	Exosome-bound proteins	Blood	SPR	2014(Im et al., 2014b)

2.3 Recent Advances and Challenges of Plasmonic Nanoarrays

Nanostructured surfaces have been implemented with a variety of surface dependent enhancement methods to enable capturing and signal transduction of EVs at different concentration multitude(Min et al., 2021). These attempts were based on the extensive use of variety of nanosize surface structuring for biosensing and catalytic sensing of other circulating cancer biomarkers, including CTCs, ct-DNA, and ct-RNA(J. Dong, Chen, et al., 2020; W. Li et al., 2019). Nanostructured surfaces demonstrated powerful enhancement not only in enhancing the interaction of the bio-probes with EVs for detection but also in providing the means for probe-free identification of them.

In view of integrating nanostructured platforms with bioassays to enhance the nano-bio interface with the EVs for efficient capturing, and testing, a variety of nanosurfaces tailoring from nanoparticles to nanopatterned arrays of convex and concave nanostructures developed for hosting the specific bioassays to the known surface proteins of EVs(Y. Liang et al., 2021). Immunoaffinity based EV detection exert antibodies targeting surface markers on EVs to resolve higher isolation specificity and purity. In spite of that, the probe-free methods allow for identification of heterogeneous EVs population regardless of yet to be discovered antibodies for their capturing(Lv et al., 2019). Patterned nanostructured arrays played a crucial role in enhancing the immunoaffinity detection of EVs and probe-free identification of them(Shao et al., 2018b).

.

1.1.1. Convex Plasmonic Nanoarray Surfaces

2.3.1 Convex Plasmonic Nanoarray Surfaces

As substrates with random nanorough surfaces, such as nanoparticle aggregation, can suffer from uneven hotspots formed due to inconsistent aggregation, which can compromise the repeatability

of results(Chin et al., 2020). By offering uniformity in hot-spot generation, platforms inquiring patterning can address this challenge.

A study carried out by the Zeng's group implemented Y-shaped microposts coated with graphene oxide (GO) induced 3D polydopamine (PDA) film with a novel layer-by-layer deposition (Figure 2-5a) (Peng Zhang et al., 2016b). Such structure provided large surface areas and enhanced mass transfer through flow control, while the rough coating surface significantly increased the number of reactive sites for covalent coupling between Protein G and mAbs to enhance the capturing affinity of sandwich ELISA assays. Using anti-CD81 mAb for capturing and a mixture of detection mAbs (CD63, CD81, EpCAM), the LOD was determined to be around 50 EVs μL^{-1} for optimized flow. The majority of retained exosomes also exhibited a much narrower size range compared to ultra-centrifugation (UC) purified samples, which further proved assay's isolation specificity. This nanosurface set up was used to identify ovarian cancer patients (n= 7) from healthy plasma donors (n= 5) based of detection of EVs in their plasma.

In another attempt same group printed a 3D sinusoidal nanopattern using colloidal inkjet printing (Figure 2-5b)(Peng Zhang et al., 2020) for multiparametric analysis of EV concentration in circulation, subtype, and enzymolytic activity (EV-CLUE). With this nanochip platform, an integrative analysis of the expression and proteolytic activity of MMP14 on EVs was monitored to detect in vitro cell invasiveness and monitor in vivo tumor metastasis, using cancer cell lines and mouse models. Analysis of clinical plasma specimen via this nanostructured platform showed that this technology hold potentials to be used for cancer detection including accurate classification of age-matched controls and patients with ductal carcinoma in situ, invasive ductal carcinoma, or locally metastatic breast cancer in a training cohort (n = 30, 96.7% accuracy) and an independent validation cohort (n = 70, 92.9% accuracy).

Nanoplasmonic surfaces have been successfully utilized to quantitatively detect EVs on account of their numerous promising properties, such as high sensitivity and real-time detection. A variety of nanorough surface engineering methods were used to develop LSPR-based assays including self-assembled gold nano-islands to detect and distinguish EVs from different cell lines(Bonyár et al., 2018; Thakur et al., 2017). Gold nano-ellipsoid arrays and functionalized with anti-CD63 antibody was used to achieve multiparameter detection of EVs (Figure 2-5c)(Lv et al., 2019). Highly ordered nano-ellipsoid arrays were fabricated on the substrate based on the use of the AAO thin film that acted as a shadow-mask for evaporating Au. EV samples from different cell lines were detected at different concentrations with a detection limit of 1 ng/mL. This plasmonic nano-ellipsoid array can be used for the detection of other types of EVs by changing the antibody on the surface of the Au nano-ellipsoids.

The bio-inspired morphologies from nature greatly affected the nanostructure-based paradigm of enhancement in EVs detection, where nanosurfaces were fabricated to mimic the natural morphologies such as Morpho butterfly wing(Han et al., 2020). Similarly, Inspired by the distinctive structures of intestinal microvilli, which are densely packed on the intestinal walls to increase their intestinal mucosal surface areas for enhanced absorption, a biostructure-inspired NanoVilli Chip featuring densely packed anti-epithelial cell adhesion molecule (anti-EpCAM)-grafted silicon (Si) nanowire arrays was fabricated to achieve highly efficient and reproducible immunoaffinity capture of tumor-derived EVs (Figure 2-5d)(J. Dong et al., 2019). A NanoVilli Chip was composed of an anti-EpCAM-grafted Si nanowire substrate (SiNWS) and a superimposed PDMS-based chaotic mixer. Even though the NanoVilli Chip system was designed to capture intact enclosed EVs, for their analytical detection, it is heavily dependant on a downstream reverse transcription Droplet Digital PCR. The assay demonstrated potential into

being applied to monitor the dynamic changes of ROS1 rearrangements and epidermal growth factor receptor T790M mutations that predict treatment responses and disease progression in non-small cell lung cancer patients.

The majority of nanosurface-based enhancement approaches to excel EV detection methods, typically use immunoaffinity to capture or label EVs, which necessitates pre-selection of molecular markers. Despite ongoing research, it has also become evident that many of the described biomarkers have failed to demonstrate comprehensive clinical validity.(Ali et al., 2021; Hanash et al., 2011; Preusser, 2014) An attractive alternative to immunoaffinity or molecular profiling-based approaches while providing biochemical information on a label-free basis is SERS, where its performance is pertained by the electromagnetic field enhancement of the plasmonic nanostructured surface. Bio inspired nanosurfaces have revolutionized the plasmonic structures for SERS which paved the way towards enhancing the sensitivity of EVs probe-free identification and indicated the simplicity and versatility of this method in cancer diagnostics. Probe-free methods not only have obvious advantages (noninvasive and timesaving) over currently clinically used tumor liquid biopsy techniques (such as western blot), which has great potentials to make vitro cancer diagnostics/monitoring as simple as diagnostics/monitoring of common diseases but also it allows for not relying on the known anti surface proteins antibodies for observing the unknown and heterogeneous EVs in patient samples.

A Beehive inspired gold-coated TiO_2 macroporous inverse opal (MIO) structure with an engineered “slow light effect” was developed for probe-free SERS identification of EVs (Figure 2-5e)(S. Dong et al., 2020). The main characteristic of this nanosurface lies in the honey-comb array structure, which allows for capturing and analyzing the protein phosphorylation status of the EVs from plasma of cancer patients without any functionalization processes. This nanosurface

assisted sensitive SERS intensity identification of EVs at 1087 cm^{-1}, supposedly arised from the P–O bond within the phosphoproteins which can be used as a criterion for tumor liquid biopsies. The intensity of the 1087 cm^{-1} SERS peak from EVs extracted from the plasma of cancer patients (prostate, lung, liver, and colon) was shown to be two times higher than that of healthy controls.

A hybrid gold quasi-periodic gold array of pyramids covered with Graphene was used for probe-free identification of EVs (Figure 2-5f) (Yan et al., 2019). The gold nano-pyramid array provides an intense surface plasmonic field upon laser illumination and thus enhances the Raman signal, while the graphene layer provides more biocompatibility and chemically stability and serves as a built-in gauge of local electromagnetic field intensity enabling quantitative Raman analysis. The Au nanopyramid fabrication is based on sphere-lithography, where polystyrene nanospheres were coated on SiO_2 /Si wafer using scooping transfer method followed by etching and ebeam deposition(P. Wang et al., 2015). The EVs Raman signal via this nanosurface system was further examined for the source of the Raman signal, using Raman mapping of low and high spatial resolution combined with morphological identification of EVs by scanning electron microscopy.

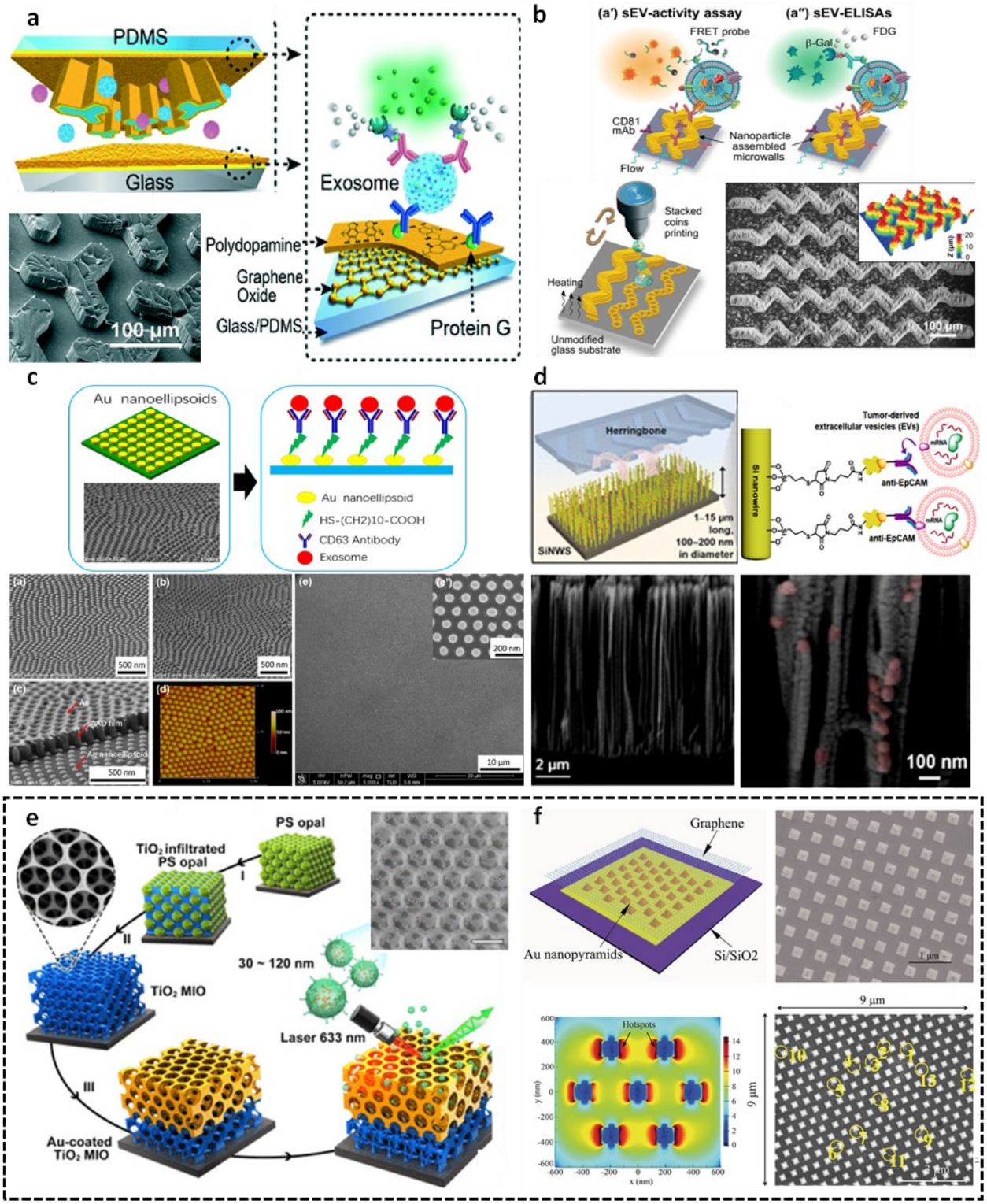

Figure 2.1-5. Convex nanostructured surfaces to enhance the optical detection of whole EVs. (a) A Y-shaped microposts coated with graphene oxide (GO) induced 3D polydopamine (PDA) film with a novel

microfluidic layer-by-layer deposition for EV analysis. Reproduced with permission(Peng Zhang et al., 2016a). Copyright 2016, the Royal Society of Chemistry. (b) A 3D sinusoidal nanostructured surface patterned using colloidal inkjet printing for multiparametric analysis of EV concentration in circulation, subtype, and enzymolytic activity (EV-CLUE). Reproduced with permission(Peng Zhang et al., 2020). Copyright 2020, Science. (c) Gold nano-ellipsoid arrays fabricated via an anodic aluminum oxide thin films shadow masks for evaporation of Au and functionalized with anti-CD63 antibody to achieve multiparameter detection of EVs. Reproduced with permission(Lv et al., 2019). Copyright 2019, American Chemical Society. (d) Grafted Si nanowire arrays modified with Anti-EpCAM for immunoaffinity detection of EVs. Reproduced with permission(J. Dong et al., 2019). Copyright 2019, American Chemical Society. (e) Beehive-Inspired gold-coated TiO_2 macroporous inverse opal (MIO) structure with an engineered "slow light effect" for probe-free SERS identification of EVs. Reproduced with permission(S. Dong et al., 2020). Copyright 2020, American Chemical Society. (f) A hybrid graphene-covered gold nanosurface in the shape of a quasi-periodic array of pyramids for probe-free identification of EVs. Reproduced with permission(Yan et al., 2019). Copyright 2019, American Chemical Society.

2.3.2 Concave Plasmonic Nanoarray Surfaces

As scaling cell isolation approaches such as microfluidics for EVs isolation has been limited by the low throughput and susceptibility to clogging of the channels(Chin et al., 2020), to address these challenges, nanostructured surfaces have been extensively utilized(Lin et al., 2021). In particular nanocavities and nanogratings have been studied in integration with bio-probes and prob-free to analyze EVs via different surface-enhanced transduction methods including fluorescent microscopy, SPR, and SERS.

A plasmonic nanohole array of gold embedded in a multichannel fluidic device (nPLEX) was first introduced by the Weissleder group (Figure 2-6a)(Im et al., 2014b) for SPR testing of EVs via

tetraspanin (CD9, CD63, CD81, CD82) specific bioprobes. The geometry of the nanoholes was optimized through 3D simulation studies to match the sensing range with the mean diameter of EVs, while the transmission-type SPR offered significant advantages over the conventional reflection configuration for EV profiling including the tunable probing depth (<200 nm) to match EV size to enhance the detection sensitivity. The nanosurface was functionalized with different known capturing antibodies, which transduced a red shift in the optical transmission spectral peaks of the nanosurface upon specific binding of EVs, due to a change in the local refractive index. The nPLEX assay demonstrated a limit of detection of ~3000 vesicles, which is 10^4 and 10^2 more sensitive than Western blotting and chemiluminescence ELISA, respectively.

Later, the same group used a similar approach utilizing gold pierced nanohole array structure called nanoplasmon sensor (NPS) to analyze pancreatic ductal adenocarcinoma (PDAC)-derived EVs in higher throughput in clinically validated pancreatic patients (Figure 2-6b)(K. S. Yang et al., 2017b). The working principle of the NPS assay, which was specifically designed for clinical workflows with small clinical sample amounts, and high-throughput detection is based on the shift in the transmitted light upon conjugation of the EVs surface proteins with EVs surface protein-specific antibodies. The sensor chip contains periodically arranged nanopores (200 nm in diameter and 500 nm in periodicity) patterned in a 100-nm-thick gold film. The function of the pores is to transmit light shone onto the gold surface which in turn demonstrates a red shift as EVs are bound in the vicinity of these pores via specific antibodies. They realized a signature marker set comprising EGFR, EpCAM, MUC1, GPC1, and WNT2 to be used with the nanosurface NSP which rendered an overall accuracy of 84% with 86% sensitivity and 81% specificity in differentiating PDAC from pancreatitis, benign, and control patient groups.

A nanoporous herringbone mixer (Figure 2-6c)(Peng Zhang et al., 2016c) structure was then developed for sandwich fluro ELISA to address the inherent limitations of detecting EVs in confined devices involving mass transfer, surface reaction and boundary conditions, as well as enriching the surface density for better binding. With an inventive approach termed as multiscale integration by designed self-assembly (MINDS), the highly flexible fabrication based on evaporation provided facile modification of surface morphology. Moreover, the unique porous structure of nano-HB with larger accessible surface area enhanced the density of immobilized Abs over the binding interface and reached a LOD as low as 10 μL^{-1}. Compared to ultra-centrifugation where the isolation efficiency for the well-characterized COLO-1 EVs was around 15.5%, optimized nano-HB chip achieved an average capture rate of 85%. EV profiling with the proposed system was further implemented to identify ovarian cancer patients (n = 20) and controls (n = 10), however, this nanosurface implemented system also showed limited on-chip sample processing capacity, as the EVs were still isolated with ultra-centrifugation.

A slightly different approach to address the isolation of EVs, was the exosome track-etched magnetic nanopore (ExoTENPO) chip which performed based on rotational magnetic traps at the edges of pores for efficient entrapment and sorting of EVs (Figure 2-6d)(Ko et al., 2017). By distributing the flow over millions of nanoscale pores, they acheived $10^6\times$ greater flow rate compared to conventional individual fluidic devices while preserved the precision of capturing via immunomagnetic sorting without risk of clogging, as the occlusion of any single nanopore results in diversion of the flow to a nearby pore. The ExoTENPO isolates specific subtypes of EVs by immunomagnetically labeling exosomal protein surface markers and subsequently capturing these targeted exosomes directly from unprocessed serum or plasma. The working principles of ExoTENPO relies on magnetization of the paramagnetic material in ExoTENPO and the

superparamagnetic magnetic nanoparticles that label the EVs by an external NdFeB disc magnet placed immediately below the ExoTENPO device. The EVs captured on the ExoTENPO were lysed on-chip, for quantitative PCR which have been then analyzed using a machine learning algorithm to predict the state of the EVs in pancreatic cancer-bearing mices.

Similar to the convex like nanostructures on the surface, most of the concave nanostructures patterned in the substrates to enhance EV detection methods, use immunoaffinity probes to capture or label EVs, that again requires pre-selection of molecular markers. By the same token, concave nanostructured surfaces played an important role to excel probe-free molecular profiling of EVs for cancer liquid biopsy enhancement. A consumer-grade compact disk technology based on soft-lithography of polycarbonate substrate was introduced for label-free analysis of EVs (Figure 2-6e)(Avella-Oliver et al., 2017). These nanostructured Substrates fabricated following the process flow of the regular recordable disks (CD-R and DVD-R) coated with silver. The groove-shaped 1D nanostructured surface assisted the concentration of the EVs in the deep sites while exhibited significant signal (SERS) enhancement, the magnitude of which directly correlated with the nanostructured surface design of the distance between grooves and the microgroove sizes.

The metal-coated nano/ micro bowl shaped surfaces were developed to lower the number of EVs entrapment on the plasmonic surface(Imanbekova et al., 2021; Rojalin et al., 2020b). A thin silver film coated nanobowl substrate was fabricated using a soft-lithography technique based on nanoparticle inverse patterning to simultaneous entrapment of EVs and enhance the signal (SERS) transduction (Figure 2-6f)(C. Lee et al., 2015). The nanoparticle shapes were patterned in a PDMS substrates to reflect on the bowl shaped nanosurface. This nanobowl structured surface initially enhanced the entrapment of bulk EVs into few EVs upon drying the liquid. The enhanced signal (SERS) was then recorded to differentiate EVs derived from SKOV3 cell line.

In a more advanced context, ebeam lithography was used for 3D patterning of a ring-shaped microcavity array connected to a nanoantenna for EVs entrapment and enhanced signal (SERS) transduction (Figure 2-6g)(Tantussi, Messina, Capozza, Dipalo, Lovato, & De Angelis, 2018). In this setting, they demonstrated that a bubble confining EVs is generated by an ultrafast IR laser pulse train focused on a resonant plasmonic antenna by the laser excitation. The rapid expansion of the water bubble can act as a fast-moving net for EVs entrapment. In addition, the metallic ring-shaped cavity acts as a nanosurface resonator, enhancing the signal (SERS) recorded from the EVs derived from Raw 264.7 cells.

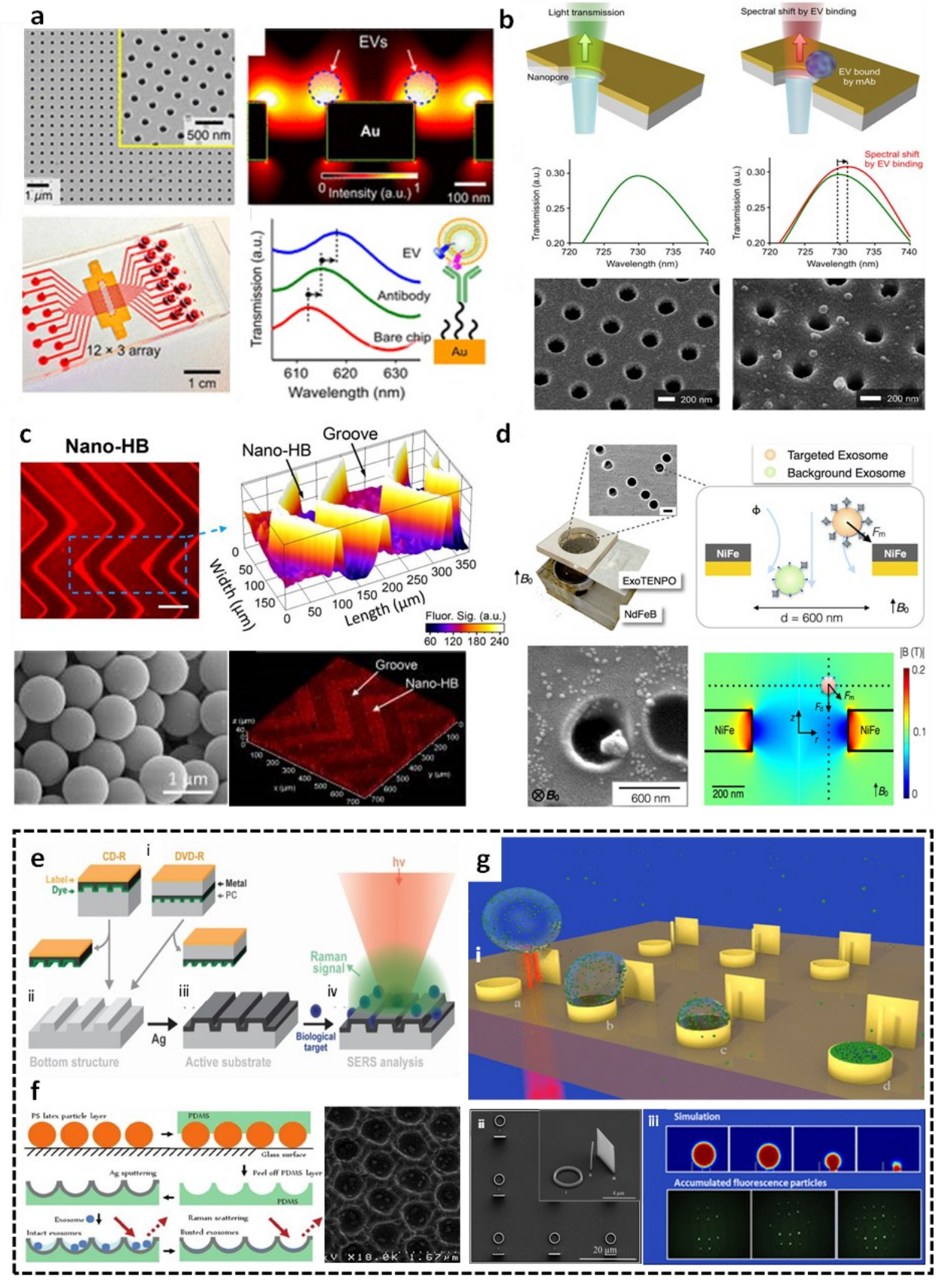
a
500 nm
1 μm
EVs
Au
Intensity (a.u.)
100 nm
12 × 3 array
1 cm
Transmission (a.u.)
EV
Antibody
Bare chip
Au
610 620 630
Wavelength (nm)
b
Light transmission
Nanopore
Spectral shift by EV binding
EV bound by mAb
Transmission (a.u.)
Wavelength (nm)
Spectral shift by EV binding
200 nm
200 nm
c
Nano-HB
Nano-HB
Groove
Width (μm)
Length (μm)
Fluor. Sig. (a.u.)
1 μm
Groove
Nano-HB
d
Targeted Exosome
Background Exosome
ExoTENPO
NdFeB
NiFe
NiFe
d = 600 nm
600 nm
200 nm
|B (T)|
e
CD-R
DVD-R
Label
Dye
Metal
PC
hv
Raman signal
Ag
Biological target
Bottom structure
Active substrate
SERS analysis
f
PS latex particle layer
PDMS
Glass surface
Ag sputtering
Peel off PDMS layer
Exosome
Intact exosomes
Raman scattering
Busted exosomes
g
Simulation
Accumulated fluorescence particles
20 μm

Figure 2.1-6. Concave nanostructured surfaces to enhance the optical detection of whole EVs. (a) Nanohole plasmonic array (nPLEX) microfluidic for SPR probing of EVs. The nPLEX sensing which is based on transmission SPR through periodic nanohole arrays (d= 200 nm) patterned in a gold film (t= 200 nm) integrated with multichannel microfluidics. The finite-difference time-domain simulation shows the enhanced electromagnetic fields tightly confined near a periodic nanohole surface. The EVs signal is recorded through monitored by transmission spectral shifts when it is conjugated with specific EV binding antibodies. Reprinted with permission from ref (Im et al., 2014b) . Copyright 2014 Nature. (b) The nano plasmon sensor chip (NPS) for detection of EVs in the clinical subjects. The working principle of the NPS is based of detecting the spectral shift in the transmitted light when EV binding to the nanopore (d= 200 nm, P= 500 nm) surface via monoclonal antibody (mAb) immobilized on the gold surface. Scanning electron micrographs show the periodically arranged nanopore array and EVs captured on the surface. Reprinted with permission from ref(K. S. Yang et al., 2017b). Copyright 2017, Science. (c) The nano-HB herringbone groove shaped structures, with the NP solution flowing through the channels. The images were acquired at approximately 15 μm below the HB surface along with partial surface plots of the images (Scale bar, 100 μm). SEM images showing minimal non-specific absorption and immunocapture of COLO-1 exosomes (10^5 μL^{-1}) on an mAb-coated device (Scale bars: 100 nm). 3D confocal fluorescence microscopy showing EVs captured inside the nano-HBs. Reprinted with permission from ref (Peng Zhang et al., 2016c). Copyright 2019, Nature. (d) The Exosome Track-Etched Magnetic Nanopore (ExoTENPO) chip for pancreatic cancer EV detection. A photograph of the ExoTENPO and the NdFeB external magnet with an SEM image of the magnetic nanopores; scale bar: 600 nm. An exosome passing through the pore experiences both a drag force F_d from the fluid flow and a magnetophoretic force F_m toward the pore's edge where the magnetic field gradient is maximized. Reprinted with permission from ref(Ko et al., 2017). Copyright 2017, American Chemical Society. (e) A metal-coated polycarbonate grooved structures based on CD-R and DVD-R discs fabrication for label-free targeting EVs. Reprinted with permission from ref(Avella-Oliver et al., 2017). Copyright 2017, Elsevier. (f) A metal deposited PDMS substrate fabricated by soft-lithography of polystyrene nanoparticles for label-free detection of EVs. Reprinted with permission

from ref(C. Lee et al., 2015). Copyright 2015, Royal Society of Chemistry. (g) An ebeam fabricated 3D cavity nanostructured sample with the antennas for prob-free detection of EVs using a bubble-collapsing strategy enabled by the nanostructured antennas. Reprinted with permission from ref (Tantussi, Messina, Capozza, Dipalo, Lovato, & De Angelis, 2018). Copyright 2018, American Chemical Society.

2.4 Plasmonic Nanoarray Platforms in Clinical EV Analysis

Due to the minimal invasion, EVs from body fluids can be obtained more frequently than those obtained from traditional biopsy, which makes them beneficial across the continuum of cancer care from diagnosis to prognosis to therapy response prediction to monitoring treatment. For the reason that the application of nanostructures in EV detection for the purpose of cancer diagnosis has been well reviewed(W. Li et al., 2019; Min et al., 2021), we mainly focus on the recent nanostructured arrays for potential applications in cancer diagnosis using EVs.

Arbitrary nanorough surfaces have been used vastly to detect cancers via EV liquid biopsy in different body fluids, mainly blood plasma. For instance metallic nanoparticle and their aggregates have been used to differentiate multiple myeloma-derived EVs via SPR(Di Noto et al., 2016), lung cancer EVs through epidermal growth factor receptor (EGFR) and programmed death-ligand 1 (PD-L1) as biomarkers as probes(C. Liu et al., 2018), breast cancer via EV -specific markers (CD9, CD63) and a cancer-specific marker (HER2)(Grasso et al., 2015; Sina et al., 2016). The clinically oriented investigations that incorporated plasmonic nanoarrays as detection platforms are summarized in Table 2-2.

For pancreatic cancer, plasmonic nanoarrays comprising nanohole structures were used and were validated with clinical samples. First, the nPLEX system pertaining a nanohole array for SPR detection using surface bio-probes for isolation (described in detail earlier)(Im et al., 2014b). In

another work by the same team, the nanohole array for SPR detection of EVs, was validated via pancreatic ductal adenocarcinoma (PDAC)-derived EVs in higher throughput. As these nanostructured array platforms rely on optical immunocapturing efficacy of EVs, they designed a signature bio-probe, $PDAC^{EV}$, comprising EpCAM, MUC1, EGFR, GPC1, and WNT2. The overall efficiency of the nanohole array functionalized with $PCAC^{EV}$ was tested to demonstrate an overall accuracy of 84% with 86% sensitivity and 81% specificity in differentiating malignant state ($M_{alignant}$= 104) pancreatitis, benign (B_{enign}= 31), and control healthy samples(K. S. Yang et al., 2017b).

For ovarian cancer, EVs derived from patient plasma samples, have been investigated with the convex plasmonic nanoarrays comprising herringbone patterns of microscale lithography(Hisey et al., 2018) and nanoscale self-assembled nanoparticles(Peng Zhang, Zhou, He, et al., 2019a). In particular, the surface-enhanced fluorescent microscopy was used pertaining a nanoscale colloidal particle pattern shaped into a herringbone nanoarray using surface bio-probes for isolation (described in detail earlier). Over detailed analysis of EVs from 30 healthy and patient samples ($n_{Healthy}$ = 10) and ovarian cancer ($n_{Patient}$ = 20), they demonstrated that the levels of EpCAM and CD24 were elevated in EVs from ovarian cancer cells which let to stratifying the patient samples with 97% accuracy(Peng Zhang, Zhou, He, et al., 2019a). Same team later demonstrated the use of colloidal inkjet printing of nanoscale micropatterns for detection of breast cancer patients at different stages. Over detailed analysis of EVs from 30 healthy and patient samples ($n_{Healthy}$ = 8) and ovarian cancer ($n_{Patient}$ = 22), they demonstrated that the levels of CD9, CD63, MMP14-A and MMP14-E were elevated in EVs from breast cancer cells which let to detection of the patients with an overall accuracy of 96.7%(Peng Zhang et al., 2020).

For breast cancer, different photonic crystals entailing nano herringbone array and self-assembled nanoporous sinusoidal array were used(X. Dong et al., 2019). To better stratify the patients cohort from healthy, machine learning has been used for finding small trace of differences and magnify them(Peng Zhang et al., 2020).

For prostate cancer a beehive-inspired structure with ability to trap laser light inside its pores to enhance Raman signals was used. The Raman signal analysis of EVs from 55 samples including controls ($n_{Healthy}$ = 10) and prostate cancer patients ($n_{Patient}$ = 45) were differentiated by directly monitoring the SERS spectra at 1087 cm^{-1}.

For lung cancer, the nano-villi array inspired by the densely packed structure of intestinal microvilli was used. The anti-EpCAM-grafted Si nanowires with optimized length and spacing increased the surface contact area, such that EVs with varying sizes can be captured both on the tips and sides of the nanowires. Tumor-derived EVs from non-small cell lung cancer (NSCLC) patients with either CD74-ROS1 rearrangement (n = 7) or EGFR T790M mutation (n = 6) were differentiated via gene alteration a recovery rate of 82% ± 8%. The same research group further advanced their studies in 2020 by incorporating click chemistry mediated EV enrichment, termed the “ES-EV Click Chip”. With similar assay structures, tetrazine (Tz) was affixed to the embedded Si nanowires while the Ewing sarcoma EVs (ES EVs) were conjugated with trans-cyclooctene (TCO)-anti-LINGO Abs complex. The highly selective and irreversible reaction between Tz and TCO offered unique advantages in reduced Ab consumption and led to a significant increase in capturing efficiency of up to 94%. The addition of 1.4-dithiothreitol (DTT) as a cleavage agent allowed facile EV elution by breaking the disulfide bonds of Tz. The clear divergence of EWS rearrangement between healthy (n = 4) and diseased samples (n = 4), which is a hallmark for ES EVs, further corroborated the great potential of ES-EV Click Chip in clinical diagnosis.

Table 2.1-2. Nanoarrays tested for cancer liquid biopsy of EVs in patient samples via surface-enhanced optical detection

Technology	Cancer	LOD	Biomarker	Patients Number	Ref
Nanohole Array for SPR (n-PLEX)	Pancreatic	-	EpCAM, CD24, CD63	20 Patient, 10 Healthy	2014(Im et al., 2014b)
Nanohole Array for SPR (nPES)	Pancreatic	-	Ephrin type-A receptor 2 (EphA2)	104 Malignant, 31 Benign	2017(K. S. Yang et al., 2017b)
(nano-IMEX)	Ovarian	50 (μl^{-1})	EpCAM, CD9, CD81	7 Patient 5 Healthy	2016(Peng Zhang et al., 2016a)
Nano-herringbone Array Embedded Microfluidic	Ovarian	4.1×10^{8} (mL^{-1})	EpCAM, CD9	3 Patient	2018(Hisey et al., 2018)
Nano-herringbone Array for SEF	Ovarian	$2.3x10^{6}$ (mL^{-1})	EpCAM, CD24, FRα,CD63, HER2, EGFR	20 Patient 10 Healthy	2019(Peng Zhang, Zhou, He, et al., 2019a)
Nano biosilicate doped with AgNPs	Ovarian	$6x10^{2}$ (μl^{-1})	-	8 Patient	2020(Rojalin et al., 2020a)
3D porous serpentine nanostructure	Ovarian	~21 (μl^{-1})	EGFR, CA125, FRα, CD24, EpCAM and HER2	15 Patient, 5 Healthy	2019(Peng Zhang,

					Zhou, & Zeng, 2019)
Photonic crystal nanostructure coupled with on-chip ultrafiltration (ExoID-Chip)	Breast	$8.9x10^3$ (mL^{-1})	CD63, CD81	6 Patient, 7 Healthy	2019(X. Dong et al., 2019)
Nano-herringbone Array based on self-assembled nanoporous sinusoidal patterns (EV-CLUE chip)	Breast	$5x10^2$ (μl^{-1})	CD9, CD63, MMP14-E and MMP14-A	22 Patient, 8 Healthy (Training set) 58 Patient, 12 Healthy (Validation set)	2020(Peng Zhang et al., 2020)
Silicon nanowire array (ES-EV Click Chip)	Ewing Sarcoma	-	trans-cyclooctene (TCO)-anti-LINGO Abs complex	4 Patient 3 Healthy	2020(J. Dong, Zhang, et al., 2020)
Staggered triangular micropillar array	Prostate	$1.6x10^2$ (mL^{-1})	EpCAM, CD63	10 Patient 8 Healthy	2020(Y. Wang et al., 2020)
Beehive-inspired 3D Au-coated MIO structure as SERS substrate	Prostate	-	-	45 Patient, 10 Healthy	2020(S. Dong et al., 2020)
Micropillar array for uniform Ab-bounded microbeads distribution	Lung	-	CD9, CEA, Cyfra21-1 and ProGRP	10 Patient, 10 Healthy	2019(Y. Bai et al., 2019)
Nanovilli array	Lung	-	EpCAM, CD74-ROS1, EGFR T790M	13 Patient	2019(J. Dong et al., 2019)

Plasmonic Au nanoring gaps (ExoSCOPE)	Lung	~1000 vesicles	CD63, EGFR, EpCAM and MUC1	46 Patient, 30 Healthy	2021(Pan et al., 2021)
Repetitive circular patterns in rippled microfluidic channels (^{new}ExoChip)	Lung and Melanoma	-	phosphatidylserine (PS)	7 Patient, 5 Healthy	2019(Kang et al., 2019)
Nanodisc array	Melanoma	$3.7x10^{7}$ (mL^{-1})	MCSP, MCAM, CD61, and CD63	20 Patient 21 Healthy	2021(Jing Wang et al., 2021)

2.5 Conclusion and Outlook

EVs encapsulate multiple molecular signals reflective of the phenotype of originating tumor cells, which makes them compliant cancer biomarkers circulating body fluids such as blood. Conventional analytical methods such as ELISA, PCR and Western Blot are often not comprehensive in EV profiling, while requiring extensive purification, large sample volumes, and different assay complexes for targeted detection. Therefore, an extensive effort has been put into enhancement of sensitivity, selectivity and accuracy of EVs stratification via different nanotechnologies that has been reviewed extensively. Here we specifically describe the superior characteristics of plasmonic nanoarrays for enhanced optical signal transduction of EVs and discuss the advances and challenges in terms of fabrication and implication of them for on-chip sensing.

Nanostructured arrays are a promising platform for optical readout of extracellular vesicles (EVs), particularly plasmonic nanostructured arrays which amplify light iridescence in the array. When light passes through a two-dimensional array of metal particles, it is scattered by various elements in the structure, resulting in enhanced signals that can be measured and analyzed to

provide information about the EVs. We discussed in detail the research and implications of using such on-chip methods, in which we could better understand the role of EVs in health and disease. In the meantime, there is ample opportunity to further develop plasmonic nanoarrays for optical profiling of EVs. We have discussed the key properties of plasmonic nanoarrays, and their lucrative properties in isolation and enhanced optical detection of EVs. We then discussed the advances and challenges in the development of plasmonic nanoarrays and how they are designed and tuned to meet the selectivity and specificity of the target EVs. The specific properties of the plasmonic nanoarrays in terms of feasibility and drawbacks and their potential applications in clinical scenarios.

There are three main optical readout systems that have been studied for their potential to better understand the heterogeneous population of EVs: fluorescence, surface plasmon resonance (SPR), and surface-enhanced Raman spectroscopy (SERS). While fluorescence and SPR have their own advantages, SERS has been shown to provide references to the underlying molecular composition of the EVs in a label-free and surface bio recognition-free way.

The potential of SERS molecular composition profiling has been utilized to sensitively distinguish EVs from non-cancer and cancer populations without the need for tagging or labelling. In addition to its high sensitivity and specificity, SERS is also a non-destructive method, which is important for maintaining the integrity of the EVs being studied. This is especially important for studying the molecular composition of EVs, as any alterations to their structure or composition could affect their biological activity and function.

However, its potential has not been investigated at the level of single EV. This is where the current thesis comes in - the hypothesis is that single EV SERS can open avenues in differentiating EVs from molecularly altered tumors and therefore offer real-time monitoring of the cancer

molecular alterations. We hypothesize that single EV SERS has the potential to provide even greater sensitivity and specificity compared to bulk SERS, as it would allow for the detection and analysis of individual EVs rather than an average signal from a population of EVs. This would enable researchers to better understand the heterogeneity of EV populations and identify subtle molecular changes that may be indicative of disease or other conditions.

Overall, the potential of SERS for studying the molecular composition of EVs is significant, and single EV SERS has the potential to open up new avenues for real-time monitoring of cencar molecular alterations (mutations). Further research in this area is needed to fully explore the capabilities of SERS for EV analysis, but the results so far are promising. We hypothesize that single EV SERS can open avenues in differentiating EVs from molecularly altered tumors and therefore offer real-time monitoring of the cancer molecular alterations which is the motivation of the current thesis.

3 Bridging Chapter (Initial Design and Fabrication)

We designed and developed multiple customizable nanoarray platforms based on the building blocks that discussed in objectives, plasmonic nanoarrays, and 2D functional mono- few layered materials in a confined space to enhance the electromagnetic field distribution and surface chemistry for an enhanced SERS interrogation of EVs. We discussed the objectives and flow of their development and integration in the following two sections: (1) Plasmonic nanostructured arrays, encompassing the arbitrary array of 3D nanorough structures, nanosphere arrays, nanotriangle arrays and nanocavity arrays. (2) 2D nanoconfined layered materials, encompassing synthesis and integration of Graphene and MoS_2 with optimized plasmonic nanostructured arrays. Even though not all these platforms rendered suitable optical readout for EVs (*Chapters 4* and *6*), we are reporting them in this chapter to introduce the physical and optical characteristics of the nanostructured surfaces and their material combinations with the hope that it might be useful to other researchers interested in such fabrication.

3.1 Plasmonic Nanostructured Arrays

Metallic nanostructured arrays are a class of plasmonic nanostructures offering a strong EM-field enhancement. Materials and spatial geometries of nanoarrays impose the location and intensity of hotspots and consequently determine the optical properties in their vicinity verified by the electric field enhancement factor (EFEF). In this thesis we limited the plasmonic material type to gold and silver as the most prominent choices of SPR supported materials and explored geometrically varied nanostructured arrays with absorption in the range of 500-540 nm (laser beam wavelength used for EVs molecular profiling). The plasmonic nanoarrays were structured in arbitrary pitches, rectangular or hexagonal lattices and their spatial geometries, optical absorption,

and EM field distribution were characterized to realize the EFEF enhancement as the crucial factor for signal amplification in molecular profiling of EVs via SERS.

Recent advances in amplifying the SERS spectrum using a variety of plasmonic nanostructures, including metallic nanoparticles(C. Lee et al., 2017; Pang et al., 2019; Weng et al., 2018), shed light on the potential of developing surpassed nanostructures for enhanced SERS detection of EVs. According to the fabrication method, lithography or fabless, the nanospheres were embedded into a rectangular or hexagonal array respectively. Figure 3-1a and b compare a schematic of each array respectively in an example situation where the horizontal pitch of the array is fixed at 400 nm and the size of nanospheres are shrined to 130 nm.

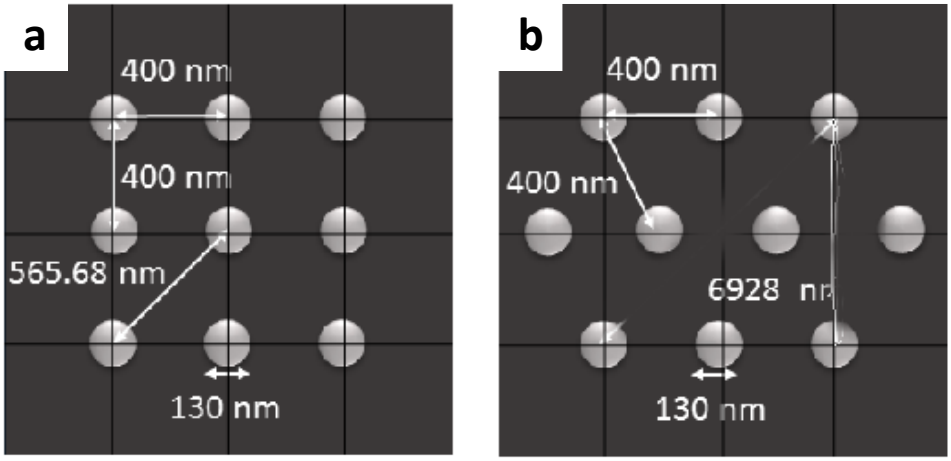

Figure 3-1. An example schematic of comparing the pitch difference (center to center) of the nanosphere structures in (a) rectangular and (b) hexagonal arrays.

3.1.1 Self-assembly Nanospheres (Hexagonal Array)

Initially a self-assembly approach using polystyrene nanoparticles with diameter ranging from 200 nm to 750 nm was used to pattern a hexagonally packed array on a silicon substrate via Langmuir-Blodget technique. Then, by deposition of a back reflector layer and plasmonic metallic layer, a plasmonic hexagonal array of nanospheres was fabricated (Figure 3-2a). Figure 3-2b and

c show the SEM micrograph and AFM surface topography of the self-assembly hexagonal pattern of the nanosphere arrays. Both illustrate the groove shaped narrow structures between the two nearby nanospheres, giving rise to the plasmonic resonance of the platform when illuminated by light which in turn can result in EM field enhancement.

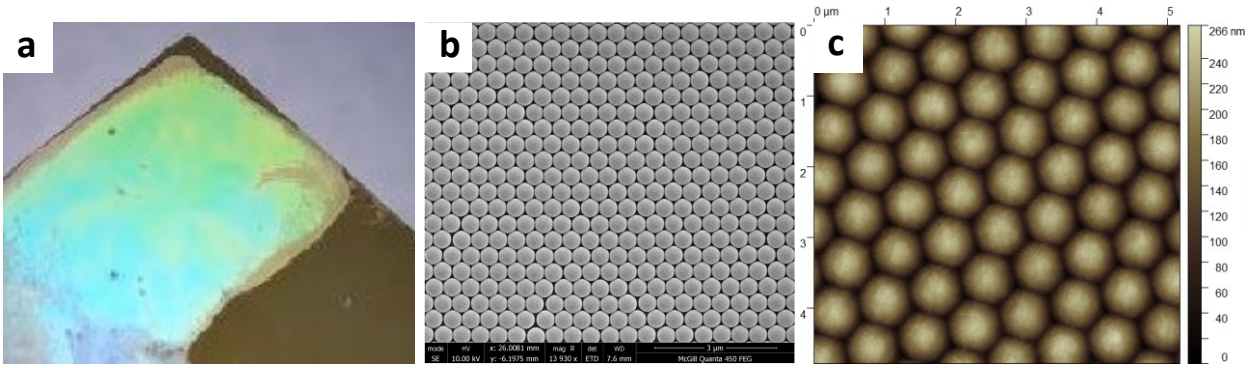

Figure 3-2. Self-assembly Nanosphere Array (a) Schematic illustration of fabrication method. (b) optical images of the self-assembly nanoparticles. (c) SEM image of the self-assembly nanoparticles and fabricated nanobowties platform after lift-off.

Even though the self-assembly nanosphere array provided us with a periodically smooth nanoarray surface, there was limitations to further enhance the EM field enhancement, including the predefined pitch between the spheres according to the size of them (i.e. self-assembly patterning of the nanospheres with diameter of 400 nm renders an array with pith size of 400 nm). Therefore, preventing the possibility of exploring dimer and trimer sphere arrays.

3.1.2 Lithography Nanospheres (Rectangular Array)

Then, in order to control the gap-size and the pitch of the nanosphere array, a positive e-beam lithography technique was used. First the positive resist PMMA was patterned with the desired monomer, dimer, and trimer lattice, followed by deposition of silver (plasmonic material) and lift-off. The pitch of the array was chosen to be 400 nm (following the previous FDTD studies

to determine 400 nm pitch effective to introduce an absorption band in the range of the 500-540 nm (which is the laser wavelength used for SERS characterization of the EVs). First, monomer arrays in the form of a rectangular lattice were fabricated on a silicon substrate (Figure 3-3a). To study the effect of the Fano resonance by patterning two spheres in their proximity (g<= 60 nm), we patterned dimers with the same lattice geometries as monomers (Figure 3-3b). Similarly, trimers were patterned to investigate whether increasing the number of gaps affects the EM field enhancement when illuminated by the polarized laser beam (Figure 3-3c).

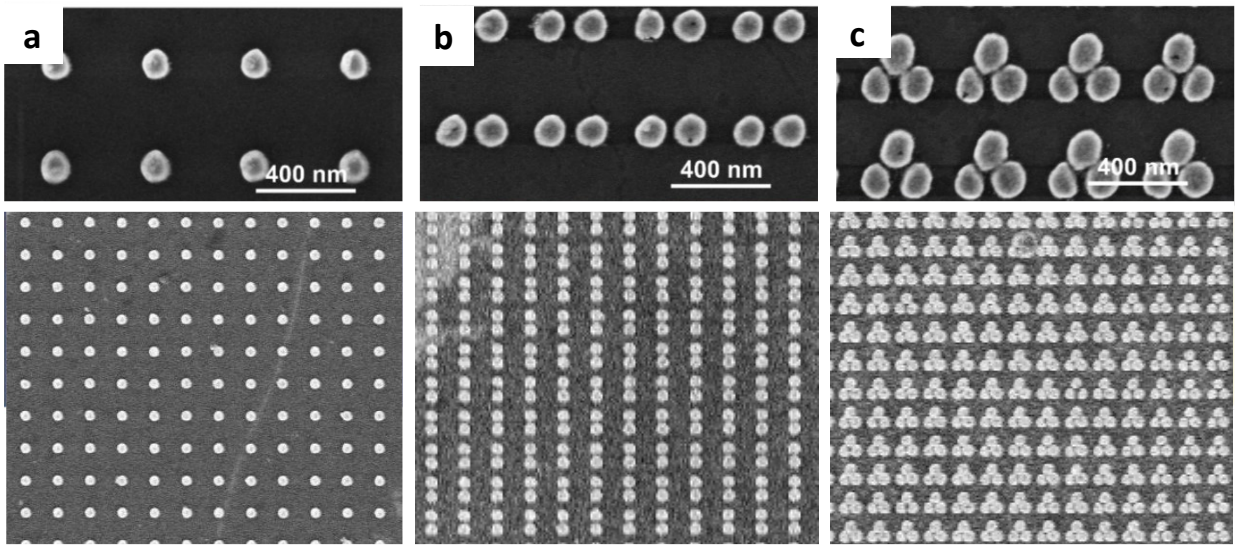

Figure 3-3. Lithography nanosphere array. (a) High- and low-resolution monomer nanospheres in a rectangular array (d~ 100 nm). (b) High- and low-resolution dimer nanospheres with gap size of ~20 nm in a rectangular array. (c) High- and low-resolution trimer nanospheres with gap size of ~10-20 nm in a rectangular array.

To understand the extent of contribution of oligomeric array of nanospheres in plasmonic based EM field enhancement, we performed a series of optical characterization and theoretical simulations via FDTD. A profound in-plane dipolar resonance was highly confined at the metal-substrate interface when the beam is polarized at the dimer's axis, allowing the study of near-field enhancement from the plasmonic resonance. The dimers demonstrated a superior EM-field

enhancement between the gaps of the silver nanospheres and therefore stronger plasmonic oscillation. The dimer silver array exhibits dipolar resonances at the laser excitation wavelength (532 nm). The near-field intensity increases with the number of silver disc, indicating the lowering of the energy level of dipolar resonances, due to the stronger coupling between the silver nanosphere within one dimer unit cell and thus strong plasmonic hybridization. The formed bonding of super-radiant modes red shift from 560 nm to 600 nm, as the nanostructure evolves from monomer to dimer. Trimers provide a greater degree of freedom in terms of laser beam polarization compared to dimer and monomer, realizing less intensity EM field distribution but with both directions of the light polarization.

Using the e-beam lithography approach, nanosphere array in shapes of multimers (dimers and trimers) were fabricated with adjustable gap size that realized enhanced EM field distribution over the surface when illuminated. Compared to the monomer nanosphere lattice, multimer nanosphere lattice provided us with enhanced EM field efficiency (EFEF < 10^4), however, this enhancement was not yet enough to distinguish the molecular traits correlated to cancer in EVs derived from different tumor cell lines (even though this platform allowed to distinguish between EVs derived from non-cancer and cancer cell lines). Therefore, in the next step we explored the EM field amplification in the context of two nearby nanotriangles (nanobowties) with sharp apex, which can provide locally enhanced EM-field in sharp and confined plasmonic gaps (*Chapter 4*).

3.2 2D Nanoconfined Layered Materials

Based on previous studies, the integration of noble metal particles with 2D materials, in specific graphene and MoS_2, can enhance the stability, intrinsic mobility, photoluminescence and raman response. (Tran et al., 2016, 2017; Q. H. Wang et al., 2012) Based on the intrinsic behaviour

of each part of this combination we assume that integration of hierarchical 3D metallic nanostructures further enhances the previously discussed points as well as providing electron transfer roots and single quantum plasmonics for the adjusted 2D materials, thus enhancing optoelectronic read-out systems for the platform. Graphene and MoS_2 are sensitive to changes corresponded to binding of biomolecules, proteins and other biological analytes at their interface due to the applied changes in their electrical properties.(Gao et al., 2013) Thus, they enabled development of label-free, fast, real-time and quantitative detection of these analytes in different media. The high sensitivity, low-cost, easy patternability and integrability of graphene and MoS_2 led the researches in past years to focus on integrating or decorating them with structured materials to enhance their stability, throughput and selectivity(Jing Chen et al., 2016; S. J. Li et al., 2013; C. Zhao et al., 2017; Y. Zhu et al., 2010).

3.2.1 Graphene (Colloidal Exfoliation)

Carbonaceous materials including graphene are being harnessed as interfaces for surface chemisorption sensing techniques. Graphene is an isolated, single or few layered honey-comb hexagon-structure of carbon molecules consisting of sp^2 hybridized C-C bonding with π-electron clouds.(Bolotin et al., 2008; Cai et al., 2009; Gale et al., 2012) Thus, it shows promising properties in establishing π- π interactions with a variety of biomolecules due to its conductance charging as a function of surface absorption and low Johnson noise.(G. Zhao et al., 2017) However, inherent thin thickness, aggregation, weak adhesion, and low surface area limits its application(Bo et al., 2017; Gan & Hu, 2011; Y. Liu et al., 2012; Zhaoyin Wang & Dai, 2015), therefore, when combined with the plasmonic nanoarrays we can expect prevention from agglomeration to some extent.

3.2.1.1 Synthesis

Graphene nanosheets were exfoliated from expandable graphite flakes through a modified, previously-reported ultrasonication method to achieve a nano-sized thickness of graphene sheets. The right-top inset shows a schematic illustration of the supramolecular interactions based on attractive and repulsive forces between graphene and adjacent molecules, leading to the selectively stacking of catecholamine molecules. Transmission electron microscopy (TEM) was first carried out to determine the degree of liquid exfoliation and the quality of the graphene nanosheets. Figure 3-4a shows a TEM image of a representative few-layer graphene nanosheet, demonstrating relatively high-quality of exfoliation. Selected area electron diffraction (SAED) pattern corresponding to graphene layer is shown in Figure 3-4b, demonstrating the hexagonal diffraction pattern of graphene lattice.

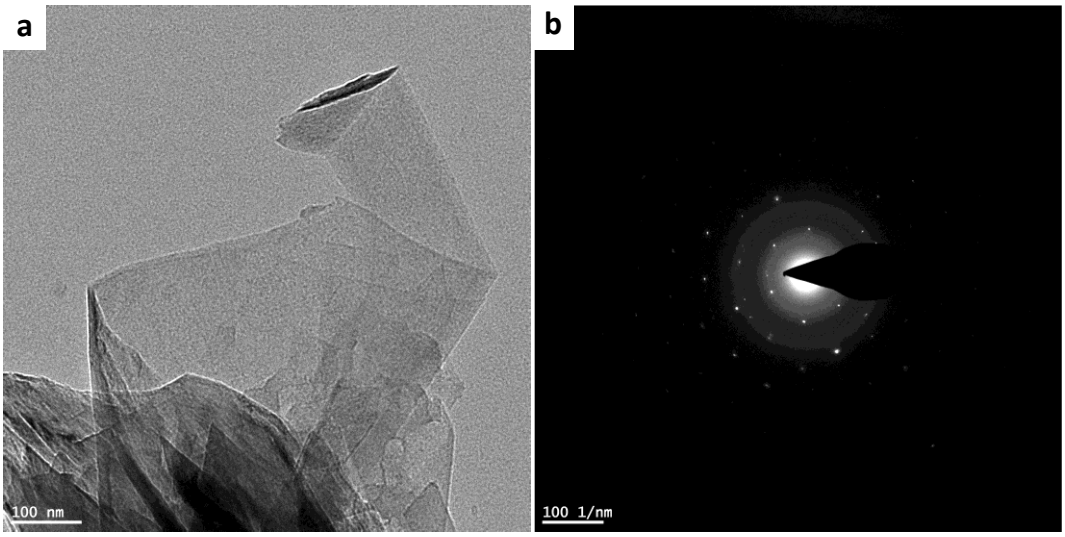

Figure 3-4. TEM Characterization of Gr/ 3D NMI Gold. (a) TEM image of a representative graphene nanosheet. Inset shows high-resolution image of gold with 0.23 nm lattice spacing, indicating (111) plane of gold. (b) SAED pattern corresponding to graphene.

3.2.1.2 Integration with Plasmonic Nanoarrays

To investigate the effect of integrating the characteristic optical and electrical properties of the colloidal exfoliated graphene layers with the plasmonic nanoarrays, we incorporated the layered graphene using a simple drop-casting approach. *First,* we attempted to reduce the bleaching effect from gold nano/micro shrubs by using graphene nanosheets*,* so we developed a combined top-down photolithography and bottom-up electrochemical approach to design a gold nano/micro island structures to host graphene nanosheets, Gr/ 3D NMI (Figure 3-5a). Similarly, we integrated the graphene nanosheets with the plasmonic nanosphere array (Figure 3-5b) and triangle array (Figure 3-5c) which for both cases led to surface agglomeration of the sheets (compared to the case with 3D NMI array).

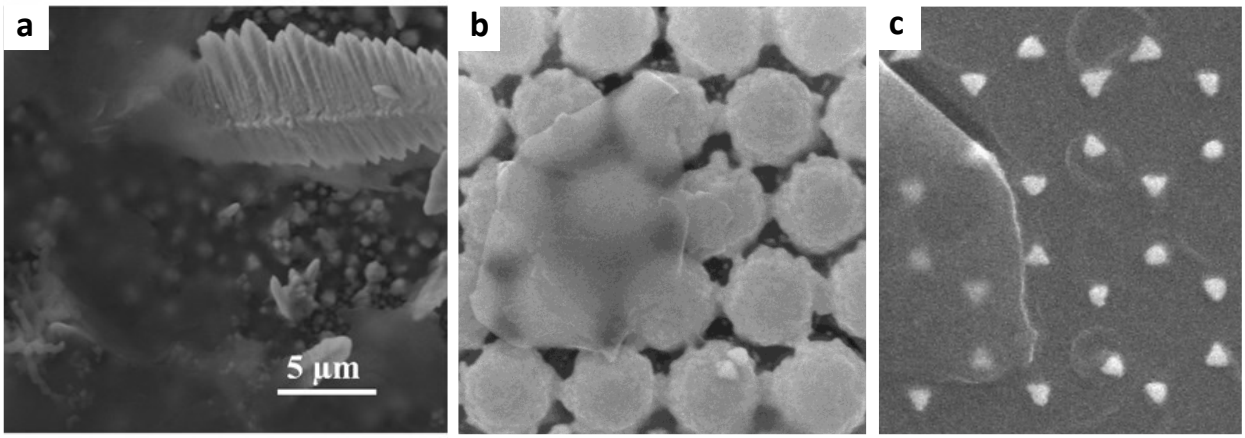

Figure 3-5. Integration of colloidal exfoliated Graphene with (a) 3D NMI nanoarray, (b) self-assembly nanosphere array, and (c) self-assembly lift-off nanotriangle array.

The inconsistency of the liquid phase exfoliated graphene nanosheets drop-casted on the gold NMI array, nanosphere array, and nanotriangle array did not allow for a consistent baseline for the SERS readouts. We found the potential of this platform for catalytic sensing of catecholamines and bacteria instead. As a proof of principle, the developed Gr-based convex platform was integrated with a sample delivery system to study the probe-free detection of

dopamine in low concentration quantitatively with clinically relevant sensitivity (Jalali, Filine, et al., 2020).

3.2.2 MoS_2 (CVD)

We predicted similar issues in the integrating intercalated few layer MoS_2 material (through colloidal or mechanical) approaches with the plasmonic structures are due similar to the same case with the few-layer Graphene. To prevent the agglomeration, non-uniform spread of the layers and therefore inconsistent baseline from the substrate in SERS signal readout, we decided to incorporate monolayer single crystalline MoS_2 material.

3.2.2.1 Synthesis

The monolayer was produced through CVD method by nucleation and growth from vapour phase solidified on the substrate of choice. Monolayer MoS_2 was grown by CVD with molybdenum trioxide (MoO_3, 99.75%, Sigma Aldrich, 20 mg) and sulfur powder (S, 99.997% Sigma Aldrich, 40 mg) following a developed procedure (Jalali, Gao, et al., 2021). An SiO_2/Si, (1 cm × 2 cm) substrate was cleaned with de-ionized (DI) water, followed by spin-coating of sodium cholate hydrate (SC, Sigma Aldrich) solution as the growth promoter. The SiO_2/Si substrate was then transferred into the furnace. The growth was carried out at 760 °C with Argon for 10 min. After growth, the furnace was rapidly cooled to room temperature. The bright-field microscope image (Figure 3-6a) shows the triangular shape of single-crystal MoS_2 (average 10 μm in size). Further study of MoS_2 using Raman spectroscopy, showing a consistent spectral intensity with 20 nm difference between A_{1g} and E^1_{2g} peaks referring to monolayer specifications of MoS_2 (Figure 3-6b). The room temperature photoluminescence from monolayer single crystalline MoS_2 can enhance the surface plasmon resonance from the plasmonic nanoarray through enhanced nearfield absorption (Figure 3-6c). It increases the light absorption in the vicinity of the

metal(Boulesbaa et al., 2016; Schuller et al., 2010), which allows for non-radiative relaxation of the electrons and therefore injecting hot-electrons to the plasmonic surface(Boulesbaa et al., 2016; Mubeen et al., 2013). Therefore, photoluminescent (PL) of the monolayer can enhance the SPR by increasing the light-exciton energy transfer rate and lowering the dissipation rate(W. Liu et al., 2016).

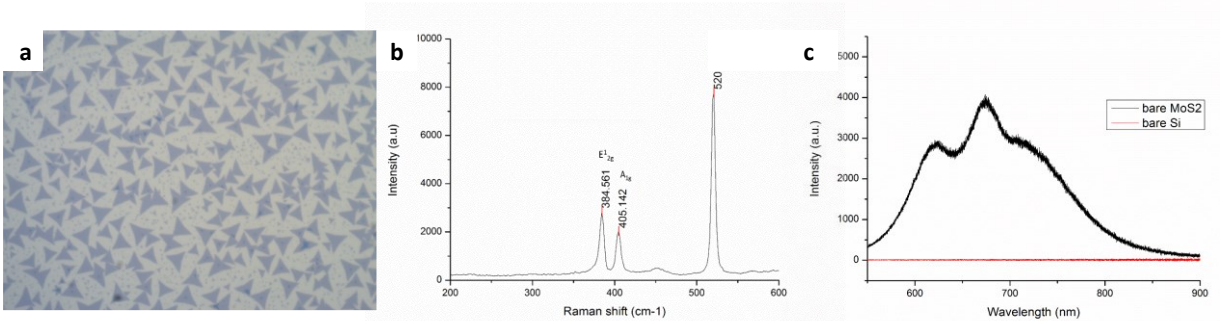

Figure 3-6. CVD grown monolayer MoS_2. (a) Microscope image of CVD grown MoS_2 in bright mode. (b) Raman spectrum of monolayer MoS_2. (c) Photoluminescent of the monolayer single crystalline MoS_2 at room temperature compared to bare crystalline silicon wafer.

3.2.2.2 Integration with Plasmonic Nanoarrays

To simultaneously harness the EVs and assimilate the SERS signal, we patterned the plasmonic nanoarrays on the CVD grown monolayer MoS_2 via e-beam lithography. Monolayer MoS_2 was patterned with Ag monomer nanospheres in hexagonal array (Figure 3-7a), Ag monomer and dimer nanospheres was patterned in rectangular array (Figure 3-7b). However, the nanosphere array did not provide the means for single EV analysis, therefore, we patterned the monolayer MoS_2 with Ag nanocavity array (Figure 3-7c) to attain single EV SERS molecular profiling. Upon CVD-growth of monolayer MoS_2 on a SiO_2/Si substrate, a negative e-beam lithography is used to pattern the nanocavities. A 532 nm laser was used for SERS to activate localized surface plasmon resonance (LSPR) from the nanocavities and record the diffraction signal from single EV SERS.

For the practical utility of the substrate for SERS liquid biopsy, we simplified the overall operation to the manual injection of purified EVs. The details of the EV studies via optimized MoS_2/ Nanocavity plasmonic array microchip is discussed in *Chapter 6*.

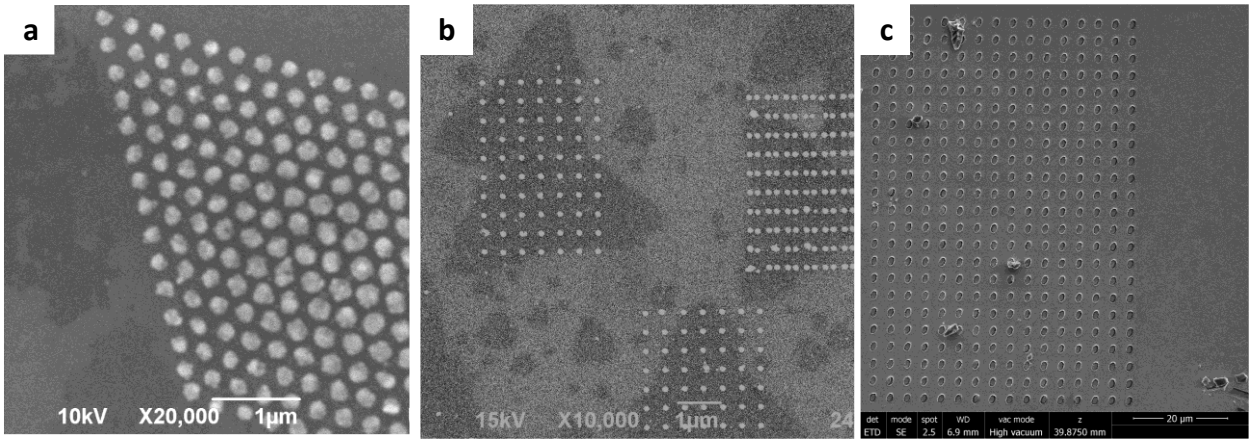

Figure 3-7. Monolayer MoS_2 patterned with (a) Ag monomer nanospheres in hexagonal array, (b) Ag monomer and dimer nanospheres in rectangular array, (c) Ag nanocavity array.

3.3 Conclusions

The limited sensitivity of current devices and analytical methods limits access to the diagnostically significant information contained in EVs. To improve the EM field distribution of the plasmonic surface and hence enhance the sensitivity of EVs SERS molecular fingerprint, we designed and developed multiple plasmonic nanoarray platforms based on plasmonic nanostructured arrays, encompassing the arbitrary array of convex structures, nanosphere arrays, and nanotriangle arrays. Additionally, we developed 2D layered materials (Graphene and MoS_2) and integrated them with the plasmonic nanoarrays to enhance optical properties and enable label-free entrapment of single EVs in confined spaces.

Different plasmonic nanoarrays with varied geometrical characteristics have been developed and characterized in this project to optimize the fabrication of hybrid plasmonic platforms for on-chip molecular identification of EVs, using cost-effective direct growth methods

to high-resolution e-beam lithography patterns. We have characterized the optical absorption and spatial geometries of the plasmonic nanoarrays with arbitrary pitches, rectangular or hexagonal lattices, in order to achieve the electromagnetic field enhancement in molecular profiling of EVs via SERS, as well as spatial entrapment of EVs using the nanostructures. The EM field enhancement of nanobowtie arrays with customizable gaps for concentrating light absorption demonstrated valuable properties in SERS. While the nanocavity array allowed single EV entrapment (with the right surface chemistry) resulting in higher sensitivity for sorting heterogeneity of EV molecular profiles.

Additionally, 2D materials (Graphene and MoS_2) were investigated as layered materials that are sensitive to changes in their properties can correspond to the binding of biomolecules, proteins, and other biological analytes at their interfaces. However, the bleaching effect caused by colloidal exfoliation of graphite during fluorescent microscopy and the inconsistency of the liquid phase exfoliated graphene nanosheets drop-cast on the gold NMI array, nanosphere array, and nanotriangle array for molecular profiling were among the disadvantages of using Graphene nanosheets. Similarly, hydrothermally grown 3D MoS_2 nanosheets exhibited jagged surfaces unsuitable for microscopy and inconsistent intensities from characteristic peaks of MoS_2 and MoO_3, making them unsuitable for molecular profiling by SERS. Using CVD-grown monolayer MoS2, however, not only prevented agglomeration, but also provided relatively consistent Raman intensity at the E^1_{2g} and A_{1g} Raman baselines. It can therefore be used for both SERS signal reading and fluorescent microscopy. Since monolayer MoS_2 exhibits a fragile texture, integration with plasmonic nanoarrays using an e-beam fabrication approach poses the lowest challenges. Particularly, single EV entrapment by the monolayer MoS_2 / plasmonic nanocavity array appeared promising for single EV SERS molecular profiling.

4 Plasmonic Nanobowtiefluidic Device for Sensitive Detection of Glioma Extracellular Vesicles by Raman Spectrometry

Mahsa Jalali,[a] Sayed Imman Isac Hosseini,[a] Tamer AbdelFatah,[a] Laura Montermini,[b] Sebastian Wachsmann Hogiu,[a] Janusz Rak,[b] Sara Mahshid*[a]

[a] Department of Bioengineering, McGill University, Montreal, QC H3A 0E9, Canada

[b] Research Institute of the McGill University Health Centre (RIMUHC), Montreal, QC, Canada

Abstract

Cancer cells shed into biofluids extracellular vesicles (EVs) — nanoscale membrane particles carrying diagnostic information. EVs shed by heterogeneous populations of tumor cells offer a unique opportunity to access biologically important aspects of disease complexity. Glioblastoma (GBM) exemplifies cancers that are incurable, because their temporal dynamics and molecular complexity evade standard diagnostic methods and confound therapeutic efforts. Liquid biopsy based on EVs offers unprecedented real-time access to complex tumour signatures, but it is not used clinically due to inefficient testing methods. We report on a nanostructured microfluidic-device that employs SERS for unambiguous identification of EVs from different GBM cell populations. The device features fabless plasmonic nanobowties for label-free and non-immunological SERS detection of EVs. This nanobowtie fluidic device combines the advanced characteristics of plasmonic nanobowties with a high throughput sample-delivery system for concentration of the analytes at the vicinity of the detection site. We showed theoretically and experimentally that the fluidic device assists monolayer distribution of the EVs, which propel the probability of EV's existence in the laser illumination area. In addition, the optimized fabless nanobowtie structures with an average electric field enhancement factor of 9×10^5 achieves distinguishable and high intensity SERS signals. Using the nanobowtie fluidic and a micro-Raman equipment, we were able to distinguish a library of peaks expressed in GBM EVs subpopulations from two distinct Glioblastomas cell lines (U373, U87) and compare to that of non-cancerous glial EVs (NHA), and artificial homogenous vesicles (e.g. DOPC/Chol). The cost-effective and easy-to-fabricate SERS platform and a portable sample-delivery system for discerning the sub-population GBM EVs and non-cancerous glial EVs, may have broader applications to different types of cancer and their molecular/oncogenic signature.

Keywords: Extracellular vesicles, plasmonic nanoantenna, nanobowtie, SERS, microfluidic device.

4.1 Introduction

Early detection of cancer cells and monitoring their evolution with minimal invasiveness is central to further improvement of disease outcomes. Glioblastoma multiforms (GBM) shows dramatically lethal course and rapid progression marked by de novo or acquired unresponsiveness to therapy. GBM exemplifies a dire need for such new solutions given that the median overall survival of patients remains approximately 15 months, despite of aggressive surgical and radio-chemotherapy treatment, along with extensive molecular profiling that fuel targeted and biological therapy trials, thus far too little success(Reifenberger et al., 2017a). Since all trials with ostensibly well rationalized targeted therapies have essentially failed, it is likely that disease complexity is not captured and factored in the decision making. Among the key traits underlying intractability of GBM is the disease cellular heterogeneity, including the complexity and divergent molecular drift of constituent cellular subpopulations along with their disease driving mechanisms(Garnier et al., 2018a; Patel et al., 2014). Since the access to intracranial tumour masses is often limited, monitoring these cellular events in real time and development of adaptive therapeutic responses presents a daunting problem(Contreras-Naranjo et al., 2017; K. Liang et al., 2020).

Precision oncology based on molecular profiling of tumor biomarkers in biofluids (liquid biopsy)(Choi, Montermini, et al., 2019) is designed to address some of these challenges, but thus far with no impact on GBM and in several other malignancies(Siravegna et al., 2017; Zachariah et al., 2018). In this regard some of the limitations associated with soluble analytes (e.g. proteins or nucleic acids) could be overcome by extracting cancer cell fingerprints from their derived heterogeneous extracellular vesicles (EVs) circulating in biofluids such as blood plasma or

cerebrospinal fluid. EVs are micro- to nanosized membrane bound cellular fragments shed from cells in a regulated manner and containing molecular signatures of donor cell identity, state and degree of transformation including cancer-driving mutations(Zachariah et al., 2018). EVs play documented roles in transmission of molecular cargo between different cellular populations. For example, cancer cell EVs carry oncogenic macromolecules to normal cells altering their behaviour in cancer. This property is associated with the massive entry of EV populations into the biofluid spaces (e.g. blood) where they could be intercepted and analysed for diagnostic purposes. It is also noteworthy that EVs carry fingerprints of cells from which they originate, including important oncogenic driver mutations, therefore unlike any other liquid biopsy analyte, they can capture remarkable and clinically important cellular traits and the heterogeneity between cellular populatons.(Al-Nedawi et al., 2008b; Ramirez et al., 2018b) Recent liquid biopsy advances based on EVs, opened up a new research avenue predicated on recovery salient features of EV parental cells, and reconstruction of their molecular fingerprint relevant for the biology, phenotype, progression, therapeutic responses and heterogeneity of cancer cell populations of interest. (Carmicheal et al., 2019; Knudson et al., 2015; C. Lee et al., 2017; Shin et al., 2018b; Shin, Oh, Hong, Kang, Kang, Ji, Choi, Choi, et al., 2020; Stremersch, Marro, Pinchasik, Baatsen, Hendrix, De Smedt, Loza-Alvarez, et al., 2016; Tantussi, Messina, Capozza, Dipalo, & Lovato, 2018; Weng et al., 2018)

Notably, EVs also carry signatures of GBM molecular subtypes which are diagnostically meaningful and essential for proper stratification of patients included in clinical studies(Lane et al., 2019). Of special interest are small EVs (50–200 nm), including exosomes, extensively studied for their content of proteins, lipids, and nucleic acids(Choi et al., 2018; Choi, Spinelli, et al., 2019; Sheng et al., 2017; J. L. Yu et al., 2005). Indeed, the emerging diversity EVs subpopulations may

reflect the cellular complexity of the underlying tumours, a diagnostic opportunity hampered by limitations of currently available analytical methods(Choi, Montermini, et al., 2019). This study proposes a new technological approach for molecular EV profiling to break the diagnostic and therapeutic gridlock in GBM. We will harness EV's for liquid biopsy with a radically different technology paradigm. Our approach combines a plasmonic nanostructure with a microfluidic sample delivery and a label-free molecular profiling based on Surface-Enhanced-Raman-Spectroscopy (SERS) to generate a fingerprint (library of signals) reflective of the bioactive cargo of glioma EVs.

Nanostructures are widely employed to enhance the sensitivity of various read-out methods to advance detection of small bioanalytes,(Jalali et al., 2018; Jalali, Filine, et al., 2020; Jalali, Moakhar, et al., 2020; Siavash Moakhar et al., 2020) including affinity sensing(M. He et al., 2014; Peng Zhang et al., 2016b, 2018), super resolution optical microscopy(Thuenauer et al., 2011), electrochemical sensing(Chien et al., 2011; Sassa et al., 2020), and surface enhanced Raman spectroscopy (SERS)(Jiangang Liu et al., 2020; Shin, Oh, Kang, et al., 2020; Xi et al., 2009; Peng Zhang, Zhou, He, et al., 2019a). Among them, probe-free (no immune-capturing of bioanalytes) SERS paved the way to facilitate development of technologies in antibody-free detection of EVs. SERS enables recovery of molecular fingerprints of the bioanalytes. The vibrational and rotational modes of chemical bonding structures reflect as spectral peaks based on the electromagnetic field (EM-field) generated in plasmonic nanopatterns(Juanjuan Liu et al., 2020b; Shin et al., 2018a). Recent advances in amplifying the SERS spectrum using a variety of plasmonic nanostructures(Knudson et al., 2015; Shin et al., 2018a; Stremersch, Marro, Pinchasik, Baatsen, Hendrix, De Smedt, Loza-Alvarez, et al., 2016; Tantussi, Messina, Capozza, Dipalo, & Lovato,

2018), shed light on the potential of this technique to integrate with fluidic delivery systems (Galarreta et al., 2013; Henkel et al., 2010; Kaufman et al., 2019).

Metallic nanobowtie structures are a class of plasmonic nanostructures offering a strong EM-field enhancement. The locally enhanced EM-field in sharp and confined plasmonic systems has been exploited to create an ultra-small, ultra-intense light concentration already incorporated in some SERS applications(Fromm et al., 2004; Hatab et al., 2010b; H. K. Huang et al., 2020) but still largely unexplored in the space of EVs in spite of several advantages. Materials and spatial geometries of nanobowtie structures impose the location and intensity of hotspots and consequently determine the optical properties in their vicinity verified by the electric field enhancement factor (EFEF)(Fraire et al., 2019). In order to amplify SERS signal intensity, it is essential to optimize the material and geometries of plasmonic structures to maximize the EFEF. Among different fabrication methods available to cast nanobowtie structures, nanosphere lift-off lithography is cost-effective and time-efficient, while offering morphological homogeneity and reproducibility.

Here, we report on a nanosurface microfluidic device based on embedded nanobowtie-shaped antennas (nanobowties) placed at the bottom of the fluidic chamber for SERS detection and identification of tumor EVs. Microfluidic devices have been successfully implemented for SERS diagnosis(S. Bai et al., 2018a; M. Fan et al., 2012; Lao et al., 2020; Sevim et al., 2020), yet they require enhanced sensitivity- one of the common difficulties in detection and investigation of nanosized EVs (<200 nm). Nanosurface microfluidics combine the advantages of nanostructured materials such as high surface area and enhanced optical and electrical properties, with the advantages of microfluidics such as small sample volume manipulation and automation(AbdelFatah et al., 2018; S. Bai et al., 2018b; Dittrich & Manz, 2006; Hoi et al., 2011;

Mahshid et al., 2015; Tsai et al., 2013; X. Zhou et al., 2019). We have previously demonstrated that nanosurface microfluidics offer high detection sensitivity in optical and electrical read-out systems, while providing high precision and control over analyte concentration(Jalali et al., 2018; Jalali, Filine, et al., 2020; Jalali, Moakhar, et al., 2020; Siavash Moakhar et al., 2020). In this work, we demonstrate the implementation of this approach to improve the resolution of SERS EVs from two different human glioma cell lines with different aggressive properties (U373 and U87) and distinguish them from synthetic liposomes. A comprehensive theoretical and experimental studies were performed to explicate the synergic potential of the nanobowtiefluidic device in amplifying SERS signal. We suggest that portable and high throughput nanosurface microfluidics based on this technology could identify a unique fingerprint for ultra-small particulate bioanalyte populations, such as cancer EVs.

The characterization of the EVs from patient plasma or biofluids is challenging due to content of EVs derived from both normal and malignant cells. However, there are multiple precedents of using other than SERS detectors to analyse clinical samples, including those of brain tumours(Shao et al., 2012a). In GBM blood brain barrier is largely compromised which allows tumour EVs to penetrate into the blood stream, while cerebrospinal fluid (CSF) offers and even greater opportunity to access this material. While the choice, nature and preparation of the sample may pose a layer of complexity for SERS molecular EV profiling, it does not preclude using this detection method to profile EVs and through this lens study tumor heterogeneity.(Carmicheal et al., 2019) That said, the current approach faces pre-analytical limits in terms of direct diagnostics applications and additional sample handling steps might be necessary to overcome this barrier(X. Li et al., 2019). In addition, chemical content of plasma may interfere with the SERS signals while speeding the deterioration of the silver thin film. Nonetheless, the ability of SERS to develop

physical profiles of molecularly distinct cancer EVs, based on purified exosome fractions prepared in buffer solutions represents the first and critical step in this direction. Our present study asks whether SERS can distinguish GBM EVs not only from those of normal cells but also from one another. This way it is possible to build up a conclusive library based on which we can define the heterogeneity of the tumor cells using purified EVs which can lead to enhanced therapeutic decisions.

4.2 Results and Discussion

4.2.1 Integrated nanobowtiefluidic device

In order to enhance Raman signals of cancer-derived EVs we first constructed a nanosurface fluidic device composed of three parallel fluidic compartments with separate inlets and outlets in which the EVs and buffer solutions flow in and out. Figure 4-1a shows a picture of the nanosurface microfluidic device embedded with plasmonic nanoantenna. The sample solution is introduced to the device through the input ports and flow through the serpentine channels (50× 250 μm^2) connecting the input ports to the analysis well (1 mm wide). The uniform distribution of analytes is studied as a function of fluid flow pressure to achieve a monolayer-like distribution of EVs on the nanosurface. The nanobowtiefluidic device offers enhanced SERS spectra based on 1) favourable electromagnetic field enhancement factor from plasmonic nanobowties and 2) controllable distribution of EVs on the surface via fluid flow manipulation. The functionality of the device is attributed to the unique synergic effect of using optimized plasmonic nanobowtie surface with EVs uniformly dispersed across the detection platform for sensitive SERS detection. The concept of distinguishing molecular fingerprint of EVs versus liposomes (a bilayer lipid membrane analogous to EVs) via probe-free SERS detection is described in Figure 4-1b.

Herein, we investigated the molecular fingerprints of glioma EVs (U373 and U87) as opposed to liposomes as a proof of concept. A combined bottom-up and top-down approach was adopted to develop the nanobowtiefluidic device as an EV analyzer (Figure S1). First, a top-down standard lithography of SU8 coated Silicon was adopted to pattern the microfluidic device composed of analysis wells in the size of 1 mm × 1 mm × 50 μm. Second, a bottom-up method based on self-assembly polystyrene monolayer was employed to pattern plasmonic nanobowtie structures followed by deposition of ZnO and metallic material (Ag, Au, and Al) thin films. The polystyrene nanoparticles will be removed to leave behind a hexagonal array of nanosized triangles in the form of a thin plasmonic layer standing on top of a triangular metal oxide. Each two triangles in the vicinity create a bowtie structure with suspended gap area to amplify the EM-field enhancement.

The SEM image (Figure 4-1c) shows a representative image of a single nanobowtie plasmonic surface (Cyan) at the bottom of the analysis well (Violet). The nanobowtie structures can project a strong EM-field distributed in the triangles. The representative maximum field enhancement is demonstrated in a contour-map via finite difference time domain (FDTD) simulation. The well-controlled suspended plasmonic nanobowties embedded in the nanosurface microfluidic device are developed based on a cost-effective method with the optimized parameters affecting SERS efficiency i.e. size, material and concentration of analytes(Juanjuan Liu et al., 2020b).

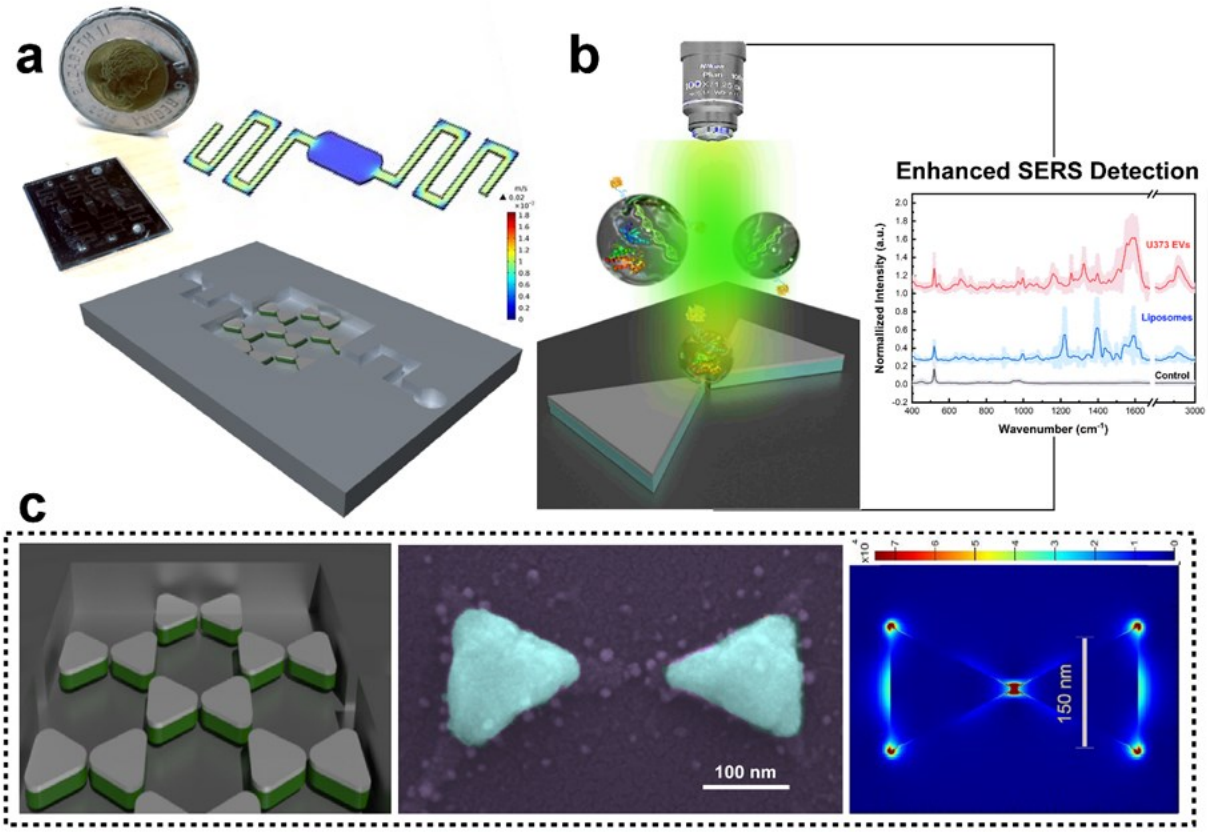

Figure 4-1. Concept of using spatially suspended nanobowtie surface microfluidic device for SERS detection of EVs. (a) Microfluidic design and prototype. (b) SERS-based detection of EVs. (c) The nanobowtie design and correlated fake-colored SEM image of the fabricated nanobowtie (Cyan). The last panel demonstrate the FDTD simulation of the maximum EM-field distributed on the surface of a nanobowtie in a honey-comb array.

4.2.2 Nanobowtie surface characterization:

The nanobowtie structures were purposefully created by tuning the size of polystyrene nanoparticles and deposition thickness of the semiconducting and plasmonic metallic layers to be 750 nm, 60 nm and 20 nm, respectively. The metallic material and the gap-size of the nanobowties play a crucial role in EM-field strength and SERS signal enhancement. Here, we conducted an extensive study on surface characterizations and optical properties of the plasmonic nanobowties,

as well as the EM-field enhancement. Figure 4-2a shows the coloured top-view SEM image of the nanobowties. The limited gap size distribution of nanobowties are demonstrated in the high-magnification SEM micrographs sorted based on increasing gap size. Generally, the size of the triangles is well-controlled at 150 nm based on the size of the polystyrene nanoparticles, while the gap size shows a limited variation between 0 – 100 nm gap size was experimentally achieved. Two main factors responsible for this variation are i) compactness of the polystyrene monolayer, and ii) the steeped angle in e-beam deposition that causes the material to diffuse beneath the polystyrene nanoparticles. Apart from gap size variation, the nanobowties impose a uniform distribution of triangles in a hexagonal array. The confined space in narrow gaps and the sharp apex of nanobowties enable the EM-field enhancement.

According to the atomic force microscopy (AFM) results (Figure 4-2b, c), the nanobowtie surface demonstrates a roughness RMS value of 0.05- 0.08 μm, which corresponds to the height of the triangles and is determined by deposition height of the thin films. Figure 4-2d and e show the UV absorption spectra, and background Raman scattering from the substrate, respectively. The mean representative absorption spectra of the nanobowties demonstrates light absorption in the visible range with plasmonic peaks placed at 410, 460 and 580 nm, that agrees with the simulated spectra (Figure S2). The background Raman spectra with the representative Si peak at 521 cm^{-1} was eliminated from the SERS spectra to process them.

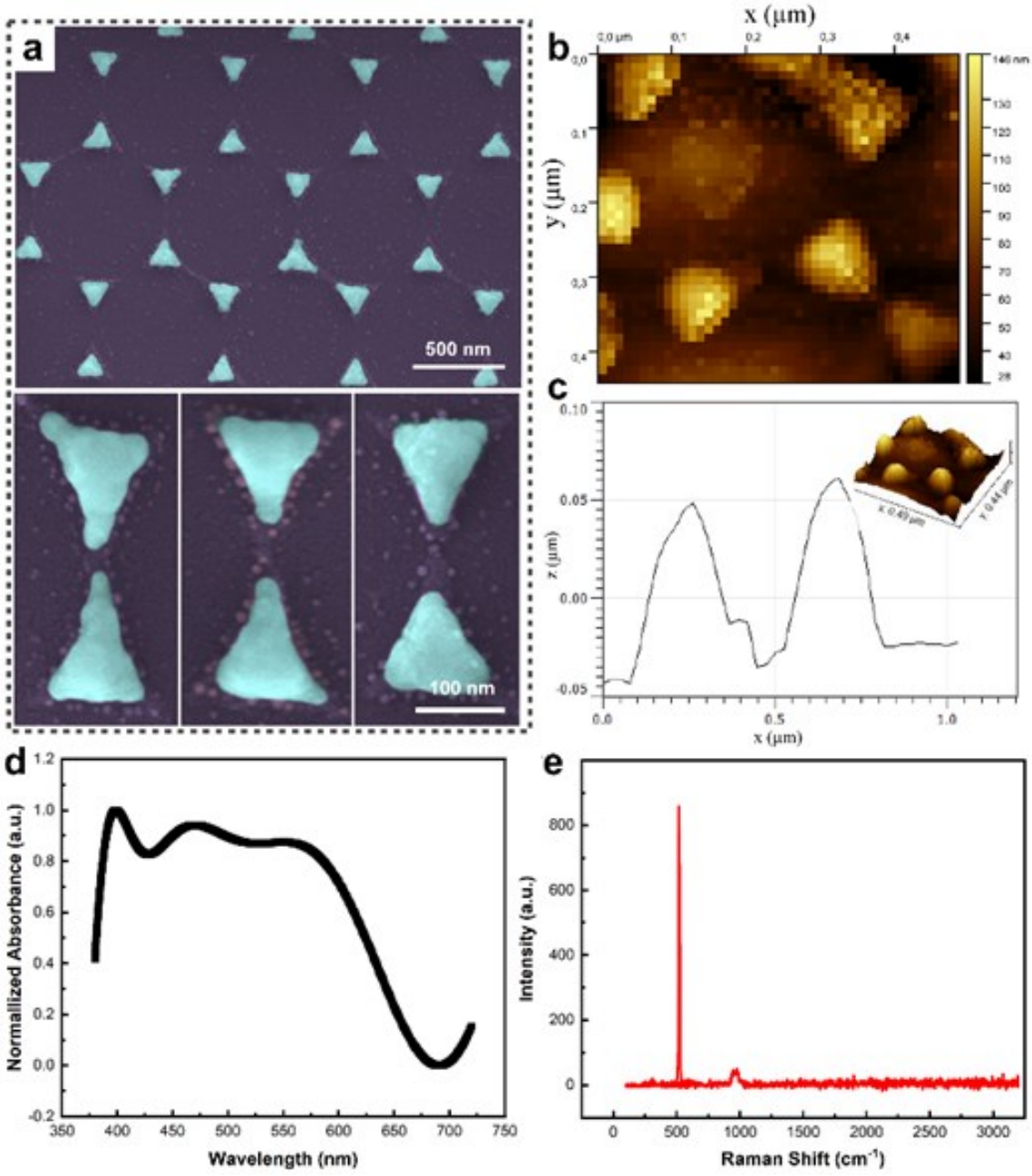

Figure 4-2. Characterizations of the nanobowties. (a) The top view SEM image of nanobowties with different gap size. (b) Top-view AFM topography of the surface, demonstrating the triangular morphology of the nanobowties on the surface. (c) The three-dimensional micrograph of triangular nanostructured platform illustrates the height and formation of nanobowties from proximity of two

triangles. (d) The absorbance spectra of nanobowtie array (black), and (e) the background Raman spectra from the nanobowtie platform (red).

4.2.3 FDTD Simulation

A strong EM field generated in plasmonic nanopatterns is of importance to amplify the Raman scattering signal. We explored these effects in the device via a simulation study based on finite-difference time-domain (FDTD) module of Lumerical Solutions. The visualization of the local EM-field enhancement is of interest to identify the modes of excitation and therefore help with the design of the optimized SERS substrates(Dodson et al., 2013). The EM-field contour plots were simulated using polarized 532 nm laser excitation. The simulation results in Figure 4-3a-c show the top-view contour plots of a nanobowtie with a 50 nm, 75 nm, and 100 nm gap size illuminated with a Gaussian beam centred at 532 nm wavelength in transverse electric (TE) and transverse magnetic (TM) modes, revealing the total EM-field enhancement, $\left|\frac{E}{E_0}\right|^2$. With noticeable hotspot along the edges of the triangles, the EM-field distribution in nanobowtie demonstrating over 900- enhancement factor at the tips of the triangles in TE mode leading to an EFEF of 9×10^5. Figure 4-3d demonstrates the EM-field sweep over the polarization angle of the beam, demonstrating a sudden drop of EM-field enhancement when polarization degree reaches over 30°. Thus, the SERS laser polarization angle was adjusted accordingly.

Figure 4-3e demonstrates the total electric field enhancement as a function of wavelength for metallic materials, Ag (Red), Au (Blue), and Al (Green), respectively. The geometrical properties of the nanobowties are optimized to maximize the EM-field (Figure S2 and S3). The contour mapping of EM-field enhancement at different wavelengths and gap-sizes (Figure 4-3f), shows that the maximum EM-field enhancement occurs at 550 nm wavelength and gap size of 5-15 nm (Figure S4). The effective EM-field in the nanobowtie gap volume is inversely proportional

to the product of the apex width (w), gap size (g), and the metallic height, therefore, for a fixed nanobowtie height, the EM-field enhancement is proportional to $(wg)^{-1}$ (Figure S4)(Hatab et al., 2010a). The maximum theoretical EFEF of 1.1×10^{9} is calculated with 10 nm gap size and 150 nm apex. However, low resolution SEM image demonstrates that the average experimental gap size is 75±5 nm. Therefore, the theoretical EFEF is calculated based on the electric field enhancement of nanobowties with gap sizes of 50-100 nm, demonstrating a value of 9×10^{5}.

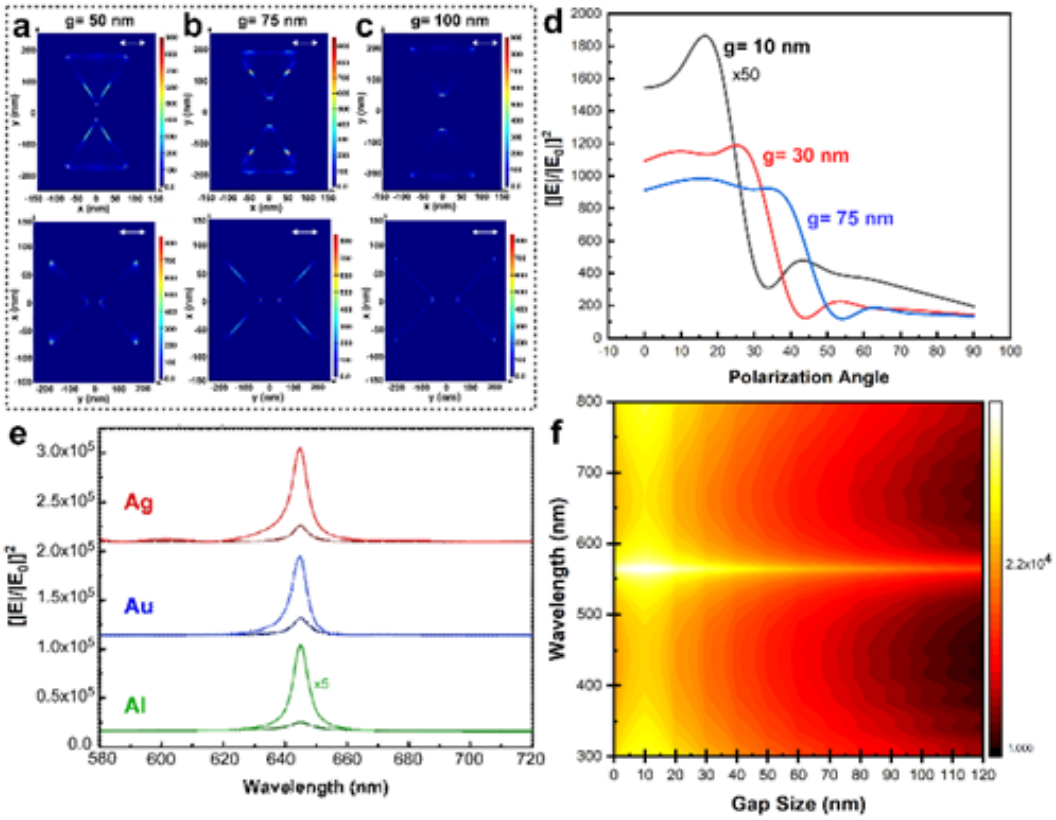

Figure 4-3. (a-c) The top view FDTD contour map of EM-field distribution $\left(\left|\frac{E}{E_0}\right|^2\right)$ in the TE and TM mode light polarization for gap sizes of 50 nm, 75 nm, and 100 nm. (d) The variation of EM-field depending on the light polarization angle. (e) Variation of $\left|\frac{E}{E_0}\right|^2$ with TM mode (dark) and TE mode (bright) excitation varying metallic material, Ag (Red), Au (Blue), and Al (Green) (f) contour

map of $\left|\frac{E}{E_0}\right|^2$ enhancement distribution with varying gap size at different wavelength. Bright yellow corresponds to higher enhancement while dark red stands for lower enhancement.

4.2.4 Nanobowtiefluidic device optimized for EVs loading:

The SERS intensity is directly proportional to the concentration of the analytes(Fraire et al., 2019), while it is inversely proportional to the 10^{th} power of distance between the test analytes and plasmonic surface(Pilot et al., 2019). In other words, the SERS signals drop rapidly by increasing the distance of analyte from the surface. Therefore, in probe-free SERS detection it is necessary to control the concentration and prevent turbulent flows in the test medium to keep analytes in close proximity to the plasmonic surface. We studied different concentrations of EVs on the surface using SEM and fluorescent microscopy to achieve the optimum concentration for formation of EVs monolayer. We also confirmed theoretically that by controlling the laminar flow in the nanobowtiefluidic device we can manipulate the forces within the fluid and precisely control the EVs distribution on the surface.

The SEM images of EVs with concentrations of 10^8 ml^{-1} and 10^6 ml^{-1} is shown in Figure 3a and Figure 3b, respectively. Figure 4a shows formation of a complete monolayer coverage on the surface at 10^8 ml^{-1} concentrations, while Figure 4b demonstrates a non-uniform distribution of EVs on the surface when the concentration is decreased to 10^6 ml^{-1}. Increasing the concentration over 10^8 ml^{-1} leads to accumulation of EVs on the surface, which can prevent receiving a direct and amplified SERS signal (Figure S5). A critical point dryer (CPD) method was used to substitute the wet content of the EVs with dried CO_2 to preserve their initial configuration(Siavash Moakhar et al., 2020). This method reveals morphological heterogeneity of EVs within the same population. The fluorescent micrograph of EVs on nanobowtie platform (Figure 4c) shows an enhanced and quantifiable image representing the EVs. The average size of the EVs deduced from nanoparticle

tracking analysis (NTA) (Figure 4d) is 157 ± 3.1 nm for the collected EVs fraction using NS500 instrument.

Supporting Figure S6 demonstrates the theoretical studies of the fluid flow and pressure inside the microfluidic device to optimize the design parameters. To analyze the movement of particles in the buffer close to the plasmonic nanobowties, 2D Brownian Dynamic (BD) simulation is performed and the drag coefficient is modified based on the Faxen's Law(T. Zhou et al., 2013). In microfluidics, low Reynolds number ($R_e \ll 1$), the drag coefficient is higher near the surface due to the creep motion of fluid flow (Happel & Brenner, 1973) (Figure S7). We show that the microfluidic device helps with concentration of higher number of EVs close to the surface of nanobowties for a same sample volume. Also, the formation of EVs monolayer on the nanobowties surface occurs at an optimum concentration. We also demonstrate that the nanosurface microfluidic device increases the probability of the presence of particles on the nanobowties due to higher surface to volume ratio. We examined the probability distribution of particles on the surface for different heights of the microfluidic device and for the same volume of sample. According to the results, the distribution of particles on the surface decreases exponentially by increasing the height of the channel (Figure 4e). The finding shows the importance of microfluidic sample delivery to increase the concentration of particles on the surface. However, the accumulation of particles on the plasmonic nanobowtie structures, results in excess amount of EVs in long-range distance from the plasmonic substrate. Therefore, we obtained the optimum EVs concentration to reach saturation without accumulation on the surface. The average number of particles near the surface was examined for different concentrations in a fluidic volume of 20 μm height and 1 μm^2 surface. The particle size was adopted from experimental data leading to a maximum number of 30 particles per 1 μm^2 (Figure 4f-inset). As

it is shown in the Figure 4f, the saturation of surface occurs when the EVs concentration reaches at 10^8 ml^{-1}, which is in agreement with the SEM observations.

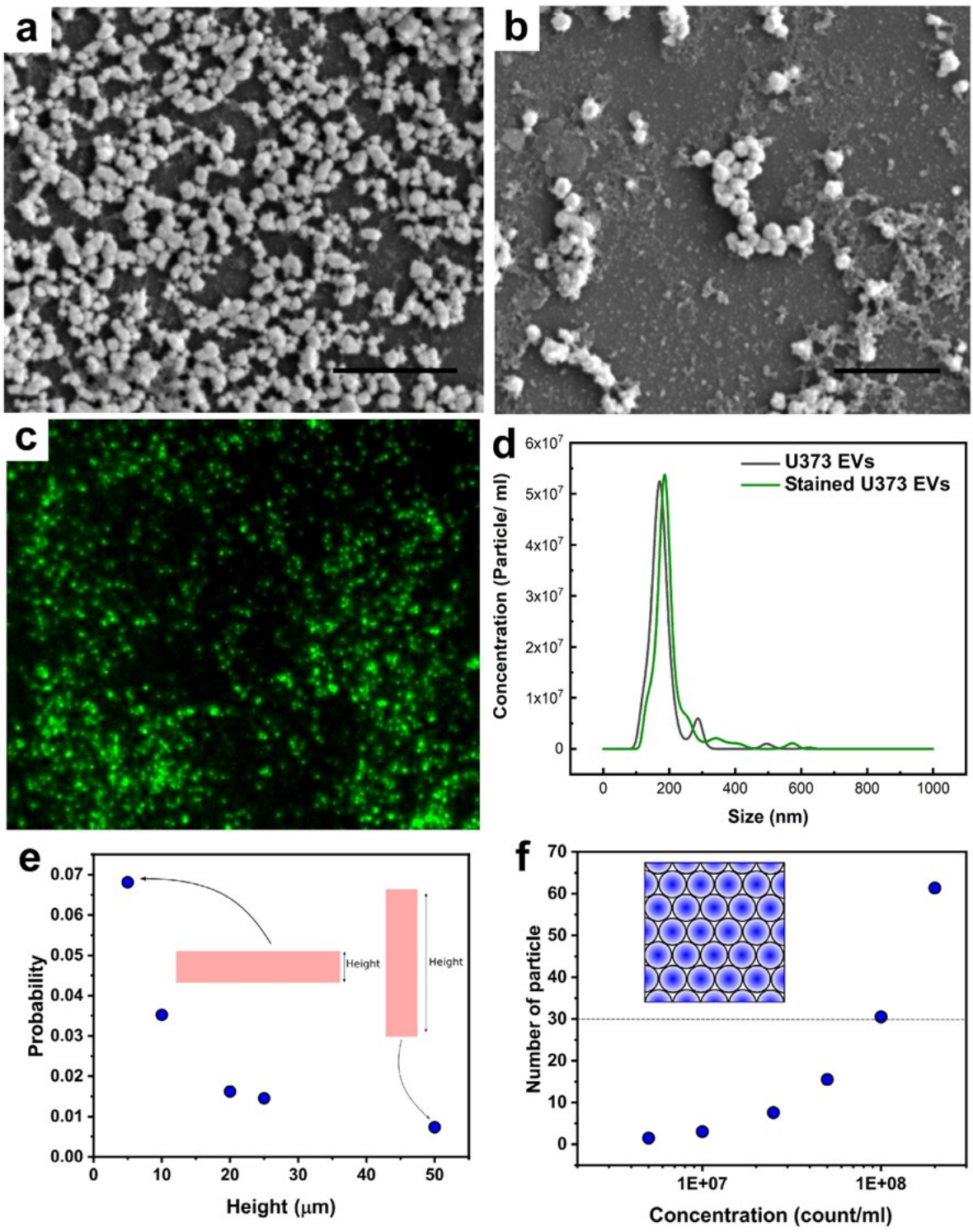

Figure 4-4. (a) The SEM image of the EVs with concentration of (a) 10^8 ml^{-1} and (b) 10^6 ml^{-1} loaded into a bare analysis chamber (scale bar: 1μm). (c) Fluorescence intensity profile of 10^8 ml^{-}

[1] EVs on nanobowtie structures. (d) Nanosight characterization of the purified fractions was conducted to determine the average size population of EVs derived from U373 cell line. BD simulation of EVs with Faxén law: (e) The effect of channel height on the probability of particles close to plasmonic nanobowties structures. (f) The number of particles close to plasmonic nanobowties structures via different concentrations of particles. The inset image shows the maximum number of particles (30 particles) with 200 nm diameter in 1μm^2 area.

4.2.5 Nanobowtiefluidic-SERS optimization for EVs analysis:

We implemented our integrated device for analysis of EVs produced by human glioma cell lines in culture. Figure 4-5 presents sensitive SERS detection of glioma EVs and liposomes with plasmonic nanobowties. The representative SERS spectra of EVs derived from glioma cells (red), non-cancerous glial cells (Magenta), liposomes (blue) and control Tris-buffer (black) is shown in Figure 4-5a, where they are vertically stacked. Each spectrum is the mean value of minimum 10 spectra collected from EVs and liposome populations and the SD value is demonstrated with a brighter colour on the graph. The sensitivity study of the NHA EVs in the range of 10^3-10^9 ml^{-1} (Figure S8a) shows the SERS fingerprint peaks intensity increases with the concentration following a sigmoidal growth function (Figure S8b). A linear range of 10^5-10^8 is detected studying the SERS integrated band area at 1000 cm^{-1} (CH_2/ CH_3 bending related to Phospholipid), demonstrating a limit of detection of 1.32×10^5 Particles ml^{-1}. Unlike non-uniform metallic nanoparticle SERS substrates that mainly form a nonuniform plasmonic substrate, the signal analysis on nanobowties substrate (produced) a coherent EM field enhancement, therefore achieving encouraging reproducibility (Figure S9a), where the fingerprint spectra can be recorded with the similar pattern in 30 trials. All the spectra were normalized based on the intensity of the Si at 521 cm^{-1}, which was shared by all data. Mean-spectra of EVs and liposome was fitted using

statistical methods available in ORIGIN PRO software. All the peaks were studied and assigned to their possible corresponding attribution (Table 1) while the existing peaks in the EVs spectrum that did not appear in liposome spectrum were graphed separately (Figure 4-5b). The peaks depicted in Figure 4b were studied for their possible attributions.

EVs and liposomes shared many similar peaks. According to previous studies, these peaks are thought to be associated with the characteristic Raman bands of bilayer lipid and proteins: 1000 cm^{-1} (phospholipid)(Knudson et al., 2015; Stremersch, Marro, Pinchasik, Baatsen, Hendrix, De Smedt, Loza-Alvarez, et al., 2016; Tantussi, Messina, Capozza, Dipalo, & Lovato, 2018), 1220 cm^{-1} (tyrosine)(Knudson et al., 2015; Stremersch, Marro, Pinchasik, Baatsen, Hendrix, De Smedt, Loza-Alvarez, et al., 2016; Tantussi, Messina, Capozza, Dipalo, & Lovato, 2018), 1435 cm^{-1} (CH_2, CH_3 deformation)(Knudson et al., 2015; Stremersch, Marro, Pinchasik, Baatsen, Hendrix, De Smedt, Loza-Alvarez, et al., 2016; Tantussi, Messina, Capozza, Dipalo, & Lovato, 2018), and 2890 cm^{-1} (cholesterol)(Shin et al., 2018b). We utilized principal component analysis (PCA) to differentiate and identify the major pattern differences between EVs and liposomes. Figure 4c shows a PCA scores plot graph. We utilized over 20 datapoints for each of the cell-derived EVs and liposomes. Each dot in the plot represents one spectrum with dimension reduction. Each data set was clustered while maximizing covariance. The first principal component (PC1), and second principal component (PC2) shown in Figure 4-5c, reveal the peaks responsible for similarity and differentiation between EVs and liposomes, respectively (Figure 4-5d). The clusters of EVs from non-cancerous NHA cells, cancer U373 cells and liposomes were distinguishable from one another. In the same color the 95% confidence ellipses are demonstrated. This confidence ellipse defines the region that contains 95% of all samples that can be drawn from the underlying distribution. In

supporting Figure S9b-c it is demonstrated that both liposome and EVs clusters were distinguished from Tris-buffer control.

Next, we establish SERS efficiency resulting from nanobowtie structures. Therefore, unlike previous studies where the SERS intensity from plasmonic substrate were compared with Raman intensity from glass, we compared the SERS intensity from nanobowtie substrate with flat Ag thin film and calculated the SERS enhancement factor (EF)(Le Ru et al., 2007; Wells et al., 2009) according to eq. 2:

$$\%\mathrm{EF}_{\mathrm{SERS}} = \frac{\mathrm{I}_{\mathrm{SERS}}\mathrm{N}_{\mathrm{Flat}}}{\mathrm{I}_{\mathrm{Flat}}\mathrm{N}_{\mathrm{SERS}}} \quad \text{(eq. 2)}$$

where the SERS integrated band area at 1000 cm^{-1} (CH_2/ CH_3 bending related to Phospholipid) is divided with that of the nonenhanced Raman signal of the same band, I_{Flat} (Figure S10). N_{Flat} and N_{SERS} are the number of analytes for the Flat Ag sample and that are excited by the localized field enhancement of the nanobowtie structure. According to SEM images, when 10^8 EVs were loaded to the chamber, they formed a relatively close-packed monolayer. Therefore, it is reasonable to estimate N_{Flat} as $C_{Flat}V_{Flat}$, that considering having a constant height, it is indicated as $C_{Flat}A_{Flat}$, where C_{Flat} and A_{Flat} are the concentration of EVs loaded onto Flat Ag and laser spot area, respectively. The $\frac{\mathrm{N}_{\mathrm{Flat}}}{\mathrm{N}_{\mathrm{SERS}}} = 267.7$ was calculated accordingly. Supporting Figure S10 shows the intensity difference of the nanobowtie SERS spectra and Flat Ag, from which $\frac{\mathrm{I}_{\mathrm{SERS}}}{\mathrm{I}_{\mathrm{Flat}}} = 1.3 \times 10^3$ was calculated. Accordingly, the estimated $\%\mathrm{EF}_{\mathrm{SERS@1000}}$ is calculated to be 3.4×10^5 for nanobowtie arrays over flat Ag surfaces. In addition, we studied the fluorescent microscopy technique on various substrates including glass, Si, Ag thin film, and nanobowtie structures (Figure S11), demonstrating that the localized surface plasmon resonance field of plasmonic nanobowties led to increase of the excitation rate of the fluorophore molecules in their vicinity. Hence, it is

expected that nanobowtie structures enhance the molecular gain of the laser while SERS characterization is in progress.

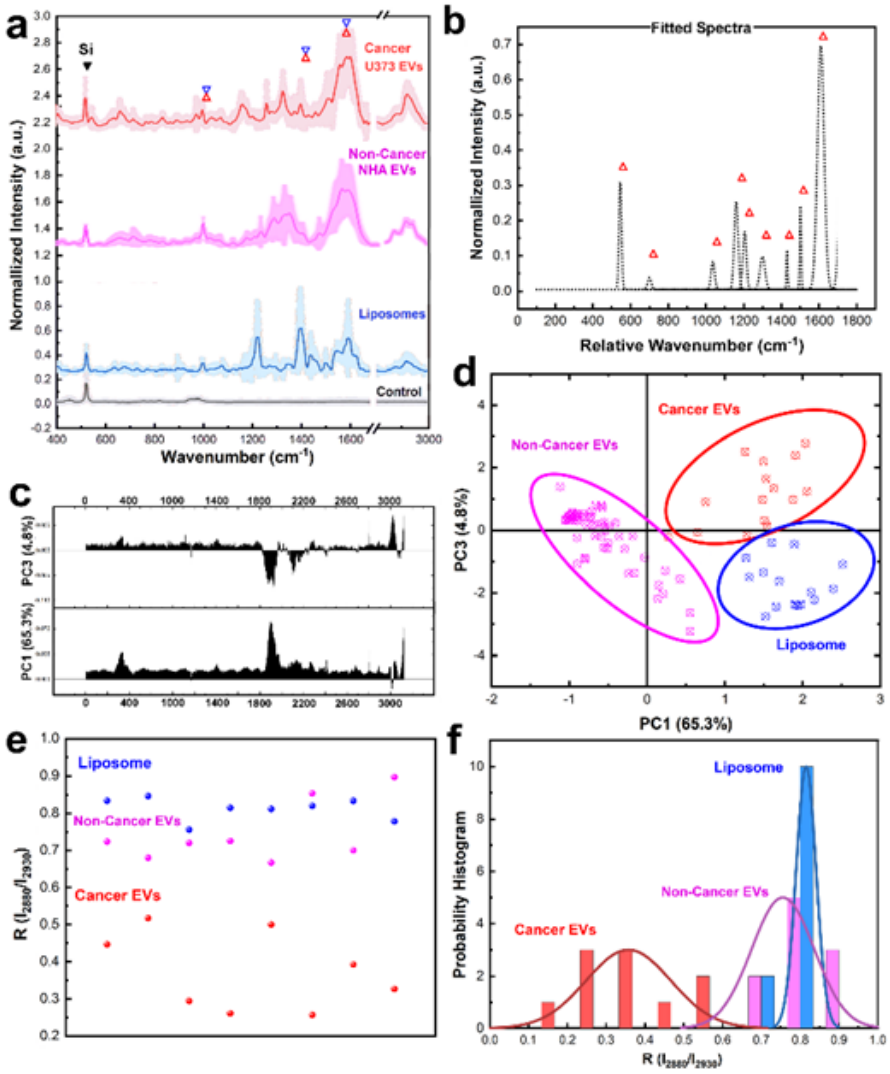

Figure 4-5. Ultrasensitive SERS detection of EVs from non-cancerous (NHA) and cancerous (U373) glial cells as well as liposomes with the nanobowtie microfluidic chip. (a) SERS characterization for investigating the specific Raman scattering signals of EVs derived from non-cancerous glial cells (NHA), cancerous glioma cells (U373) and liposomes. Each spectrum is the mean value of the spectra and the SD is demonstrated in with lighter color. For each sample minimum 15 data point was used after normalization process and elimination of the out of range

data points. (b) Unique peaks existing in EVs spectra that are not appeared for liposomes or were considerably weak. (c) the shown PC1 and PC2 loading Raman bands based on which the (d) PCA score plot of the SERS data, demonstrating the distinguished position of the spectra from each sample is defined. Each point is related to one experiment. In the same color the 95% confidence ellipses are demonstrated. (e) Comparison analyses of lipid membrane properties (Chol amount) based on R= I_{2880} / I_{2930} intensity ratio distribution. Each point is related to one trial. (f) The Histogram and correlated fit of R-value for liposomes and EVs, demonstrating the composition of DOPC: Chol while showing the heterogeneity.

4.2.6 Analysis of lipid membrane properties of nanoparticles:

In Raman analysis for lipid membranes, both fingerprint (500−2000 cm^{-1}) and C−H stretching regions (2700−3000 cm^{-1}) can be used to appreciate the properties of lipid membranes. In particular, the I_{2850}/I_{2880} parameter directly monitors acyl chain disorder/order arising from lateral chain-chain interactions while the I_{2880}/I_{2930} ratio also furnishes an index of the degree of interchain disorder/order, but with superimposed gauche/trans isomerization effects. Therefore, the peak intensity at 2930 and 2880 cm^{-1} were evaluated from cholesterol (Chol) and 1,2-Dioleoyl-sn-glycero-3-phosphocholine (DOPC): $$R = \frac{I_{2880}}{I_{2930}} \quad \text{(eq. 3)}$$

where R represents the packing density of the lipid membrane in the CH region and I is the intensity of Raman spectroscopy at 2930 or 2880 cm^{-1}. This peak intensity ratio may indicate the lateral packing density of the acyl chain in the CH region and, consequently, represent the level of conformational arrangement and interchain coupling in the lipid. The increase of intensity indicates the increment in chain decoupling from the membrane leading to less susceptible membranes to accept proteins(Faried et al., 2019).

Figure 5e and 5f demonstrates the distribution of R-value for multiple test samples of Liposomes and EVs and correlated distribution histogram, respectively. Each point is related to one trial. The distribution of R-value for liposomes is relatively narrow with a mean-value of 0.81. This indicates DOPC: Chol (55:45) constitution of bilayer lipid composition which is in agreement with the report on the molecular mass of the synthetic liposomes. Unlike liposomes, the cancer EVs (U373) demonstrate a wide distribution histogram and lower R-values with a mean-value of 0.38. The mean R-value in EVs indicates a DOPC:Chol (70:30) constitution of bilayer lipid composition. Similarly, the R-value of non-cancerous EVs is calculated to be 0.75 which indicates a lipid bilayer composition similar to liposomes rather than cancer EVs.

Table 4-1. Summary of peak assignments from fitted SERS spectra of liposomes and EVs

Liposome		EVs (U373)		EVs (U87)		EVs (NHA)		Lit
Peak Position	Possible attribution	Peak Position	Possible attribution	Peak Position	Possible attribution	Peak Position	Possible attribution	Peak Position Range
521	Substrate (Si)	521	Substrate (Si)	521	Substrate (Si)	521	Substrate (Si)	
-	-	545	Cholesterol	-	-			546 (Stremersch, Marro, Pinchasik, Baatsen, Hendrix, De Smedt, Loza-Alvarez, et al., 2016)
-	-	660	(C-C) twisting Tyrosine	-	-	662	(C-C) twisting Tyrosine	645-660 (Knudson et al., 2015; Tantussi, Messina, Capozza, Dipalo, & Lovato, 2018)

-	-	830	Tyrosine	830	Tyrosine			828 (Notingher et al., 2003)
1000	CH2/ CH3 bending (Phospholipid)(Knudson et al., 2015; Stremersch, Marro, Pinchasik, Baatsen, Hendrix, De Smedt, Loza-Alvarez, et al., 2016; Tantussi, Messina, Capozza, Dipalo, & Lovato, 2018)	1000	CH2/ CH3 bending (Phospholipid) (Knudson et al., 2015; Stremersch, Marro, Pinchasik, Baatsen, Hendrix, De Smedt, Loza-Alvarez, et al., 2016; Tantussi, Messina, Capozza, Dipalo, & Lovato, 2018)	1000	CH2/ CH3 bending (Phospholipid)(Knudson et al., 2015; Stremersch, Marro, Pinchasik, Baatsen, Hendrix, De Smedt, Loza-Alvarez, et al., 2016; Tantussi, Messina, Capozza, Dipalo, & Lovato, 2018)	1000	CH2/ CH3 bending (Phospholipid)(Knudson et al., 2015; Stremersch, Marro, Pinchasik, Baatsen, Hendrix, De Smedt, Loza-Alvarez, et al., 2016; Tantussi, Messina, Capozza, Dipalo, & Lovato, 2018)	1000-1036 (Knudson et al., 2015; Stremersch, Marro, Pinchasik, Baatsen, Hendrix, De Smedt, Loza-Alvarez, et al., 2016; Tantussi, Messina, Capozza, Dipalo, & Lovato, 2018)
1070	(C-C) stretching (lipid)(Knudson et al., 2015)	1070	(C-C) stretching (lipid) (Knudson et al., 2015)	1070	(C-C) stretching (lipid) (Knudson et al., 2015)	1065	(C-C) stretching (lipid) (Knudson et al., 2015)	1050-1066 (Knudson et al., 2015; Notingher et al., 2003; Tantussi, Messina, Capozza, Dipalo, & Lovato, 2018)
1122	(C-C) stretching (Lipid) (Stremersch, Marro, Pinchasik, Baatsen, Hendrix, De Smedt, Loza-Alvarez, et al., 2016; Tantussi, Messina, Capozza,	1128	(C-C) stretching (Lipid) (Stremersch, Marro, Pinchasik, Baatsen, Hendrix, De Smedt, Loza-Alvarez, et al., 2016; Tantussi, Messina, Capozza,	1128	(C-C) stretching (Lipid) (Stremersch, Marro, Pinchasik, Baatsen, Hendrix, De Smedt, Loza-Alvarez, et al., 2016; Tantussi, Messina, Capozza,	1124	(C-C) stretching (Lipid) (Stremersch, Marro, Pinchasik, Baatsen, Hendrix, De Smedt, Loza-Alvarez, et al., 2016; Tantussi, Messina,	1124-1128 (Knudson et al., 2015; Notingher et al., 2003; Tantussi, Messina, Capozza, Dipalo, & Lovato, 2018)

	Dipalo, & Lovato, 2018)		Dipalo, & Lovato, 2018)		Dipalo, & Lovato, 2018)	Capozza, Dipalo, & Lovato, 2018)	
-	-	1150	(C-H) stretching (Protein) (Stremersch, Marro, Pinchasik, Baatsen, Hendrix, De Smedt, Loza-Alvarez, et al., 2016)	1150	(C-H) stretching (Protein) (Stremersch, Marro, Pinchasik, Baatsen, Hendrix, De Smedt, Loza-Alvarez, et al., 2016)	1175	(C-H) in-plane bend	1158-1176 (Knudson et al., 2015; Notingher et al., 2003; Tantussi, Messina, Capozza, Dipalo, & Lovato, 2018)
1220	Amide III (Protein), Tyrosine	1210	Amide III (Protein), Tyrosine	1210	Amide III (Protein), Tyrosine	1210	Amide III (Protein), Tyrosine	1209-1224 (Knudson et al., 2015; Notingher et al., 2003; Tantussi, Messina, Capozza, Dipalo, & Lovato, 2018)
-	-	1254	Asymmetric phosphate stretching (nucleic acid) (Stremersch, Marro, Pinchasik, Baatsen, Hendrix, De Smedt, Loza-Alvarez, et al., 2016)	1230	Asymmetric phosphate stretching (nucleic acid) (Stremersch, Marro, Pinchasik, Baatsen, Hendrix, De Smedt, Loza-Alvarez, et al., 2016)	1238	Asymmetric phosphate stretching (nucleic acid) (Stremersch, Marro, Pinchasik, Baatsen, Hendrix, De Smedt, Loza-Alvarez, et al., 2016)	1234 (Stremersch, Marro, Pinchasik, Baatsen, Hendrix, De Smedt, Loza-Alvarez, et al., 2016)
-	-	-	-	1300	C-N stretching (protein)(Stremersch, Marro, Pinchasik, Baatsen, Hendrix, De Smedt, Loza-	1300	C-N stretching (protein)(Stremersch, Marro, Pinchasik, Baatsen, Hendrix, De Smedt, Loza-	1312 (Stremersch, Marro, Pinchasik, Baatsen, Hendrix, De Smedt, Loza-Alvarez, et al., 2016)

					Alvarez, et al., 2016)		Alvarez, et al., 2016)	
-	-	1340	Guanine (Nucleic acid)(Tantussi, Messina, Capozza, Dipalo, & Lovato, 2018)	1335	Guanine (Nucleic acid)(Tantussi, Messina, Capozza, Dipalo, & Lovato, 2018)	1332	Guanine (Nucleic acid)(Tantussi, Messina, Capozza, Dipalo, & Lovato, 2018)	1320-1352 (Notingher et al., 2003; Stremersch, Marro, Pinchasik, Baatsen, Hendrix, De Smedt, Loza-Alvarez, et al., 2016; Tantussi, Messina, Capozza, Dipalo, & Lovato, 2018)
-	-	-	-	1360	Guanine/ Phospholipid(Stremersch, Marro, Pinchasik, Baatsen, Hendrix, De Smedt, Loza-Alvarez, et al., 2016)	1360	Guanine/ Phospholipid(Stremersch, Marro, Pinchasik, Baatsen, Hendrix, De Smedt, Loza-Alvarez, et al., 2016)	1354-1367 (Stremersch, Marro, Pinchasik, Baatsen, Hendrix, De Smedt, Loza-Alvarez, et al., 2016)
1395	CH3 scissoring (Lipid)(Tantussi, Messina, Capozza, Dipalo, & Lovato, 2018)	1395	CH3 scissoring (Lipid) (Tantussi, Messina, Capozza, Dipalo, & Lovato, 2018)	1395	CH3 scissoring (Lipid) (Tantussi, Messina, Capozza, Dipalo, & Lovato, 2018)	1394	CH3 scissoring (Lipid) (Tantussi, Messina, Capozza, Dipalo, & Lovato, 2018)	1381-1394 (Knudson et al., 2015; Tantussi, Messina, Capozza, Dipalo, & Lovato, 2018)
1435	CH2/CH3 scissoring (Lipid, Protein) (Tantussi, Messina, Capozza, Dipalo, & Lovato, 2018)	1435	CH2/CH3 scissoring (Lipid, Protein) (Tantussi, Messina, Capozza, Dipalo, & Lovato, 2018)	1435	CH2/CH3 scissoring (Lipid, Protein) (Tantussi, Messina, Capozza, Dipalo, & Lovato, 2018)			1437-1443 (Knudson et al., 2015; Stremersch, Marro, Pinchasik, Baatsen, Hendrix, De Smedt, Loza-

								Alvarez, et al., 2016; Tantussi, Messina, Capozza, Dipalo, & Lovato, 2018)
1455	Lipid(Stremersch, Marro, Pinchasik, Baatsen, Hendrix, De Smedt, Loza-Alvarez, et al., 2016)	1455	Lipid(Stremersch, Marro, Pinchasik, Baatsen, Hendrix, De Smedt, Loza-Alvarez, et al., 2016)	1455	Lipid(Stremersch, Marro, Pinchasik, Baatsen, Hendrix, De Smedt, Loza-Alvarez, et al., 2016)			1442-1465 (Knudson et al., 2015; Stremersch, Marro, Pinchasik, Baatsen, Hendrix, De Smedt, Loza-Alvarez, et al., 2016; Tantussi, Messina, Capozza, Dipalo, & Lovato, 2018)
-	-	-	-	1480	4-dimethylaminopyridine (Lipid, Protein)(Stremersch, Marro, Pinchasik, Baatsen, Hendrix, De Smedt, Loza-Alvarez, et al., 2016)	1480	4-dimethylaminopyridine (Lipid, Protein)(Stremersch, Marro, Pinchasik, Baatsen, Hendrix, De Smedt, Loza-Alvarez, et al., 2016)	1477 (Stremersch, Marro, Pinchasik, Baatsen, Hendrix, De Smedt, Loza-Alvarez, et al., 2016)
1510	(C=C) conjugated stretching(Tantussi, Messina, Capozza, Dipalo, & Lovato, 2018)	1510	(C=C) conjugated stretching(Tantussi, Messina, Capozza, Dipalo, & Lovato, 2018)	1515	(C=C) conjugated stretching(Tantussi, Messina, Capozza, Dipalo, & Lovato, 2018)			1519-1528 (Knudson et al., 2015; Stremersch, Marro, Pinchasik, Baatsen, Hendrix, De Smedt, Loza-

								Alvarez, et al., 2016; Tantussi, Messina, Capozza, Dipalo, & Lovato, 2018)
1550	Tryptophan(Tantussi, Messina, Capozza, Dipalo, & Lovato, 2018)	1550	Tryptophan(Tantussi, Messina, Capozza, Dipalo, & Lovato, 2018)	-	-	1563	Tryptophan (Tantussi, Messina, Capozza, Dipalo, & Lovato, 2018)	1552-1563 (Knudson et al., 2015; Stremersch , Marro, Pinchasik, Baatsen, Hendrix, De Smedt, Loza-Alvarez, et al., 2016; Tantussi, Messina, Capozza, Dipalo, & Lovato, 2018)
-	-	1580	Guanine (nucleic acid) (Stremersch, Marro, Pinchasik, Baatsen, Hendrix, De Smedt, Loza-Alvarez, et al., 2016)	1580	Guanine (nucleic acid) (Stremersch, Marro, Pinchasik, Baatsen, Hendrix, De Smedt, Loza-Alvarez, et al., 2016)	1588	Guanine (nucleic acid) (Stremersch, Marro, Pinchasik, Baatsen, Hendrix, De Smedt, Loza-Alvarez, et al., 2016)	1576-1580 (Notingher et al., 2003; Stremersch , Marro, Pinchasik, Baatsen, Hendrix, De Smedt, Loza-Alvarez, et al., 2016)
1600	phenylalanine(Knudson et al., 2015; Stremersch, Marro, Pinchasik, Baatsen, Hendrix, De Smedt, Loza-Alvarez, et al., 2016)	1610	phenylalanine(Knudson et al., 2015; Stremersch, Marro, Pinchasik, Baatsen, Hendrix, De Smedt, Loza-Alvarez, et al., 2016)	1600	phenylalanine(Knudson et al., 2015; Stremersch, Marro, Pinchasik, Baatsen, Hendrix, De Smedt, Loza-Alvarez, et al., 2016)	1600	phenylalanine(Knudson et al., 2015; Stremersch, Marro, Pinchasik, Baatsen, Hendrix, De Smedt, Loza-Alvarez, et al., 2016)	1600-1608 (Notingher et al., 2003; Stremersch , Marro, Pinchasik, Baatsen, Hendrix, De Smedt, Loza-Alvarez, et al., 2016)

1620	C=C vibration (Stremersch, Marro, Pinchasik, Baatsen, Hendrix, De Smedt, Loza-Alvarez, et al., 2016)	1615	C=C vibration(Stremersch, Marro, Pinchasik, Baatsen, Hendrix, De Smedt, Loza-Alvarez, et al., 2016)	1615	C=C (protein) (Stremersch, Marro, Pinchasik, Baatsen, Hendrix, De Smedt, Loza-Alvarez, et al., 2016)			
-	-	-	-	2860	(CH2) stretching(Faried et al., 2019)	2855	(CH2) stretching(Faried et al., 2019)	2852 (Faried et al., 2019)
2890	(CH2)-Chol stretching(Faried et al., 2019)	2890	(CH2)-Chol stretching(Faried et al., 2019)	2890	(CH2)-Chol stretching(Faried et al., 2019)	2890	(CH2)-Chol stretching(Faried et al., 2019)	2872-2890 (Faried et al., 2019; Suga et al., 2018)
2930	(CH3) stretching(Faried et al., 2019)	2930	(CH3) stretching(Faried et al., 2019)	2930	(CH3) stretching(Faried et al., 2019)	2930	(CH3) stretching(Faried et al., 2019)	2930 (Faried et al., 2019)

4.2.7 SERS-based identification of EVs derived from distinct glioma cell populations:

While nanobowtiefluidic-SERS analysis of membrane lipids distinguishes EVs from liposomes it is of great interest whether EVs reflective of different cancer cell populations can be unambiguously identified in view of possible diagnostic applications. Glioblastoma multiforms (GBMs), exemplifies a dire need for early detection of cancer cells and monitoring their evolution with minimal invasiveness which is central to further improvement of disease outcomes. The median overall survival of patients remains approximately 15 months in spite of aggressive surgical and radio-chemotherapy treatment, along with extensive molecular profiling that fuel targeted and biological therapy trials, thus far too little success.(Reifenberger et al., 2017b) To investigate this question, we isolated EVs from a non-cancerous glial cell line (NHA) and two different cancerous glioma cell lines (i.e. U373 and U87) and analysed their nanobowtie SERS

spectra (Figure 6a). All the peaks were studied and assigned to their possible corresponding attributions in Table 1. The spectra of all EVs populations demonstrated unique peaks near 1250 cm^{-1}, 1325 cm^{-1}, and 1580 cm^{-1} corresponding to asymmetric phosphate stretching and guanine, which can be correlated to nucleic acid content(Stremersch, Marro, Pinchasik, Baatsen, Hendrix, De Smedt, Loza-Alvarez, et al., 2016; Tantussi, Messina, Capozza, Dipalo, & Lovato, 2018).

The covariance PCA algorithm, exploited to differentiate liposomes and U373 EVs, was applied to the SERS measurements of the EVs samples from glioma cell lines (Figure 6b), which shows discriminated classifications of U373 and U87 glioma EVs according to PC1 and PC2 profile. Each dot in the plot represents one spectrum with dimension reduction. Each data set was clustered while maximizing covariance. The clusters of cancer EVs from U373 and U87 not only were distinguishable from non-cancerous EVs (NHA) but also were distinguishable from one another according to PC1 and PC2, that reveals the peaks responsible for differentiation of EV (Figure 6c). The 95% confidence ellipses of the distributed PCA show all clusters can be discern by 95% certainty. The specific discerning of purified EVs from U373 and U87 glioma cells is shown in Supporting Figure S12. The nanobowtiefluidic SERS is capable of distinguishing purified EVs properties representative of their donor glioma cells.

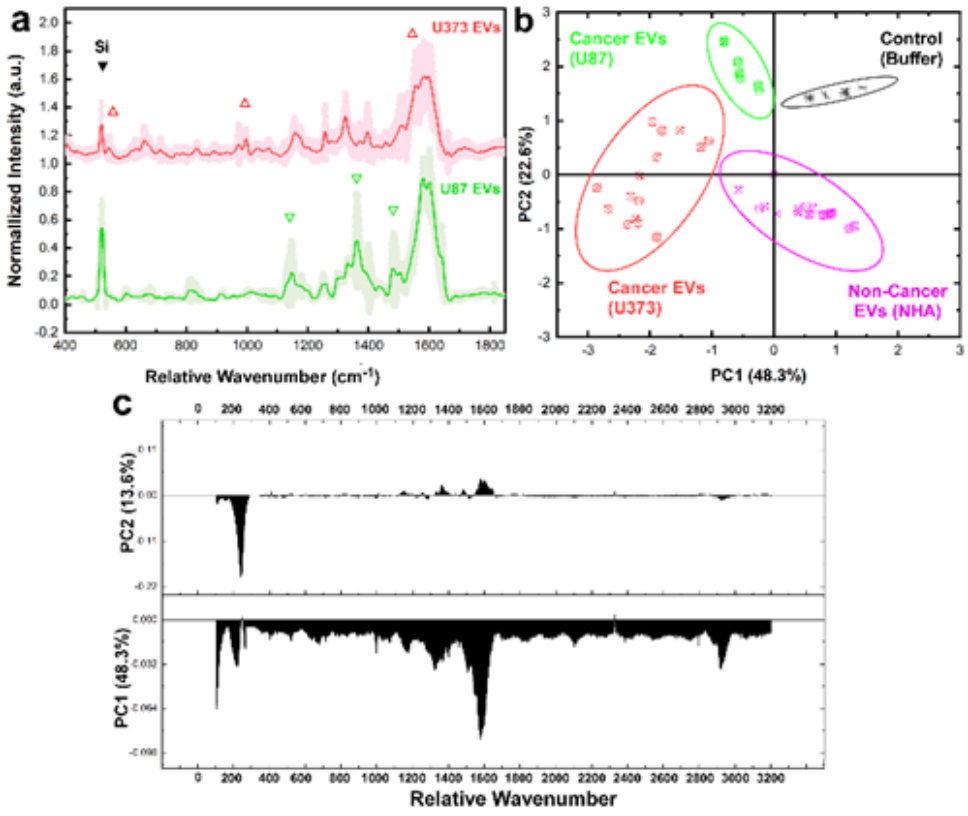

Figure 4-6. Ultrasensitive SERS detection of non-cancerous glial NHA EVs versus cancerous glioma U87 and U373 EVs with the nanobowtie microfluidic chip. (a) SERS characterization for investigating the specific Raman scattering signals of EVs derived from glioma U87 EVs (Green) in comparison with glioma U373 EVs (Red) (b) PCA score plot of the SERS data, showing the distinguished position of the spectra of each cancer EV sample with non-cancerous NHA EVs (Magenta) as the healthy control according to the (c) PC1 and PC2 loading Raman bands. The 95% confidence ellipses are shown in the same colors.

4.3 Experimental

4.3.1 Fabrication

A combined bottom-up and top-down approach was used to develop the SERS microfluidic device based on free-standing plasmonic nanobowtie substrate embedded in the analysis chamber. First,

top-down standard photolithography technique was used to pattern microfluidic chamber, and channels in negative SU8 photoresist. Second, self-assembly monolayer polystyrene nanoparticles with the size of 730 nm in diameter was used to pattern a hexagonal close-packed lattice inside the analysis chamber. Third, a 60 nm biocompatible ZnO layer and a 20 nm Ag, Au, and Al layer was deposited (via BJD 1600) on the developed chip as back-reflector and plasmonic layer, respectively. The CMOS-compatible platform enable integration with any existing type of microfluidic devices. Last, the polystyrene nanoparticles were lift-off via a mechanical process to leave the free-standing plasmonic nanobowtie pattern.

4.3.2 Characterization

To characterize the properties of the plasmonic platform, physical characterization techniques including fluorescent microscopy, scanning electron microscopy (SEM), atomic force microscopy (AFM). The SEM was performed using the FEI Quanta 450 environmental scanning while the AFM was performed with a Bruker, MultiMode8 equipment. The optical characterizations were performed via a Lambda750 NIR-UV-Visible equipment and a NanoSpec reflection spectro-microscopy. The fundamental electric-field distribution of the platform was studied using finite difference time domain (FDTD) module (v8.21.1781, Lumerical Solutions, Inc.).

EVs samples were prepared for SEM in three steps: (1) The purified EVs in PBS solution (100 μL, 1 mM) were introduced to the recognition substrate for 2 min followed by incubation with glutaraldehyde 3% in sodium cacodylate (0.1 mM) overnight. (3) Dehydration of EVs was performed by immersion in ethyl alcohol (30–100%) to exchange their cytoplasm with alcohol (10 min immersion in each). Then, a critical point dryer (Leica Microsystems EM CPD030) was

employed to substitute alcohol content with dry CO_2 with minimum damage to the EVs morphology.

4.3.3 EV purification

EVs were purified from growth media of cancer cells using optimized protocol(Choi, Montermini, et al., 2019). Briefly, the conditioned medium (CM) was collected from cells grown for 72 h in culture media containing 10% EV-depleted FBS (generated by centrifugation at 150,000g for 18 h at 4ºC). CM was centrifuged one time at 400xg and then passed through 0.2 µm pore-size filter. The resulting CM filtrate was concentrated to 500ul using Amicon Ultra-15 Centrifugal Filter Unit (EMD Millipore, Billerica, MA) with 100,000 NMWL molecular cut off. The concentrated media was further purified using qEV single SEC column (Izon Science, UK) 500 µL of sample was loaded, and 4 fractions of 500 µL of eluent was collected after 3.5 mL of initial eluent. The concentration and size distribution of EVs in the purified media was obtained using the nanoparticle tracking analysis, NanoSight NS500 instrument (NanoSight Ltd., UK). Three recordings of 30 s at 37ºC were obtained and processed using NTA software (version 3.0).

4.3.4 Labelling EVs

A fluorescent dye, DiI, was used to label the cells (indirect labelling of EVs). A total of $3x10^6$ cells were labelled with 5 ml of DiI (Invitrogen) in 2ml of DMEM without FBS for 20 minutes at 37C. The cells were washed twice with DMEM without FBS, resuspended in 30 ml of DMEM containing 10% EV-depleted FBS (generated by centrifugation for 18hrs at 150,000xg) and cultured for 72hrs at 37ºC, 5% CO_2.

4.3.5 Raman Spectroscopy

Surface enhanced Raman spectroscopy (SERS) spectra were collected in back scattering geometry, using an InVia Raman microscope (Renishaw plc, Wotton-under-Edge, UK) equipped

with a 532 nm HeNe laser (Melles-Griot, Voisins Le Bretonneaux, France) delivering 25 mW of laser power at the sample. The laser was polarized along the x-axis direction. The platform injected with biosamples was mounted on a ProScan II motorized stage (Prior, Cambridge, UK) under the microscope. A Leica 50x microscope objective (N.A. 0.95) focused the laser on the sample into a spot of ~0.8 μm diameter. A 1800 l/mm grating yielded a spectral resolution of 754 cm^{-1}. A thermoelectrically cooled charge coupled device (CCD) camera was used for detection. The spectrograph was calibrated using the Silicon substrate. The Raman spectra were collected with an exposure time of 30 s at 250 μW of laser power, collecting spectra with steps of 1.5 μm. Spectra, consisting of 2924 data points each, were obtained in the 100–3200 cm^{-1} region using the synchro mode of the instrument software WiRE 5.1 (Renishaw). In the synchro mode, the grating is continuously moved to obtain Raman spectra of extended spectral regions. The dimensions of the map depended on the zone of interest investigated.

4.3.6 Data pre-processing and analysis

All data pre-processing and analysis was performed within the Origin Pro 2019b software, ImageJ, and WiRE 5.1 environment for statistical computing and graphics. The background spectra of the substrate is deducted from the SERS spectra. In particular we used principal component analysis for spectroscopy v.1.2 App in OriginPro 2019 for PCA analysis. The pre-processing of SERS spectra consisted of four steps: i) cosmic rays' identification and removal, ii) baseline correction, iii) intensity vector-normalization according to Si peak and iv) outliers' detection and removal. For the baseline correction, a linear baseline was fit automatically to the whole spectral range and was subtracted from each spectrum of the dataset. Outliers detection was done by identifying suspicious points on the PCA score maps and inspecting the corresponding spectra. In

the pre-processing stage, PCA is thus used as a method to identify suspicious spectra, exploiting its sensitivity to outliers. These suspects were then individually examined before deleting them.

4.3.7 PCA

PCA reduces the number of variables by condensing all the spectral information contained in a large number of spectra into less latent variables (the principal components or PCs). Hyperspectral data are thus decomposed by PCA into the latent spectra (loadings) and scores. This approach is closely related to describing each spectrum in a Raman study as a product between components concentrations and pure constituents' spectra, where the latent spectra are used instead of those of the pure constituents, which are unknown. In the present study, PCA was performed on pre-processed data, and the first two principal components PC 1 and PC 2, which could be interpreted in terms of the biochemical components of the EVs, were considered for discussion. The PCA analysis were computed based on the covariance matrix, which is considered to implicitly perform the centering. Variance, by definition, is the average squared deviation from the mean value. Therefore, the covariance PCA analysis centered the data following this procedure: Data→ Covariance matrix→ Eigen-decomposition.

4.4 Conclusion

Nanosurface fluidic devices bring together the advantages of robust optoelectrical properties of the nanostructures as well as rapid and high throughput sample delivery properties of fluidic device. In this study, we demonstrated that combining the unique characteristics of nanosurface microfluidics with strong plasmonic effect of suspended nanobowties possessing enhanced EM-field, results in development of a sensitive SERS detection device for nanosized bioanalytes. We were able to record and discern the SERS fingerprint of EVs from non-cancerous glial cells (NHA) and two sub-populations of the GBM EVs (i.e. U87 and U373). The assembly

of such signals is the initial step in building a comprehensive library of data that can ultimately inform clinicians as to diversity and relevant traits of cancer cells. Our studies revealed that narrow gaps of nanobowtie structure comprises strong electromagnetic field (theoretical EFEF of 9.0×10^5) integrated with microfluidic channels that regulate distribution of EVs on the plasmonic surface and is crucial to achieve SERS intensity efficiency of 3.4×10^5. Theoretical and experimental evidence presented herein, demonstrates lateral fluid flow control in the nanosurface microfluidic device is essential to guide the nanoscale EVs on the detection surface. We successfully implemented this nanosurface microfluidic device to distinguish a library of peaks expressed in non-cancerous glial EVs (NHA cell line) and glioma EVs (U373 and U87 cell lines) vs. synthetic liposomes and assign them to possible band attributions. In particular, we were able to identify a set of band peaks that can be considered as a distinguished fingerprint for the glioma U373 and U87 EVs which demonstrate the potential of the nanosurface microfluidic device in providing a library for future antibody-free glioma (cancer) diagnosis and prognosis.

4.5 Acknowledgment

The authors thank Faculty of Engineering at McGill University, Natural Science and Engineering Research Council of Canada (NSERC, 247765), Canada Foundation and Innovation (248924), and New Frontiers in Research Fund (250326) for financial support. The authors appreciate the efforts of Dr. Roozbeh Siavash Moakhar in physical characterization of the platform as well as his contribution in writing process of the manuscript. The authors acknowledge Nanotools-Microfab and the Facility for Electron Microscopy Research at McGill University and the shared facility in the Department of Bioengineering. The authors would like to thank CMC Microsystems for MNT and CAD tools support.

4.6 Author Contributions

M.J. initiated the idea, design and fabrication protocols, performed the physical characterizations including SEM, and fluorescent microscopy; performed FDTD modelling, assisted in EV isolation and purification, performed SERS data collection and multivariate analysis, performed data analysis and contributed to writing the manuscript. S.I.I.H. performed the theoretical studies of the fluid flow and pressure inside the microfluidic device to optimize the design parameters and contributed to the COMSOL studies of the fluid flow. T.A. designed and fabricated the microfluidic device and contributed to the COMSOL studies of the fluid flow. L.M. contributed in EVs sample preparation, purification, and running the standard tests. J.R. provided the EVs and samples from GBM cell lines for the entire project, advice on the EV's biological and contributed to the writing of the manuscript. S. M. supervised the project from the idea to development, contributed to the design of the figure sets and writing of the manuscript.

4.8 Supporting Information

4.8.1 Fabrication

Recent advances in amplifying the SERS spectrum using a variety of plasmonic nanostructures, including metallic nanoparticles(C. Lee et al., 2017; Pang et al., 2019; Weng et al., 2018), metallic bowl-patterns(Knudson et al., 2015; S. Zhu et al., 2018), nanohole arrays (Im et al., 2014a; Tantussi, Messina, Capozza, Dipalo, Lovato, & Angelis, 2018) and *etc.*(Shin et al., 2018a; Stremersch, Marro, Pinchasik, Baatsen, Hendrix, De Smedt, Loza-Alvarez, et al., 2016) shed light on the potential of developing surpassed nanostructures for enhanced SERS detection of EVs. Here, a combined bottom-up and top-down approach was adopted to develop an array of plasmonic nanobowties standing on triangular-shaped metal-oxide to further enhance the plasmonic-assisted EM-field (Figure S4-1a). Figure S4-1b and Figure S4-1c shows the brightfield microscopy and SEM images of the closed-packed nanoparticles self-assembly pattern, respectively. The inset demonstrates the fabricated nanobowties after lift-off. The high-resolution images via fake-color demonstrate the nanobowties in cyan.

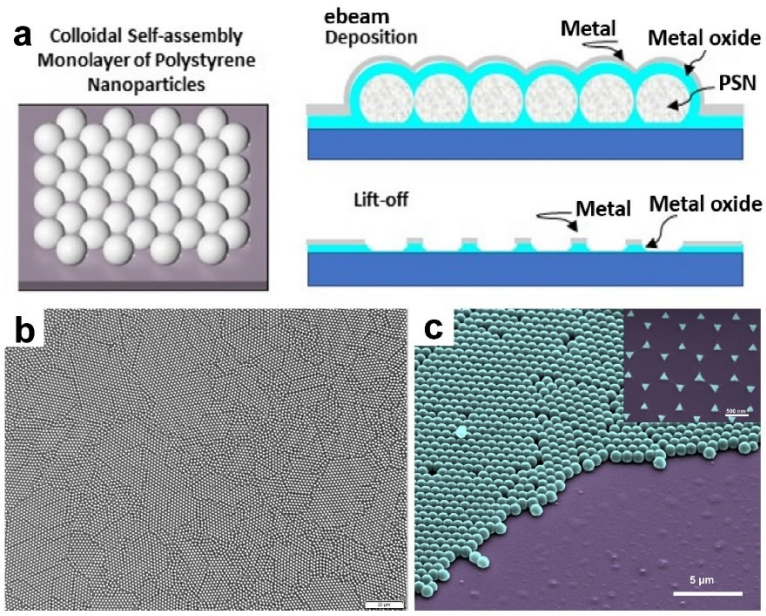

Figure S 4-1. (a) Schematic illustration of fabrication method. (b) optical images of the self-assembly nanoparticles. (c) SEM image of the self-assembly nanoparticles and fabricated nanobowties platform after lift-off.

4.8.2 FDTD Simulation:

In general, Raman spectroscopy is an optical read-out system which translates the vibrational and rotational motions of chemical bonding structures into spectral peaks based on the recorded scattering of a coherent beam (laser) by the analyte. SERS amplifies subtle signal intensities based on strong EM fields generated in a plasmonic substrate(Shin et al., 2018a). Figure S4-2a demonstrates the apex, gap, materials, and boundary parameters used for simulations. The reflectance spectra of plasmonic nanobowties illuminated by a broad-band plane wave (Figure S4-2b) demonstrates the gap-dependent plasmonic light absorption pattern. The EM-field was then swept for optimized triangle apex size, gap and material. The electric field distribution (Re) sweep on the nanobowties with different gap size at lattice diffraction mode, fundamental mode and

higher order mode (Figure S4-2c) confirmed the enhanced EM-field from the nanobowties with gap size of 15 nm under white light.

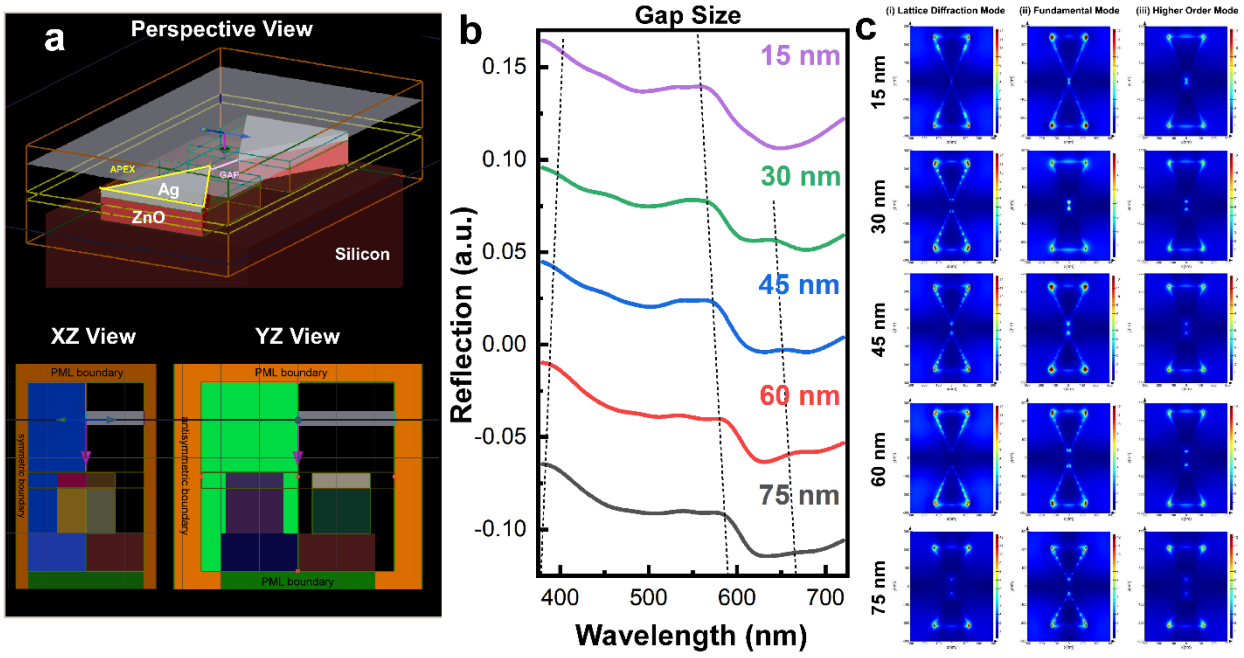

Figure S 4-2. (a) The FDTD sketch of the nanobowtie pattern. (b) Simulated Reflectance spectra of plasmonic nanobowties using plane wave with different gap size. (c) The electric field distribution (Re) on the nanobowties with different gap size.

A TFSF source was used to simulate only a small region of the periodic structure, in order to find the maximally possible EM-field. The electromagnetic field enhancement factor $EFEF$, which is an essential part to enhance SERS signal, scales with the 4th power of the electric field enhancement E(ω)/ E_0(ω) according to eq. S1:

$$EFEF = \left(\frac{|E(\omega)|}{|E_0(\omega)|}\right)^4 \qquad \text{(eq. S4-1)}$$

As shown in the contour plots, the polarization mode can heavily affect the EFEF and place of the local field enhancement. Figure S4-3a shows the FDTD simulation of absorption spectra of

the nanobowties with different distribution of gap-size using a total-field scattered-field (TFSF) light source. All broad-band absorbance spectra showed three defined absorption peaks between 450- 650 nm correlated to the diffraction mode. FDTD simulations of the maximum electric field enhancement as a function of the triangle size, defined by its apex length, are shown in supporting Figure S4-3b, while FDTD simulations of the maximum electric field enhancement as a function of the varying apex gap, are shown in supporting Figure S4-3c.

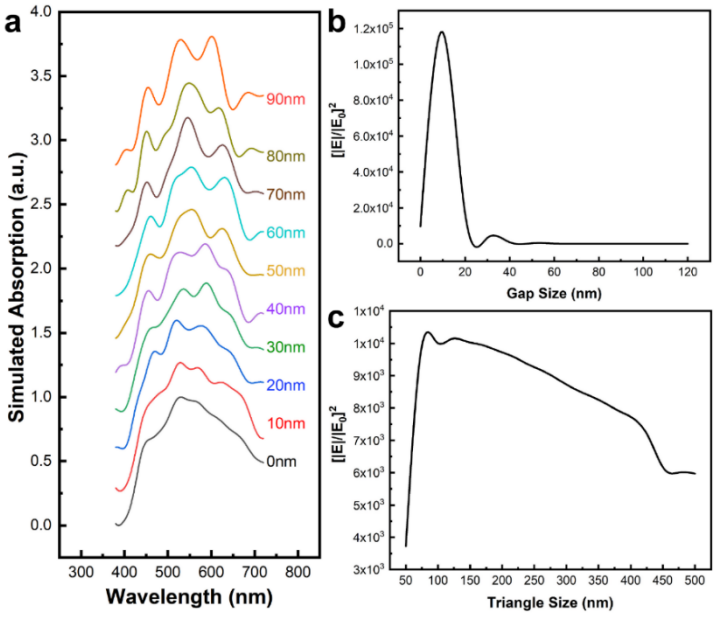

Figure S 4-3. (a) Simulated absorption spectra of plasmonic nanobowties using TSFS wave centered at 532 nm with different gap size. (b) variation of $\sqrt{EFEF}$ versus bowtie size (triangle width) (c) variation of $\sqrt{EFEF}$ versus bowtie apex gap.

The EM-field intensity in a plasmonic nanoantenna is a function of the geometry and quality factor. A general equation to describe this field intensity for all plasmonic structures is unattainable. Therefore, a semiquantitative approach is used in the present study to describe the bowtie nanoantenna effect. For a bowtie, the field intensity is inversely proportional to the effective

volume. For a small gap size, the field is highly confined in the gap region and the radiation loss is neglected for simplicity in analyses because the field is highly confined at the resonant frequency. While the effective volume of the bowtie gap cavity with fixed height is proportional to the product of the apex size (w), the gap size (g), the EM-field enhancement is proportional to $(wg)^{-1}$ (Figure S4-4) (Hatab et al., 2010a).

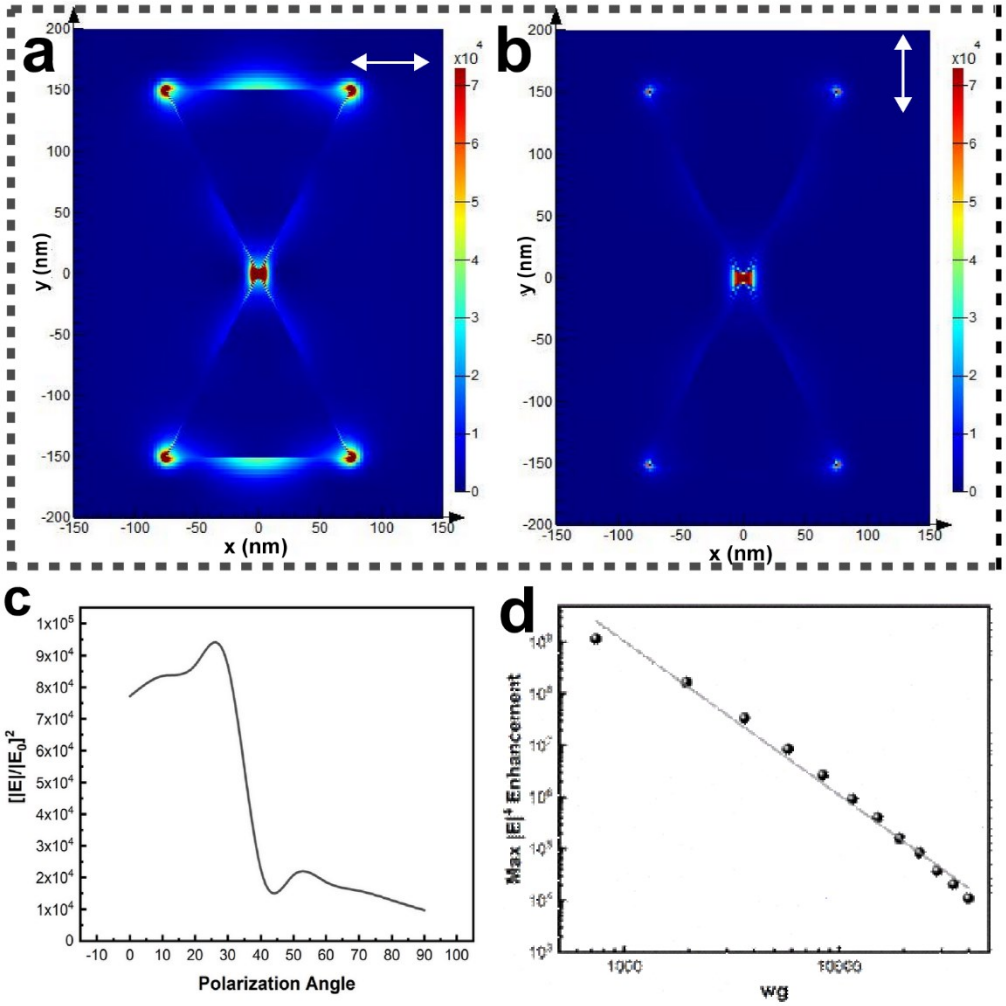

Figure S 4-4. The maximum electric field distribution on nanobowties with gap size of 10 nm in (a) TE and (b) TM modes. (c) The variation of EM-field depending on the light polarization angle in a nanobowtie with 10 nm gap size. The maximum field enhancement $|E|^4$ calculated by FDTD as a function of the product of the apex width and the gap size, wg.

4.8.3 Concentration

The SERS intensity (I_{SERS}) is directly proportional to the concentration of EVs according to(Fraire et al., 2019):

$$I_{SERS} = F_s \sigma_s C_{SERS} EFEF \quad \text{(eq. S4-2)}$$

where F_s is an instrumental factor related to Renishaw micro-Raman, σ_s is the Raman cross section of a particular analyte, and C_{SERS} is the concentration of the test analyte. When EFEF is optimized the I_{SERS} is directly proportional to C_{SERS}. According to eq. S4-2 increasing the concentration of the small particulate analyte (in this case EVs) enhances the I_{SERS}, while overpopulating the substrate can hinder interaction of the analyte with plasmonic nanobowtie surface.

Figure S4-5a shows the SEM image representative of EVs from different fractions collected from purifying columns. A mixture of 7^{th} to 10^{th} fractions were used to study the EVs SERS fingerprint in this study. The size distribution decreases while going from lower fractions (i.e. 7^{th}) to higher fractions (i.e. 10^{th}), rendering an average size distribution of 157 ± 3.1 nm over the purified EVs mixture (detected by nanoparticle tracking analysis). The inset SEM image shows a low-resolution micrograph of accumulated EVs at 10^9/ml concentration. Figure S4-5b shows representative SERS spectra of U373 EVs at different concentrations demonstrating that maintaining the concentrations at 10^8/ml results in achieving more informative signals. Figure S4-5c shows the energy dispersion spectroscopy (EDS) of the surface demonstrating existence of carbon, nitrogen and phosphorus components illustrating the organic origin of the features.

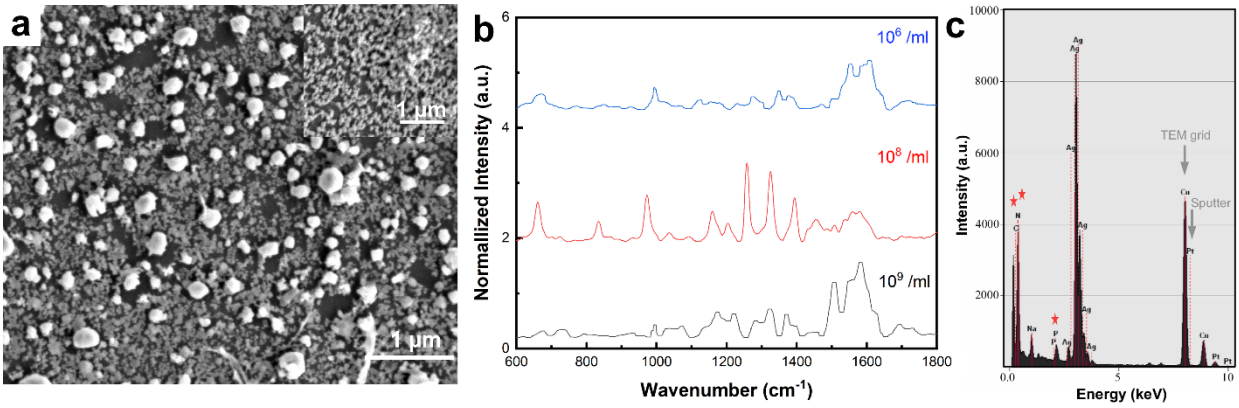

Figure S 4-5. (a) Representative SEM image of EVs. Inset shows low resolution image of agglomeration with 10^9/ml concentration. (b) representative SERS spectra of U373 EVs at different concentrations. (c) the EDS characterization of the surface.

4.8.4 COMSOL Simulation:

COMSOL Multiphysics is used to analyse the fluid flow in the microfluidic channel (Figure S4-6). Due to the creeping motion in microfluid devices, laminar flow was defined in the simulation settings. The mesh independency of results is evaluated in the settings, based on which the fluid flow inside the channel is investigated. In addition, the effect of bowtie structure on fluid flow and the correlated streamlines is studied. This study demonstrated a pressure drop in the microfluidic device along the centre line of bowtie structures.

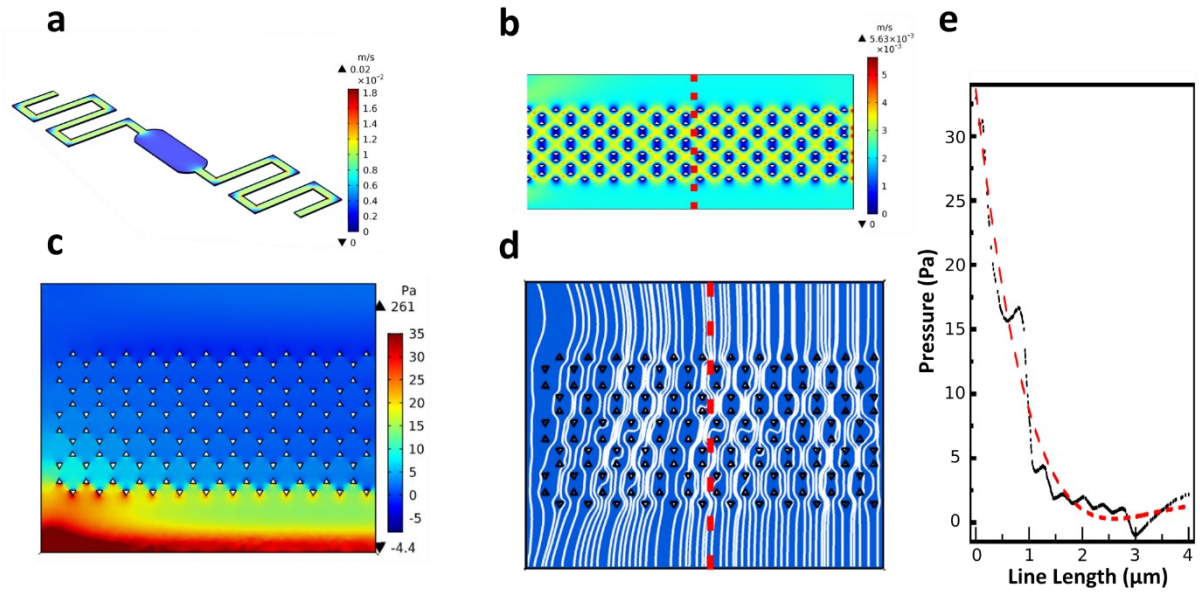

Figure S 4-6. COMSOL simulation (a) 3D simulation showing velocity distribution through the microfluidic device note lower flow velocities at the fluidic chamber to facilitate EV detection. (b) 2D flow velocity in the plan of the Nanobowties. The simulation shows the velocity gradient in a 4 µm×10 µm section of the fluidic chamber. (c) 2D pressure distribution plot for a 4 µm×5 µm section in the fluidic chamber. (d) Streamlines (in white) representing the fluid flow paths around the Nanobowtie structures. (e) line pressure distribution (red line in d) through an array of 3×11 nanobowtie structures as expected a pressure drop is observed through the length of the line. The pressure drop through the section is fitted by a polynomial fit shown by dotted red fit.

4.8.5 Brownian Dynamic Simulation:

Based on Faxén law(Brenner, 1961), the drag force that particles sense in parallel of a surface is a function of the distance of the particle from the surface:

$$\gamma_{\parallel} = \frac{\gamma_0}{1-\frac{9R}{16h}+\frac{R^3}{8h^3}-\frac{45R^4}{256h^4}-\frac{R^5}{16h^5}} \qquad \text{(eq. S4-3)}$$

In which, $\gamma_0 = 6\pi\mu R$ is the bulk drag coefficient ($y \to \infty$) when the viscosity of the fluid is μ (considered as $8.90e^{-4}$) and the radius of a particle is R while the axial drag force is.

$$\gamma_{\perp} = \frac{\gamma_0}{1-\frac{9R}{8h}+\frac{R^3}{2h^3}-\frac{57R^4}{100h^4}+\frac{R^5}{5h^5}+\frac{7R^{11}}{200h^{11}}-\frac{R^{12}}{25h^{12}}} \quad \text{(eq. S4-4)}$$

The gradient of the drag coefficient leads to a higher number of particles near the surface and therefore keep the EVs in close proximity of the plasmonic surface. In Figure S4-7, the Brownian dynamic simulation of results is shown. The overdamped model of Langevin-Equation is used to analyze the Brownian motion of particles as follows: $\gamma V = \eta(t)$. $\eta(t)$ is thermal noise which is Gaussian distribution with correction function as: $\langle \eta_i(t)\eta_i(\acute{t})\rangle = 2\mu k_B T\delta_{i,j}\delta(t-\acute{t})$. k_B is Boltzman constant, T is the temperature (considered 298 K) and δ is a delta function. In the Langevin-Equation, the drag coefficient is updated based on the distance of particle (EVs) to the surface.

The size of the particles is chosen randomly based on NTA results. Particles are distributed homogenously in the channel. Our analysis shows that particles reach an equilibrium after 1 s (Figure S4-7a). However, the data is collected after 10 seconds (9 seconds after equilibrium) to make sure that results represent the equilibrium condition. Here, we presented the data after 10 s to make sure that particles are in the final equilibrium. In Figure S4-7b the Brownian motion of a particle along the y-axis is shown. As can be interpreted, the vibration of the particle is more restricted as much as it is closer to the surface. The probability distribution of particles along the y-axis is shown in Figure S4-7c for 10^8 ml^{-1} concentration in a box with 2 μm height. The bar width is chosen based on the average particle size (0.18 μm). Particles are more concentrated near the surface and the probability of particles 1.5 time is more than the concentration of particles far from the surface. Our analysis shows that this distribution of particles in the box is independent of the

concentration of particles. The bars in Figure S4-7c show for different concentration (10^7-10^9 ml^{-1}). We can see that the probability distribution follows same value.

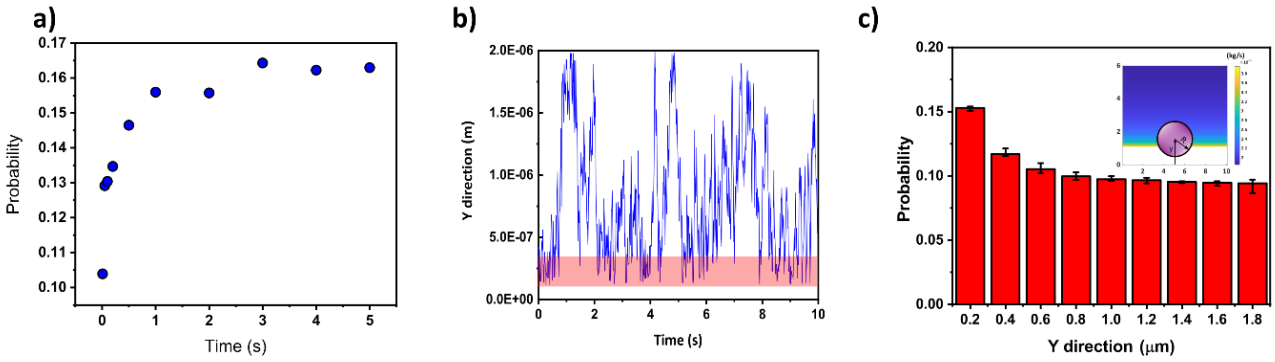

Figure S 4-7. Brownian Dynamic simulation of EVs (a) the probability of particles for a box with $2\mu m$ height. (b) Brownian motion of EVs near the surface along the y-axis, (c) the probability of particles along for a box with $2\mu m$ height.

4.8.6 SERS

Sensitivity- The sensitivity study of the NHA EVs in the range of 10^3-10^9 Particles ml^{-1} (Figure S4-8a) shows the SERS fingerprint peaks are detectable for concentrations over 10^6 ml^{-1}. The minimum concentration in which the SERS integrated band area at 1000 cm^{-1} (CH_2/ CH_3 bending related to Phospholipid) is clearly defined is 10^5 Particles ml^{-1} (Inset). Figure S4-8b demonstrates the peak intensity variation at different relative wavenumbers. The intensity of the peaks increased similarly with the concentration of EVs from 10^3-10^9 Particles ml^{-1} leads to increment of the fingerprint peaks of the SERS spectra. The intensity fits with a sigmoidal growth function of $y=V_{max}*x^n/(k^n+x^n)$ with an average R^2= 0.985 over the entire concentrations. The intensity augmentation shows a higher slope until 10^8 ml^{-1} concentration, while the slope starts to plateau when further increasing the concentration which could be due to the agglomeration of EVs

and is in agreement with the physical simulations in Figure 4e-f. While a linear range is detected from 10^5-10^8 concentration demonstrating a limit of detection of 1.32×10^5 Particles ml^{-1}.

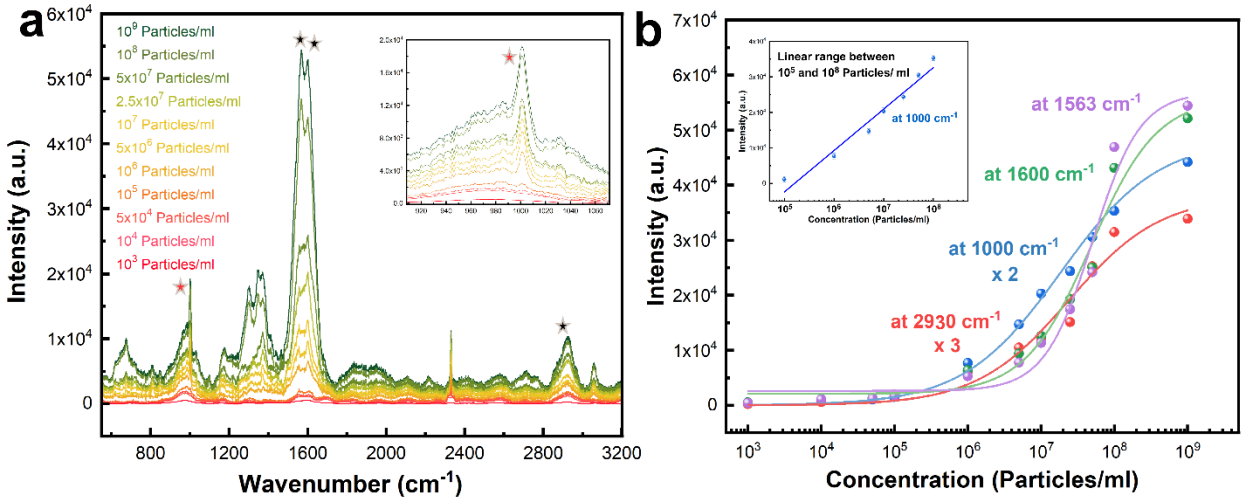

Figure S 4-8. (a) The sensitivity study of NHA EVs demonstrating the fingerprint spectra of NHA EVs and the peak resolution variation with respect to the concentration of EVs. Inset: the intensity variation of the peak at 1000 cm^{-1} with respect to the concentration of the EVs. (b) The peak intensity variation at different relative wavenumbers fitted with a sigmoidal growth function in the concentration range of 10^3-10^9 particle ml^{-1}. Inset: shows the linear detection range of 10^5-10^8.

Figure S4-9a presents unprocessed SERS spectra of 30 trials on U373 glioma EVs with plasmonic nanobowties. Unlike non-uniform metallic nanoparticle SERS substrates that mainly form a nonuniform plasmonic substrate, the signal analysis on nanobowties substrate (produced) a coherent EM field enhancement, therefore achieving encouraging reproducibility. The spectra are shifted vertically. Figure S4-9b shows the PCA analysis of the cancer U373 EVs, Liposomes and buffer (95% confidence ellipse). The first principal component (PC1), and second principal component (PC2) shown in Figure S4-9c, reveal the peaks responsible for similarity and differentiation between EVs and liposomes, respectively.

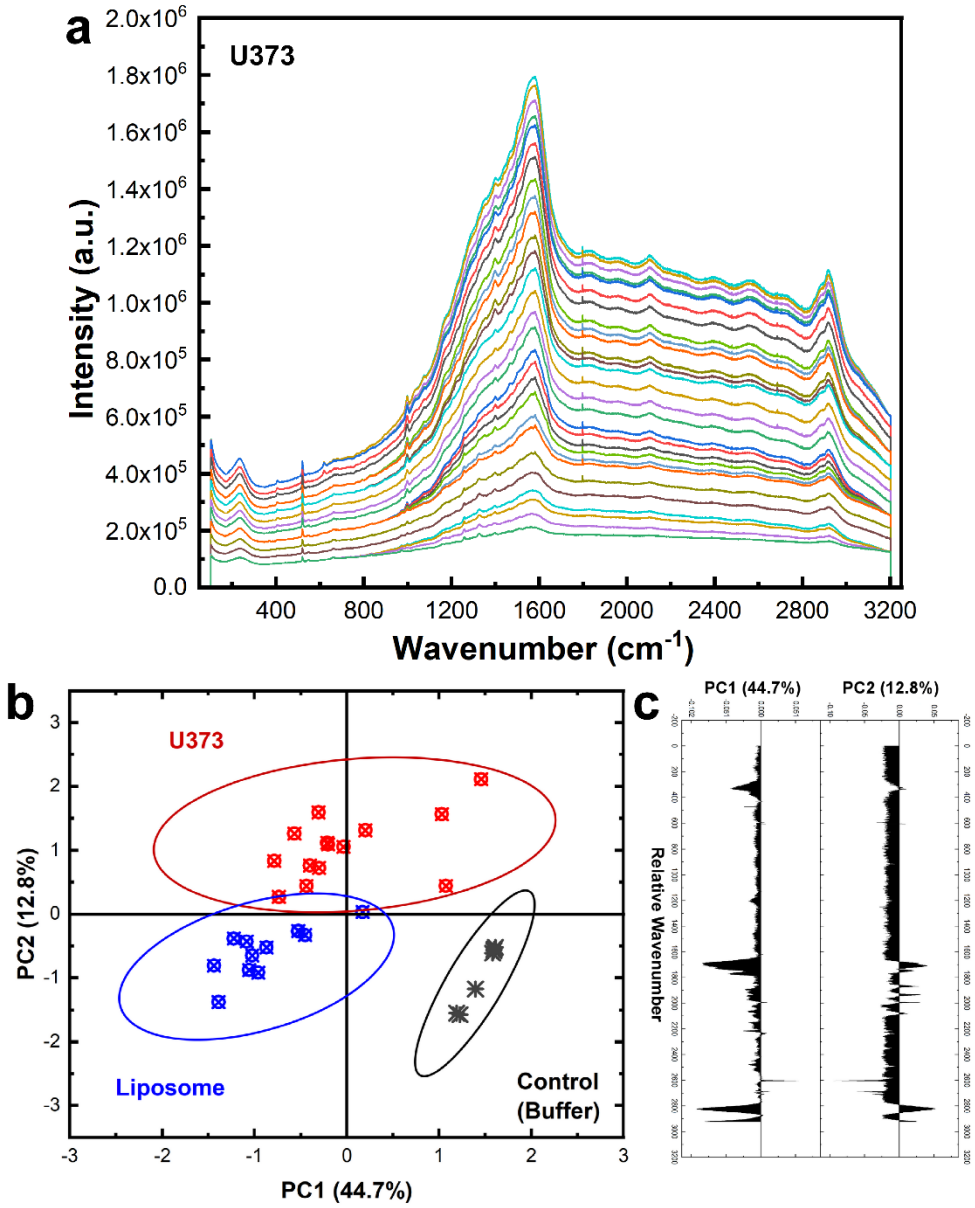

Figure S 4-9. (a) Unprocessed SERS spectra of 30 trials on U373 glioma EVs with plasmonic nanobowties. (b) PCA score plot of the SERS data, demonstrating the distinguished position of the spectra from each sample according to (c) the shown PC1 and PC2 loading Raman bands.

To establish SERS efficiency of nanobowtie structures compared with silver thin film, it is necessary to compare the signals in similar conditions. The SERS integrated band area at 1000 cm^{-1} (CH_2/ CH_3 bending related to Phospholipid) was chosen to perform the comparison. The

integration boundaries were defined according to the average FWHM of the peak. The center was chosen to be 1000 cm^{-1}. The $\frac{\sum FWHM}{n}$ where, n is the number of trials, and FWHM is derived from the spectra of the n trials shows the margin of the boundaries to be 1000 cm^{-1} ± 10. The SERS signal from nanobowties at 1000 cm^{-1} is divided with that of the less enhanced Raman signal of the same band from silver thin film (Figure S4-10) to calculate the $\frac{I_{SERS}}{I_{Flat}}$.

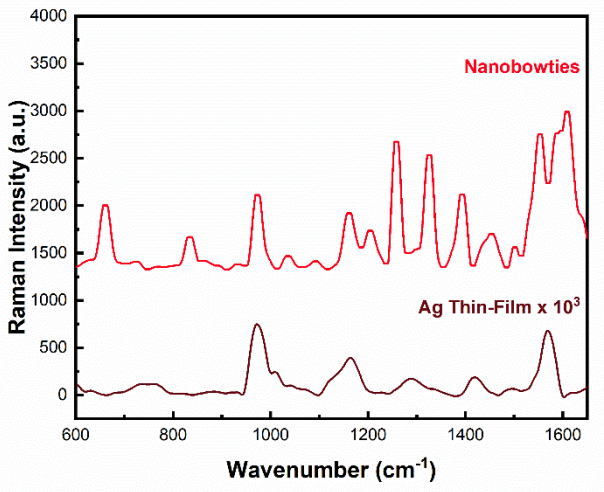

Figure S 4-10. the intensity difference of the nanobowtie SERS spectra and Flat Ag thin film, from which $\frac{I_{SERS}}{I_{Flat}} = 1.3 \times 10^5$ was calculated at 1000 cm^{-1}.

4.8.7 Nanobowite plasmonic surface enhances quantitative EV fluorescence impacting

To further investigate the EVs population, a fluorescent microscopy technique was studied on various substrates. The fluorescent micrograph of EVs loaded on glass (a), Si (b), Ag thin film (c), and nanobowtie structures (d) are shown in Figure S4-11 (a-d). The initial concentration of test samples was fixed at 10^6/ml. Plasmonic behaviour of Ag thin film and nanobowtie structures lead to surface enhanced fluorescent microscopy of ultra-small structures such as EVs. In particular,

localized surface plasmon resonance (LSPR) behaviour of nanobowtie structures, leads to high sensitivity to the changes of effective refractive index of the surrounding media. The normal fluorescent microscopy of organic dyes is based on irradiation of the media via a single wavelength temporally coherent laser beam which is absorbed by the fluorophore and re-emitted in a different wavelength. There are several factors that cause fluorescent signal fluctuations in fluorescent ultra-small analytes like EVs leading to have dark states in microscopy, including formation of triplet state, polarization effect, and photo-induced isomerization of the fluorophores. When using a LSPR substrate the LSP fields increase the excitation rate of the fluorophore molecules in their vicinity due to the coupling of light with the SPs, followed by re-emission to the second surface (fluorophores) and secondary absorption of light by fluorescent molecules. Figure S4-11e shows the corresponding fluorescent intensity count of fluorescently labelled EVs. The inset shows the efficiency of fluorescent intensity profile based on estimated loading of EVs to be 5000 counts per 0.005 mm^2 microscope field of view. The initial labelling process, and bleaching effect are the main reasons for low efficiency of fluorescent microscopy for all substrates. However, considering that the loading EVs were from same aliquot, the change in the efficiency can be due to enhanced gain of the fluorophore molecules which as explained earlier could be resulted from enhanced plasmonic resonances. This visualization provided a visible understanding of how SP resonances assist secondary absorption of laser beam by the molecules where LSPR of nanobowtie structures provide 15 times enhanced gain. Similarly, it is predicted that nanobowtie structures enhance the molecular gain of the laser while SERS characterization.

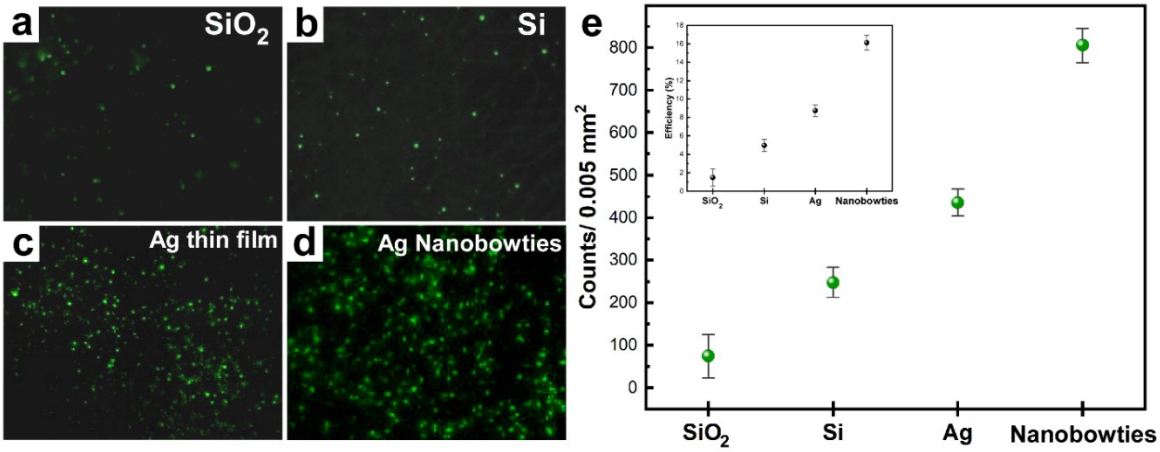

Figure S 4-11. Fluorescence intensity profile of 10^6 ml^{-1} EVs on (a) glass, (b) Silicon, (c) Ag thin film, and (d) nanobowtie structures. (e) Comparison between the fluorescence intensity obtained from EVs on each substrate. Inset: Fluorescent microscopy efficiency calculated based on estimated 5000 EVs on 0.005 mm^2 area of microscope view.

The PCA analysis of EVs derived from two glioma cancer cells (i.e U373 and U87) shows distinguished the correlated 95% confidence ellipse of their fingerprints (Figure S4-12).

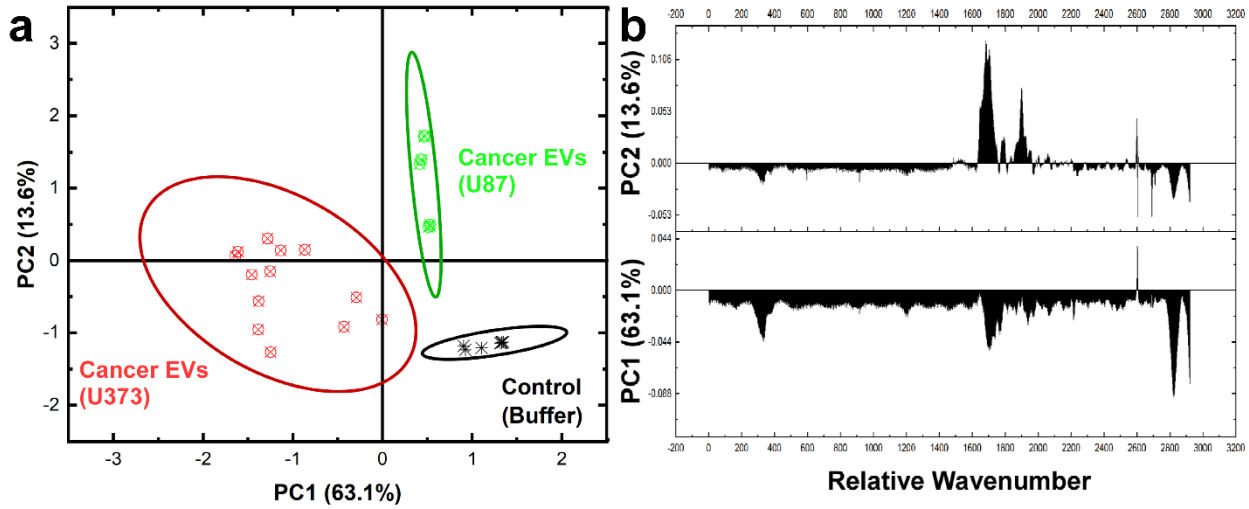

Figure S 4-12. (a) SERS characterization for investigating the specific Raman scattering signals of EVs derived from glioma U87 EVs (Green) in comparison with glioma U373 EVs (Red). (b) PCA score plot of the SERS data, showing the distinguished position of the spectra of each sample according to the PC1 loading Raman bands.

4.9 References

AbdelFatah, T., Jalali, M. & Mahshid, S. (2018). A nanofilter for fluidic devices by pillar- assisted self-assembly microparticles. *Biomicrofluidics*, *12*, 064103.

Al-Nedawi, K., Meehan, B., Micallef, J., Lhotak, V., May, L., Guha, A. & Rak, J. (2008). Intercellular transfer of the oncogenic receptor EGFRvIII by microvesicles derived from tumour cells. *Nature Cell Biology*, *10*(5), 619–624.

Bai, S., Serien, D., Hu, A. & Sugioka, K. (2018a). 3D Microfluidic Surface-Enhanced Raman Spectroscopy (SERS) Chips Fabricated by All-Femtosecond-Laser-Processing for Real-Time Sensing of Toxic Substances. *Advanced Functional Materials*, *28*(23), 1706262.

Bai, S., Serien, D., Hu, A. & Sugioka, K. (2018b). 3D Microfluidic Surface-Enhanced Raman Spectroscopy (SERS) Chips Fabricated by All-Femtosecond-Laser-Processing for Real-Time Sensing of Toxic Substances. *Advanced Functional Materials*, *28*(23), 1706262.

Carmicheal, J., Hayashi, C., Huang, X., Liu, L., Lu, Y., Krasnoslobodtsev, A., Lushnikov, A., Kshirsagar, P. G., Patel, A., Jain, M., Lyubchenko, Y. L., Lu, Y., Batra, S. K. & Kaur, S. (2019). Label-free characterization of exosome via surface enhanced Raman spectroscopy for the early detection of pancreatic cancer. *Nanomedicine: Nanotechnology, Biology, and Medicine*, *16*, 88–96.

Chien, F.-C., Kuo, C. W., Yang, Z.-H., Chueh, D.-Y. & Chen, P. (2011). Exploring the Formation of Focal Adhesions on Patterned Surfaces Using Super-Resolution Imaging. *Small*, *7*(20), 2906–2913.

Choi, D., Montermini, L., Jeong, H., Sharma, S., Meehan, B. & Rak, J. (2019). Mapping Subpopulations of Cancer Cell-Derived Extracellular Vesicles and Particles by Nano-Flow Cytometry. *ACS Nano*, *13*(9), 10499–10511.

Choi, D., Montermini, L., Kim, D. K., Meehan, B., Roth, F. P. & Rak, J. (2018). The impact of oncogenic egfrviii on the proteome of extracellular vesicles released from glioblastoma cells. *Molecular and Cellular Proteomics*, *17*(10), 1948–1964.

Choi, D., Spinelli, C., Montermini, L. & Rak, J. (2019). Oncogenic Regulation of Extracellular Vesicle Proteome and Heterogeneity. In *Proteomics* (Vol. 19, Issues 1–2, p. 1800169).

Contreras-Naranjo, J. C., Wu, H. J. & Ugaz, V. M. (2017). Microfluidics for exosome isolation and analysis: Enabling liquid biopsy for personalized medicine. In *Lab on a Chip* (Vol. 17, Issue 21, pp. 3558–3577). Royal Society of Chemistry.

Dittrich, P. S. & Manz, A. (2006). Lab-on-a-chip: Microfluidics in drug discovery. *Nature Reviews Drug Discovery*, *5*(3), 210–218.

Dodson, S., Haggui, M., Bachelot, R., Plain, J., Li, S. & Xiong, Q. (2013). Optimizing electromagnetic hotspots in plasmonic bowtie nanoantennae. *Journal of Physical Chemistry Letters*, *4*(3), 496–501.

Fan, M., Wang, P., Escobedo, C., Sinton, D. & Brolo, A. G. (2012). Surface-enhanced Raman scattering (SERS) optrodes for multiplexed on-chip sensing of nile blue A and oxazine 720. *Lab on a Chip*, *12*(8), 1554–1560.

Faried, M., Suga, K., Okamoto, Y., Shameli, K., Miyake, M. & Umakoshi, H. (2019). Membrane Surface-Enhanced Raman Spectroscopy for Cholesterol-Modified Lipid Systems: Effect of Gold Nanoparticle Size. *ACS Omega*, *4*(9), 13687–13695.

Fraire, J. C., Stremersch, S., Bouckaert, D., Monteyne, T., De Beer, T., Wuytens, P., De Rycke, R., Skirtach, A. G., Raemdonck, K., De Smedt, S. & Braeckmans, K. (2019). Improved Label-Free Identification of Individual Exosome-like Vesicles with Au@Ag Nanoparticles as SERS Substrate. *ACS Applied Materials and Interfaces*, *11*(43), 39424–39435.

Fromm, D. P., Sundaramurthy, A., James Schuck, P., Kino, G. & Moerner, W. E. (2004). Gap-dependent optical coupling of single "bowtie" nanoantennas resonant in the visible. *Nano Letters*, *4*(5), 957–961. https://doi.org/10.1021/nl049951r

Galarreta, B. C., Tabatabaei, M., Guieu, V., Peyrin, E. & Lagugné-Labarthet, F. (2013). Microfluidic channel with embedded SERS 2D platform for the aptamer detection of ochratoxin A. *Analytical and Bioanalytical Chemistry*, *405*(5), 1613–1621.

Garnier, D., Meehan, B., Kislinger, T., Daniel, P., Sinha, A., Abdulkarim, B., Nakano, I. & Rak, J. (2018). Divergent evolution of temozolomide resistance in glioblastoma stem cells is reflected in extracellular vesicles and coupled with radiosensitization. *Neuro-Oncology*, *20*(2), 236–248.

Happel, J. & Brenner, H. (1973). *Low Reynolds number hydrodynamics.* (Vol. 1). Springer Netherlands.

Hatab, N. A., Hsueh, C. H., Gaddis, A. L., Retterer, S. T., Li, J. H., Eres, G., Zhang, Z. & Gu, B. (2010a). Free-standing optical gold bowtie nanoantenna with variable gap size for enhanced Raman spectroscopy. *Nano Letters*, *10*(12), 4952–4955.

Hatab, N. A., Hsueh, C. H., Gaddis, A. L., Retterer, S. T., Li, J. H., Eres, G., Zhang, Z. & Gu, B. (2010b). Free-standing optical gold bowtie nanoantenna with variable gap size for enhanced Raman spectroscopy. *Nano Letters*, *10*(12), 4952–4955.

He, M., Crow, J., Roth, M., Zeng, Y. & Godwin, A. K. (2014). Integrated immunoisolation and protein analysis of circulating exosomes using microfluidic technology. *Lab on a Chip*, *14*(19), 3773–3780. https://doi.org/10.1039/c4lc00662c

Henkel, T., Popp, J. & März, A. (2010). SERS and Microfluidics. In *Surface Enhanced Raman Spectroscopy: Analytical, Biophysical and Life Science Applications* (pp. 173–190). Wiley-VCH Verlag GmbH & Co. KGaA.

Hoi, S.-K., Chen, X., Kumar, V. S., Homhuan, S., Sow, C.-H. & Bettiol, A. A. (2011). A Microfluidic Chip with Integrated Colloidal Crystal for Online Optical Analysis. *Advanced Functional Materials*, *21*(15), 2847–2853.

Huang, H. K., Cheng, H. W., Liao, C. C., Lin, S. J., Chen, Y. Z., Wang, J. K., Wang, Y. L. & Huang, N. T. (2020). Bacteria encapsulation and rapid antibiotic susceptibility test using a microfluidic microwell device integrating surface-enhanced Raman scattering. *Lab on a Chip*, *20*(14), 2520–2528.

Jalali, M., AbdelFatah, T., Mahshid, S. S., Labib, M. & Mahshid, S. (2018). Hierarchical 3D Nanostructured Microfluidic Device for Sensitive Detection of Pathogenic Bacteria. *Small*, *1801893*, 1–15.

Jalali, M., Filine, E., Dalfen, S. & Mahshid, S. (2020). Microscale reactor embedded with Graphene/hierarchical gold nanostructures for electrochemical sensing: application to the determination of dopamine. *Microchimica Acta*, *187*(1), 90.

Jalali, M., Moakhar, R. S., Abdelfattah, T., Filine, E., Mahshid, S. S. & Mahshid, S. (2020). Nanopattern-Assisted Direct Growth of Peony-like 3D MoS2/Au Composite for Nonenzymatic Photoelectrochemical Sensing. *ACS Applied Materials and Interfaces*, *12*(6), 7411–7422.

Kaufman, L., Cooper, T. T., Wallace, G. Q., Hawke, D. C., Betts, D., Hess, D. A. & Lagugné-Labarthet, F. (2019). Trapping and SERS identification of extracellular vesicles using nanohole arrays. In T. Vo-Dinh, H.-P. A. Ho & K. Ray (Eds.), *Plasmonics in Biology and Medicine XVI* (Vol. 10894, p. 10). SPIE.

Knudson, A., Hazari, S., Carney, R. P., Robertson, C. S., Lam, K. S., Wachsmann-Hogiu, S., Lee, C. & Smith, Z. J. (2015). 3D plasmonic nanobowl platform for the study of exosomes in solution. *Nanoscale*, *7*(20), 9290–9297.

Lane, R., Simon, T., Vintu, M., Solkin, B., Koch, B., Stewart, N., Benstead-Hume, G., Pearl, F. M. G., Critchley, G., Stebbing, J. & Giamas, G. (2019). Cell-derived extracellular vesicles can be used as a biomarker reservoir for glioblastoma tumor subtyping. *Communications Biology*, *2*(1), 1–12.

Lao, Z., Zheng, Y., Dai, Y., Hu, Y., Ni, J., Ji, S., Cai, Z., Smith, Z. J., Li, J., Zhang, L., Wu, D. & Chu, J. (2020). Nanogap Plasmonic Structures Fabricated by Switchable Capillary-Force Driven Self-Assembly for Localized Sensing of Anticancer Medicines with Microfluidic SERS. *Advanced Functional Materials*, *30*(15), 1909467.

Le Ru, E. C., Blackie, E., Meyer, M. & Etchegoint, P. G. (2007). Surface enhanced raman scattering enhancement factors: A comprehensive study. *Journal of Physical Chemistry C*, *111*(37), 13794–13803.

Lee, C., Carney, R., Lam, K. & Chan, J. W. (2017). SERS analysis of selectively captured exosomes using an integrin-specific peptide ligand. *Journal of Raman Spectroscopy*, *48*(12), 1771–1776.

Li, X., Corbett, A. L., Taatizadeh, E., Tasnim, N., Little, J. P., Garnis, C., Daugaard, M., Guns, E., Hoorfar, M. & Li, I. T. S. (2019). Challenges and opportunities in exosome research—Perspectives from biology, engineering, and cancer therapy. *APL Bioengineering*, *3*(1), 011503.

Liang, K., Li, Z., Luo, Y., Zhang, Q., Yin, F., Xu, L., Chen, H. & Wang, H. (2020). Intelligent Nanocomposites with Intrinsic Blood–Brain-Barrier Crossing Ability Designed for Highly Specific MR Imaging and Sonodynamic Therapy of Glioblastoma. *Small*, *16*(8), 1906985.

Liu, Jiangang, Cai, C., Wang, Y., Liu, Y., Huang, L., Tian, T., Yao, Y., Wei, J., Chen, R., Zhang, K., Liu, B. & Qian, K. (2020). A Biomimetic Plasmonic Nanoreactor for Reliable Metabolite Detection. *Advanced Science*, *1903730*.

Liu, Juanjuan, Jalali, M., Mahshid, S. & Wachsmann-Hogiu, S. (2020). Are plasmonic optical biosensors ready for use in point-of-need applications? In *Analyst* (Vol. 145, Issue 2, pp. 364–384). Royal Society of Chemistry.

Mahshid, S., Ahamed, M. J., Berard, D., Amin, S., Sladek, R., Leslie, S. R. & Reisner, W. (2015).

Development of a platform for single cell genomics using convex lens-induced confinement. *Lab Chip*, *15*(14), 3013–3020.

Notingher, I., Verrier, S., Haque, S., Polak, J. M. & Hench, L. L. (2003). Spectroscopic study of human lung epithelial cells (A549) in culture: Living cells versus dead cells. *Biopolymers - Biospectroscopy Section*, *72*(4), 230–240.

Patel, A. P., Tirosh, I., Trombetta, J. J., Shalek, A. K., Gillespie, S. M., Wakimoto, H., Cahill, D. P., Nahed, B. V., Curry, W. T., Martuza, R. L., Louis, D. N., Rozenblatt-Rosen, O., Suvà, M. L., Regev, A. & Bernstein, B. E. (2014). Single-cell RNA-seq highlights intratumoral heterogeneity in primary glioblastoma. *Science*, *344*(6190), 1396–1401.

Pilot, R., Signorini, R., Durante, C., Orian, L., Bhamidipati, M. & Fabris, L. (2019). A review on surface-enhanced Raman scattering. *Biosensors*, *9*(2).

Ramirez, M. I., Amorim, M. G., Gadelha, C., Milic, I., Welsh, J. A., Freitas, V. M., Nawaz, M., Akbar, N., Couch, Y., Makin, L., Cooke, F., Vettore, A. L., Batista, P. X., Freezor, R., Pezuk, J. A., Rosa-Fernandes, L., Carreira, A. C. O., Devitt, A., Jacobs, L., … Dias-Neto, E. (2018). Technical challenges of working with extracellular vesicles. In *Nanoscale* (Vol. 10, Issue 3, pp. 881–906). Royal Society of Chemistry.

Reifenberger, G., Wirsching, H. G., Knobbe-Thomsen, C. B. & Weller, M. (2017a). Advances in the molecular genetics of gliomas-implications for classification and therapy. In *Nature Reviews Clinical Oncology* (Vol. 14, Issue 7, pp. 434–452). Nature Publishing Group.

Reifenberger, G., Wirsching, H. G., Knobbe-Thomsen, C. B. & Weller, M. (2017b). Advances in the molecular genetics of gliomas-implications for classification and therapy. In *Nature Reviews Clinical Oncology* (Vol. 14, Issue 7, pp. 434–452). Nature Publishing Group.

Sassa, F., Biswas, G. C. & Suzuki, H. (2020). Microfabricated electrochemical sensing devices. In *Lab on a Chip* (Vol. 20, Issue 8, pp. 1358–1389). Royal Society of Chemistry.

Sevim, S., Franco, C., Chen, X., Sorrenti, A., Rodríguez-San-Miguel, D., Pané, S., deMello, A. J. & Puigmartí-Luis, J. (2020). SERS Barcode Libraries: A Microfluidic Approach. *Advanced Science*, 1903172.

Shao, H., Chung, J., Balaj, L., Charest, A., Bigner, D. D., Carter, B. S., Hochberg, F. H., Breakefield, X. O., Weissleder, R. & Lee, H. (2012). Protein typing of circulating microvesicles allows real-time monitoring of glioblastoma therapy. *Nature Medicine*, *18*.

Sheng, Y., Jiang, S., Yang, C., Liu, M., Liu, A., Zhang, C., Li, Z., Huo, Y., Wang, M. & Man, B. (2017). Three-dimensional nanoporous MoS 2 framework decorated with Au nanoparticles for surface-enhanced Raman scattering. *Chemical Physics Letters*, *682*, 64–70.

Shin, H., Jeong, H., Park, J., Hong, S. & Choi, Y. (2018a). Correlation between Cancerous Exosomes and Protein Markers Based on Surface-Enhanced Raman Spectroscopy (SERS) and Principal Component Analysis (PCA) [Research-article]. *ACS Sensors*, *3*(12), 2637–2643.

Shin, H., Jeong, H., Park, J., Hong, S. & Choi, Y. (2018b). Correlation between Cancerous Exosomes and Protein Markers Based on Surface-Enhanced Raman Spectroscopy (SERS) and Principal Component Analysis (PCA) [Research-article]. *ACS Sensors*, *3*, 2637–2643.

Shin, H., Oh, S., Hong, S., Kang, M., Kang, D., Ji, Y. G., Choi, B. H., Choi, B. H., Kang, K. W., Jeong, H., Park, Y., Hong, S., Kim, H. K., Kim, H. K., Choi, Y., Choi, Y., Choi, Y. & Choi,

Y. (2020). Early-Stage Lung Cancer Diagnosis by Deep Learning-Based Spectroscopic Analysis of Circulating Exosomes. *ACS Nano*, *14*(5), 5435–5444. https://doi.org/10.1021/acsnano.9b09119

Shin, H., Oh, S., Kang, D. & Choi, Y. (2020). Protein Quantification and Imaging by Surface-Enhanced Raman Spectroscopy and Similarity Analysis. *Advanced Science*, *1903638*, 1–9.

Siavash Moakhar, R., Abdelfatah, T., Sanati, A., Jalali, M., Flynn, S. E., Mahshid, S. S. & Mahshid, S. (2020). A Nanostructured Gold/Graphene Microfluidic Device for Direct and Plasmonic-Assisted Impedimetric Detection of Bacteria. *ACS Applied Materials and Interfaces*, *12*(20), 23298–23310.

Siravegna, G., Marsoni, S., Siena, S. & Bardelli, A. (2017). Integrating liquid biopsies into the management of cancer. In *Nature Reviews Clinical Oncology* (Vol. 14, Issue 9, pp. 531–548). Nature Publishing Group.

Stremersch, S., Marro, M., Pinchasik, B. El, Baatsen, P., Hendrix, A., De Smedt, S. C., Loza-Alvarez, P., Skirtach, A. G., Raemdonck, K. & Braeckmans, K. (2016). Identification of individual exosome-like vesicles by surface enhanced raman spectroscopy. *Small*, *12*(24), 3292–3301.

Suga, K., Otsuka, Y., Okamoto, Y. & Umakoshi, H. (2018). Gel-Phase-like Ordered Membrane Properties Observed in Dispersed Oleic Acid/1-Oleoylglycerol Self-Assemblies: Systematic Characterization Using Raman Spectroscopy and a Laurdan Fluorescent Probe. *Langmuir*, *34*(5), 2081–2088.

Tantussi, F., Messina, G. C., Capozza, R., Dipalo, M. & Lovato, L. (2018). Long-Range Capture and Delivery of Water-Dispersed Nano-Objects by Microbubbles Generated on 3D Plasmonic Surfaces. *ACS Nano*, *12*, 4116–4122.

Thuenauer, R., Juhasz, K., Mayr, R., Frühwirth, T., Lipp, A. M., Balogi, Z. & Sonnleitner, A. (2011). A PDMS-based biochip with integrated sub-micrometre position control for TIRF microscopy of the apical cell membrane. *Lab on a Chip*, *11*(18), 3064–3071. https://doi.org/10.1039/c1lc20458k

Tsai, S. S. H., Wexler, J. S., Wan, J. & Stone, H. A. (2013). Microfluidic ultralow interfacial tensiometry with magnetic particles. *Lab on a Chip*, *13*(1), 119–125.

Wells, S. M., Retterer, S. D., Oran, J. M. & Sepaniak, M. J. (2009). Controllable nanofabrication of aggregate-like nanoparticle substrates and evaluation for surface-enhanced Raman spectroscopy. *ACS Nano*, *3*(12), 3845–3853.

Weng, Z., Zong, S., Wang, Y., Li, N., Li, L., Lu, J., Wang, Z., Chen, B. & Cui, Y. (2018). Screening and multiple detection of cancer exosomes using an SERS-based method. *Nanoscale*, *10*(19), 9053–9062.

Xi, Z. Y., Xu, Y. Y., Zhu, L. P., Wang, Y. & Zhu, B. K. (2009). A facile method of surface modification for hydrophobic polymer membranes based on the adhesive behavior of poly(DOPA) and poly(dopamine). *Journal of Membrane Science*, *327*(1–2), 244–253.

Yu, J. L., May, L., Lhotak, V., Shahrzad, S., Shirasawa, S., Weitz, J. I., Coomber, B. L., Mackman, N. & Rak, J. W. (2005). Oncogenic events regulate tissue factor expression in colorectal cancer cells: Implications for tumor progression and angiogenesis. *Blood*, *105*(4), 1734–1741.

Zachariah, M. A., Oliveira-Costa, J. P., Carter, B. S., Stott, S. L. & Nahed, B. V. (2018). Blood-based biomarkers for the diagnosis and monitoring of gliomas. *Neuro-Oncology*, *20*(9), 1155–1161.

Zhang, P., Crow, J., Lella, D., Zhou, X., Samuel, G., Godwin, A. K. & Zeng, Y. (2018). Ultrasensitive quantification of tumor mRNAs in extracellular vesicles with an integrated microfluidic digital analysis chip. *Lab on a Chip*, *18*(24), 3790–3801.

Zhang, P., He, M. & Zeng, Y. (2016). Ultrasensitive microfluidic analysis of circulating exosomes using a nanostructured graphene oxide/polydopamine coating. *Lab on a Chip*, *16*(16), 3033–3042.

Zhang, P., Zhou, X., He, M., Shang, Y., Tetlow, A. L., Godwin, A. K. & Zeng, Y. (2019). Ultrasensitive detection of circulating exosomes with a 3D-nanopatterned microfluidic chip. *Nature Biomedical Engineering*, *3*(6), 438–451.

Zhou, T., Liu, Z., Wu, Y., Deng, Y., Liu, Y. & Liu, G. (2013). Hydrodynamic particle focusing design using fluid-particle interaction. *Biomicrofluidics*, *7*(5), 054104.

Zhou, X., Ravichandran, G. C., Zhang, P., Yang, Y. & Zeng, Y. (2019). A microfluidic alternating-pull-push active digitization method for sample-loss-free digital PCR. *Lab on a Chip*, *19*(24), 4104–4116.

5 Bridging Chapters 4 and 6

In this work, knowing that we had to increase the EM field enhancement of the structures to amplify the optical readout signal for high-resolution peak distinguishment in SERS molecular profiling of EVs, we fabricated an array of nanotriangles with sharp apex and in close proximity (nanobowties). The nanobowtie structures provided a strong EM field due to the plasmonic effect of suspended gaps rendering a maximum theoretical EFEF of 9.0×10^5. The enhanced EM-field from plasmonic nanobowtie structures results in development of a sensitive SERS detection device for nanosized EVs, able to distinguish the synthetic liposomes and EVs from human glial cells (NHA), and different glioma tumor cells.

The locally enhanced EM-field in sharp and confined plasmonic systems has been exploited to create an ultra-small, ultra-intense light concentration already incorporated in some SERS applications(Fromm et al., 2004; Hatab et al., 2010b; H. K. Huang et al., 2020) but still largely unexplored in the space of EVs in spite of several advantages. The nanobowtie structures provided a strong EM field due to the plasmonic effect of suspended gaps rendering a maximum theoretical EFEF of 9.0×10^5. The enhanced EM-field from plasmonic nanobowtie structures results in the development of a sensitive SERS detection device for nanosized EVs, able to distinguish the synthetic liposomes and EVs from human glial cells (NHA), and different glioma tumor cells (details are explained in chapter IV).

However, like most approaches that can yield molecular level information, this approach gathered the spectral results by averaging over multiple EVs which limited access to the diagnostically significant information contained in single EV molecular profiling (Jongmin Park et al., 2021). In order to address that we aimed to design the plasmonic nanoarray in the shape of nanocavities for single EV isolation.

We observed that confined microfluidic chambers designed with convex nanostructures is not a suitable option to entrap single layer of EVs most possibly due to a phenomenon called the "coffee-ring effect" through the time span of a SERS interrogation. When a liquid containing particles evaporates slightly on a surface, the particles tend to accumulate at the edges of the evaporating droplet, forming a ring-like pattern. This happens because as the liquid evaporates, the flow of liquid toward the edges of the droplet concentrates the particles there. The convex nanostructures create a surface with many edges and corners, which leads to a more pronounced flow of liquid toward those regions and therefore amplify the coffee-ring effect. As a result, any particles in the liquid tend to accumulate at the edges and corners of the chamber. Furthermore, the small size of the nanostructures means that there is a significant amount of surface area relative to the volume of the chamber. This creates a large surface tension that can cause the liquid to bead up and pull away from the edges of the nanostructures, further reducing the likelihood of particles being trapped.

Solution 1/ nanocavities- Using concave nanostructures in microfluidic chambers can provide advantages for trapping single nanoparticles inside a cavity-like pattern. The concave nanostructures are designed to create a depression or cavity in the surface, which can be used to confine particles in a specific location. One advantage of using concave nanostructures is that they can create a low-pressure region in the cavity, which helps to keep the particles trapped inside. The depression created by the concave structure can also act as a barrier that prevents particles from moving out of the cavity. In addition, the concave structure can be designed to have a specific size and shape, which allows for precise control over the size and shape of the cavity. To address single EV scanning, a nanocavity array was developed consists of arrays of circular nanocavites (with different diameters) embedded in an Ag/ZnO bilayer (optimized thickness for enhanced EM field

distribution: Ag 60 nm/ZnO 100 nm). The cavities have a pitch of >2 μm to ensure each cavity can be scanned independently. However, the cavity filling was not promising as the EVs tended to escape the nanocavities (observed by fluorescent microscopy).

Solution 2/ monolayer MoS_2- We hypothesized that advantage of using concave nanostructures with a positive attraction between the materials used inside the cavity and the bilayer lipid, is that they can reduce the impact of the coffee-ring effect as they can provide a localized low-pressure environment that counteracts the coffee-ring effect and helps to keep the particles trapped inside the cavity. Theoretical studies have indicated a positive attraction between monolayer MoS_2 and bilayer lipid membranes in a water-based environment (Gu et al., 2018, 2019; L. Zhang et al., 2019). Different molecules including phthalocyanines are used at the surface of monolayer MoS_2 material through noncovalent interactions, while various sulfur-bearing organic molecules are recognized as covalent binding moieties at sulfur vacancies of monolayer MoS_2 (Gerkman et al., 2019). In particular, different modes of interactions were found between monolayer MoS_2 and bilayer lipid including a van der Waals interaction of -1419.72 kJ mol^{-1}, and an electrostatic interaction of -1380.17 kJ mol^{-1} (Rongrong Wu et al., 2018). The high sensitivity, low-cost, easy patternability and integrability of graphene and MoS_2 raised attentions in past few years on integrating and decorating them with other materials to enhance their properties in sensing applications(Jing Chen et al., 2016; S. J. Li et al., 2013; C. Zhao et al., 2017; Y. Zhu et al., 2010). In addition, the surface plasmon resonance platforms integrated with these confined materials have been widely studied for their superior optical absorption over the past decades for biological and chemical sensing applications(Anker et al., 2008; Lodewijks et al., 2013).

Critically, as each EV represents a specific cell, the cancer markers contained in the tumor-derived EV landscape relate to the properties of a given cellular population reflecting its diversity.(Zachariah et al., 2018) Consequently, the information contained in a population of individual EVs can capture the remarkable and clinically important traits reflective of cellular heterogeneity,(Al-Nedawi et al., 2008b; Ramirez et al., 2018b) and mutational and epigenetic driver events(Boriachek et al., 2018; Im et al., 2014b; Mollaei et al., 2017; C.-Y. Wu et al., 2017) in cancer. In the next chapter, our attempt to design nanocavity plasmonic array for hosting single EVs are discussed.

6 MoS_2- Plasmonic Nanocavities for Raman Spectra of Single Extracellular Vesicles Reveal Molecular Progression in Glioblastoma

Mahsa Jalali[1], Carolina del Real Mata[1], Laura Montermini[2], Olivia Jeanne[1], Imman I. Hosseini[1,3], Zonglin Gu[4], Cristiana Spinelli[2], Yao Lu[1], Nadim Tawil[2], Marie Christine Guiot[5], Zhi He[6], Sebastian Wachsmann-Hogiu[1], Ruhong Zhou[6], Kevin Petrecca[5], Walter W. Reisner[3], Janusz Rak[2], Sara Mahshid[1,7*]

[1] Department of Bioengineering, McGill University, Montreal, QC, H3A 0E9 Canada

[2] Research Institute of the McGill University Health Centre (RIMUHC), Montreal, Quebec, H4A 3J1 Canada

[3] Department of Physics, McGill University, Montreal, QC, H3A 2T8 Canada

[4] College of Physical Science and Technology, Yangzhou University, Jiangsu, 225009 China

[5]Department of Neuropathology, Montreal Neurological Institute-Hospital, McGill University, Montreal, Quebec, H3A 2B4 Canada

[6] Institute of Quantitative Biology, College of Life Sciences, Zhejiang University, Hangzhou, 310058 China

[7] Division of Experimental Medicine, McGill University, Montreal, QC, H4A 3J1 Canada

Abstract

Extracellular vesicles (EVs) are continually released from cancer cells into biofluids, carrying actionable molecular fingerprints of the underlying disease with considerable diagnostic and therapeutic potential. The scarcity, heterogeneity and intrinsic complexity of tumour EVs present a major technological challenge in real-time monitoring of complex cancers such as glioblastoma (GBM). Surface-enhanced Raman spectroscopy (SERS) outputs a label-free spectroscopic fingerprint for EV molecular profiling. However, it has not been exploited to detect known biomarkers at the single EV level. We developed a multiplex fluidic device with embedded arrayed nanocavity microchips (MoSERS microchip) that achieves 97% confinement of single EVs in a minute amount of fluid (<10 µl) and enables molecular profiling of single EVs with SERS. The nanocavity arrays combine two featuring characteristics: (1) An embedded MoS_2 monolayer that enables label-free isolation and nanoconfinement of single EVs due to physical interaction (Coulomb and van der Waals) between the MoS_2 edge sites and lipid bilayer; and (2) A layered plasmonic cavity that enables sufficient electromagnetic field enhancement inside the cavities to obtain single EV level signal resolution for stratifying the molecular alterations. We used the GBM paradigm to demonstrate the diagnostic potential of the SERS single EV molecular profiling approach. MoSERS multiplexing fluidic achieves parallel signal acquisition of glioma molecular variants (EGFRvIII oncogenic mutation and MGMT expression) in GBM cells. The detection limit of 1.23% was found for stratifying these key molecular variants in the wild-type population. When interfaced with a convolutional neural network (CNN), MoSERS improved diagnostic accuracy (87%) with which GBM mutations were detected in 12 patient blood samples, on par with clinical pathology tests. Thus, MoSERS demonstrates the potential for molecular stratification of cancer patients using circulating EVs.

Keywords: single extracellular vesicle analysis, surface-enhanced Raman spectroscopy, plasmonic nanocavity, monolayer MoS_2, glioblastoma cancer.

6.1 Introduction

Extracellular vesicles (EVs) are heterogeneous lipid-bilayer encapsulated vesicular structures shed into biofluids from cancer cells. EVs are an attractive option for liquid biopsy because they contain a wide range of molecular cargo, such as proteins and nucleic acids, that may serve as cancer-specific markers.(Boriachek et al., 2018; Im et al., 2014; Mollaei et al., 2017; C.-Y. Wu et al., 2017; Y. G. Zhou et al., 2016) Critically, as each EV represents a specific cell, the cancer markers contained in the tumor-derived EV landscape relate to the properties of a given cellular population while reflecting its diversity.(Zachariah et al., 2018) Consequently, the information contained in a population of individual EVs can capture the clinically important traits reflective of cellular heterogeneity,(Al-Nedawi et al., 2008; Ramirez et al., 2018) and mutational and epigenetic driver events(Boriachek et al., 2018; Im et al., 2014; Mollaei et al., 2017; C.-Y. Wu et al., 2017) in cancer. In particular, extracellular vesicles represent a promising platform for liquid biopsy application in Glioblastoma (GBM), the most common and aggressive primary astrocytic brain tumor. (Louis et al., 2016; Nawaz et al., 2014; Wirsching et al., 2016; P. Wu et al., 2019)

Notably, EVs carry signatures paradigmatic for GBM molecular subtypes and traits,(Lane et al., 2019; Pan et al., 2021; Reifenberger et al., 2017; Shao et al., 2012, 2015) including the mutant oncogenic variant of epidermal growth factor receptor (EGFR), known as EGFRvIII,(Al-Nedawi et al., 2008; Ramirez et al., 2018) as well as O^6-Methylguanine-DNA Methyltransferase (MGMT), a marker of resistance to temozolomide (TMZ) chemotherapy. These changes are important due to their functional impact and prevalence as EGFRvIII is expressed in approximately 20-35% of GBM cases and impacts cellular aggressiveness as well as vesiculation,(Choi et al.,

2018) while MGMT expression is normally silenced by promoter methylation in approximately 45% of GBM cases, a factor that renders these tumours sensitive to treatment with TMZ, which may be lost during disease progression. As only 2-3% of blood-circulating EVs are believed to carry GBM signatures due to the blood-brain barrier, EVs carrying these mutations can be easily missed against a large background of EVs released from healthy cells.(Ang et al., 2022) Thus, there is great interest in developing technologies with single EV resolution for early detection and monitoring of GBM-derived EVs for the emergence of resistance during chemotherapy.

Classic EV analysis techniques based on bench top protocols e.g. polymerase chain reaction (PCR), Western blot or ELISA, average over very large numbers of EVs ($10^5 - 10^8$ EVs contained in a µl to ml of sample).(Res, 2017) More recent approaches utilize microfluidic mixing and filtration combined with chemical capture,(Res, 2017) for example exploiting device surfaces or microspheres functionalized with antibodies(Zhao et al., 2016) or aptamers(K. Zhang et al., 2019) specific to common EV markers. Such approaches average over at least 10 EVs bound per bead or surface element.(Z. Yang et al., 2022; Zhao et al., 2016) A third wave of technologies has extended existing fluorescence based single-cell and single-molecule analytical approaches to perform individualized EV analysis. Nano flow cytometry can now profile populations of 1000's of EVs down to 100nm in size stained for a limited number of surface biomarkers.(Choi et al., 2019; van der Vlist et al., 2012) Alternatively, single EVs can be surface immobilized and then exposed sequentially to a series of fluorescent antibody probes targeting specific markers,(Chen, Yan, et al., 2019; Ferguson et al., 2022; Lee et al., 2018a) achieving higher multiplexing and signal at the expense of throughput. This latter approach has been extended to the detection of EV-encapsulated RNA via fusing of surface bound EVs to liposomes containing molecular beacon probes that hybridize to given RNA/microRNA targets.(J. Zhou et al., 2020) These existing single

EV approaches are already showing promise in research and clinical application.(Ferguson et al., 2022; Lee et al., 2018a) However, they have two intrinsic disadvantages. Firstly, current methods inevitably pre-select biomarkers of interest from the pool of biomarkers for which reliable fluorescent probes exist. Secondly, these methods entail a trade-off between high marker multiplexing and throughput, with high multiplexing necessitating many sequential probe washing cycles (with each cycle taking as long as one hour).(Lee et al., 2018b)

Surface-enhanced Raman spectroscopy (SERS) is a conceptually distinct alternative that in principle avoids the need for marker pre-selection and the multiplexing/throughput trade-off. SERS is a label-free approach that converts the entire biochemical signature of an EV, including surface chemistry and molecular cargo, into a single spectroscopic pattern, or "fingerprint"(Liang et al., 2021; Park et al., 2017a) (see supporting Table S1). SERS is inherently non-invasive, fast, reliable, and can be adapted for use in low-resource clinical settings, especially with the emergence of handheld instruments and fiberoptic probes.(S Rickard et al., 2020; P. Zhang et al., 2019) SERS applied at an ensemble level, coupled with machine learning methods, can already differentiate between EVs in blood samples collected from healthy and diseased donors of cancers.(Park et al., 2017b; Shin et al., 2020) The working principle of SERS is based on the adsorption of analyte molecules to a plasmonic surface that allows for a strong enhancement of the Raman signal from the analyte. Nanocavities with independently tunable harmonics achieve strong electromagnetic (EM) field enhancement at distinct wavelengths.(Akselrod et al., 2015) At the same time, monolayer direct gap semiconductors of transition metal dichalcogenides (like monolayer MoS_2) ensure relatively strong light-matter interactions when coupled with the EM field enhancements at their absorption wavelength.(Eda & Maier, 2013)

Here we demonstrate a SERS based nanosurface microfluidic approach for molecular profiling of single EVs that can output information on EV surface properties and encapsulated cargo for early detection and monitoring of the cell transformation events during cancer progression and therapy (Figure 6-1a). Our MoSERS micro-chip embedded in a simple microfluidic device for sample delivery, is produced via a combined bottom-up and top-down fabrication strategy. The MoSERS microfluidic is a user-friendly platform with attached accessories for flow actuation that automates the assay process when placed for SERS interrogation (Figure 6-1b). The MoSERS microchip assimilates the SERS signal from EVs trapped in nanocavities constructed from a plasmonic silver/non-plasmonic ZnO bilayer with an embedded MoS_2 floor. It can achieve single EV resolved SERS spectrum due to three main factors. Firstly, our optimized photonic design achieves sufficiently strong in-cavity field enhancement to produce sufficient signal to obtain SERS spectra from single EVs. Secondly, relying on attractive interactions between the EV lipid membrane and the MoS_2 monolayer, we obtain EV entrapment in nanocavities without requiring biological recognition elements. Thirdly, as the cavities are made sufficiently small to accommodate only single EV, we ensure that the spectrum obtained from a single cavity in fact corresponds to the spectrum of a single EV (Figure 6-1c).

The MoSERS micro-chip is benchmarked by identifying and distinguishing signals from single EVs derived from non-cancerous glial cells (NHA), glioma cells (U373, U87) and glioma stem cells (GSC83, GSC1005, and GSC1123). These cell lines were either wild-type or manipulated to express relevant molecular alterations, such as oncogenic epidermal growth factor receptor variant III (EGFRvIII), phosphatase and tensin homologue (PTEN), which is naturally lost during GBM progression, and MGMT, a marker and effector of GBM resistance to temozolomide. Next, to maximize our technique's ability to discriminate between SERS spectra

with subtle differences and to achieve more accurate and sensitive multidimensional identification of EVs, we combined single EV SERS readouts with deep learning techniques based on a computational neural network (CNN). CNN machine learning was then applied to discriminate between EVs derived from GBM patient blood samples. The CNN approach outputs the probability that each EV carries specific oncogenic markers including EGFR amplification, EGFRvIII mutation and MGMT expression. This information can then be combined to differentiate EVs into marker negative and positive classes and render information that can be built into a diagnostic workflow.

Table 6-1. Single EV technologies validated by clinical samples.

Technology	Cancer	Media	Biomarker	Patients Number	Ref
Immunoaffinity Labelling					
Nanoplasmon-Enhanced (n-PLEX)	Pancreatic	Plasma	Protein-conjugated primary antibodies	104 Malignant 31 Benign	2014(Im et al., 2014) 2017(K. S. Yang et al., 2017)
Single EV Analysis (SEA) Multiplex immunostaining and fluorescent imaging	Pancreatic	Plasma	Optimized mutation-conjugated antibodies	20 Patient 5 Healthy	2018(Lee et al., 2018c) 2022(Ferguson et al., 2022)
Single Large EV Characterization Immunostaining and fluorescent imaging	Glioblastoma	Plasma	Protein-conjugated primary antibodies	8 Patient 2 Healthy	2019(Fraser et al., 2019)
TIRF Microscopy ~80 EVs Sequential detection of DNA-PAINT	Breast, ovarian, liver	Plasma	DNA-conjugated primary antibodies	7 Patient per Cancer	2019(Chen, Zong, et al., 2019)
Label-Free					
Single EV SERS (MoSERS) Microchip Label-Free SERS and ML assisted data analysis of mutations	Glioblastoma	Plasma	-	12 Patient 8 Healthy	This work

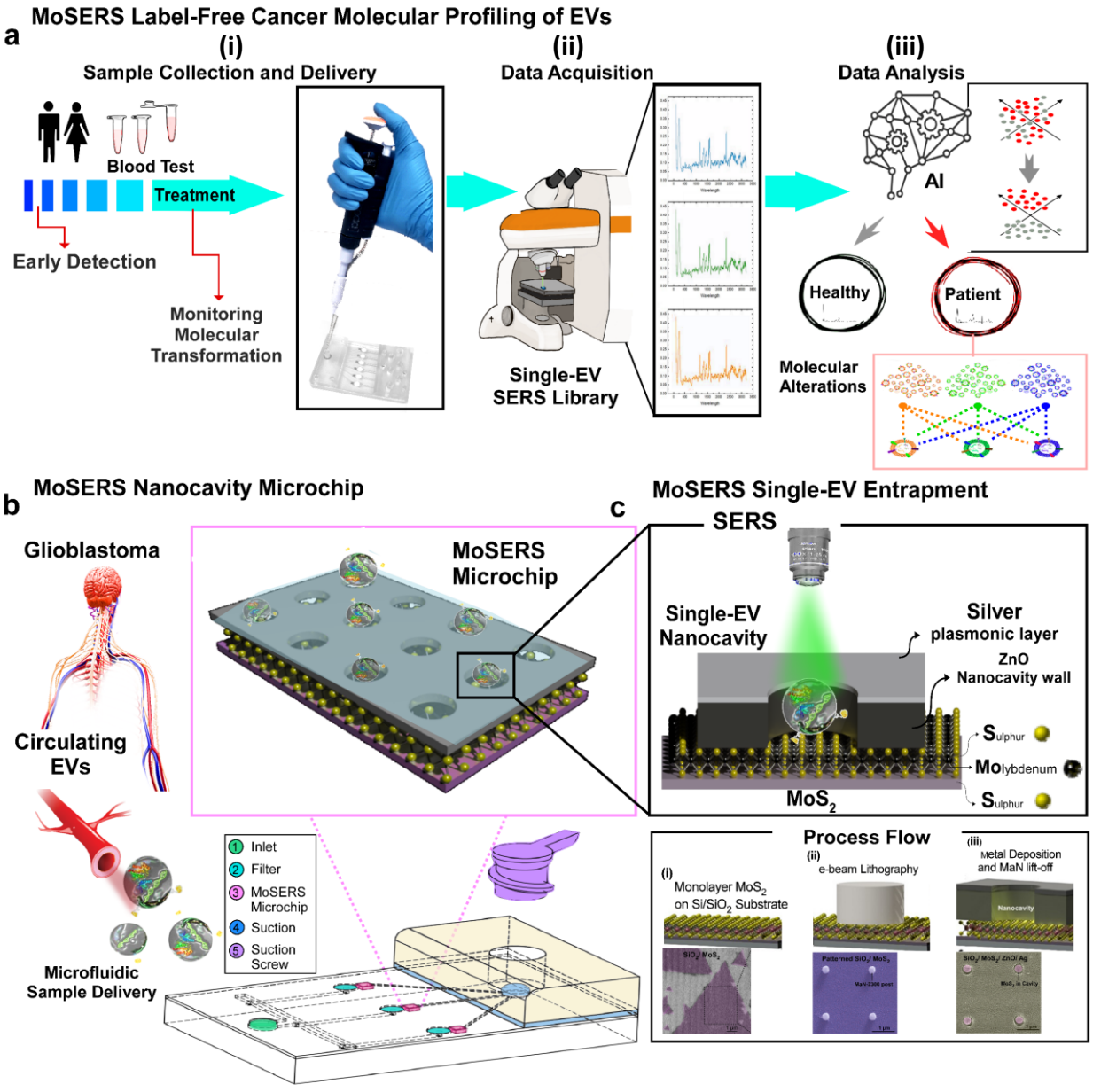

Figure 6-1. The concept of using single EV SERS approach in liquid biopsy of GBM patients. (a) Possibilities of using MoSERS microchip embedded microfluidic device for liquid biopsy of blood EVs for early detection and monitoring of cancer (i): A microfluidic prototype embedded with MoSERS microchips with the size of 0.1 cm x 0.1 cm for sample delivery and detection (ii). Single EV SERS spectrum analyzed by machine learning algorithm (CNN) to stratify molecular

alterations (iii). (b) The nanosurface microfluidic embedded with MoSERS microchip perform for SERS identification of single EVs of Glioblastoma cancer. Single EVs are entrapped in the plasmonic nanocavities, with one EV per cavity, and SERS is performed utilizing high-field enhancement at the nanocavity edges. (c) Single EV entrapment in the MoS_2 encapsulated nanocavities of MoSERS microchip. Schematic of MoSERS microchip fabrication and related SEM images of each step.

6.2 Results

6.2.1 Plasmonically active MoS_2 nanocavities

The MoSERS micro-chip consists of arrays of circular 250 nm diameter nanocavites embedded in a Ag/ZnO bilayer (Ag 60 nm/ZnO 100 nm). The cavities have a pitch of 3 μm to ensure each cavity can be scanned independently. The bilayer is placed on top of CVD-grown monolayer MoS_2 resting on a SiO_2/Si substrate, so that the nanocavity floor contains an exposed MoS_2 monolayer (Figure 6-2a). The nanocavites are produced using a negative e-beam lithography process (the step-by-step process flow is shown in Figure S6-1).

Our nanocavity design confers an enhanced SERS response arising from the intense electric field generated by the exposed Ag present at the nanocavity edge (Figure 6-2b). The collective coherent excitations of free electrons in the Ag thin film, known as surface plasmon resonance (SPR), lead to an enhanced localized electromagnetic (EM) field confinement in the vicinity of the nanocavities. Patterning the Ag thin film with nanocavities smaller than the laser wavelength gives rise to a localized strong electronic excitation at the nanocavity edges (LSPR). The SERS response can be quantified via the EM-field enhancement factor $EFEF$, scaling as the 4th power of the EM-field enhancement $\left(\frac{|E(\omega)|}{|E_0(\omega)|}\right)^4$.(Shin et al., 2018a) In order to determine the $EFEF$ factor for our nanocavity design, we used finite-difference time-domain (FDTD) simulation

(Lumerical Solutions, Inc.) incorporating the experimental cavity geometry, material optical properties and excitation conditions (532 nm diffraction-limited Gaussian laser beam focus). Figure 6-2c gives the EM-field distribution in the nanocavities. The EM-field is enhanced at the cavity edge and maximal for a cavity diameter of 250 nm (Figure 6-2d-e), with a corresponding quantitative enhancement of ~800 fold at the cavity edges. The simulated broad-band reflectance spectra show a sharp peak around the laser beam wavelength correlated to the diffraction mode (Figure 6-2f). These EM-field enhancements correspond to an overall EFEF of 6.4×10^5 (see Figure S6-2 for more details).

Next, we benchmarked the experimental SERS response of the MoSERS platform using the well-known SERS marker Rhodamine 6G (R6G). Nanocavity arrays were loaded with 1 μM R6G solution and scanned at 532 nm. Figure 6-2g gives the spatial variation of the SERS response over the array. Note that SERS hot spots corresponding to cavity positions are arranged along a rectangular lattice (the lattice has a horizontal pitch of 6 μm and vertical pitch of 2 μm). Regions of low response that are observed between cavities in the horizontal direction correspond to cases where the laser spot failed to overlap any cavities. Figure 6-2h compares SERS spectra from the flat thin film background region (blue), and nanocavities (red). The SERS signal from R6G at the nanocavity sites is over 300 times stronger than the signal from the background region.

To quantify the SERS enhancement resulting from the nanocavities, we compared the SERS signal in the presence of the MoSERS nanocavity with the signal arising from a flat substrate consisting of only an Ag/ZnO bilayer. The average peak intensity difference was calculated at the major peak positions (Figure 6-2i). The SERS intensity (I_{SERS}) is directly proportional to the EFEF according to the formula: $I_{SERS} = F_S \sigma_S C_{SERS}$ EFEF,(Fraire et al., 2019) where F_S is an instrumental factor related to Renishaw micro-Raman, σ_S is the Raman cross-section of a particular analyte, and

C_{SERS} is the concentration of the test analyte. Quantitatively, the SERS enhancement factor (EF) is calculated according to $\%EF_{MoSERS} = \frac{I_{NC}N_F}{I_F N_{NC}}$,(Le Ru et al., 2007; Wells et al., 2009) with the quantities I_F, I_{NC}, N_F, N_{NC} referring respectively to the SERS intensity of the flat bilayer, the SERS intensity of the MoSERS device, the number of analytes for the flat thin-film sample and the number of analytes excited by the localized field enhancement of the MoSERS structure. The SERS intensity values are computed from the representative peaks at 1362 cm^{-1}, 1510 cm^{-1}, and 1650 cm^{-1}, with the exact values obtained from the integrated band areas at the given peak positions resulting in a linear range from 0.1- 200 μM with an R^2 value of 0.996 and a limit of detection of 0.1 μM (Figure 6-2j). The experimental SERS enhancement factor (EF) was found to be 0.8 x 10^5, yielding reasonable order of magnitude agreement with the theoretical estimate (see Figure S6-3 for more details).

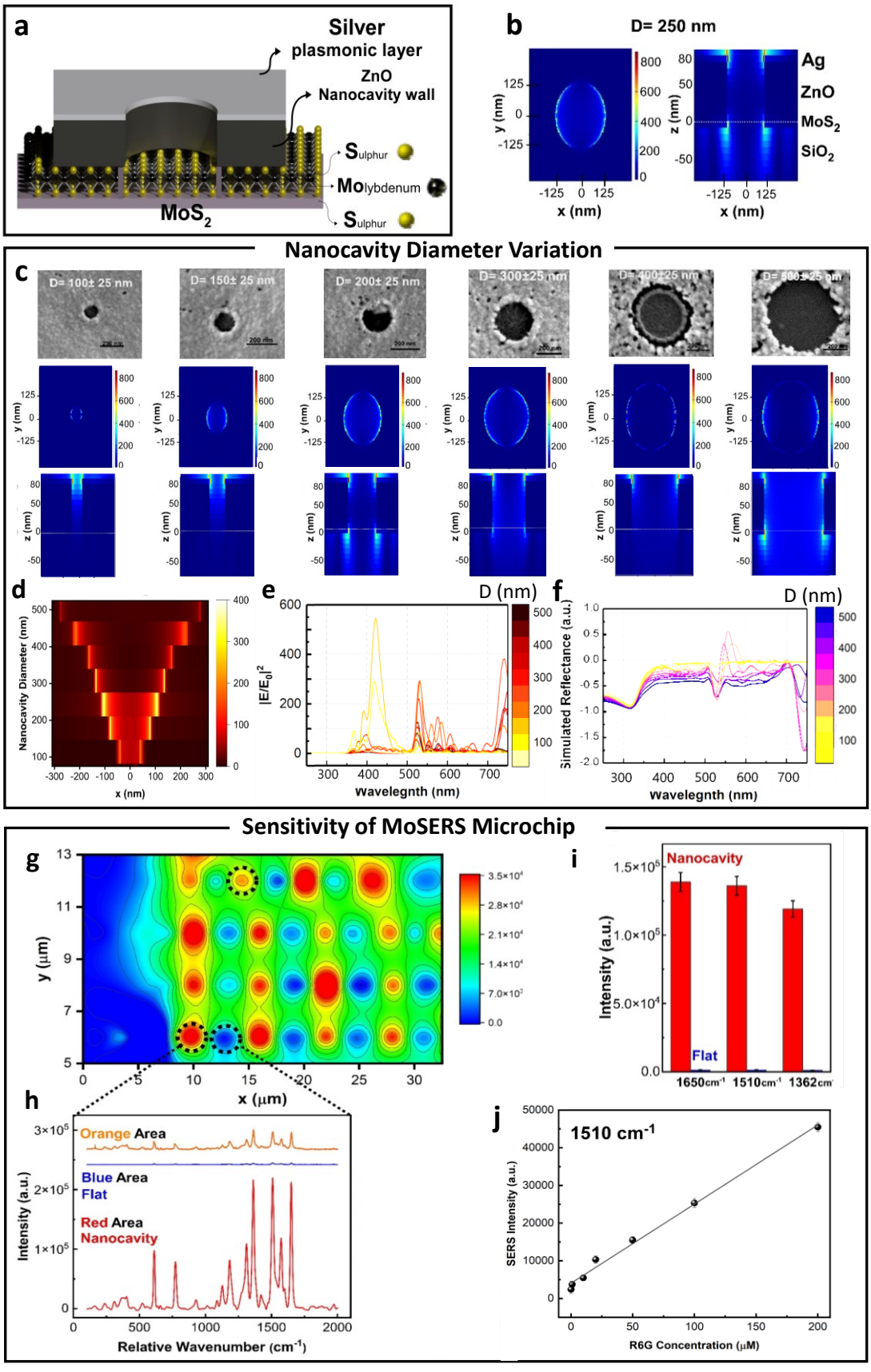
a
Silver
plasmonic layer
ZnO
Nanocavity wall
Sulphur
Molybdenum
Sulphur
MoS2
b
D= 250 nm
Ag
ZnO
MoS2
SiO2
y (nm)
z (nm)
x (nm)
Nanocavity Diameter Variation
c
D= 100± 25 nm
D= 150± 25 nm
D= 200± 25 nm
D= 300±25 nm
D= 400±25 nm
D= 500±25 nm
d
Nanocavity Diameter (nm)
x (nm)
e
D (nm)
|E/E0|2
Wavelegnth (nm)
f
D (nm)
Simulated Reflectance (a.u.)
Wavelegnth (nm)
Sensitivity of MoSERS Microchip
g
y (μm)
x (μm)
h
Orange Area
Blue Area
Flat
Red Area
Nanocavity
Intensity (a.u.)
Relative Wavenumber (cm-1)
i
Nanocavity
Flat
Intensity (a.u.)
1650cm-1
1510cm-1
1362cm-1
j
1510 cm-1
SERS Intensity (a.u.)
R6G Concentration (μM)

Figure 6-2. Benchmarking of SERS performance. (a) Schematic of MoSERS microchip fabrication and related SEM images of each step. (b) The electric field distribution in 250 nm diameter nanocavities simulated using a 532 nm TSFS light source. (c) The SEM image and correlated EM field distribution in the nanocavities with different diameters via a 532 nm TSFS light source. (d) The simulated EM-field distribution at the nanocavity edges as a function of nanocavity diameter. Simulated (e) EM-field enhancement and (f) reflectance spectra and the of plasmonic nanocavities with different diameters. (g) Spatial variation of SERS response over nanocavity array obtained from averaging the response from spectral peaks in the R6G spectra. (h) The corresponding SERS intensity of the representative areas (blue= flat, red= nanocavity). (i) The average SERS peak intensity at 1650 cm^{-1}, 1510 cm^{-1} and 1362 cm^{-1} obtained from R6G for MoSERS nanocavities (red) and the flat silver thin film (blue). (j) The sensitivity test of R6G on MoSERS substrate showed a linear range from 0.1-200 μM with R^2 value of 0.996.

6.2.2 Monolayer MoS2 and EVs interaction

The The SERS identification of single EV is closely related to the ability of trapping the EVs in the plasmonic nanocavities for the test time to enhance the subtle SERS signal from single EVs. The hydrophobic interactive behaviour of the MoS_2 layer with the EVs as a physical interaction can be one of the reasons for the absorption of EVs in the nanocavities. Theoretically, single crystalline monolayer MoS_2 demonstrates potential interaction with bilayer lipid materials.(R. Wu et al., 2018; Ye et al., 2021) Here we first used electron microscopy to visualize the physical connection between monolayer MoS_2 and phospholipid (Figure 6-3a-c) after sample preservation. The SEM image showing attachment of EVs to the 2H-phase monolayer MoS_2 demonstrated that

the majority of the EVs were attracted to the edges of the monolayer. A ratio of 10:1 EVs on average was found at the edges of the monolayer versus at the basal plane of the triangular single crystalline monolayer MoS_2. There are substantial atomic defects present at the edges of the monolayer MoS_2 that can actively interact with lipid bilayers. In addition, to ensure the edge sites expression in the nanocavities, a pre-treatment e-beam positive lithography on monolayer MoS_2 was used to introduce defect sites on the basal plane of the monolayer, which in turn promotes the adhesion of the EVs to the MoS_2 in the nanocavities (see Figure S6-4 for more details).

We used molecular dynamics (MD) simulation to probe the physical origin of the interactions between monolayer MoS_2 and phospholipid (Figure 6-3d-e), using a realistically constructed phospholipid bilayer incorporating previously reported components of the EV membrane (cholesterol (CHL), POPC, TSM, POPS and POPE). When a phospholipid bilayer gets close to a MoS_2 layer, the gradient of potential energy resulting from Van der Waals and Coulomb energies makes the phospholipid membrane interact with the MoS_2 layer. In parallel, understanding the origin of this interaction is essential to further study the inorganic entrapment sites for single EVs biomarkers. The MD simulation analysis confirms a higher attraction force between the phospholipid bilayer of EVs and the edge sites of the monolayer MoS_2 compared with the basal plane (Figure 6-3f). We started the simulation by positioning the MoS_2 layer parallel to the constructed phospholipid membrane and the membrane freely moves. The MoS_2 layer is freely flipping, and there is no considerable attraction force between the MoS_2 layer and the membrane before 100 ns when the monolayer rotates approximately 90 degrees, and the edge of the layer gets closer to the membrane. Once the phospholipid membrane and the monolayer MoS_2 start to interact with each other, the level of energy reaches a minimum level resulted by absorption of the layer inside the membrane. The simulations were carried out (using GROMACS software package) with

the design of phospholipid bilayer to integrate five different lipid components, while the force field parameters of MoS_2 were derived from a previous study.(Gu et al., 2019) PME method was applied to handle the long-range electrostatic interactions and the van der Waals (vdW) interactions were computed with a cut-off of 1.2 nm (see the materials and methods section for more details). To evaluate the free energy changes during the insertion process, we calculated the potential of mean force (PMF) along the direction perpendicular to the phospholipid bilayer surface. The PMF is able to evaluate the binding free energy, which was calculated according to the umbrella sampling simulations. During PMF calculations, the MoS_2 nanosheet (selected from the final conformation in the second simulation) was vertically pulled away from the membrane-forming various configurations (see Figure S6-5 for more details). Then, the perpendicular distance of the center of mass of MoS_2 nanosheet with its corresponding initial position was regulated at reference distances (d_0) via a harmonic force, $F = k \times (d - d_0)$, where k is the force constant (2000 kJ mol^{-1} nm^{-2}). Consistent with our previous findings, we demonstrated an attractive force between the monolayer MoS_2 and phospholipid bilayer (Figure 6-3g). When a phospholipid bilayer comes close to a MoS_2 layer, the gradient of potential energy resulting from van der Waals and Coulomb energies causes the phospholipid membrane to interact with the MoS_2 layer. The energies reach a minimum value of -3133.02 kJ mol^{-1} and -809.04 kJ mol^{-1} for van der Waals and Coulomb, respectively. A stable membrane comprising the five components listed above served to study the minimum energy level after absorption of a layer inside the membrane and the attraction forces of

the phospholipid bilayer interaction and MoS_2 (Figure 6-3h), while the overall contact number of each component of the phospholipid bilayer was also simulated.

Through the combination of theory and experiment, we demonstrated that the interaction forces corroborate the preference of MoS_2 edge sites to interact with EVs lipid bilayer which is essential for high-capacity entrapment of EVs.

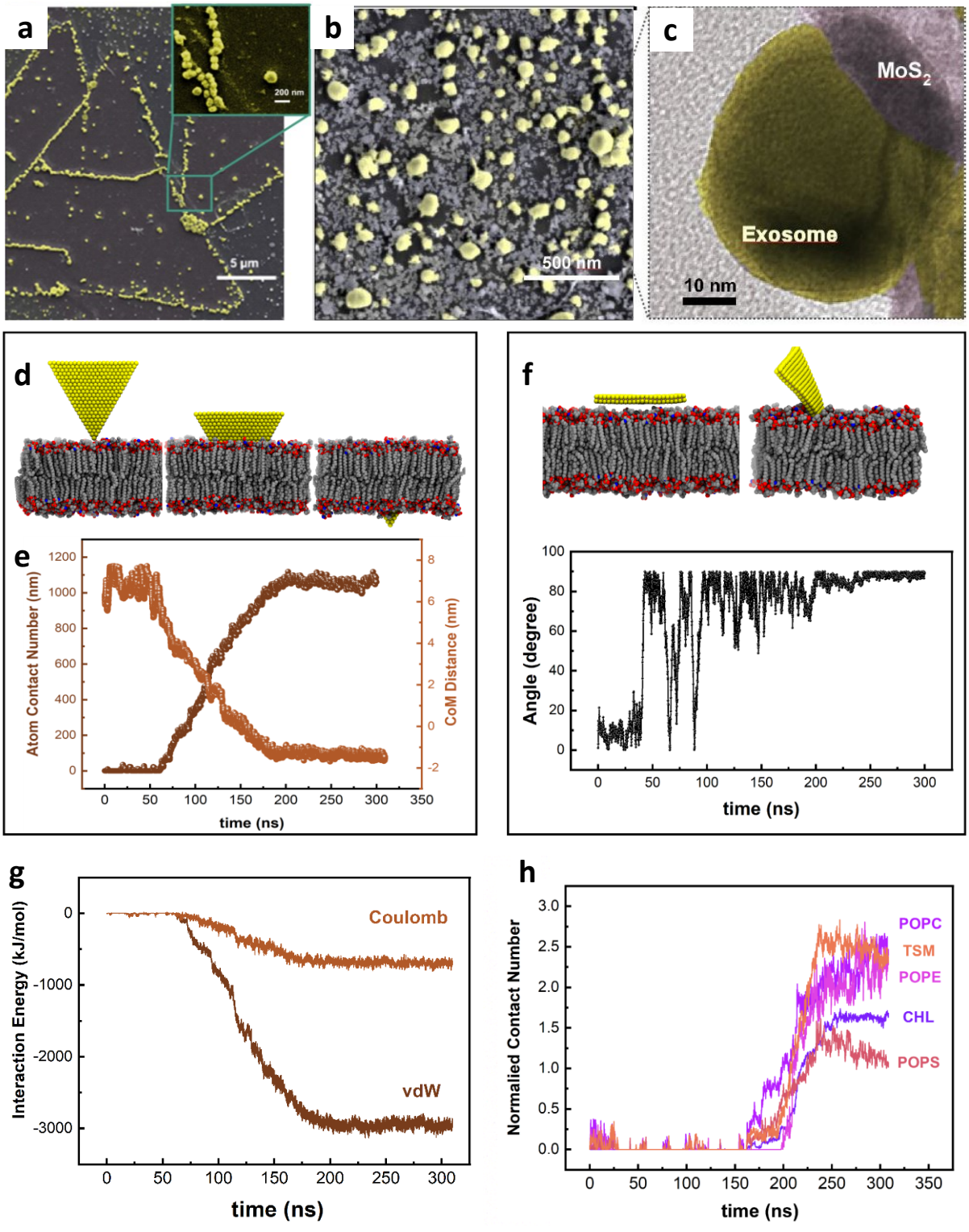

Figure 6-3. EVs Interaction of EVs with monolayer MoS_2 embedded in MoSERS microchip. (a) The SEM image of the EVs immobilized on a triangular single crystalline monolayer MoS_2

demonstrating the attraction of the nanocavity array. (b) High-resolution SEM image of the EVs. (c) High-resolution TEM image of co-existing monolayer MoS_2 and EV. (d) Representative simulated trajectory of the restrictive simulation (e) The atom contacts number and the centre of mass (COM) distance between the MoS_2 nanosheet and the lipid membrane. (f) Representative trajectories of the released simulation. Angle between the lipid bilayer and the MoS_2 basal. (g) The interaction energy between the MoS_2 nanosheet and the EV's bilayer lipid. (h) Normalized contact number of each component of the phospholipid bilayer.

6.2.3 EV Entrapment in Nanocavities

The EV-nanocavity interaction with EVs that drives the uniform array loading is critical to MoSERS performance. These rectangular arrays of nanocavities with variety of diameter size can be fabricated into arbitrary shapes (see Figure S6-6 for more details). The EVs are introduced into the array by direct pipetting of a 1-10 µl drop of EV-containing solution into the MoSERS fluidic device (Figure 6-4a). The EVs have a size range between 150-200 nm in diameter (as measured via NTA Figure S6-7). Fluorescent labelling is used (Dil) to study EV interaction with the MoS_2 monolayer and observe how this interaction affects EV loading in the nanocavity array.

Figure 6-4b-e compares nanocavities that contain monolayer MoS_2 (Figure 6-4b) to nanocavities without MoS_2 (Figure 6-4d). We find that the presence of the MoS_2 monolayer strongly enhances cavity loading, with the MoS_2 monolayer promoting complete cavity occupancy (Figure 4c,e). While the cavity loading appears to be uniform at the resolution of fluorescence microscopy, we used SEM imaging to gain a higher resolution picture of the EV-nanocavity interaction and confirmed that only one EV binds per well (Figure 6-4f,g).

One of the important challenges to address is the ability of confining the EVs within the nanocavities during the test time (Figure S6-6). The normalized fluorescent intensity of the EVs on different substrates has been investigated over time within the same field of view (Figure 6-4h). This comparison shows that fluorescent EVs fluoresce longer on MoSERS microchip, compared to single crystal monolayer MoS_2, nanocavities without MoS_2, and Silica, respectively. This shows the fluorescent intensity remains steadier on MoSERS microchip compared to the other substrates. The mapping of the normalized intensity from fluorophores attached to exosomes in a fixed microscope field of view confirms the longer lifetime of the fluorescent EVs on MoSERS nanochip and the hindrance in the bleaching of fluorophores over test time in the presence of MoS_2, which can be due to the non-linear absorption and large exciton binding energy(Splendiani et al., 2010) of the MoS_2. The normalized fluorescent intensity of the EVs entrapped in the nanocavities with and without MoS_2 in different diameter sizes (100 - 500 nm) were compared with the normalized fluorescent intensity of the EVs on SiO_2 (Figure 6-4i). The normalized fluorescent intensity for each substrate was obtained from over three tests and 10 different random fields of view of the microscope with a 200 pixels x 250 pixels size. The fluorescent intensity collected from nanocavities with MoS_2 (i.e. MoSERS nanocavities) was twice the intensity from the nanocavities without MoS_2, confirming the higher entrapment efficiency of EVs via MoSERS. The nanocavities with 200-250 nm in diameter, which is a better match with the mean size of the EVs to fit in the cavities, have slightly higher fluorescent intensity compared to the nanocavities with other diameters.

The ability to entrap and isolate single EVs in the MoSERS nanocavities suggests that our approach has potential to perform SERS on a single vesicle basis. To explore this possibility, we first obtained MoSERS spectra from synthetic liposomes. Liposomes are chemically uniform and

provide an estimate of the expected intrinsic variation of the single-vesicle SERS recordings. Next, we analyzed EVs produced by human glial cells (NHA, non-cancerous) and then investigated EVs produced by cultured human glioma cells (Figure 6-4j-m). All recordings were obtained by scanning a vesicle loaded MoSERS device cavity by cavity at 532 nm. For each raw SERS spectrum recorded, the spectrum baseline is subtracted, and the resulting spectrum is normalized and smoothed (Figure S6-8). The averaged processed spectra obtained from the EV populations (Figure 6-4j) indicate shared peaks associated with the characteristic Raman bands of bilayer lipids and common proteins in EVs. To characterize the variation of spectra obtained from single EVs, we performed a multivariate principal component analysis (PCA). PCA reveals principal component loadings with clearly separated clusters that quantitatively reflect the major differences in single EV spectra, effectively discriminating between EVs of the human non-cancer cells, glioma cells and liposomes (Figure 6-4k). The first principal component (PC1) and second principal component (PC2) shown in Figure 6-4l reveal the peaks enabling differentiation of the distinct vesicle populations. Each point in the plot represents one single EV spectrum with dimension reduction (Figure 6-4m). As expected, the chemically uniform single liposome recordings show the least scatter between single cavity recordings, the NHA recordings exhibit slightly greater scatter, and the EVs produced by the cultured glioma cells show considerably greater scatter, indicating the increased heterogeneity and molecular complexity of individual EVs.

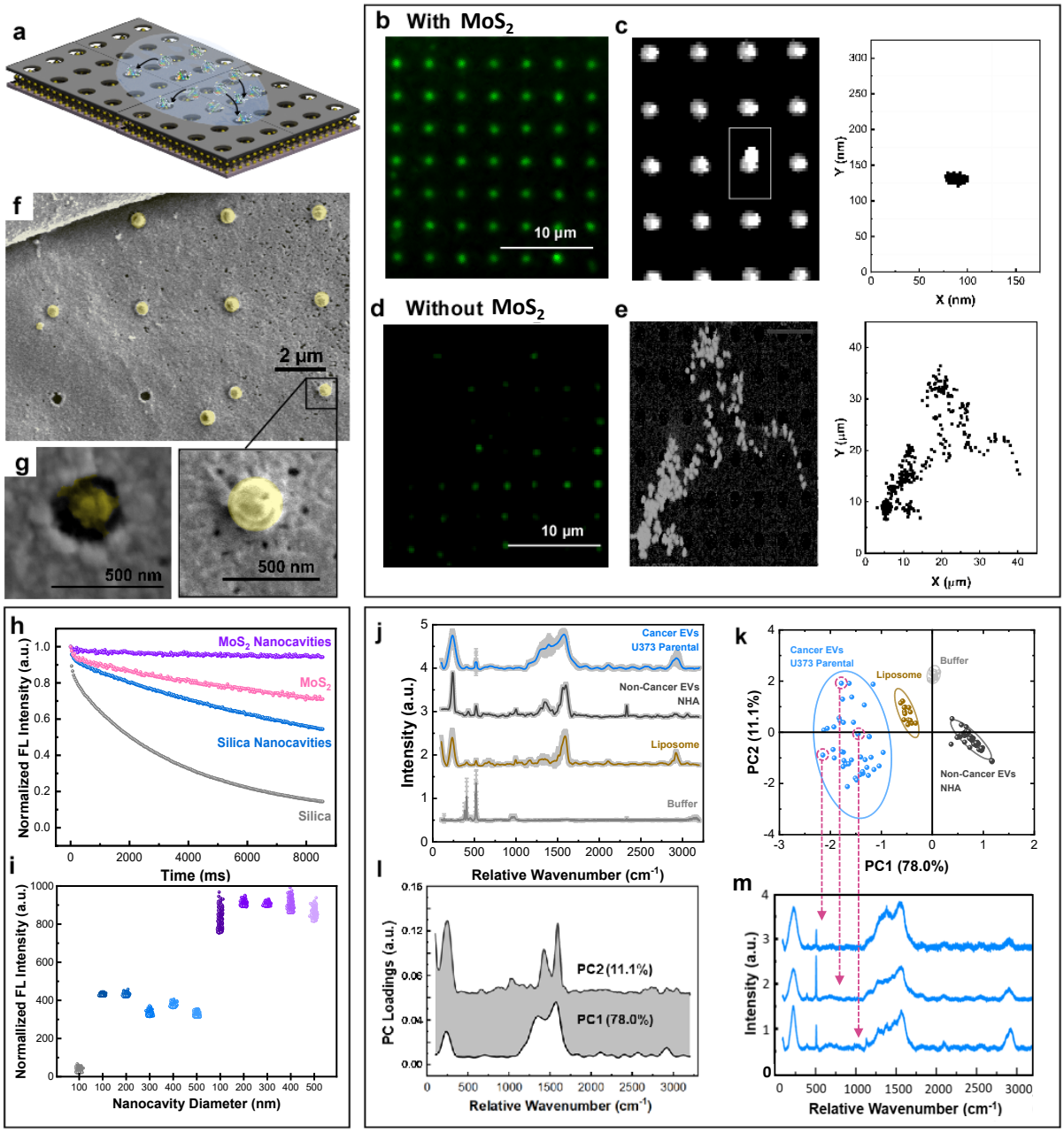

Figure 6-4. EVs entrapment in MoSERS nanocavities. (a) Schematic illustrating the EVs introduced to the MoSERS nanocavities and entrapment of the fluorescently labelled EVs in the nanocavities. Fluorescent micrograph of EVs loaded in cavities (b) with embedded monolayer MoS_2 and (d) without MoS_2. The correlated movement of a single EV through the incubation time in cavities (c) with embedded monolayer MoS_2 and (e) without MoS_2. (f) Low-magnification SEM

image of single EVs entrapped in the nanocavities. (g) High-magnification SEM image of a single cancer EV (U373) entrapped in a nanocavity. (Inset: the TEM image showing the co-existence of MoS_2 and a single EV.) (h) The comparison of fluorescent intensity of the EVs over time shows smallest bleaching slope for nanocavities on MoS_2, monolayer MoS_2, Nanocavities and Silica, respectively. (i) Comparison between the mean fluorescence intensity obtained from EVs on SiO_2, Nanocavities on SiO_2, and nanocavities on MoS_2 with different diameters. (j) The averaged SERS spectra from empty cavities (buffer), liposomes, EV populations derived from non-cancerous glial cells (NHA) and cultured glioma cells (U373). Each spectrum is obtained from averaging 50 EVs; the SD is indicated in grey. (k) PCA components (i.e. PCA score plot) for single EV recordings obtained with the MoSERS platform. (l) PC1 and PC2 loading Raman bands used to produce the PCA score plot shown in (k). (m) SERS spectra for single EVs released from heterogeneous U373 cancer cells.

6.2.4 Single EV Characterization with MoSERS Micro-Chip

The ability to entrap and isolate single EVs in the MoSERS nanocavities suggests that our approach has the potential to perform SERS on a single vesicle basis. To explore this possibility, we first obtained MoSERS spectra from cell lines as a comparison library (Figure 6-5a).

To determine if the MoSERS spectra are sensitive to the presence of mutations, we analyzed well-characterized EVs released from isogenic GBM cells with different patterns of oncogene expression.(Al-Nedawi et al., 2008; Garnier et al., 2018; Jalali, Isaac Hosseini, et al., 2021) In particular, we obtained EVs from glioma and glioma stem cell lines positive or negative for mutant oncogenic variants of EGFR, such as EGFRvIII, or loss of the PTEN tumour suppressor gene. We also examined glioma cells positive and negative for MGMT, a marker of resistance to TMZ. The averaged processed spectra obtained from the EV derived from parental and EGFRvIII expressing U87 cells (Figure 6-5b) indicate shared peaks associated with their characteristic Raman bands. EVs were obtained from either U87 and U373 parental (control) glioma cell lines or their variants engineered to express this EGFRvIII oncogene. This change led to profound phenotypic transformation and altered molecular composition of GBM EVs, including their content of EGFRvIII(Choi et al., 2018) (Figure S6-10-11). PCA applied to the multiplex cell variant set revealed principal component loadings with clearly separated clusters that recapitulate the fine spectral differences of the individual SERS spectra, effectively discriminating between EVs of the variant cell lines versus controls. While EGFRvIII is a part of the EV cargo, the oncogenic influence of this receptor reprograms molecular composition of cancer cells, impacting processes leading to EV formation(Al-Nedawi et al., 2008; Choi et al., 2018) and thereby can give rise to the observed large changes in SERS spectra.

MoSERS was also used to investigate the impact of EGFRvIII on EVs released by patient-derived glioma stem cell lines GSC83 and GSC1005 that naturally express oncogenic EGFRvIII (Figure 6-5c,d). We also studied the consequences of EGFRvIII knock-out (CRISPR/Cas9), and restoration of the naturally lost PTEN tumour suppressor gene in several glioma stem cells via PCA and established cell lines in all of which changes in the MoSERS signal of the respective EVs were detected as a function of cellular genotype. Thus, genes involved in oncogenic transformation may alter the process of formation and cargo loading of tumour EVs in a manner that can be sensitively detected by MoSERS.

Indeed, while EGFRvIII represents an informative molecular paradigm of processes that impact EVs in the course of GBM progression, other molecular changes may also be of interest, especially those that occur in the context of therapy and disease recurrence. In this regard, our earlier study revealed differential EV profiles in glioma stem cells rendered resistant to TMZ during experimental chemotherapy in vivo, including the expression of MGMT. To assess the representation of these changes in EVs by MoSERS, we interrogated this model system in several ways. The effects of MGMT methylation/expression on EV profiles were studied in a series of cell lines derived from GSC1123 glioma stem cells and their variants (Figure 6-5e). Also, in this case PCA profiles extracted from MoSERS data readily differentiated between EVs generated on the background of therapy susceptible and therapy resistant-cells (GSC1123 and GSC1123IC9R, respectively). However, in this case, the separation occurred with relatively lower efficiency relative to EGFRvIII, as expected for the lower scattering power from the EVs RNA content compared to the surface proteins.

Our results clearly demonstrate that MoSERS can identify EVs released by cells carrying mutant EGFRvIII. We next explored the sensitivity at which MoSERS based identification of

EGFRvIII carrying EVs can be performed. The SERS signal generated by relative SERS spectra of glioma derived EVs carrying EGFRvIII relative to EVs derived from parental culture carrying wildtype EGFR, often at low levels (see Figure S6-12 for details) shows an increased intensity at 1430 cm^{-1} and a decreased intensity at 1345 cm^{-1}. The ratio of the SERS intensity at 1430 cm^{-1} relative to 1345 cm^{-1} is therefore a good indicator of the amount of EGFRvIII relative to wildtype EGFR present in a given EV. The increase in this intensity ratio for EGFRvIII relative to wildtype EGFR likely correlates with the more pronounced expression of leucine/histidine over tyrosine in EGFRvIII carrying EVs. The intensity ratio for 1430 cm^{-1} /1345 cm^{-1} relative wavenumbers, averaged over all EVs measured at each EGFRvIII dilution, is linearly fitted with an R^2 value of 0.995, demonstrate a detection limit of 1.23% for EGFRvIII carrying EVs in the pool of wild type EGFR carrying EVs. This low detection limit of variants in the wild-type population suggests that MoSERS can potentially detect EVs carrying GBM related mutations that are diluted to low concentrations in the bloodstream. In order to assess the extent to which EGFRvIII impacts the cellular machinery involved in EV biogenesis, we evaluated the profiles of vesiculation-related genes in EGFRvIII-positive and -negative cells using polymerase chain reaction (PCR) assays, which revealed considerable differences (Figure 6-5f) (see Figure S6-9 for more details). It should be noted that the cell lines used in this study were fully characterized for their molecular profiles including proteomic analysis (see materials and method section for referral). This includes the subsequent western blotting validation of EVs as a correlative gold standard test, which revealed the EGFRvIII band in EVs population derived from U373vIII and U87vIII with phenotypic transformation and altered molecular composition, whereas this band disappears in EVs derived from GSC83 EGFRvIII-knocked-out glioma stem cells (Figure 6-5g). The clusters of EVs from each fully characterized cellular model including U87 and U373 systems, in PCA graphs

demonstrate their differentiation according to the spectral traits that could potentially be assigned to the anomalies connected to the corresponding molecular transition. The potential of existence of EGFRvIII molecular alteration compared to parental glioma U87 and U373 cells were distinguished from one another with the 95% confidence ellipses. This confidence ellipse defines the region that contains 95% of all samples that can be drawn from the underlying Gaussian distribution. Similarly, for each GSC cells it is possible to distinguish the potential existence of the traits of molecularly altered cells. However, a higher dimension analysis is required to take into account the spectral differences in all cells and classify them simultaneously according to the record of their similarity.

We turned to machine-learning methods to fully exploit the information in the MoSERS spectra for fine-grained discrimination of EVs representative of variant cell lines. The convolutional neural network (CNN) method has been applied to a limited number of spectral studies, but with considerable success,(Ho et al., 2019) while support-vector machine (SVM) was considered as a popular type of machine learning method based on a supervised classification algorithm.(Ho et al., 2019; Walter et al., 2011) We chose a CNN architecture for binary algorithm consisting of a first convolution layer, followed by a batch normalization, two residual layers and a final fully connected layer. The residual layers are composed of 3 blocks, each of two convolutional layers followed by a batch normalization and an activation function and contain a shortcut connection. The residual blocks connected to a shortcut connection boost solving the exploding/ vanishing gradient problems recurrent in deep networks. The convergence of training and validation values for loss and accuracy verify that the algorithm has been successfully trained (Figure 6-5h). Here, we collected 946 SERS fingerprint spectra from cell lines and divided into two datasets, i.e. the training dataset with 70% and the test dataset with 30% of SERS spectra from

each EV population. The average accuracy of the algorithm in correctly classifying single EV spectra into the corresponding cell types over 8 times repetitions demonstrated an overall accuracy of 89.3 % (Figure 6-5i). Further classifying the single EV spectra datasets into the parental and molecularly altered cell lines, demonstrated a relatively higher global accuracy towards EGFRvIII compared with MGMT- methylation, which is in correlation with the multivariate studies (Figure 6-5j). The ROC curve of classification of the single EV spectra according to the cell lines indicates the sensitivity of the algorithm in determining the true positive rate of the prediction over the selectivity of it based on the true negative rate (Figure 6-5k). The area under the cure demonstrates a 91% global accuracy in classifying the cell lines according to MoSERS single EV SERS approach.

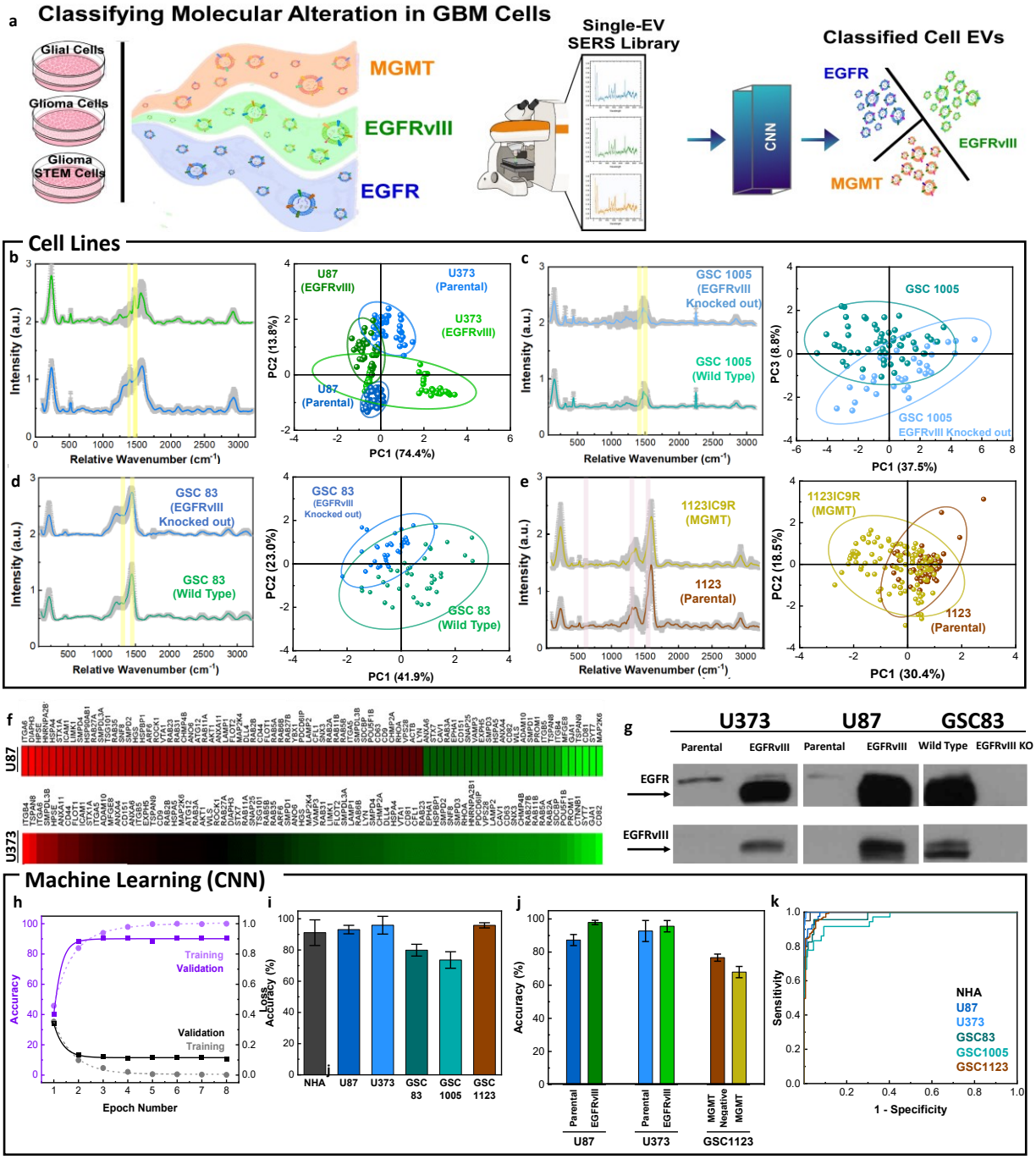

Figure 6-5. Single EV Characterization with MoSERS Microchip for classifying molecular alterations in GBM cell lines. (a) Schematic showing single EV-resolved SERS analysis of glial, glioma and glioma stem cell EVs with GBM derived molecular alterations and their classification using a CNN algorithm (training set 70%, test set 30%). (b) The mean SERS spectra of EVs

released from parental and oncogenic EGFRvIII expressing U87 cells. The PCA score plot of the SERS data comparing parental, and EGFRvIII expressed cancer (U87 and U373). (c) The mean SERS spectra and PCA score plot of EVs released from wild type GSC83 glioma stem cells that intrinsically contained EGFRvIII and EGFRvIII knock-out (CRISPR/Cas9) GSC83. (d) The mean SERS spectra and PCA score plot of EVs released from wild type GSC1005 glioma stem cells that intrinsically contained EGFRvIII and EGFRvIII knock-out (CRISPR/Cas9) GSC1005. (e) The mean SERS spectra and PCA score plot differentiating EVs from GSC1123 glioma stem cells with MGMT molecular alterations (GSC1123 Parental and GSC1123IC9R). (f) Quantitative PCR Study of EVs demonstrating gene expression levels in U87 EGFRvIII and U373 EGFRvIII EVs in a heat map. (g) The standard western blotting test, revealing the EGFRvIII phenotypic transformation in EVs population. Antibodies against total EGFR (both wild type and mutant - top lanes) or specific to EGFRvIII (bottom lanes) were used to visualise the presence of the respective signals in EVs. (h) Accuracy and loss versus epoch number for training and validation of the cell line classification. (i) The classification accuracy of the cell-lines based on single EV analysis using CNN algorithm and (j) the classification of the molecularly altered cell lines over 9 iterations. (k) The ROC curve of classification of the single EV spectra according to the cell lines with an area under the curve of 0.91.

6.2.5 Single-EV MoSERS Profiles in Biofluids Reflect Tumor Fingerprints in Patients

While experiments with molecularly defined cancer cells document the ability of MoSERS to detect distinct EV spectra, we asked whether this approach can be used for more complex biological samples containing EVs from multiple cellular sources, such as blood. Thus, MoSERS spectra were obtained from EVs isolated from blood samples drawn from 8 healthy individuals and 12 patients (Figure S6-13-14) clinically diagnosed with GBM (Figure 6-6a). We received

clinical annotation of 10 patients to correlate with the SERS study in the following section from a pathology study at the Montreal Neurological Institute and Hospital (MNI) (Table 6-2). Prior to start the SERS characterization, the isolated EVs were tested using PCR via EGFR cDNA amplification to correlate with the clinical data (Figure 6-6b). To analyze the single EV spectra, the residual neural network (Resnet)-based CNN algorithm (Table S6-3) was used, as a proof-of-concept to classify their possible cellular sources and infer molecular hallmarks of the underlying disease. (Ho et al., 2019) To this end the CNN algorithm was trained with the spectra from healthy and cancerous cell lines, as well as unseen (blinded) spectra set of 2 healthy and 2 patient samples, followed by testing the MoSERS spectra in the remaining samples. The probability that sampled EVs carry one of the three molecular GBM-associated alterations (EGFR amplification, EGFRvIII, and MGMT methylation) were determined based on a Mahalanobis distance. A total of 70 EVs were measured for each blood sample. The probability score for each individual sample shows a higher similarity between the test EVs from patient samples and cancerous variants compared to the ones derived from healthy individuals (Figure 6-6c). The convergence of training and validation values for loss and accuracy verifies that the algorithm has been successfully trained. We used ROC curve to assess the overall true positive rate versus false negative rate of the MoSERS-based single EV prediction of underlying molecular traits, which resulted in an overall area under the curve (AUC) of 85% (Figure 6-6d).

To achieve the correlation of these results with clinical annotations, we compared the probability scores of positive-variant patients with negative-variant patients and healthy subjects (Figure 6-6e-g). We assessed the healthy control, negative-variant patient group and individual positive-variant patients using one-way analysis of variance (ANOVA) with post hoc Tukey's test (Figure 6-6h-j). ANOVA detected an overall significant difference among the majority of the positive-variant individuals ($P < 0.001$) compared to the negative-variant pool.

The samples were grouped as healthy subjects, GBM patients negative for genetic variant and GBM patients positive for genetic variant. Positive variant patients demonstrate a relatively higher probability of having the variant gene compared to negative variant patients and samples from healthy donors (Figure 6-6k). The ROC curve for the individual patients based on the accumulative probabilities of the single EVs carrying one of the three molecular GBM-associated alterations demonstrates an overall area under the curve (AUC) of 91% (Figure 6-6l).

Table 6-2. Clinical annotations corresponding to patient mutation status. Plasma was obtained from 12 patients, clinically diagnosed with GBM. MoSERS was performed on 10 μL of purified EVs from plasma. *ND = not determined. EGFR amplification, EGFRvIII and MGMT methylation status was determined by sequencing of the primary tumour.

Patient	Status	EGFR amplification	EGFR vIII	MGMT methylation
P-1	Glioblastoma	Negative	Negative	Positive
P-2	Glioblastoma	Negative	ND	Negative
P-3	Glioblastoma	ND	ND	ND
P-4	Glioblastoma	Positive	Positive	Positive
P-5	Glioblastoma	Negative	ND	Negative
P-6	Glioblastoma	Negative	Negative	Negative
P-7	Glioblastoma	Positive	Positive	Negative
P-8	Glioblastoma	Positive	Negative	Negative
P-9	Glioblastoma	Positive	Positive	Negative
P-10	Glioblastoma	Negative	ND	Negative
P-11	Glioblastoma	ND	ND	ND
P-12	Glioblastoma	ND	ND	ND
H-1	Healthy	-	-	-
H-2	Healthy	-	-	-
H-3	Healthy	-	-	-
H-4	Healthy	-	-	-
H-5	Healthy	-	-	-
H-6	Healthy	-	-	-
H-7	Healthy	-	-	-
H-8	Healthy	-	-	-

.

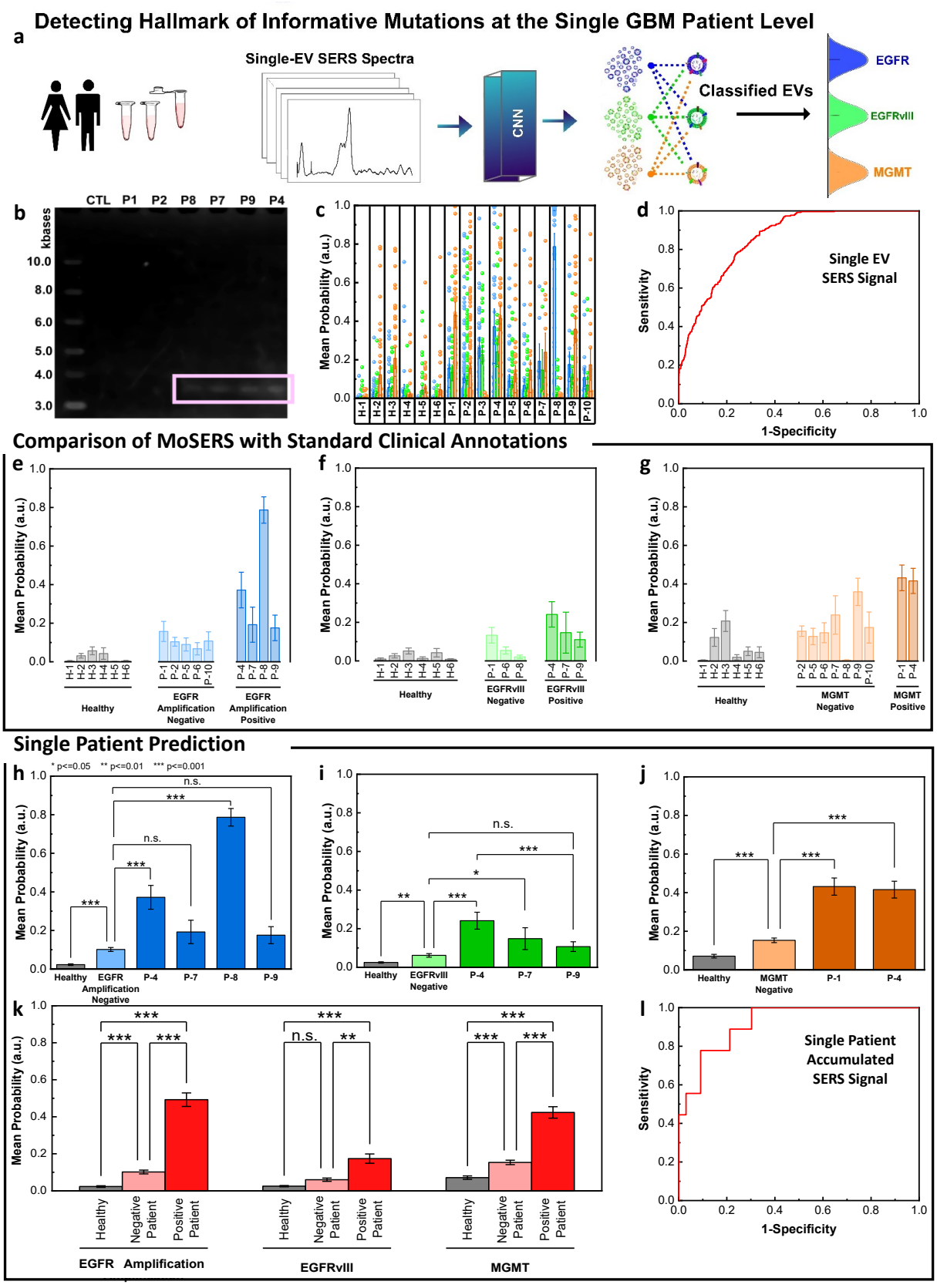
Detecting Hallmark of Informative Mutations at the Single GBM Patient Level
a
Single-EV SERS Spectra
CNN
Classified EVs
EGFR
EGFRvIII
MGMT
b
CTL P1 P2 P8 P7 P9 P4
kbases
10.0
8.0
6.0
5.0
4.0
3.0
c
Mean Probability (a.u.)
H-1 H-2 H-3 H-4 H-5 H-6 P-1 P-2 P-3 P-4 P-5 P-6 P-7 P-8 P-9 P-10
d
Sensitivity
1-Specificity
Single EV
SERS Signal
Comparison of MoSERS with Standard Clinical Annotations
e
Healthy
EGFR Amplification Negative
EGFR Amplification Positive
f
Healthy
EGFRvIII Negative
EGFRvIII Positive
g
Healthy
MGMT Negative
MGMT Positive
Single Patient Prediction
h
* p<=0.05 ** p<=0.01 *** p<=0.001
n.s.
Healthy
EGFR Amplification Negative
P-4
P-7
P-8
P-9
i
Healthy
EGFRvIII Negative
P-4
P-7
P-9
j
Healthy
MGMT Negative
P-1
P-4
k
Healthy
Negative Patient
Positive Patient
EGFR Amplification
EGFRvIII
MGMT
l
Single Patient
Accumulated
SERS Signal
Sensitivity
1-Specificity

Figure 6-6. MoSERS profiles of blood-borne EVs from GBM patients harbouring distinct molecular alterations. (a) Schematic illustrating the classification of patient derived EVs using MoSERS single EV fingerprints analyzed by machine learning. Each class represents a different GBM marker. (b) RT-PCR Agarose Gel of EGFR and EGFRvIII cDNA in control and patient derived circulating EV samples. (c) The probability distribution of belonging to each of the classes based on CNN output, EGFR amplification (blue), EGFRvIII (green) and MGMT methylation (orange). (d) The ROC curve of assessing the single EV spectra prediction accuracy over clinical annotation demonstrates an overall AUC of 0.85. The probability that EVs are positive for (e) EGFR amplification, (f) EGFRvIII and (g) MGMT partitioned into classes based on clinical read-out: healthy (grey), negative-variant patients (light color), and individual positive-variant patients (dark color). (h-j) ANOVA analysis of all spectra partitioned based on clinical annotations, demonstrating the ability to distinguish samples from negative and positive variant patients as well as healthy patients. (k) Samples with positive variants of EGFR amplification, EGFRvIII and MGMT methylation were pooled and classified by the probability distribution of each sample. (l) The ROC curve of assessing the overall MoSERS prediction accuracy of individual patients carrying one of the three molecular GBM-associated alterations over clinical annotation demonstrates an overall AUC of 0.91.

6.2.6 Performing Tumour Diagnosis via Blood Derived EVs:

One One area where binary determination of patient subsets through EC-based liquid biopsy would be at the time of recurrence where predicting efficacy or failure of adjuvant treatment could have actionable consequences. To further explore this avenue, we developed a binary benchmark to predict the overall health status (with respect to GBM) of an individual from our

single EV spectra classifications, e.g. to determine whether the spectrum analyzed belongs overall to a "GBM-positive" or "GBM-negative" state (Figure 6-7a). In this case, the prediction of whether an EV belongs to a certain cell line is not sufficient because patient samples might contain EVs from other cells in the body.

We used the CNN binary algorithm to classify the EVs into two classes which rendered higher accuracy of 83% compared with SVM binary algorithm (Figure S6-15). The training dataset (Table S6-3) was comprised of 80% of the single-EV spectral acquisitions from healthy donors and from the supernatant of non-cancerous cells, designated as GBM-negative class (grey). Similarly, this set contained 80% of the single-EV spectral acquisitions of 3 GBM patient donors and the EVs isolated from the supernatant of glioma cells, collectively designated as GBM-positive class (red). The EVs from the rest of the healthy (n_H^{test}=8) and patient (n_P^{test}=12) blood donors were used to determine the accuracy of binary classification into the healthy and patient groups. To avoid overfitting of our pattern-learning algorithm to the data, we validated the training process using a validation set (10% of the training set).

The distribution of the probability of belonging to each binary class generated was based on a total of 70 measurements collected from each blood sample (Figure 6-7b). We used Platt scaling to calculate the probability of each dataset belonging to each class.(Platt & others, 1999) The similarity score for each individual sample based on the Mahalanobis distance shows a higher similarity between the test EVs from patient samples and cancerous cellular variants compared to the ones derived from the healthy individuals. The distribution of calculated probabilities associated with each class (i.e. GBM negative and GBM positive) shows that the single EV spectra from healthy samples have a higher probability of belonging to the GBM negative class, while the single EV spectra from patient samples tend to be classified into the GBM positive class (Figure

6-7c). The *post hoc* comparisons via Tukey's honest significant difference demonstrated P-value below 0.001 for the probability of the single EV spectra correctly classified into healthy and patient classes.

To verify the proficiency of the algorithm competence in training, the loss and accuracy of the training and validation sets (Figure 6-7d) were studied, demonstrating the convergence of the training datasets after 11 epochs. At this point, the outputs from the fully connected layer of the training and test data were separated into two classes as the number of epochs increased (Figure S6-16). The convergence of training and validation values for loss and accuracy verifies that the algorithm is successfully being trained. The ROC curve demonstrates the true positive rate as a function of the false positive rate (Figure 6-7e), to assess the overall dexterity of the true positive rate versus false negative rate of the MoSERS prediction over clinical annotation resulted in an overall AUC of 89%.

The outputs of the CNN also enable us to determine an average relative similarity for each patient spectrum based on Mahalanobis distance to differentiate healthy and GBM-positive samples. The average relative similarity plot of the ensemble output of the EVs from each blood sample (Figure 6-7f) indicates successful discrimination of the healthy samples with lower similarity scores (GBM-negative class) and the patient samples with higher similarity scores (GBM-positive class). The average similarity value for each sample was calculated by taking in over 1200 single EV SERS spectra. High similarity means high risk of cancer, while low similarity means low risk of cancer. We benchmarked a cut-off average similarity value for binary classification of the dataset into healthy and patient categories. GBM-negative class was used as the threshold to predict a measure for the possibility of diagnosis with cancer. According to this designation, all healthy samples belonged to GBM-negative class rather than the GBM-positive

class. The *post hoc* comparisons demonstrated P-value below 0.001 for the average similarity of the healthy and patient samples being correctly classified based on the ensembled single EV spectra (Figure 6-7g).

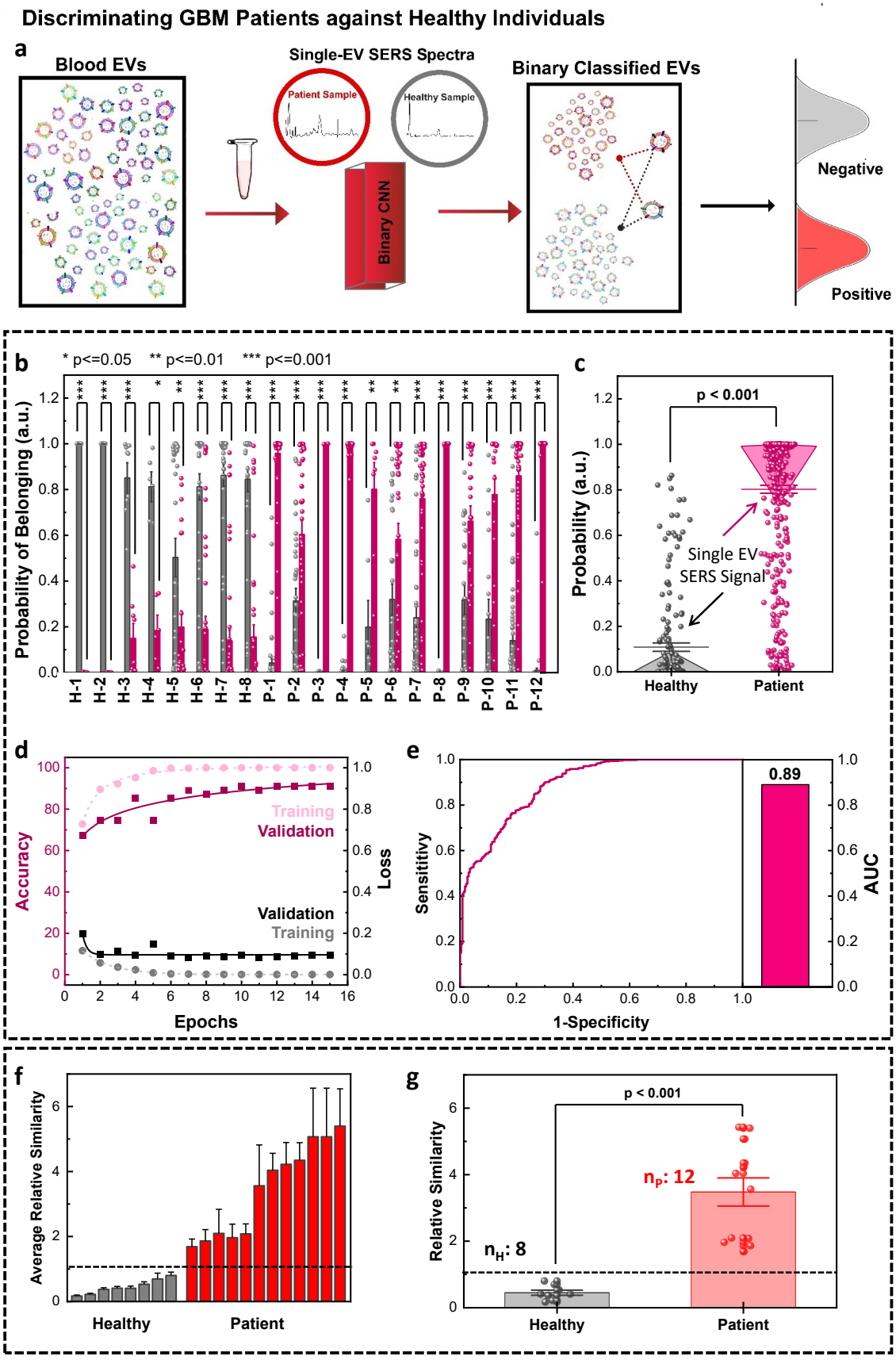
Discriminating GBM Patients against Healthy Individuals
a
Blood EVs
Single-EV SERS Spectra
Patient Sample
Healthy Sample
Binary CNN
Binary Classified EVs
Negative
Positive
b
* p<=0.05 ** p<=0.01 *** p<=0.001
Probability of Belonging (a.u.)
H-1 H-2 H-3 H-4 H-5 H-6 H-7 H-8 P-1 P-2 P-3 P-4 P-5 P-6 P-7 P-8 P-9 P-10 P-11 P-12
c
p < 0.001
Probability (a.u.)
Single EV SERS Signal
Healthy
Patient
d
Accuracy
Loss
Training
Validation
Validation
Training
Epochs
e
Sensitivity
1-Specificity
0.89
AUC
f
Average Relative Similarity
Healthy
Patient
g
p < 0.001
Relative Similarity
n_P: 12
n_H: 8
Healthy
Patient

Figure 6-7. MoSERS-based separation of EV signals from blood samples of healthy subjects and glioblastoma patients. (a) Schematic showing single EV SERS analysis and binary classification of blood EVs into healthy and GBM patient groups using CNN algorithm trained with a library of cell lines and blood samples. (b) The distribution of the probabilities of the single EV spectra from GBM-negative and GBM-positive samples associated with their belonging to healthy and patient classes. (c) The one-way ANOVA comparison analysis of mean probabilities associated with the single EV spectra. (d) The loss and accuracy of the training and validation sets based on the CNN algorithm. (e) The ROC curve of the CNN prediction of probabilities of single EV spectra to belong to the right class resulted in an overall AUC of 0.89. Binary classification of blood sample EVs into patient and healthy classes based on the average similarity scores. (f) The average similarity of blood samples based on CNN prediction results of single EV spectra, differentiating the data sets into healthy and patient classes with a deterministic cut-off value. (g) Binary classification of blood samples into healthy and patient classes based on the average similarity scores via one-way ANOVA comparison.

6.3 Conclusion

EVs encapsulate multiple molecular signals reflective of the phenotype of their originating tumor cells. The MoSERS microchip successfully revealed the molecular diversity of GBM cells by converting them into highly granular, actionable physical fingerprints, combining the complexities of individual EVs and their heterogeneous subpopulations. Current EV-based diagnostic approaches average the signals contained in multiple EVs, thereby obscuring the important subtleties of the EV landscape. Here, we were able to observe changes parallel to the expression of MGMT and EGFR VIII, molecular paradigms for therapeutic resistance and

aggressiveness in GBM, at the level of individual cell lines and patients. Indeed, the convolutional neural network (CNN) algorithm demonstrated the potential of MoSERS analysis of circulating EVs to determine the MGMT status in GBM patients - an observation that merits validation in a larger clinical cohort. Thus, MoSERS technology may be applicable as a versatile tool for liquid-biopsy diagnostics to track the evolving landscape of GBM in individual patients while providing clinically actionable information.

The *first* key feature of the MoSERS system is the patented MoSERS microchip platform confined in microfluidics that overcomes key challenges required to perform SERS with single EV resolution. Our optimized photonic design leads to high in-cavity electric field enhancement and can thereby provide sufficient signal to obtain meaningful single EV spectra. The EVs are loaded in the nanocavities at high efficiency due to attractive interactions with the embedded MoS_2 layer. Finally, as only one EV can occupy a given cavity, a single EV can be isolated in a single laser focus. When light is concentrated into subdiffraction volume of a single nanocavity with patterned monolayer MoS_2 at the bottom, the electric field in the small volume becomes very intense, leading to enhancement in the local density of the states in the nearby molecules and the formation of hot spots which in turn enhances the incident field intensity. Therefore, the hot spot improves the efficiency of the optical excitation process when placing a single EV in the nanocavity. In addition, when an EV approaches a MoS_2 layer, it forms a strong electrostatic interaction comprised of van der Waals and Coulomb forces. MoS_2 forms the Coulomb interactions primarily through contact with the polar head regions of lipid molecules, while the van der Waals interactions mainly arise from contact with the hydrophobic tail regions of lipid chains. As proof-of-principle, we show that MoSERS enhanced by machine learning based prediction can discriminate EVs from healthy and cancer cells in GBM cell-lines, detect EVs released by GBM

variant cell-lines and differentiate EVs carrying GBM genetic variants in patient blood samples. The label-free single EV SERS technique functions on the basis of strong EM-field enhancement that is highly dependent on the physical distance between the biomolecule of interest and the nanocavities. We studied this effect for the impact of the oncogenic transformation involving surface proteins, since those are often better characterised and more relevant for the application, as well as often present on the outer surface of tumor-derived EVs.

The *second* feature of the MoSERS system is the integrated microfluidic sample delivery system that allows for real-time monitoring blood circulating EVs. In cancer, diagnostic procedures based on minimally invasive blood sampling are highly attractive. Currently GBM diagnostics follows clinical, imaging and operative biopsy steps. These protocols are time consuming and fraught with risks of surgical complications. Even if molecular diagnosis is carried out, it only offers a single snapshot of otherwise dynamic disease, with little opportunity to explore alternative management. In contrast, a blood test is rapid, safe and can be performed multiple times over a disease time course to assess impact of a given prescribed treatment, including distinction between disease subtypes, therapeutic vulnerabilities, and molecular evolution. The main challenge in using blood as the source of EVs is the considerably lower concentration of the tumor-derived EVs amidst other EV sources (platelets, blood cells).[6] We demonstrate a detection limit of 1.23% for EVs from variant cells suspended in a wild-type EV population. This allows for processing blood samples where the GBM biomarkers are diluted to 3-10%. In addition, our analysis of plasma EVs captures global differences in the EV populations in blood of GBM patients and healthy counterparts, which may include alterations in EVs in non-cancerous cellular populations (e.g. due to horizontal transfer of EVs from cancer cells or other influences).

Determining dynamics and nature of a particular tumour with minimal invasiveness is equally important. Currently, healthcare providers rely on traditional characteristics, such as tumour appearance, to diagnose a given tumor subtype and determine optimum treatment, with relatively few molecular markers in use (IDH1 mutations, MGMT). For patients diagnosed with GBM, however, if more complex underlying molecular characteristics of the tumour could be defined, it may be possible to explore more personalized care and evaluate treatment approaches in a more controlled manner. To this end, our MoSERS approach has potential to classify different molecular tumor subtypes on the basis of spectroscopic fingerprints drawn from single EVs as a form of liquid biopsy. In addition to that, single EV SERS approach allows to statistically investigate the tumour heterogeneity and monitor complex tumor cell alterations for the post-surgery treatment.

The main limitation of the current MoSERS platform is the time required for data acquisition. A large number of single EV SERS spectra are required to identify the fingerprint spectra for the classification algorithm. Considering the heterogeneity of EVs and preferential enhancement of the Raman modes corresponding to molecular vibrations perpendicular to the SERS surface, at least 50-100 single EV SERS spectra is necessary for a conclusive result. Indeed, over one hour is presently needed to generate 100 data points for each sample. With testing samples in parallel using multiple devices, it is possible to reduce the time to less than 30 minutes per sample. To this end, within 90 minutes and using up to 10-100 μl of purified blood serum, it is possible to generate comprehensive landscape of EVs at a single EV resolution. In the context of a disease as complex and dynamic as GBM this minimally invasive technology may have considerable diagnostic potential.

6.4 Acknowledgment

The authors thank the Faculty of Engineering at McGill University, the Canadian Cancer Society (255878 CCSRI), Natural Science and Engineering Research Council of Canada (NSERC, G247765), New Frontiers in Research Fund (250326), and Canada Foundation for Innovation (CFI, G248924), for financial support. JR was supported by Foundation Grant from the Canadian Institutes of Health Research (CIHR), Cancer Research Society (CRS) and Genome Quebec (GQ) Operating Grant, McGill Interdisciplinary Initiative in Infection and Immunity (MI4) seed grant, Canadian Foundation for Innovation (CFI), NET program sponsored by Fondation Charles Bruneau (FCB), and Jack Cole Chair in Pediatric Hematology/Oncology. RZ was supported by the National Key Research and Development Program of China (2021YFA1201201 and 2021YFF1200404), the National Natural Science Foundation of China (U1967217), National Independent Innovation Demonstration Zone Shanghai Zhangjiang Major Projects (ZJZX2020014), the Starry Night Science Fund at Shanghai Institute for Advanced Study of Zhejiang University (SN-ZJU-SIAS-003/006/009), and BirenTech Research (BR-ZJU-SIAS-001). The authors acknowledge Nanotools-Microfab and the Facility for Electron Microscopy Research at McGill University, the Laboratoire de microfabrication (LMF) at Polytechnique, Montreal, and the research facilities of NanoQAM at the Université du Québec à Montréal. MJ appreciates McGill Engineering Award (MEDA) and Fonds du Recherche du Quebec (FRQnet) scholarships. CDRM and IH thank MEDA scholarship.

6.5 Authors Contributions

M.J. initiated the idea, design, and fabrication protocols, performed the physical characterizations, sample preparation, SERS data collection, FDTD modelling, data processing and analysis as well as writing the manuscript. C.D.R.M. contributed to the SERS data collection, running machine learning algorithm and writing the manuscript. O.J. contributed with the machine learning algorithms and data analysis. L.M. and N.T. contributed in EVs sample preparation, purification, and running the standard tests. I.I.H. contributed to the fabrication of the fluidic device and theoretical studies with MD. Z.G. and Z.H. contributed to the MD simulations and data collection. C.S. contributed to providing CAS-9 gene altered glioma stem cell lines. Y.L. contributed to the SERS experiments. K.P. provided patient samples and clinical annotations. M.C.G contributed to patient samples phenotyping and pathological tests. R.Z. provided the design and analyses on the theoretical studies with MD. S.W.H. provided advice on SERS optimization and functionality of the platform. W.R. provided advice on single EVs confinement and contributed to writing of the manuscript. J.R. provided the EV samples from GBM cell lines for the entire project, advice on the EV's biological and contributed to the writing of the manuscript. S.M. supervised the project from the idea to development, contributed to the design of the figure sets and writing of the manuscript.

6.6 Materials and Methods

6.6.1 Fabrication:

A combined bottom-up and top-down approach was used to develop the single exosome analyzer nanoelectrodes. First, chemical vapor deposition (CVD) technique was used to grow single-crystalline monolayer MoS_2.(Jalali, Gao, et al., 2021) The monolayer was produced through CVD

method by nucleation and growth from vapour phase solidified on the substrate of choice. Second, ebeam lithography (Reith) was used to pattern the nanohole array in a 300 nm thick layer of negative photoresist (MaN-2300). Third, an 80 nm biocompatible ZnO layer and a 10-100 nm Ag layer were deposited (via BJD 1600) as back-reflector and plasmonic layer, respectively. Fourth, the plasmonic nanohole array was formed via lift-off. The CMOS-compatible platform enables integration with any existing type of microfluidic devices.

6.6.2 Characterization:

The SEM was performed using the FEI Quanta 450 environmental scanning, the AFM with a Bruker, MultiMode8 equipment, while the TEM with a FEI Tecnai G2 F20 200 kV Cryo-STEM. The optical characterizations were performed via a Lambda750 NIR-UV-Visible equipment and a NanoSpec reflection spectro-microscopy. EVs samples were prepared for SEM in three steps: (1) The purified EVs in PBS solution (100 μL, 1 mM) were introduced to the recognition substrate for 2 min followed by incubation with glutaraldehyde 3% in sodium cacodylate (0.1 mM) overnight. (3) Dehydration of EVs was performed by immersion in ethyl alcohol (30–100%) to exchange their cytoplasm with alcohol (10 min immersion in each). Then, a critical point dryer (Leica Microsystems EM CPD030) was employed to substitute alcohol content with dry CO_2 with minimum damage to the EVs morphology.

6.6.3 Finite Difference Time-Domain (FDTD) Simulation

The electric-field distribution over the nanocavity array was modeled using the finite difference time domain (FDTD) module (v8.21.1781, Lumerical Solutions, Inc.). The electric field distribution was simulated under the laser excitation wavelength of 532 nm using a plane wave and a total field scattered field (TFSF) light source that resembled the laser.

6.6.4 Molecular Dynamic (MD) Simulation

The MoS_2 nanosheet was modeled as a triangle with each side length of about 7.0 nm. The bilayer membrane was constructed based on a realistic EV lipid with a dimension of 10.7×10.7 nm^2. Five different lipid components (including cholesterol, POPC, TSM, POPS and POPE) were considered in the bilayer membrane while ignoring the components with a ratio lower than 5%, and finally yielding their numbers of 276, 96, 102, 72 and 36. This membrane was firstly performed a 300-ns simulation to obtain a stable membrane bilayer structure. Then this stable membrane was utilized to explore its interaction with the MoS_2 nanosheet. Two simulation setups were built. In the first simulation, the MoS_2 was perpendicularly placed on the membrane with its corner pointing to the membrane surface. During this simulation, the movement of MoS_2 along the directions parallel to the membrane surface was fixed whereas the movement along the direction vertical to the membrane surface was free. In the second simulation, the MoS_2 was initially placed on the membrane with its basal plane parallel to and touching the membrane surface. During this simulation, all atoms were free for movement. Both of these two systems were dissolved in a 0.15 M NaCl solution, which was separately conducted for 300 ns trajectory.

6.6.5 Processing EVs

(i) EVs Isolation of EVs from cell cultures

EVs were purified from the growth media of cancer cells using optimized protocol(Choi, Montermini, et al., 2019). Briefly, the conditioned medium (CM) was collected from cells grown for 72 h in culture media containing 10% EV-depleted FBS (generated by centrifugation at 150,000g for 18 h at 4ºC). CM was centrifuged one time at 400xg and then passed through 0.2 μm pore-size filter. The resulting CM filtrate was concentrated to 500ul using Amicon Ultra-15 Centrifugal Filter Unit (EMD Millipore, Billerica, MA) with 100,000 NMWL molecular cut-off.

The concentrated media was further purified using qEV single SEC column (Izon Science, UK); 500 µL of the sample was loaded, and 4 fractions of 500 µL of eluent were collected after 2.5 mL of the initial eluent. The concentration and size distribution of EVs in the purified media was obtained using the nanoparticle tracking analysis, NanoSight NS500 instrument (NanoSight Ltd., UK). Three recordings of 30 s at 37ºC were obtained and processed using NTA software (version 3.0).

(ii) EV Isolation from Cerebrospinal Fluid

The patient cerebrispinal fluid (CSF) samples were filtered through 0.2 µm pore-size filters. The filtered samples were further purified using qEV single SEC column (Izon Science, UK); 500 µL of each sample was loaded, and 4 fractions of 500 µL of eluent were collected after 2.5 mL of the initial eluent.

(iii) EV Isolation from Patient Blood Samples

The patient blood samples were centrifuged one time at 200xg for 20 minutes and then the supernatants were centrifuged at 1000xg for 15 minutes. The resulting liquid phase was further centrifuged at 1500xg for 20 minutes to remove platelets and achieve platelet-poor plasma (PPP) which was passed through 0.2 µm pore-size filter. The EVs contained in filtered PPP samples were further purified using qEV single SEC column (Izon Science, UK); 500 µL of the sample was loaded, and 4 fractions of 500 µL of eluent were collected after 2.5 mL of the initial eluent.

(iv) Labeling EVs

A fluorescent lipid binding dye, DiI, was used to label the EV producing cells (indirect labelling of EVs). A total of $3x10^6$ cells were labelled with 5 ml of DiI (Invitrogen) in 2ml of DMEM without FBS for 20 minutes at 37C. The cells were washed twice with DMEM without FBS, resuspended

in 30 ml of DMEM containing 10% EV-depleted FBS (generated by centrifugation for 18hrs at 150,000x*g*) and cultured for 72hrs at 37ºC, 5% CO_2 to generate CM for EV isolation.

6.6.6 Raman Spectroscopy:

(i) Spectra Collection

Surface-enhanced Raman spectroscopy (SERS) and mapping SERS spectra were collected in back scattering geometry, using an InVia Raman microscope (Renishaw plc, Wotton-under-Edge, UK) equipped with a 532 nm HeNe laser (Melles-Griot, Voisins Le Bretonneux, France) delivering 15 mW of laser power at the sample. The laser was polarized along the x-axis direction. The platform loaded with biosamples was mounted on a ProScan II motorized stage (Prior, Cambridge, UK) under the microscope. A Leica 50x microscope objective (N.A. 0.95) focused the laser on the sample into a spot of ~0.8 μm diameter. An 1800 l/mm grating and a thermoelectrically cooled charge coupled device (CCD) camera was used for detection. The spectrograph was calibrated using the Silicon substrate. Single spectra were collected with an exposure time of 30 s. Mapping was achieved by collecting spectra with steps of 1 μm, with an exposure time of 20 s for each spectrum. Spectra, consisting of 2924 data points each, were obtained in the 100–3200 cm^{-1} region using the synchro mode of the instrument software WiRE 5.1 (Renishaw). In the synchro mode, the grating is continuously moved to obtain Raman spectra of extended spectral regions. The dimensions of the map depended on the zone of interest investigated. To characterize the SERS signals, we measured Raman spectra using a 150 second measurement time via a 532 nm HE laser on close to dry samples (0.5 μl- 10 μl). The EVs were also isolated from a non-cancerous normal human astrocytic (glial) cell line (NHA), five glioma cell lines (U87, U373, 1123) and two glioma stem cell lines (GSC83 and GSC1005).

(ii) Data pre-processing and analysis

All data pre-processing and analysis were performed within the Origin Pro 2019b software, ImageJ, WiRE 5.1, and CanvasX 2019 environment for statistical computing and graphics. In particular, we used principal component analysis for spectroscopy v.1.2 App in OriginPro 2019 for PCA analysis. The pre-processing of SERS spectra consisted of four steps: i) cosmic rays identification and removal, ii) baseline correction, iii) intensity vector-normalization according to Si peak and iv) outliers detection and removal. For the baseline correction, a linear baseline was fit automatically to the whole spectral range and was subtracted from each spectrum of the dataset. Outliers detection was done by identifying suspicious points on the PCA score maps and inspecting the corresponding spectra. In the pre-processing stage, PCA is thus used as a method to identify suspicious spectra, exploiting its sensitivity to outliers. These suspects were then individually examined before deleting them.

(iii) PCA

PCA reduces the number of variables by condensing all the spectral information contained in a large number of spectra into fewer latent variables (the principal components or PCs). Hyperspectral data are thus decomposed by PCA into the latent spectra (loadings) and scores. This approach is closely related to describing each spectrum in a Raman study as a product between components concentrations and pure constituents' spectra, where the latent spectra are used instead of those of the pure constituents, which are unknown. In the present study, PCA was performed on pre-processed data, and the first three principal components PC 1 and PC 2, and PC 3 which could be interpreted in terms of the biochemical components of the EVs, were considered for discussion. The loadings and score maps for the principal components are difficult to interpret.

6.6.7 Machine Learning Algorithms

(i) Cell Classification

As a way to ascertain that our ML pipeline is working properly, we aimed to use a multiclass ML to categorize different spectra into the 10 pre-determined classes (NHA, U87 Parental, U87 EGFRvIII, U87 PTEN, U373 Parental, U373 EGFRvIII, GSC83 wt, GSC83ko (EGFR-KO), GSC1005 wt, GSC1005 ko (EGFR-KO)).

SVM-A Support Vector Machine (SVM) is a classification ML algorithm that finds hyperplanes that best separate the input datapoints into different classes. In order to find the optimal hyperparameters (C and the kernel) needed for our classification task, we used a Bayesian search.(De Maesschalck et al., 2000) and the parameters were tested using 5 fold cross validation on the training set. C was explored from 10-6 to 100 using a log uniform distribution, and 2 different kernels were tested: a linear and a radial basis function kernel. The hyperparameters kept were C:0.4 and a linear kernel, as those that gave the best overall accuracy over the 5 folds. The hyperparameters used were C: 0.4 and kernel: linear.

CNN- To compare against a more advanced modeling architecture that can appreciate non-linear relationships in our data, we subsequently used a Convolutional Neural Network (CNN). This is a type of neural network that uses convolutional layers to extract the distinguishing features between classes. The final outputs of the network are then used to generate a prediction. The CNN here established is derived from Ho et al.,(Ho et al., 2019) which in turn is based on a code from He's algorithm.(K. He et al., 2016) It consists of a first convolution layer, followed by a batch normalization, two residual layers and a final fully connected layer (Figure 5-4l). The residual layers are composed of 3 blocks, each of two convolutional layers followed by a batch normalization and an activation function, rectified linear activation function (ReLU), containing a shortcut connection, which links the input to the output. The implementation of residual blocks facilitates solving exploding/vanishing gradients problems recurrent of deep networks. The

hyperparameters (the number of hidden filters, the number of blocks) were determined through grid search. The number of blocks was chosen between 2 and 3, the hidden filters were explored between 10 and 40, with an incrementation of 10, and the number of layers was between 1 and 6. The batch size was set to 5. The loss function is cross-entropy, and the optimizer function is the Adam optimizer.(Kingma & Ba, 2015) Training was done on the training set, with 10% kept as a validation set, to monitor the performance of the algorithm through loss and accuracy. Early stopping after 5 iterations with no improvement of the accuracy on the validation set was also implemented.

(ii) Binary

SVM- The SVM was redesigned for the binary classification, the hyperparameters were optimized as previously mentioned, giving the following hyperparameters: C:100, gamma:0.13 kernel: rbf. The algorithm was trained on 80% of the datasets with the 20% left as a testing set. The *healthy* dataset included the spectra from healthy samples 1-8 and the NHA cell line, while the *unhealthy* dataset included the spectra from patients 1-7 and the U87 P and U373 P cell lines. The patient samples were collected from individuals with confirmed diagnosis of the glioblastoma moments prior they underwent surgery.

CNN- The CNN algorithm was also implemented for the second stage, the binary classification task. The architecture is identical to the previous one, only with the final output layer being 2 neurons instead of 10. Loss and accuracy curves were obtained to verify the appropriate training of the algorithm, and the convergence was reached after 10 epochs.

6.7 Supporting Information

Abbreviations used

GBM	Glioblastoma multiforme
EVs	Extracellular Vesicles
MVs	Micro Vesicles
ELV	Exosome-like vesicles
POC	Point-of-care
EGFR	Epidermal growth factor receptor
rh-EGFR	Human recombinant EGFR
EGFRvIII	EGFR variant III
rh-EGFRvIII	Human recombinant EGFRvIII
EGFRvIII KO	EGFR variant III knockout
PTEN	Phosphatase and tensin homolog
MGMT	O^6-methylguanine-DNA-methyltransferase
TMZ	Temozolomide
ZnO	Zinc Oxide
SiO_2	Silicon Dioxide
MoS_2	Molybdenum Disulfide
NHA	Non-cancerours glial cells
GSC	Glioma stem cells
FBS	Fetal bovine serum
CSF	Cerebral spinal fluid

LOD	Limit of detection
R6G	Rhodamine 6G
ML	Machine Learning
ReLU	Rectified linear activation function
NTA	Nanoparticle tracking analysis
PCR	Polymerase chain reaction
PC	Principal component
PCA	Principal component analysis
SEM	Scanning Electrode microscopy
TEM	Transmission Electrode Microscopy
AFM	Atomic force microscopy
SERS	Surface Enhanced Raman Spectroscopy
FDTD	Finite-difference time-domain
TFSF	Total-Field Scattered-Field
EF	Enhancement factor
EFEF	Electromagnetic field enhancement factor
EM	Electromagnetic
MD	Molecular dynamics
PMF	Potential of mean force
WHAM	Weighted Histogram Analysis Method
SPR	Surface plasmon resonance
LSPR	Localized surface plasmon resonance
CVD	Chemical vapour deposition
PDMS	polydimethylsiloxane

LDA	Linear discriminant analysis
SVM	Support vector machine
CNN	Convolutional neural network
ROC	Receiving operaing characteristic
AUC	Area under the curve
ANOVA	One-way analysis of variance

6.7.1 Overview

Emerging new treatments and technologies for cancer are proven to be effective at the early stages of the disease before advancing beyond the localized stage *i.e.* metastasis which accounts for more than 90% of cancer deaths. (Wirsching et al., 2016) A recent increase in the occurrence of metastasis in the brain and central nervous system urged researchers to develop novel technologies for early recognition of brain tumours and differentiate them according to their level of malignancy with minimum invasiveness(Louis et al., 2016). Among, Gliomas are the most common type of primary malignant brain tumour accounting for 80% of brain tumour cases, which includes different tumour mutations at different grades of malignancy.

Grade I gliomas are considered benign, non-infiltrative tumours, and susceptible to surgical cure. In contrast, diffuse astrocytomas (Grade II, III, or IV) are considered malignant. In particular, *glioblastomas* Grade IV are the most lethal glioma due to their rapid growth and high resistance to current therapies, leaving the patient with a median survival rate of a year after diagnosis. (Nawaz et al., 2014)

Monitoring cell transforming events throughout different cancer processes is an important key for treatment decisions. Mutational and epigenetic driver events profoundly alter the release, molecular composition, and biological activity of extracellular vesicles (EVs). (Boriachek et al.,

2018; H. Im et al., 2014; Mollaei et al., 2017; Wu et al., 2017) EVs are membranous cellular fragments filled with bioactive molecular cargo, (Boriachek et al., 2018; H. Im et al., 2014; Mollaei et al., 2017; Wu et al., 2017) exosomes, a class of EVs with a size range of 30–250 nm and released by all cells, are composed by a lipid bilayer membrane enclosing proteins, lipids, and nucleic acids. (Boriachek et al., 2018; H. Im et al., 2014; Mollaei et al., 2017; Wu et al., 2017) Investigating the molecular fingerprints of single exosomes to study the cancer cell transforming events can lead to the identification of mutational events responsible for the transformation of benign cancer cells to aggressive ones. (Choi et al., 2019) Among the potential targets involved in the development of cancerous cells there are variants of the epidermal growth factor receptor (EGFR) including the EGFR variant III (EGFRvIII), which nurture an in-frame deletion of exons and therefore results in a truncated extracellular ligand-binding domain. (Morgan et al., 2012) EGFRvIII figures prominently in glioblastomas pathogenesis with approximately 20-30% of patients harbouring the EGFRvIII mutated gene, which is associated with increased glioma proliferation and invasiveness. Therefore, investigating the EGFRvIII mutations in glioma cell lines as well as glioma stem cells is an important target for single exosome SERS studies.

Although the conventional clinical modalities are cornerstones of cancer diagnosis, there is an urgent need for fast, sensitive, low-cost, and easy-to-operate portable devices. The development of on-chip diagnostic methods that are central to a minimally invasive diagnosis based on blood has the potential to revolutionize cancer and in particular GBM diagnosis. The main challenge of using blood as the reservoir of tumour biomarkers lies in considerably lower concentrations of them requiring exceptionally high sensitivity. With the current portable detection technologies, we are subjected to use bioassays based on enzyme-linked immunosorbent assays (ELISAs) and polymerase chain reaction (PCR), as well as newer commercial technologies, such as NanoString©,

Luminex© and iSEA©. As the binding assays are governed by the principles of chemical equilibrium, the range of measurable target concentrations is prone to a dynamic range centered around the constant dissociation of the reagents to their target. The ongoing quest to develop and enhance on-chip diagnosis modalities is summarized in (Table S6-1).

Table S6-1. Technologies developed for cancer liquid biopsy of EVs.

Technology	Cancer	ML	LOD (EVs/mL)	Receptor antibodies	Readout	Ref
Aptamer triggered padlock probe-based exponential rolling circle amplification	Lung	NO	4.2×10^4	A549-EVs aptamer	Fluorescence Microscopy	(He et al., 2022)
Integrated magneto-electrochemical device based on a 96-well assay and antibody-coated magnetic beads for the rapid profiling of tumour extracellular vesicles	Colorectal	NO	10^4	EGFR, EpCAM, CD24, GPA33	Electrochemistry	(Tian et al., 2021)
Thermophoretic aptasensor	Breast	YES (LDA)	3.7×10^7	Cy5-conjugated aptamers	Fluorescence Microscopy	(Tian et al., 2021)

Microfluidic chip for EVs multiplex phenotyping based on Raman reporters barcoding	Melanoma	NO	10^3	MCSP, MCAM, CD61, and CD63	SERS	(Wang et al., 2021)
Microscale biosilicate nanofilter doped with AgNPs and treated with cysteamine	Ovarian and Endometrial	NO	600	-	SERS	(Rojalin et al., 2020)
SERS nanotags EVs protein profiling via sandwich immunoassay	Colorectal, Bladder, and Pancreatic	NO	2.3×10^6	CD63, Glypican-1, EpCAMs, CD44V6	SERS	(Zhang et al., 2020)
Aggregated spherical AuNP substrate on APTES-coated glass coverslip.	Lung	YES (SVM, CNN)	$2.3x10^6$	-	SERS	(Shin et al., 2020)
Microfluidic chip based on nanosurface herringbone nanopatterns	Ovarian	NO	10^6	EpCAM, CD24, FRα, CD63, HER2, EGFR	Fluorescence Microscopy	(P. Zhang et al., 2019)
Sequential detection of EVs via DNA-PAINT on PEI modified cover glass	Ovarian and Breast,	YES (LDA)	Single EV	-	TIRF microscopy ~80 EVs	(Chen et al., 2019)
Electrically reconfigurable network of gold-coated magnetic nanoparticles enables microRNA detection	Lung	NO	10 aM	Probe DNA	Electrochemistry	(Tavallaie et al., 2018)

Multiplex immunostaining and imaging chip for EVs biomarkers profiling	Glioblastoma	YES	Single EV	CD63	Fluorescence microscopy $>10^3$ EVs per field of view	(Lee et al., 2018)
Biotinated EVs/ MVs immobilization on streptavidin-coated coverslip	Glioblastoma	NO	Single EV	Integrin β1, CD81,61,9 EGFR, EGFRvIII	Fluorescence microscopy ~2000 MVs per field of view	(Fraser et al., 2019)
Intravenously injected rare-earth-doped albumin-encapsulated nanoparticles for emitting short-wave infrared light (SWIR)		NO	NO	ReANCs cancer biomarker CXCR4	SWIR imaging	(Kantamneni et al., 2017)
A nanoplasmon-enhanced scattering (nPES) assay that directly quantifies tumour-derived EVs from as little as 1 µl of plasma	Pancreatic	NO	NO	Ephrin type-A receptor 2 (EphA2)	Fluorescence Microscopy	(Liang et al., 2017)
n-PLEX Chip Microfluidic chip based on periodic nanohole arrays	Ovarian	NO	YES	EpCAM, CD24, CD63	SPR	(Hyungsoon Im et al., 2014)

Microfluidic device based on functionalized graphene oxide nanosheets on a patterned gold surface for CTC isolation	Pancreatic, Breast, and Lung	NO	NO	EpCAM	Fluorescence Microscopy	(Yoon et al., 2013)
Microfluidic system with magnetic nanoparticles and miniaturized nuclear magnetic resonance system	Glioblastoma	NO	NO	CD63	MRI	(Shao et al., 2012)
MoSERS (MoS_2 embedded silver nanocavity for single EV SERS identification	Glioblastoma	YES (CNN)	YES	-	SERS	This work

6.7.2 MoSERS System

6.7.2.1 MoSERS Microchip

Here, we designed a novel SERS platform to study the molecular profile of a single EV. A combined bottom-up and top-down approach was used to develop the MoSERS nanochip as a single EV analyzer (Figure S6-1a). First, the bottom-up chemical vapour deposition (CVD) technique was used to grow single crystalline monolayer MoS_2. The monolayer was produced through CVD method by nucleation and growth from the vapour phase solidified on the substrate of choice. We acquired a large area of single crystalline, monolayer MoS_2 on a SiO_2/Si substrate and pierced it via electron beam (e-beam). Second, the top-down negative e-beam lithography technique was used to pattern a silver plasmonic nanohole array in a 300 nm thick layer of negative photoresist (MaN-2403) via Reith equipment. Direct-write technology of e-beam lithography

allowed us to develop plasmonic nanostructures with a high patterning resolution, placement accuracy, and design degree of freedom. Using a negative photoresist e-beam lithography, a square array of circular nanocavities with 100-500 nm was recorded in a 300 nm thickness of Ma-N resist layer. After the development of the pattern, this was deposited with ZnO and silver (via BJD 1600), as back-reflector and plasmonic layer, respectively followed by an overnight lift-off process in 1165 remover. The floating plasmonic silver nanocavity pattern with a diameter between 100-500 nm was fabricated with and without embedded monolayer MoS_2 to study the effect of integrating monolayer MoS_2 for single EV isolation and augmentation of the SERS response.

6.7.2.2 MoSERS Microfluidics

To integrate the MoSERS microchip as SERS sensitive sensing platform into the microfluidics and enable control over sample delivery, a 3D printed polydimethylsiloxane (PDMS) microfluidic approach was followed (Figure S6-1b). Then, the MoSERS microchip was bonded to the 3D molded substrate and covered with a thin PDMS film that is pierced for inlet and suction compartments. The MoSERS microfluidic provides a user-friendly, automated, rapid actuation system, which enables significant reductions in user errors during testing. A key technology for manipulating fluid flow is the mechanical actuation of PDMS suction cups, which results in creating pressure gradients in channels. A PDMS suction cup's internal volume is directly correlated with its fluid manipulation capacity. Based on a screw-nut actuation setup, we empirically evaluated the relationship between the volume of the suction cup and the volume of fluid pumped.

6.7.2.3 MoSERS Single EV Stratification

We used isolated cell EVs to investigate the single EV entrapment in the nanocavities of MoSERS (Figure S6-1c). EVs were purified from conditioned growth media of cancer cells into 5

fractions (7-11) using an optimized protocol via qEV single SEC column (Izon Science, UK). The handling of the MoSERS microchip begins by pipetting the EVs fraction into the PDMS inlet, the application of the suction compartment for flow actuation required a volume of 2-10 µl to perform adequately. MoSERS microchip capture efficiency was studied via electron microscopy and fluorescence microscopy. The loaded MoSERS system was then characterized by micro-Raman equipment (Renishaw Ltd©) for the collection of SERS signals.

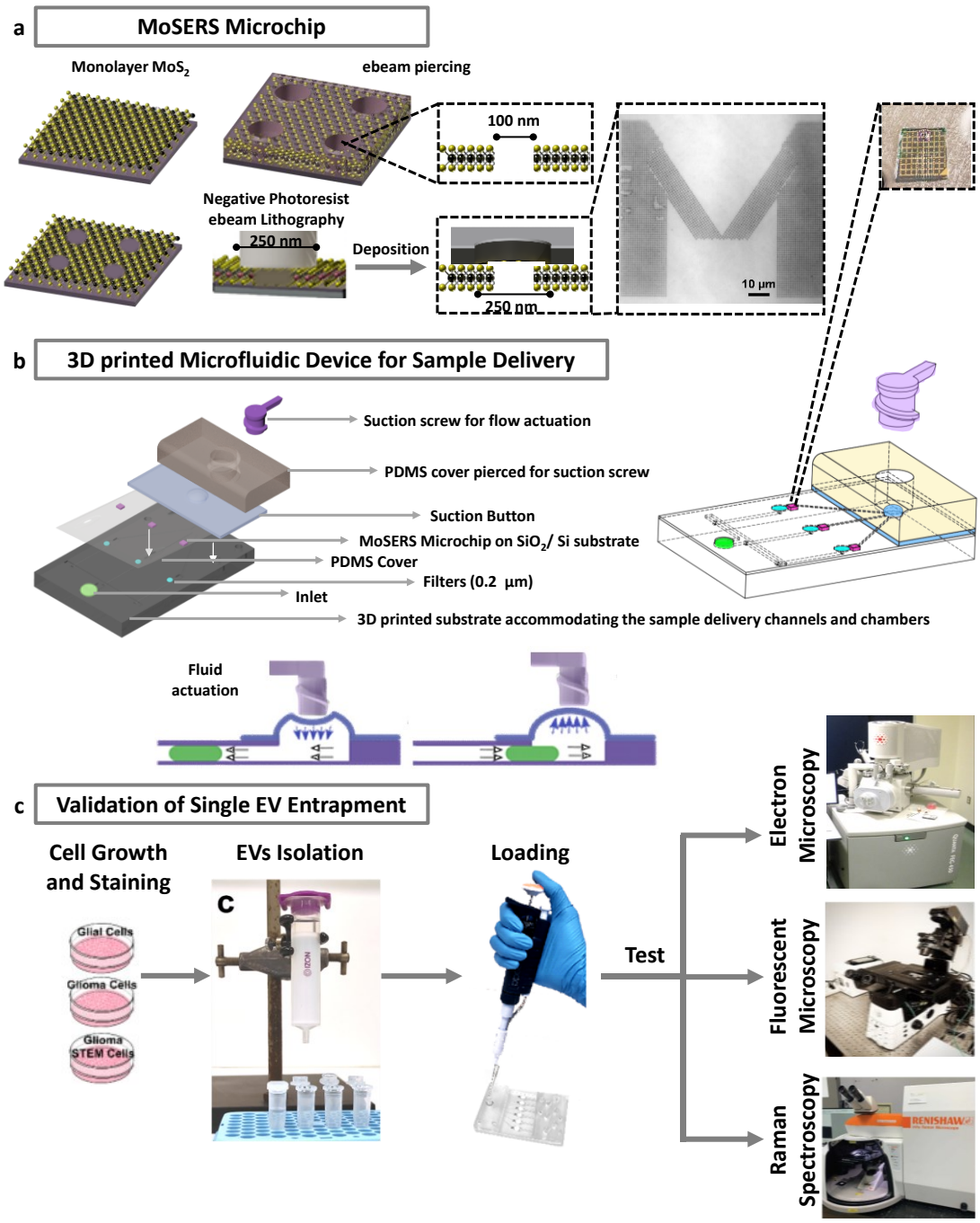

Figure S6-1. Schematic of the MoSERS single EV analysis workflow. (a) Process flow of fabricating the pierced MoS_2 embedded nanocavities for SERS enhancement (MoSERS). (b) The sample delivery microfluidic device accommodates the MoSERS microchip and fluid actuation.

(c) EV isolation and validation of single EV investigation via electron microscopy, fluorescent microscopy and Raman spectroscopy.

6.7.3 SERS Enhancement

6.7.3.1 FDTD Simulation

To theoretically study the electromagnetic field (EM-field) enhancement of plasmonic nanocavities in the presence of monolayer MoS_2, a series of simulations were performed via finite-difference time-domain (FDTD) module of Lumerical Solution (v8.21.1781, Lumerical Solutions, Inc.). A Toal-Field Scattered-Field (TFSF) source was used to simulate only a small region of the periodic structure, to find the maximally possible EM-field. The Ag/ZnO plasmonic layer was supported by a monolayer MoS_2-covered SiO_2 substrate to match the experimental configuration. All the metallic materials were simulated based on Palik refractive indices, while the refractive index of the non-linear MoS_2 material was determined from a previous work.(Jalali, Gao, et al., 2021) The EM-field enhancement distribution $\left(\frac{|E(\omega)|}{|E_0(\omega)|}\right)^2$ was simulated in the laser excitation wavelength of 532 nm using a TFSF light source to resemble the Gaussian laser beam.

After the material was studied, the effect of the light source is investigated. The reflectance spectra of nanocavities with different cavity sizes and optimized parameters were simulated (Figure S6-2a) to study diameter (D) variation under planewave illumination. Similarly, the simulation of the EM-field enhancement under a planewave light source demonstrates the maximum conceivable EM-field enhancement with nanocavities with a diameter of 150-250 nm (Figure S6-2b). A comparison simulation sweep was designed to compare the EM-filed enhancement based on the light source i.e. TFSF and planewave (Figure S6-2c), showing an increase in the EM-filed at the center of the cavities with the size of 150-250 nm. The 2D contour plot of the EM-field enhancement on a single nanocavity of silver, gold, aluminum, and copper

using a TFSF light source at 532 nm wavelength demonstrating the premier competence of silver at 500-550 nm period (Figure S6-2d).

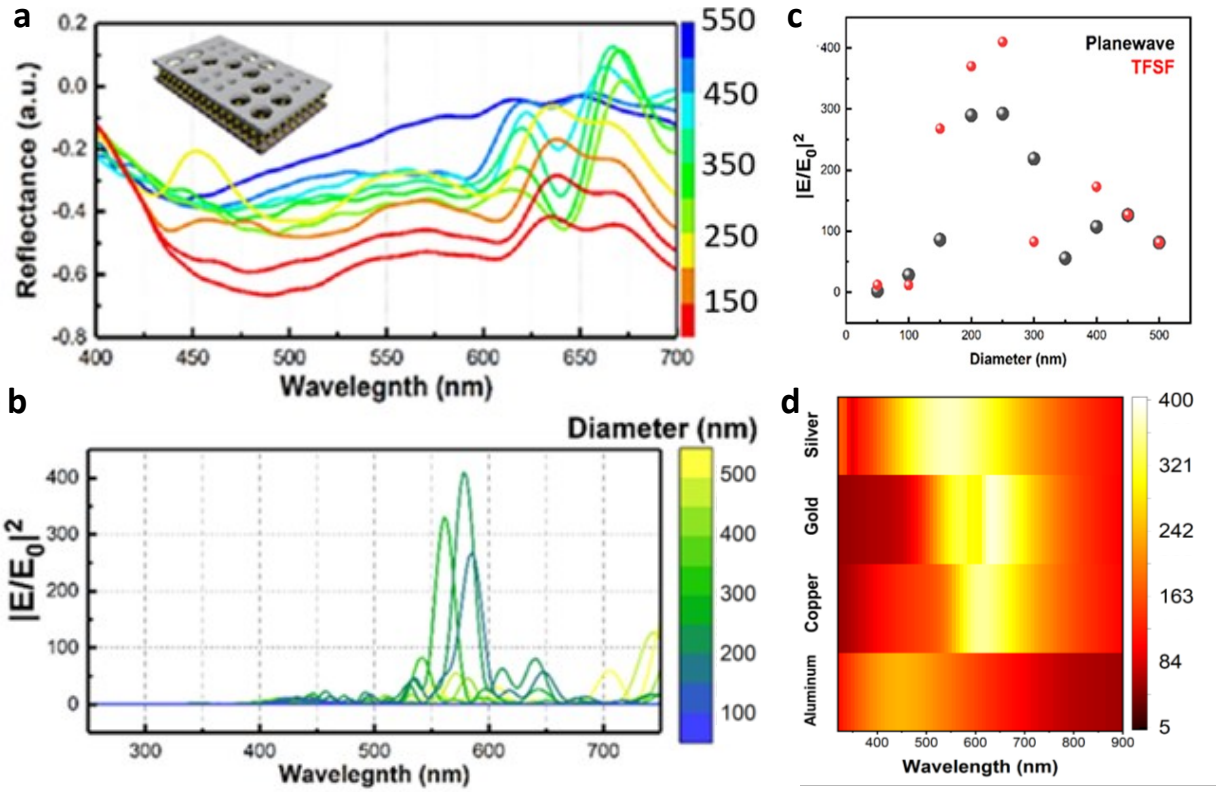

Figure S 6-2. EM-field enhancement of nanocavities under TSFS light source. (a) The electric field distribution in the nanocavities with different diameters via a 532 nm TSFS light source. (b) Simulated reflectance spectra and (c) the ($|E|/|E_0|$) EM-field distribution of plasmonic nanocavities with different diameters embedded with the monolayer MoS_2. (d) The 2D contour plot comparing the ($|E|/|E_0|$) EM-field distribution for different materials as a function of wavelength.

6.7.3.2 MoSERS Sensitivity (R6G)

An initial experimental efficiency of the MoSERS nanocavity was characterized by using Rhodamine 6G (R6G), a well-known marker SERS. The greatly enhanced SERS intensity achieved by the MoSERS nanochip compared to two thin films (Ag/ZnO and Ag) is shown in Figure S6-3a, this intensity is directly related to the EM field enhancement that the MoSERS achieves thanks to the improvement of the electric field distribution generated by the nanocavity pattern. A simple study of laser intensity in the function of the laser power was performed. The results are shown in Figure S6-3b to assist in deciding the percentage of laser intensity to be used onwards. A study of R6G SERS spectra in a concentration range of 0.01 to 200 µM, shown in Figure S6-3a, resulted in a linear range from 0.1- 200 µM and a limit of detection of 0.1 µM at 0.1% laser power.

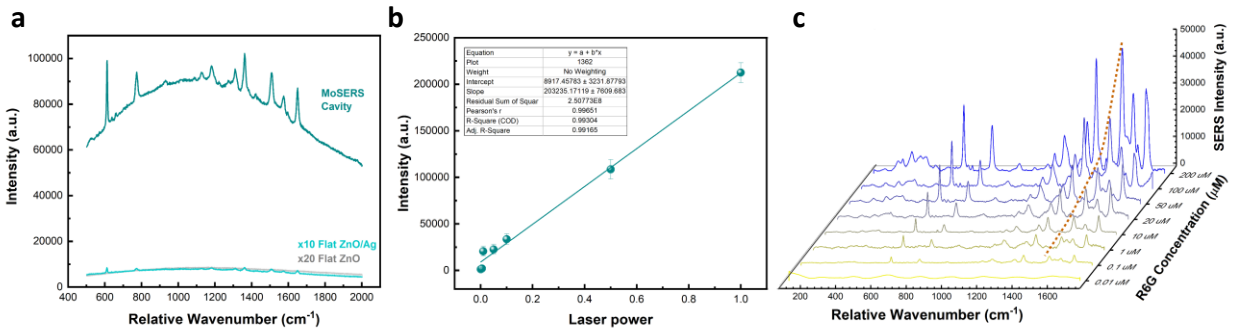

Figure S6-3. MoSERS sensitivity study using R6G. (a) the SERS spectra of R6G in a range of concentrations from 0.01-200 µM. (b) Linear intensity increases as a function of laser intensity percentage at 20 seconds dwelling time with R^2 value of 0.993. (c) The SERS spectra of R6G in a range of concentrations from 0.01-200 µM.

6.7.4 MoS_2 -EV Interaction

6.7.4.1 Electron microscope characterization

Ad

The MoS_2 monolayer, particular to the MoSERS chip, was studied in detail. MoS_2 demonstrates the characteristics of a triangular, single-crystalline 2H-phase monolayer (Figure S4a). The bright-field microscope image shows the triangular shape of single-crystal MoS_2 while the dark field microscope image shows only bright edges of the triangles, indicating the monolayer characteristic of MoS_2 as no signal is received from the basal plane of the material. The micro-Raman characterization of the CVD-grown MoS_2, showing 22 nm difference between A^1_g and E^1_{2g} peaks which can be referred to as the monolayer characteristics of MoS_2. We also investigated the encapsulation of the single EVs in the nanocavities of MoSERS using the transmission electron microscopy (TEM) approach. The high-resolution TEM image of monolayer MoS_2 (Figure S4b) and corresponding SAED pattern in the inset confirming the 2H-phase of the monolayer MoS_2 with 0.27 ± 0.1 nm lattice d-spacing fringes corresponding to the (100) hexagonal plane of Mo atoms and S atoms. To ensure the attachment of the EVs in the nanocavities, a pre-treatment was used to form circular holes in the cavities with diameters smaller than those of the nanocavities (Figure S4c). The large area EDS mapping with correlated high angle annular dark field (HAADF) image in the inset enlightens the elemental distribution of C, N, and P related to the EV and Ag, Mo, and S related to the MoSERS micro-chip (Figure S4d-e)

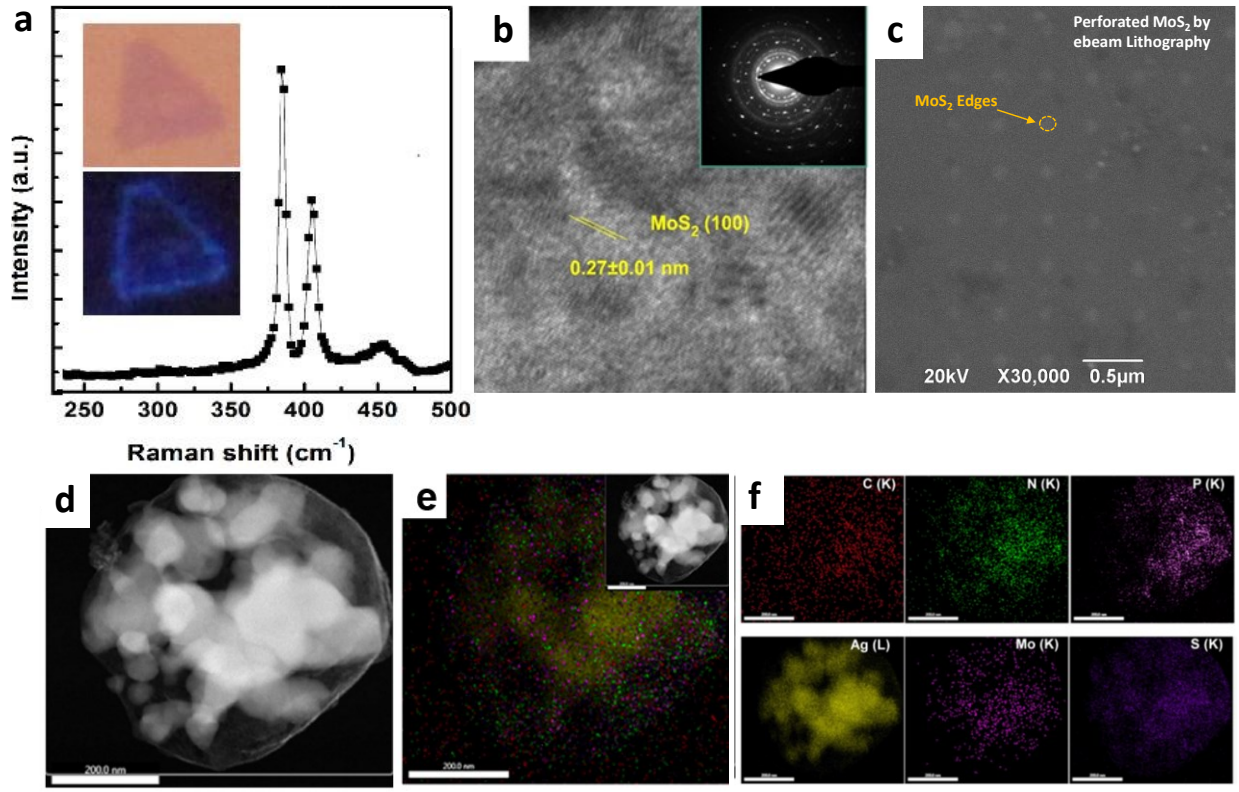

Figure S6-4. Microscopic imaging of EV interactions with MoSERS micro-chips. a, Microscope images (bright mode and dark mode) of a CVD grown MoS_2 with corresponding Raman shift spectra. b, High-resolution TEM image of monolayer MoS_2 and corresponding SAED pattern in the inset confirming the 2H-phase of the monolayer MoS_2. c, Creation of edge site MoS_2 in the single crystalline monolayer via the electron beam piercing treatment. d, HAADF image of brushed EVs/ MoSERS nanocavities on a Cu TEM grid and correlating e, large area EDS mapping of the MoSERS micro-chip demonstrating f, single component mapping.

6.7.4.2 Molecular Dynamics

A potential of mean force (PMF) was calculated along a perpendicular direction to the surface of the phospholipid bilayer to evaluate free energy changes during insertion (Figure S5a).The PMF is able to evaluate the binding free energy calculated according to the umbrella

sampling simulations. (Roux, 1995; Torrie & Valleau, 1977) The MoS_2 nanosheet (which was selected from the final conformation in the second simulation) was vertically pushed away from the membrane during PMF calculations. Then, the perpendicular distance of center of mass of MoS_2 nanosheet with its corresponding initial position was regulated at reference distances (d_0) via a harmonic force, $F = k \times (d - d_0)$, where k was the force constant (2000 kJ mol^{-1} nm^{-2}). The adjacent windows had an interval of 0.1 nm. At each d_0, the system was conducted for 2 ns equilibration, followed by a 10 ns productive run. The free energy profile was acquired by the g_wham tool of its the Weighted Histogram Analysis Method (WHAM). (Hub et al., 2010; Kumar et al., 1995) A stable membrane comprising the five components listed above served to study the minimum energy level after absorption of a layer inside the membrane and the attraction forces of the phospholipid bilayer interaction and MoS_2 (Figure S6-5b).

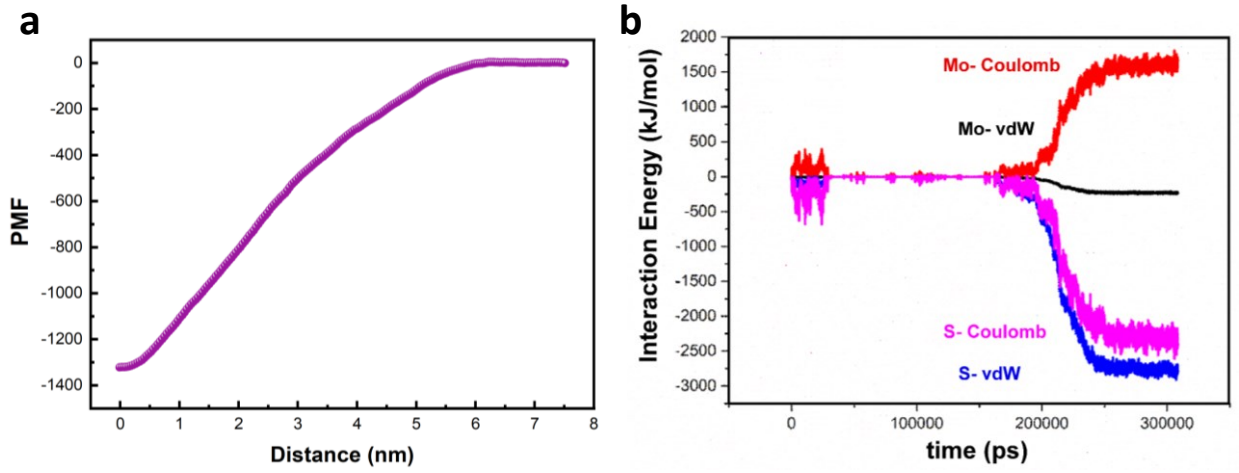

Figure S6-5. Molecular Dynamics simulation the MoS_2 and phospholipid layer interaction. a, The PMF calculated along a perpendicular direction to the surface of the phospholipid bilayer to evaluate free energy changes during insertion b, Time evolution of interaction energy of the MoS_2 nanosheet with the EVs sample for 300 ns.

6.7.4.3 Surface-Enhanced Fluorescent Microscopy

The confinement efficiency of the MoSERS nanochip is studied via fluorescence microscopy. For this, fluorescently labelled EVs are recorded during 14 s of microscopy after being washed with PBS buffer. A high oil resolution microscopy was performed by washing with PBS after the EVs entrapment, followed by the addition of oil to seal the cavities before inverting the opaque chip to perform the high-resolution microscopy (Fig. S6-6a). A low-resolution cropped area of the micrograph demonstrates that these rectangular arrays of nanocavities with variety of diameter size can be fabricated into arbitrary shapes (Fig. S6-6b).

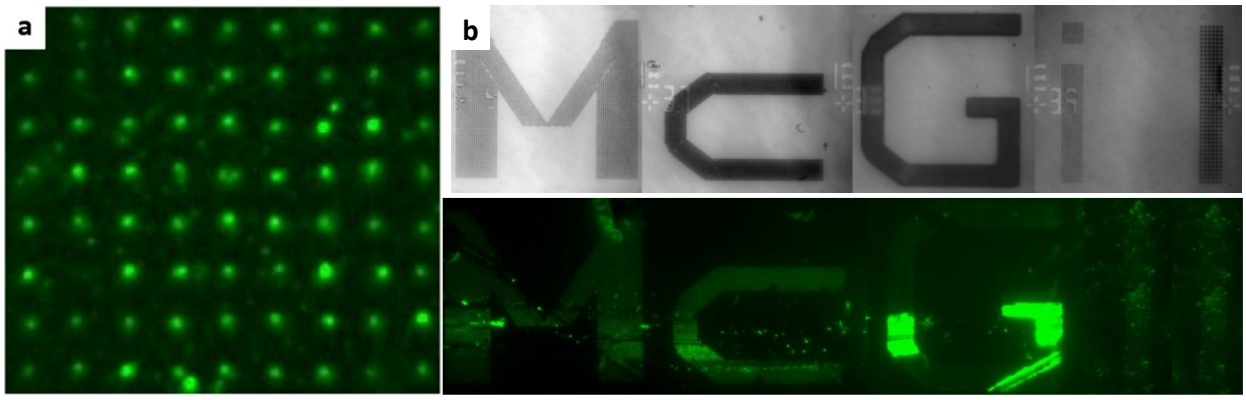

Figure S6-6. EVs entrapment in the nanocavities. (a) high resolution oil microscopy of the inverted MoSERS microchip loaded with EVs and washed with PBS buffer solution. (b) A low magnification cropped area with EVs confined in MoSERS nanocavities in arbitrary shaped rectangular arrays.

6.7.5 Characterization of Cell Line EVs

6.7.5.1 Nanoparticle Tracking Analysis (NTA)

Once the MoSERS platform design was optimized and characterized with a known SERS marker, we proceeded to study our target sample. The purified fractions of EVs derived from

glioma cell lines and the stained glioma cell lines were characterized with NTA to measure the particles' concentration and the size distribution (Figure S6-7a). The quantitative profiles mostly show simple patterns, except for 2 or 3 cell lines (U87 EGFRvIII and U373 EGFRvIII) where a broader size distribution of EV subpopulations is suggested by their complex profiles containing multiple peaks (Figure S6-7a). The mode value represents the size of the majority of the EVs which was found to be 165 nm on average while the mean value size for the EVs was determined to be 179 nm on average (Figure S6-7b).

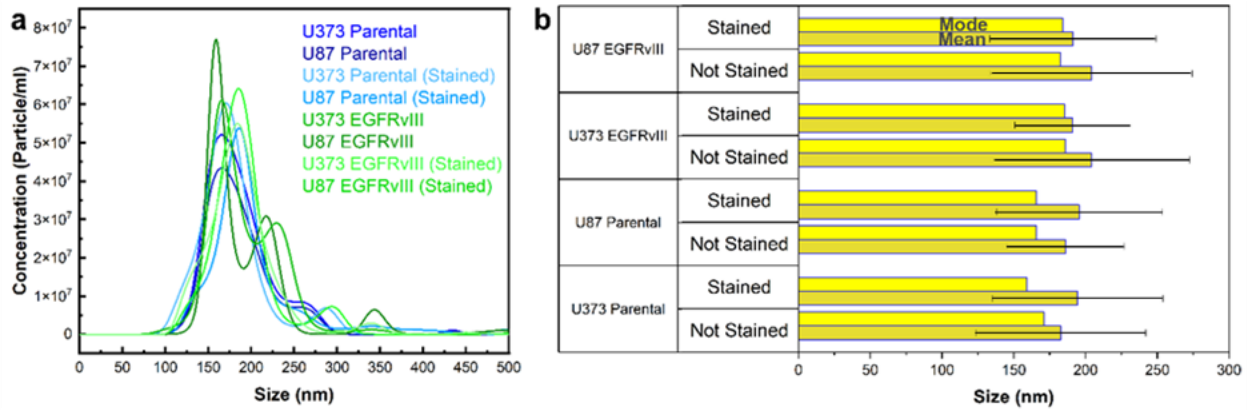

Figure S6-7. NTA profiles of glioma cell derived EVs. (a) Nanosight characterization of the purified fractions of EVs from stained and unstained glioma cell lines. (b) The mode and mean size value of the EVs population.

6.7.5.2 Unprocessed (raw) Spectra of Cell-Derived EVs

In order to study the MoSERS capabilities to differentiate various EVs cell lines, a library was integrated. The library comprised 6 different cell lines (Glioma U87, Glioma U373, GSC1005, GSC83, Glioma 1123, and NHA) and some variations of them. A dataset of each cell line type is then formed from approximately 50 single EVs collected spectra. Figure S6-8 shows the collection of the individual raw spectra from two of the previous cell lines (Gliomas) U87 and U373 (Figure

S6-8a-c), including the their types (Parental, EGFRvIII,); as well as GSC1005 and GSC83 (Figure S6-8d-f) stem cell lines of two types (Wild type and EGFRvIII Knocked out). The raw datasets need to be registered before they can be analysed. Briefly, first, a baseline is subtracted from the spectra, followed by the data smoothing and normalization. To clearly express the single EVs characteristic of each database, the graphs in Figure S6-8 (both pre and post-processed) show the stacked spectrum in each cell line set (the SERS intensity values in the y axis are arbitrary). The display of all spectra demonstrates similar profiles within its data sets.

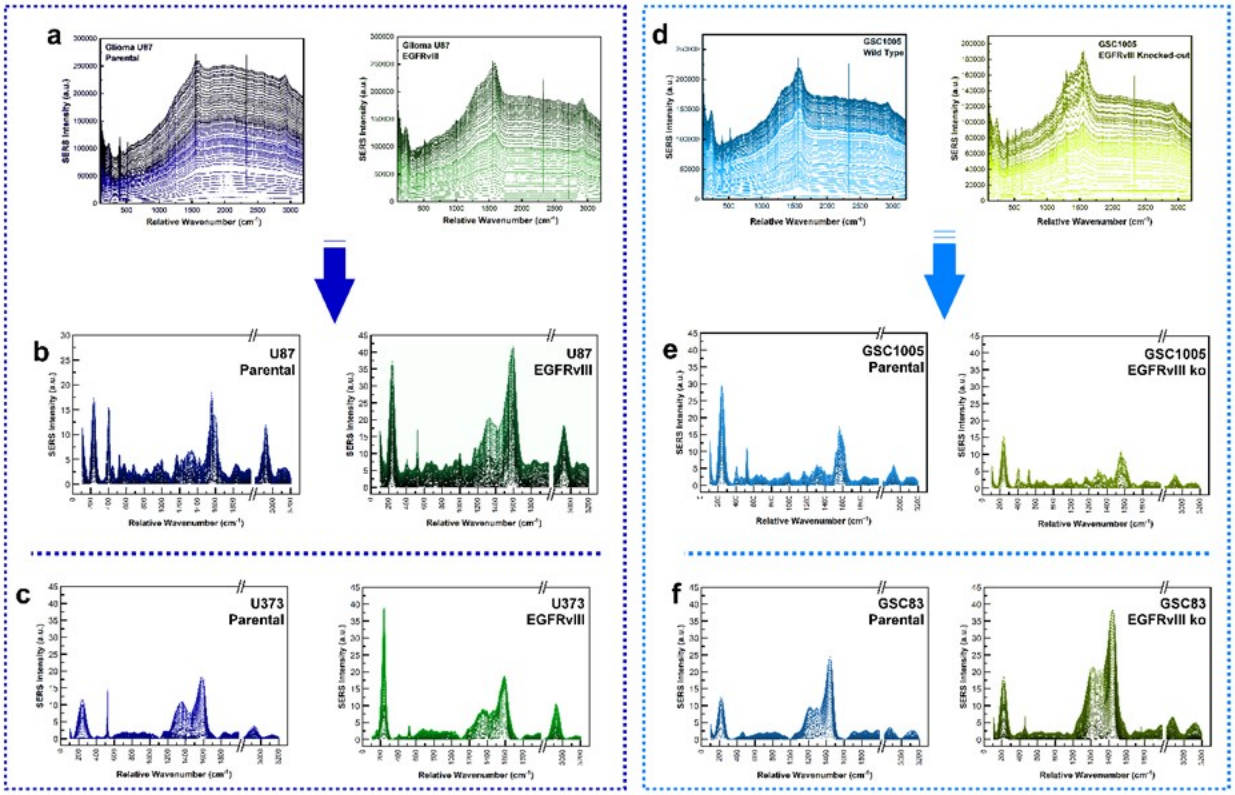

Figure S6-8. Raw SERS spectra of the glioma cell lines including the different subtypes. Parental, EGFRvIII, and PTEN (a) for raw spectra and (b) after registration - while for (c) Glioma U373 were only Parental and EGFRvIII. Spectra from GSC1005 Wild type, and GSC1005 EGFRvIII Knocked out (d) before and (e) after registration. Spectra from Glioma 1123-9 MGMT and Glioma 1123-7 MGMT Knocked out (e) before and after registration.

.

6.7.5.3 PCR Study of EVs and cells

In order to assess the complexity of the influence EGFRvIII has in the EVs formation, we study the profiles of vesiculation-related genes using quantitative real-time polymerase chain reaction (Rt-qPCR) assays. Specifically, we studied EVs genes derived from EGFRvIII expressing variant cells of both U87 and U373 glioma cell lines. We used RT2 profiler™ PCR array to study the expression of 84 key genes involved in the EVs from EGFRvIII expression in U87 and U373 glioma cell lines presented in a heatmap format. The relative fold gene expression was calculated by using the correlative ΔC_t method to visualize 2-fold or greater differentials in mRNA levels between paired Parental/EGFRvIII variants of the U87 cell line (Figure S6-9). Similarly, at least 2-fold change was detected when comparing the corresponding pair ratio in U373 glioma cell line. Along these lines, the PCR analysis (Table S6-2) confirmed the expression of EGFRvIII mRNA in EVs derived from both U87vIII and U373vIII cell lines, documenting the direct involvement of this oncogene in the EV cargo formation. These analyses suggest that oncogenic mutations in EGFR and PTEN impact the multiplicity of genes and potentially create unique complexities in profiles of the resulting EVs, beyond the content of EGFRvIII.

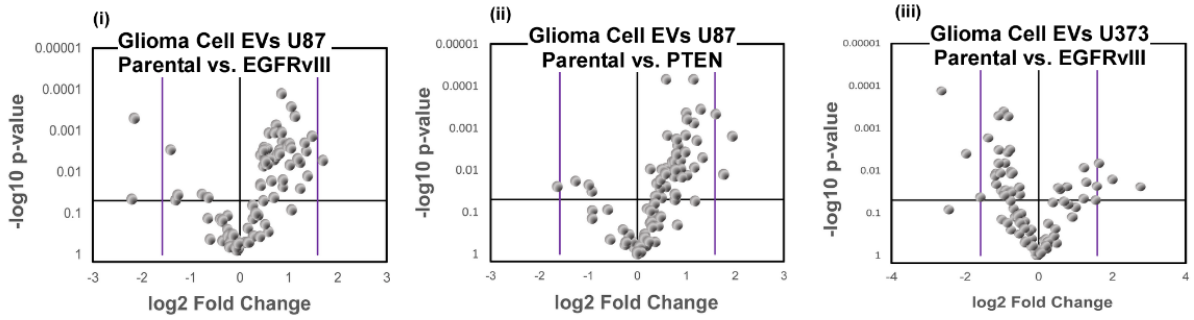

Figure S6-9. PCR Study of EVs derived from U373 and U87 cells. The PCR results of the EGFR and EGFRvIII expression of EVs derived from mutated U87 and U373 cell lines.

Table S6-2. Gene expression levels.

	U87/PTEN vs U87par	U87 EGFR (vIII) vs U87par	p value	p value	Average raw Ct	Average raw Ct	Average raw Ct
	Fold Change	Fold Change	T-TEST	T-TEST	U87par	U87PTEN	U87 vIII
ITGA6	1.111	15.219	0.546	0.000	27.96	27.69	24.13
DIAPH3	3.029	3.098	0.016	0.011	27.08	25.36	25.54
HPSE	1.245	2.659	0.504	0.004	28.37	27.93	27.05
HNRNPA2B1	2.003	2.499	0.016	0.014	20.65	19.53	19.42
HSPA4	2.254	2.453	0.002	0.002	23.27	21.98	22.07
STX1A	3.424	2.397	0.000	0.001	26.94	25.04	25.77
ICAM1	1.575	2.252	0.295	0.033	28.18	27.41	27.1
LIMK1	2.017	2.247	0.028	0.004	23.38	22.25	22.31
SMPD4	1.539	2.170	0.040	0.007	25.18	24.44	24.15
RAB27A	1.780	2.087	0.016	0.003	24.26	23.31	23.29
SMPDL3A	2.192	1.983	0.000	0.000	26.91	25.65	26.01
TSG101	1.756	1.969	0.005	0.003	24.77	23.84	23.89
RAB35	1.654	1.938	0.007	0.007	25.14	24.3	24.28
SNF8	1.522	1.938	0.015	0.001	23.6	22.87	22.73
SMPD2	1.522	1.876	0.005	0.001	27.25	26.53	26.44
HGS	1.989	1.759	0.000	0.015	27.9	26.78	27.17
HSPBP1	1.608	1.759	0.006	0.015	26.67	25.86	25.94
ARF6	1.340	1.742	0.009	0.003	24.08	23.53	23.37
ROCK1	0.981	1.726	0.793	0.000	24.01	23.91	23.31
VTA1	1.557	1.722	0.002	0.002	25.29	24.53	24.6
RAB23	1.554	1.683	0.002	0.003	25.2	24.45	24.54
RAB31	1.797	1.675	0.003	0.006	23.48	22.52	22.83

CHMP4B	1.515	1.630	0.000	0.001	22.6	21.88	21.98
ANO6	1.340	1.607	0.033	0.005	24.78	24.24	24.19
ATG12	1.463	1.600	0.005	0.000	24.69	24.02	24.1
RAB11A	1.259	1.570	0.003	0.000	23.07	22.61	22.51
AKT1	1.066	1.549	0.506	0.007	23.51	23.29	22.97
ANXA11	1.013	1.545	0.970	0.022	22.97	22.83	22.44
LAMP1	1.650	1.496	0.000	0.008	22.67	21.82	22.18
FLOT2	1.764	1.442	0.000	0.011	24.19	23.25	23.75
MAP2K4	1.337	1.442	0.002	0.001	25.96	25.42	25.52
DLL4	1.145	1.435	0.650	0.340	31.43	31.12	31
RAB2B	1.151	1.422	0.151	0.010	26.67	26.35	26.26
CD44	1.976	1.419	0.005	0.050	20.99	19.89	20.58
FLOT1	0.793	1.383	0.062	0.009	23.02	23.23	22.64
RAB5A	1.132	1.367	0.180	0.010	24.99	24.69	24.63
RAB6B	0.979	1.367	0.881	0.305	32.62	32.53	32.26
RAB27B	2.711	1.364	0.001	0.021	24.01	22.45	23.66
PDCD6IP	1.259	1.345	0.010	0.003	23.49	23.04	23.15
CFL1	0.886	1.333	0.213	0.023	18.66	18.71	18.33
LAMP2	0.930	1.333	0.544	0.018	21.69	21.68	21.37
SNX3	1.069	1.327	0.404	0.004	22.48	22.27	22.17
RAB11B	1.081	1.282	0.010	0.001	24.5	24.26	24.23
RAB2A	1.236	1.282	0.021	0.009	22.92	22.5	22.66
RAB5B	0.896	1.282	0.025	0.007	23.52	23.56	23.26
ITGA5	1.797	1.238	0.021	0.379	22.93	21.96	22.71
SMPDL3B	0.468	1.196	0.015	0.211	31.34	32.31	31.17
SDCBP	1.673	1.163	0.010	0.290	21.53	20.67	21.41
POU5F1B	0.750	1.155	0.388	0.506	31.47	31.76	31.35
CD63	1.233	1.152	0.031	0.087	18.77	18.35	18.66
CD9	1.175	1.147	0.176	0.112	21.89	21.53	21.78
CHMP2A	0.941	1.090	0.584	0.563	22.59	22.56	22.56

RHOA	0.917	1.070	0.317	0.447	21.38	21.38	21.37
VPS28	0.886	1.068	0.135	0.405	23.68	23.73	23.68
LYN	1.586	1.024	0.000	0.747	27.97	27.19	28.03
ANXA6	0.932	0.938	0.151	0.235	22.84	22.82	23.02
STX7	1.025	0.929	0.754	0.270	24.32	24.16	24.51
CAV1	0.852	0.925	0.550	0.674	19.79	19.9	19.99
EPHA1	0.607	0.915	0.355	0.718	30.22	30.82	30.44
RAB3A	0.759	0.915	0.128	0.499	27.17	27.45	27.39
CD151	0.829	0.906	0.007	0.135	21.47	21.62	21.7
SNAP25	1.322	0.904	0.225	0.602	25.66	25.13	25.89
VAMP3	1.069	0.867	0.173	0.050	22.5	22.28	22.8
EXPH5	1.037	0.830	0.825	0.392	32.12	31.94	32.48
SMPD3	0.935	0.824	0.895	0.617	32.28	32.26	32.65
CTNNB1	1.119	0.807	0.319	0.134	24.25	23.96	24.65
HSPA5	1.365	0.804	0.099	0.211	26.17	25.6	26.58
ANXA4	1.340	0.802	0.065	0.087	23.69	23.15	24.1
CD82	2.069	0.746	0.020	0.413	24.29	23.12	24.8
WLS	1.094	0.746	0.160	0.018	22.8	22.55	23.31
ADAM10	0.952	0.741	0.605	0.015	21.66	21.61	22.18
SMPD1	0.728	0.723	0.017	0.016	23.13	23.46	23.69
PROM1	0.372	0.628	0.013	0.348	33.6	34.91	34.37
ITGB5	1.511	0.612	0.003	0.006	24.53	23.81	25.33
TSPAN8	1.199	0.608	0.448	0.099	34.1	33.71	34.91
ITGB4	0.586	0.559	0.009	0.013	30.04	30.69	30.97
MFGE8	0.286	0.397	0.007	0.012	23.75	25.43	25.17
GJA1	0.471	0.385	0.130	0.087	21.33	22.3	22.8
TSPAN9	0.448	0.359	0.009	0.000	29.08	30.12	30.65
CD81	0.990	0.214	0.860	0.000	22.42	22.31	24.73
SYT7	0.469	0.207	0.071	0.022	30.84	31.81	33.2
MAP2K6	1.522	0.087	0.028	0.000	28.98	28.25	32.59

6.7.5.4 EGFRvIII knocked out and loss of PTEN gene study

The PCA was used to reduce the dimensions of the signal spectra. Each dot represents a spectrum of reduced dimensions. Each data set was clustered while maximizing covariance. A comparison of PC1 and PC2 in Figure S10 reveals the peaks responsible for the similarity and differentiation between EVs derived from different cell lines. Figure S6-10a shows the peaks associated with differentiation of EVs derived from parental glioma U373 and U87 cells and expressed with acquisition of the EGFRvIII mutation, correlating with PCA results in Figure 6-5b. Figures S10b and c illustrate peaks that differentiate EVs derived from GSC 1005 and GSC83, whether in wild-type form expressing oncogenic EGFRvIII, or in CRISPR/Cas9 knockout edited form lacking EGFR expression. Similarly, Figures S6-10b and c demonstrate the peaks responsible for differentiating between EVs derived from GSC 1005 and GSC83, in wild type form (that naturally express oncogenic EGFRvIII) and EGFR/EGFRvIIIknock-out (CRISPR/Cas9), in correlation with Figure 5c and d respectively. Figure S6-10d correlating with Figure 6-5e shows the principal peak components to primarily distinguish between EVs derived from GSC1123 cell line in wild type form and TMZ resistant form (GSC1123IC9R) expressing MGMT following gene demethylation.

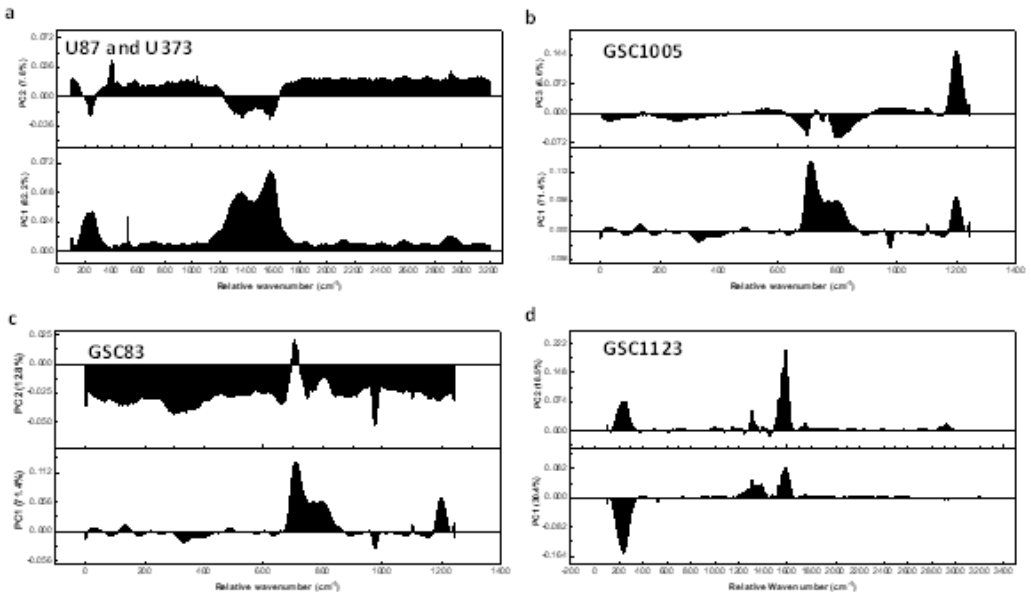

Figure S6-10. PC components of clustering of MoSERS profiles of EVs derived from genetically defined glioma cell lines. PC loading Raman bands of the (a) U373 and U87 in parental cells and their EGFRvIII expressing counterparts, (b) GSC1005 wild type cells and their EGFRvIII knocked-out variants, (c) GSC83 wild type cells and EGFRvIII knocked-out subline, (d) GSC1123 wild type cells and their in vivo derived variant resistant to TMZ due to expression of MGMT.

The consequences of EGFRvIII knock-out (CRISPR/Cas9) were also investigated in patient-derived glioma stem cells GSC83 and GSC1005, which naturally express oncogenic EGFRvIII. The PCA in Figure S11a shows the sensitivity of MoSERS microchip in the separation of EVs derived from these glioma cell lines. On the other hand, loss of PTEN tumour suppressor is common (>70%) and highly consequential for GBM progression by virtue of enabling major growth and survival pathways driving cancer cells. Therefore, we assessed the signatures of PTEN reconstituted cells derived from U87 cell line and compared it with EVs fingerprint derived from parental and EGFRvIII expressing variant cells of U87 glioma cell lines (Figure S11b). The comparison demonstrates the separation of EGFRvIII EVs from parental and PTEN expressed EVs.

Unlike EGFRvIII, PTEN is a gene that helps stop cells from replicating and growing. We found similar molecular fingerprint of EVs from cells with loss of PTEN and EVs from parental cells, which correlates with the cell morphology similarity.

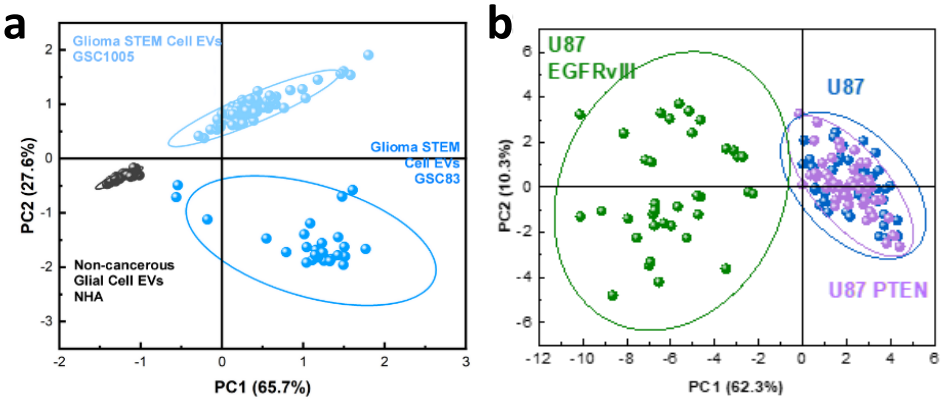

Figure S6-11. PCA clustering of MoSERS profiles of EVs derived from genetically defined glioma cell lines. a, PCA score plot of the GSC83 and GSC1005 SERS data, demonstrating the sensitivity of MoSERS in distinguishing them. b, PCA score plot of the SERS data comparing Parental, EGFRvIII and PTEN expressed cancer (U87 and U373).

6.7.5.5 Sensitivity for EVs

As MoSERS can identify EVs released by cells harboring mutant EGFRvIII, we next examined how sensitive we could identify EGFRvIII positive EVs among EVs with wild type EGFR. SERS signals generated by glioma-derived EVs expressing EGFRvIII relative to EVs derived from parental culture carrying wildtype EGFR (see Figure S12 for details) are stronger at 1430 cm^{-1} and weaker at 1345 cm^{-1}. A given EV's SERS intensity ratio at 1430 cm^{-1} versus 1345 cm^{-1} can, therefore, be used to determine how much EGFRvIII is present in comparison to wildtype EGFR (Figure S6-12a).

The detection limit for EGFRvIII was determined by creating a series of dilutions of EGFRvIII EVs suspended in the parental EVs and obtaining related single EV spectrums. In Figure S6-12b, the average intensity ratios for the relative wavenumbers of 1430 cm^{-1} versus 1345 cm^{-1} for each EGFRvIII dilution for each EV is plotted versus the percentage of cells expressing the EGFRvIII at the given dilution for each EV. Our results, linearly fitted with an R^2 value of 0.995, demonstrate a detection limit of 1.23% for EGFRvIII carrying EVs in the pool of wild type EGFR or EGFR-low carrying EVs (Figure S6-12c). This low detection limit of variants in the wild-type population suggests that MoSERS can potentially detect EVs carrying GBM related mutations that are diluted to low concentrations in the bloodstream.

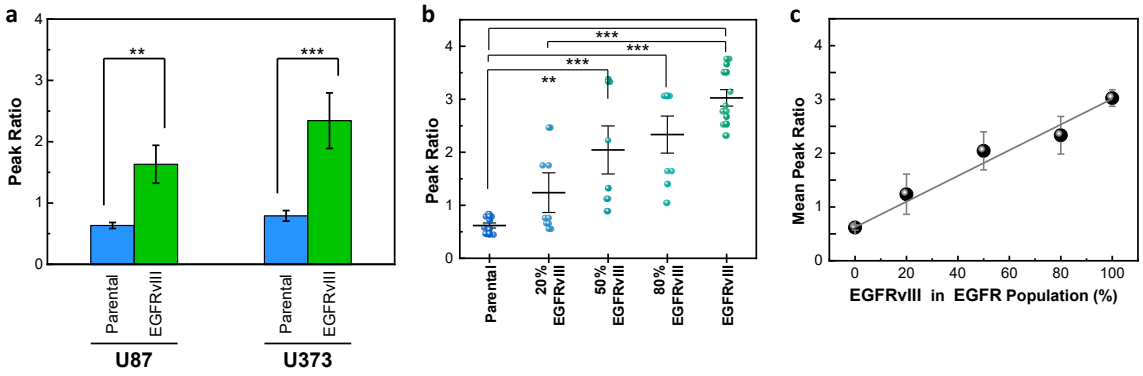

Figure S6-12. Sensitivity of MoSERS for EVs. (a) Peak intensity ratio analysis at 1430/1345 cm^{-1} relative wavenumber, for EVs derived from U87 and U373 glioma cell-lines (parental and EGFRvIII expressing). (b) The SERS intensity ratio at 1430/1345 cm-1 obtained from EVs derived from cell cultures containing a fraction of EGFRvIII expressing cells diluted in the parental cell culture (wildtype EGFR expressing). The blue and green points represent the intensity ratio for the single EV recordings. (c) The calibration plot of MoSERS for distinguishing molecular alteration EGFRvIII in wild type EGFR based on the averaged SERS intensity ratio at 1430/1345 cm^{-1} (black points).

6.7.5.6 Machine-Learning (Databases)

To overcome the complexity of EV heterogeneity, machine learning (ML) methods were employed and exploited to classify the subpopulations of EVs in their group of origin based on subtle changes in the single EV SERS fingerprints recorded. ML algorithms allow performing different types of analysis with the datasets in our library. Once the sample spectra are processed as previously described (Fig. S9), the database are given as an input to the ML algorithms, which then predict which of our predetermined classes it belongs to. The algorithms are trained using the datasets composed of a total of 946 spectra from 6 cell lines (harboring different cell mutations), making a total of 11 classes; or datasets formed by a total 1267 spectra from plasma samples of glioma patients and healthy donors. The distribution of the datasets for the training and testing set is summarized in Table S3. Each spectra is one-dimensional and contains 1245 observations (i.e. the intensity value as a function of the wavelength). Two ML algorithms were implemented, a convolutional neural network (CNN) discussed in detail in the main manuscript which had superior performance compared to the support vector machine (SVM).

As a first stage, we aimed to use a multiclass ML to categorize different spectra into the 1 pre-determined classes according to the cell lines and their variations (NHA, U87 Parental, U87 EGFRvIII, U87 PTEN, U373 Parental, U373 EGFRvIII, GSC83 wt, GSC1005 wt, GSC1123, GSC1123 MGMT). In the second stage, a straightforward answer was sought: we aimed for the ML algorithm to predict the health status of an individual. In this case, the prediction of the cell lines was not sufficient because these samples might contain EVs from several other cell lines in the body. Thus, we aimed to generate a binary classification, to determine whether the individual's spectra analyzed belong to a healthy individual or a patient. determining them as "GBM-positive" or "GBM-negative". The final step aimed to train the algorithms in order to classify spectra and

differentiate between healthy, and the mutations EGFR amplified, EGFRvIII and MGMT methylation. For which a 2-step training was implemented on both the SVM and CNN algorithms separately. To better capture patient variability, it is necessary to include in the training set previously categorized spectra belonging to patient samples. For that, we used patients whose clinical results showed only a few mutations: patient 1 only has MGMT methylation, and patient 7 has only EGFR amplification and EGFRvIII. We first trained both algorithms using the following classes: healthy (with the NHA cell line, and one healthy human sample), and MGMT methylation with spectra from MGMT 1123IC9R cell line. Then, we tested the algorithms on 70% of the spectra from patient 7. We then trained the algorithms again on 3 different classes: healthy, EGFR amplified and EGFRvIII, and tested them on 70% of the spectra from patient 1 (single-EV spectra of CSF and blood samples). CSF is included in the training set since it represents a naturally enriched reservoir of GBM EVs in clinically accessible settings for more precise training of the algorithm, and as such would provide potentially important translational clues.

Table S6-3. Summary of sets used for each algorithm for the three different conditions.

	CNN		SVM	
	Training set	Testing set	Training set	Testing set
Cell Lines	• 70% of the dataset* with all cell lines and variations.	• 30% remaining of that dataset	• 70% of the dataset with all cell lines and variations.	• 30% remaining of that dataset
Binary	• 80% of healthy samples (1,2,3,4) and of the NHA cell line.	• 20% remaining	• 80% of healthy samples (1,2,3,4) and of the NHA cell line.	• 20% remaining

	• 80% of patient samples (3,5 and 8) and the U373 viii, U87 viii and GSC 1123-9 cell lines.	healthy controls • 20% remaining patient samples	• 80% of patient samples (3,5 and 8) and the U373 viii, U87 viii and MGMT 1123-9 cell lines.	healthy controls • 20% remaining patient samples
Variants	• NHA, 100% of 2 healthy samples (healthy class) • U87 and U373 parental spectra classified as EGFR amp from a subset of 70% of the spectra of patient 7 (EGFR amp class) • U87 and U373 EGFRvIII and spectra classified as EGFRvIII from a subset of 70% of spectra from patient sample which clinically diagnosed with EGFRvIII (EGFRvIII class) • MGMT9 and spectra classified as MGMT methylation from a subset of 70% of spectra from patient sample which clinically diagnosed with (MGMT methylation)	• Remaining Healthy controls and Patient samples. (Including the 30% of sample which clinically diagnosed with EGFRvIII that have not been used in the training)	• NHA, 100% of 2 healthy samples (healthy class); • U87 and U373 parental, EGFR protein and the spectra classified as EGFR amp from a subset of 70% of the spectra of patient 7 (EGFR amp class); • U87 and U373 EGFRvIII and spectra classified as EGFRvIII from a subset of 70% of spectra from patient sample which clinically diagnosed with EGFRvIII (EGFRvIII class) • MGMT9 and spectra classified as MGMT methylation from a subset of 70% of spectra from patient sample which	• Remaining Healthy controls and Patient samples. (Including the 30% of sample which clinically diagnosed with EGFRvIII that have not been used in the training)

			clinically diagnosed with (MGMT methylation)	

*Dataset: NHA, U87 Parental, U87 EGFRvIII, U373 Parental, U373 EGFRvIII, GSC83 wt, GSC83 ko, GSC1005 wt, GSC1005 ko, GSC 1123, GSC 1123 MGMT.

6.7.6 Characterization of Human Circulating EVs

6.7.6.1 Human Blood Sample Study (Patient and Healthy)

To achieve a binary classification, we redesigned the SVM, the hyperparameters were optimized as previously mentioned, giving the following hyperparameters: a rbf kernel, C: 10.09, gamma: 0.0658. The algorithm was trained on two class of dataset, (1) healthy: containing 80% of spectra from 4 healthy samples and the non-cancer glial NHA cell line, (2) patient: 80% of spectra of 3 of the patient samples and the U373vIII, U87vIII and GSC 1123-9 cell lines (Table S6-3). The testing set contained all remaining healthy and patient samples. The patient samples were collected from individuals, with a confirmed glioblastoma diagnosis, moments prior to undergoing surgery. The patients/healthy datasets were generated by EVs samples derived from the plasma of eight healthy donors and ten diagnosed patients'plasma. The dataset of raw spectra is composed of approximately 70 raw spectra collected from of each heathy donors and diagnosed patients, shown in Fig. S6-13a and b, respectively. Following the protocol described earlier for data processing in the collection of spectra ready for analysis are shown in Fig. S6-14a and b.

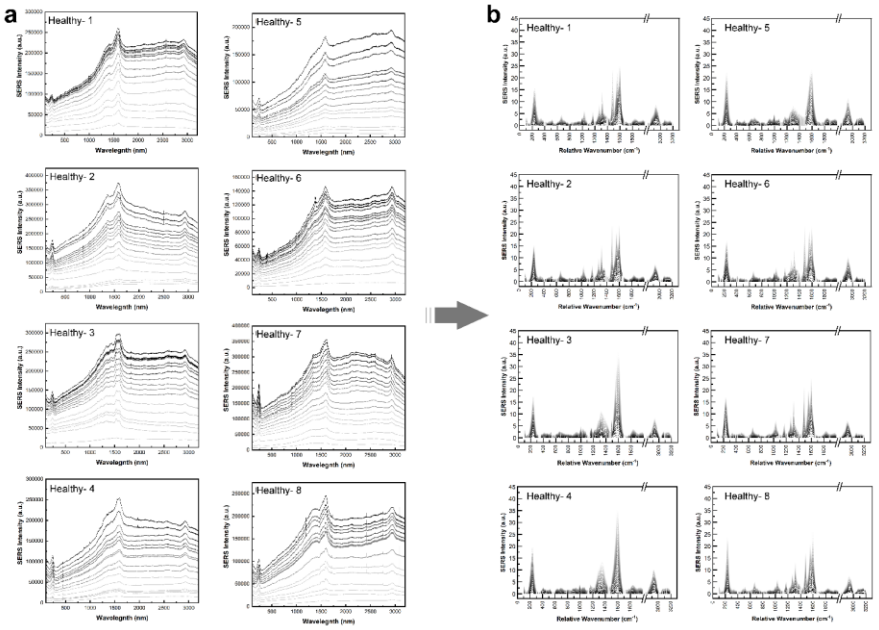

Figure S6-13. SERS single EV characterization. Healthy plasma (a) before and (b) after processing.

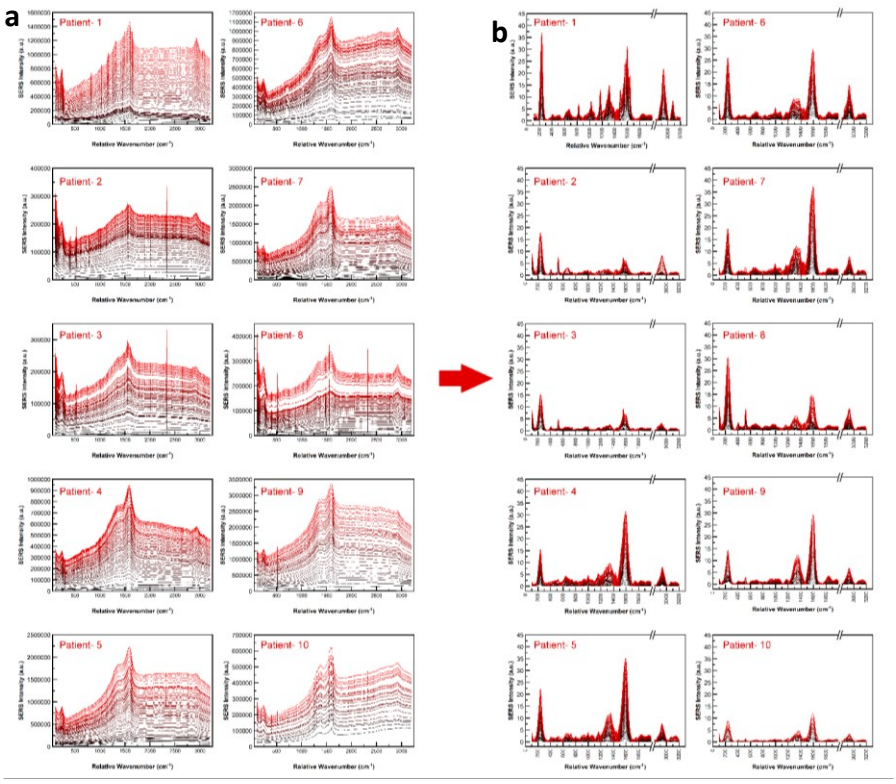

Figure S6-14. SERS single EV characterization. GBM patient's plasma a, before and b, after processing.

6.7.6.2 Machine Learning Algorithms (Human Samples)

The CNN here established is derived from Ho et al.'s paper (Ho et al., 2019), which in turn based its code on He's algorithm (He et al.). The implementation of residual blocks facilitates the resolution of exploding/vanishing gradients problems recurrent in deep networks (He et al.). The hyperparameters (number of hidden filters, number of blocks, learning rate and betas for the optimizer) were determined through grid search. The batch size was set to 5. The loss function is cross-entropy, and the optimizer function is the Adam optimizer (Kingma & Ba). To provide a base comparison between the two ML algorithms, the training and testing datasets are identical to the ones utilized for SVM. To prevent the overfitting of the data, the training process is validated using a validation set (10% of the training set). (Yang et al.) For the cell line classification, the CNN'sining was stopped at 8 epochs since convergence was reached.

To verify that the algorithm is successfully being trained, the loss of the training and validation sets, as well as the accuracy of both were monitored. Training is deemed successful when these values converge, towards 0 for the loss, and 1 for the accuracy. The results of the test set showed the CNN algorithm outperformed the SVM algorithm on this task, with a global accuracy of 79.80%. The same behavior is shown when the 11 cell line classes, including mutations, are classified into the 6 cell lines, with the CNN achieving better accuracy for each group, compared to the SVM. For the binary classification of the human samples, the outputs of the fully connected CNN layer are plotted to show the accuracy, which remains higher than that of the SVM. A comparison of their ROC and AUC is shown in Figure S6-15.

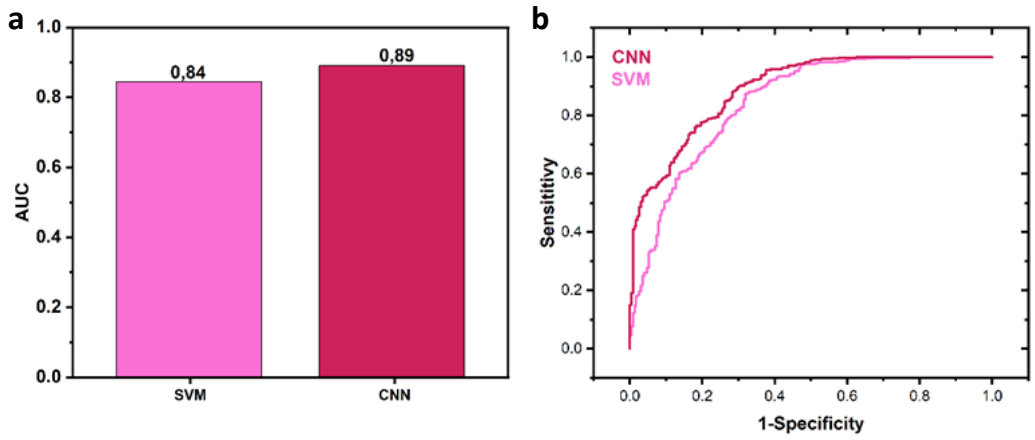

Figure S6-15. Machine learning binary classification performance comparison between SVM and CNN. (a) ROC curves for both algorithms (b) AUC graph comparing the performance of the models.

To In Figure S16, we illustrate the successful training process of the CNN algorithm for the binary classification. The outputs from the fully connected layer are shown for the training and test data, in relation to the increase in epochs number. Each dot in the graphs represents a single EV spectrum, either from the healthy (negative) or patient (positive) class. We can clearly see how the training data goes from being indistinguishable (Epoch 1), to two clearly separated classes (Epoch 15). The loss and accuracy curves were obtained to verify the appropriate training of the algorithm, and the convergence was reached after 15 epochs.

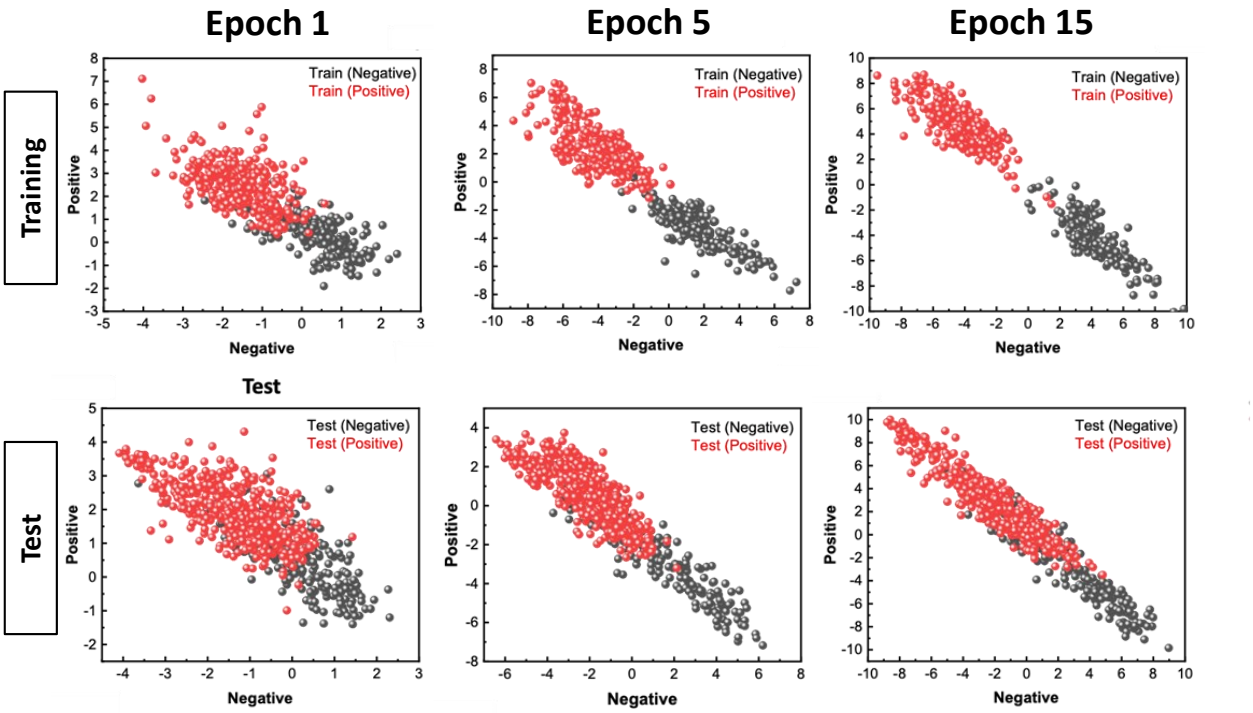

Figure S6-16. The distinction of two classes as CNN epochs increase. The algorithm starts with two indistinguishable classes (positive and negative) in Epoch 1, (the first iteration of the algorithm with the data set). As the Epoch increases, the classes become more defined, until it reaches convergence in Epoch 15.

6.8 References

Adnani, L., Kassouf, J., Meehan, B., Spinelli, C., Tawil, N., Nakano, I. & Rak, J. (2022). Angiocrine extracellular vesicles impose mesenchymal reprogramming upon proneural glioma stem cells. *Nature Communications*, *13*(1), 1–14.

Akselrod, G. M., Ming, T., Argyropoulos, C., Hoang, T. B., Lin, Y., Ling, X., Smith, D. R., Kong, J. & Mikkelsen, M. H. (2015). Leveraging nanocavity harmonics for control of optical processes in 2d semiconductors. *Nano Letters*, *15*(5), 3578–3584.

Al-Nedawi, K., Meehan, B., Micallef, J., Lhotak, V., May, L., Guha, A. & Rak, J. (2008). Intercellular transfer of the oncogenic receptor EGFRvIII by microvesicles derived from tumour cells. *Nature Cell Biology*, *10*(5), 619–624.

Ang, M. J. Y., Yoon, J., Zhou, M., Wei, H. L., Goh, Y. Y., Li, Z., Feng, J., Wang, H., Su, Q., Ong, D. S. T. & Liu, X. (2022). Deciphering Nanoparticle Trafficking into Glioblastomas Uncovers an Augmented Antitumor Effect of Metronomic Chemotherapy. *Advanced Materials*, *34*(3), 2106194.

Bastola, S., Pavlyukov, M. S., Yamashita, D., Ghosh, S., Cho, H., Kagaya, N., Zhang, Z., Minata, M., Lee, Y., Sadahiro, H., Yamaguchi, S., Komarova, S., Yang, E., Markert, J., Nabors, L. B., Bhat, K., Lee, J., Chen, Q., Crossman, D. K., … Nakano, I. (2020). Glioma-initiating cells at tumor edge gain signals from tumor core cells to promote their malignancy. *Nature Communications*, *11*(1), 1–17.

Boriachek, K., Islam, M. N., Möller, A., Salomon, C., Nguyen, N. T., Hossain, M. S. A., Yamauchi, Y. & Shiddiky, M. J. A. (2018). Biological Functions and Current Advances in Isolation and Detection Strategies for Exosome Nanovesicles. *Small*, *14*(6), 1–21.

Chen, C., Yan, D., Wang, Y., Zhou, Y., Zou, Y., Li, Y. & Wang, S. (2019). B□N Pairs Enriched Defective Carbon Nanosheets for Ammonia Synthesis with High Efficiency. *Small*, *15*(7), 1805029.

Chen, C., Zong, S., Liu, Y., Wang, Z., Zhang, Y., Chen, B. & Cui, Y. (2019). Profiling of Exosomal Biomarkers for Accurate Cancer Identification: Combining DNA-PAINT with Machine-Learning-Based Classification. *Small*, *15*(43), 1901014.

Choi, D., Montermini, L., Jeong, H., Sharma, S., Meehan, B. & Rak, J. (2019). Mapping Subpopulations of Cancer Cell-Derived Extracellular Vesicles and Particles by Nano-Flow Cytometry. *ACS Nano*, *13*(9), 10499–10511. https://doi.org/10.1021/acsnano.9b04480

Choi, D., Montermini, L., Kim, D. K., Meehan, B., Roth, F. P. & Rak, J. (2018). The impact of oncogenic egfrviii on the proteome of extracellular vesicles released from glioblastoma cells. *Molecular and Cellular Proteomics*, *17*(10), 1948–1964.

Daniel, P., Meehan, B., Sabri, S., Jamali, F., Sarkaria, J. N., Choi, D., Garnier, D., Kitange, G., Glennon, K. I., Paccard, A., Karamchandani, J., Riazalhosseini, Y., Rak, J. & Abdulkarim, B.

(2022). Detection of temozolomide-induced hypermutation and response to PD-1 checkpoint inhibitor in recurrent glioblastoma. *Neuro-Oncology Advances*, *4*(1).

Del Real Mata, C., Siavash Moakhar, R., Hosseini, I. I., Jalali, M. & Mahshid, S. (2021). A nanostructured microfluidic device for plasmon-assisted electrochemical detection of hydrogen peroxide released from cancer cells. *Nanoscale*, *13*(34), 14316–14329.

Eda, G. & Maier, S. A. (2013). Two-dimensional crystals: Managing light for optoelectronics. *ACS Nano*, *7*(7), 5660–5665.

Ferguson, S., Yang, K. S., Zelga, P., Liss, A. S., Carlson, J. C. T., del Castillo, C. F. & Weissleder, R. (2022). Single-EV analysis (sEVA) of mutated proteins allows detection of stage 1 pancreatic cancer. *Science Advances*, *8*(16).

Fraire, J. C., Stremersch, S., Bouckaert, D., Monteyne, T., De Beer, T., Wuytens, P., De Rycke, R., Skirtach, A. G., Raemdonck, K., De Smedt, S. & Braeckmans, K. (2019). Improved Label-Free Identification of Individual Exosome-like Vesicles with Au@Ag Nanoparticles as SERS Substrate. *ACS Applied Materials and Interfaces*, *11*(43), 39424–39435.

Fraser, K., Jo, A., Giedt, J., Vinegoni, C., Yang, K. S., Peruzzi, P., Chiocca, E. A., Breakefield, X. O., Lee, H. & Weissleder, R. (2019). Characterization of single microvesicles in plasma from glioblastoma patients. *Neuro-Oncology*, *21*(5), 606–615.

Garnier, D., Meehan, B., Kislinger, T., Daniel, P., Sinha, A., Abdulkarim, B., Nakano, I. & Rak, J. (2018). Divergent evolution of temozolomide resistance in glioblastoma stem cells is reflected in extracellular vesicles and coupled with radiosensitization. *Neuro-Oncology*, *20*(2), 236–248.

Gu, Z., Chen, S. H., Ding, Z., Song, W., Wei, W., Liu, S., Ma, G. & Zhou, R. (2019). The molecular mechanism of robust macrophage immune responses induced by PEGylated molybdenum disulfide. *Nanoscale*, *11*(46), 22293–22304.

Ho, C. S., Jean, N., Hogan, C. A., Blackmon, L., Jeffrey, S. S., Holodniy, M., Banaei, N., Saleh, A. A. E., Ermon, S. & Dionne, J. (2019). Rapid identification of pathogenic bacteria using Raman spectroscopy and deep learning. *Nature Communications*, *10*(1), 1–8.

Im, H., Shao, H., Park, Y. Il, Peterson, V. M., Castro, C. M., Weissleder, R. & Lee, H. (2014). Label-free detection and molecular profiling of exosomes with a nano-plasmonic sensor. *Nature Biotechnology*, *32*(5), 490–495.

Jalali, M., Gao, Z., Yu, Y., Siavash Moakhar, R., Ding, Y., Zhuang, M., Zhou, N., König, T., Fery, A., Mahshid, S. & Luo, Z. (2021). Synergistic enhancement of photoluminesent intensity in monolayer molybdenum disulfide embedded with plasmonic nanostructures for catalytic sensing. *2D Materials*, *8*(3), 035049.

Jalali, M., Isaac Hosseini, I., AbdelFatah, T., Montermini, L., Wachsmann Hogiu, S., Rak, J. & Mahshid, S. (2021). Plasmonic nanobowtiefluidic device for sensitive detection of glioma extracellular vesicles by Raman spectrometry. *Lab on a Chip*, *21*(5), 855–866.

Jalali, M., Moakhar, R. S., Abdelfattah, T., Filine, E., Mahshid, S. S. & Mahshid, S. (2020). Nanopattern-Assisted Direct Growth of Peony-like 3D MoS2/Au Composite for Nonenzymatic Photoelectrochemical Sensing. *ACS Applied Materials and Interfaces*, *12*(6), 7411–7422.

Lane, R., Simon, T., Vintu, M., Solkin, B., Koch, B., Stewart, N., Benstead-Hume, G., Pearl, F. M. G., Critchley, G., Stebbing, J. & Giamas, G. (2019). Cell-derived extracellular vesicles can be used as a biomarker reservoir for glioblastoma tumor subtyping. *Communications Biology*, *2*(1), 1–12.

Le Ru, E. C., Blackie, E., Meyer, M. & Etchegoint, P. G. (2007). Surface enhanced raman scattering enhancement factors: A comprehensive study. *Journal of Physical Chemistry C*, *111*(37), 13794–13803.

Lee, K., Fraser, K., Ghaddar, B., Yang, K., Kim, E., Balaj, L., Chiocca, E. A., Breakefield, X. O., Lee, H. & Weissleder, R. (2018a). Multiplexed Profiling of Single Extracellular Vesicles. *ACS Nano*, *12*(1), 494–503.

Lee, K., Fraser, K., Ghaddar, B., Yang, K., Kim, E., Balaj, L., Chiocca, E. A., Breakefield, X. O., Lee, H. & Weissleder, R. (2018b). Multiplexed Profiling of Single Extracellular Vesicles. *ACS Nano*, *12*(1), 494–503.

Lee, K., Fraser, K., Ghaddar, B., Yang, K., Kim, E., Balaj, L., Chiocca, E. A., Breakefield, X. O., Lee, H. & Weissleder, R. (2018c). Multiplexed Profiling of Single Extracellular Vesicles. *ACS Nano*, *12*(1), 494–503.

Liang, Y., Lehrich, B. M., Zheng, S. & Lu, M. (2021). Emerging methods in biomarker identification for extracellular vesicle-based liquid biopsy. In *Journal of Extracellular Vesicles* (Vol. 10, Issue 7, p. e12090). John Wiley & Sons, Ltd.

Louis, D. N., Perry, A., Reifenberger, G., Deimling, A. Von, Figarella, D., Webster, B., Hiroko, K. C., Wiestler, O. D., Kleihues, P. & Ellison, D. W. (2016). The 2016 World Health Organization Classification of Tumors of the Central Nervous System : a summary. *Acta Neuropathologica*, *131*(6), 803–820.

Magnus, N., Garnier, D., Meehan, B., McGraw, S., Lee, T. H., Caron, M., Bourque, G., Milsom, C., Jabado, N., Trasler, J., Pawlinski, R., Mackman, N. & Rak, J. (2014). Tissue factor expression provokes escape from tumor dormancy and leads to genomic alterations. *Proceedings of the National Academy of Sciences of the United States of America*, *111*(9), 3544–3549.

Mao, P., Joshi, K., Li, J., Kim, S. H., Li, P., Santana-Santos, L., Luthra, S., Chandran, U. R., Benos, P. V., Smith, L., Wang, M., Hu, B., Cheng, S. Y., Sobol, R. W. & Nakano, I. (2013). Mesenchymal glioma stem cells are maintained by activated glycolytic metabolism involving aldehyde dehydrogenase 1A3. *Proceedings of the National Academy of Sciences of the United States of America*, *110*(21), 8644–8649.

Mollaei, H., Safaralizadeh, R. & Pouladi, N. (2017). A brief review of exosomes and their roles in

cancer. *Meta Gene*, *11*, 70–74.

Nawaz, M., Fatima, F., Zanetti, B. R. & Martins, I. D. L. (2014). *Microvesicles in Gliomas and Medulloblastomas : An Overview*. *February*.

Pan, S., Zhang, Y., Natalia, A., Lim, C. Z. J., Ho, N. R. Y., Chowbay, B., Loh, T. P., Tam, J. K. C. & Shao, H. (2021). Extracellular vesicle drug occupancy enables real-time monitoring of targeted cancer therapy. *Nature Nanotechnology*, *16*(6), 734–742.

Park, J., Hwang, M., Choi, B., Jeong, H., Jung, J. H., Kim, H. K., Hong, S., Park, J. H. & Choi, Y. (2017a). Exosome Classification by Pattern Analysis of Surface-Enhanced Raman Spectroscopy Data for Lung Cancer Diagnosis. *Analytical Chemistry*, *89*(12), 6695–6701.

Park, J., Hwang, M., Choi, B., Jeong, H., Jung, J. H., Kim, H. K., Hong, S., Park, J. H. & Choi, Y. (2017b). Exosome Classification by Pattern Analysis of Surface-Enhanced Raman Spectroscopy Data for Lung Cancer Diagnosis. *Analytical Chemistry*, *89*(12), 6695–6701.

Platt, J. & others. (1999). Probabilistic outputs for support vector machines and comparisons to regularized likelihood methods. *Advances in Large Margin Classifiers*, *10*(3), 61–74.

Ramirez, M. I., Amorim, M. G., Gadelha, C., Milic, I., Welsh, J. A., Freitas, V. M., Nawaz, M., Akbar, N., Couch, Y., Makin, L., Cooke, F., Vettore, A. L., Batista, P. X., Freezor, R., Pezuk, J. A., Rosa-Fernandes, L., Carreira, A. C. O., Devitt, A., Jacobs, L., … Dias-Neto, E. (2018). Technical challenges of working with extracellular vesicles. In *Nanoscale* (Vol. 10, Issue 3, pp. 881–906). Royal Society of Chemistry.

Reifenberger, G., Wirsching, H. G., Knobbe-Thomsen, C. B. & Weller, M. (2017). Advances in the molecular genetics of gliomas-implications for classification and therapy. In *Nature Reviews Clinical Oncology* (Vol. 14, Issue 7, pp. 434–452). Nature Publishing Group.

Res, E. S. (2017). Exosomes in blood and cancer. *Translational Cancer Research*, *6*, 1316–1320.

S Rickard, J. J., Di-Pietro, V., Smith, D. D. J., Davies, D. J., Belli, A. & Goldberg Oppenheimer, P. (2020). *Rapid optofluidic detection of biomarkers for traumatic brain injury via surface-enhanced Raman spectroscopy*. *4*(6), 610–623.

Shao, H., Chung, J., Balaj, L., Charest, A., Bigner, D. D., Carter, B. S., Hochberg, F. H., Breakefield, X. O., Weissleder, R. & Lee, H. (2012). Protein typing of circulating microvesicles allows real-time monitoring of glioblastoma therapy. *Nature Medicine*, *18*(12), 1835–1840.

Shao, H., Chung, J., Lee, K., Balaj, L., Min, C., Carter, B. S., Hochberg, F. H., Breakefield, X. O., Lee, H. & Weissleder, R. (2015). Chip-based analysis of exosomal mRNA mediating drug resistance in glioblastoma. *Nature Communications*, *6*(1), 1–9.

Shin, H., Jeong, H., Park, J., Hong, S. & Choi, Y. (2018). Correlation between Cancerous Exosomes and Protein Markers Based on Surface-Enhanced Raman Spectroscopy (SERS) and Principal Component Analysis (PCA) [Research-article]. *ACS Sensors*, *3*, 2637–2643.

https://doi.org/10.1021/acssensors.8b01047

Shin, H., Oh, S., Hong, S., Kang, M., Kang, D., Ji, Y. G., Choi, B. H., Kang, K. W., Jeong, H., Park, Y., Kim, H. K. & Choi, Y. (2020). Early-Stage Lung Cancer Diagnosis by Deep Learning-Based Spectroscopic Analysis of Circulating Exosomes. *ACS Nano*, *14*(5), 5435–5444. https://doi.org/10.1021/acsnano.9b09119

Siavash Moakhar, R., Abdelfatah, T., Sanati, A., Jalali, M., Flynn, S. E., Mahshid, S. S. & Mahshid, S. (2020). A Nanostructured Gold/Graphene Microfluidic Device for Direct and Plasmonic-Assisted Impedimetric Detection of Bacteria. *ACS Applied Materials and Interfaces*, *12*(20), 23298–23310. https://doi.org/10.1021/acsami.0c02654

Siavash Moakhar, R., del Real Mata, C., Jalali, M., Shafique, H., Sanati, A., de Vries, J., Strauss, J., AbdElFatah, T., Ghasemi, F., McLean, M., I. Hosseini, I., Lu, Y., Yedire, S. G., Mahshid, S. S., Tabatabaiefar, M. A., Liang, C. & Mahshid, S. (2022). A Versatile Biomimic Nanotemplating Fluidic Assay for Multiplex Quantitative Monitoring of Viral Respiratory Infections and Immune Responses in Saliva and Blood. *Advanced Science*, *9*(33), 2204246.

Splendiani, A., Sun, L., Zhang, Y., Li, T., Kim, J., Chim, C. Y., Galli, G. & Wang, F. (2010). Emerging photoluminescence in monolayer MoS 2. *Nano Letters*, *10*(4), 1271–1275.

Tawil, N., Bassawon, R., Meehan, B., Nehme, A., Montermini, L., Gayden, T., de Jay, N., Spinelli, C., Chennakrishnaiah, S., Choi, D., Adnani, L., Zeinieh, M., Jabado, N., Kleinman, C. L., Witcher, M., Riazalhosseini, Y., Key, N. S., Schiff, D., Grover, S. P., … Rak, J. (2021). Glioblastoma cell populations with distinct oncogenic programs release podoplanin as procoagulant extracellular vesicles. *Blood Advances*, *5*(6), 1682–1694.

van der Vlist, E. J., Nolte-’t Hoen, E. N. M., Stoorvogel, W., Arkesteijn, G. J. A. & Wauben, M. H. M. (2012). Fluorescent labeling of nano-sized vesicles released by cells and subsequent quantitative and qualitative analysis by high-resolution flow cytometry. *Nature Protocols*, *7*(7), 1311–1326.

Walter, A., März, A., Schumacher, W., Rösch, P. & Popp, J. (2011). Towards a fast, high specific and reliable discrimination of bacteria on strain level by means of SERS in a microfluidic device. *Lab on a Chip*, *11*(6), 1013–1021.

Wells, S. M., Retterer, S. D., Oran, J. M. & Sepaniak, M. J. (2009). Controllable nanofabrication of aggregate-like nanoparticle substrates and evaluation for surface-enhanced Raman spectroscopy. *ACS Nano*, *3*(12), 3845–3853.

Wirsching, H. G., Galanis, E. & Weller, M. (2016). Glioblastoma. In *Handbook of Clinical Neurology* (Vol. 134, pp. 381–397). Elsevier.

Wu, C.-Y., Du, S.-L., Zhang, J., Liang, A.-L. & Liu, Y.-J. (2017). Exosomes and breast cancer: a comprehensive review of novel therapeutic strategies from diagnosis to treatment. *Cancer Gene Therapy*, *24*(1), 6–12.

Wu, P., Cai, J., Chen, Q., Han, B., Meng, X., Li, Y., Li, Z., Wang, R., Lin, L., Duan, C., Kang, C.

& Jiang, C. (2019). Lnc-TALC promotes O 6 -methylguanine-DNA methyltransferase expression via regulating the c-Met pathway by competitively binding with miR-20b-3p. *Nature Communications*, *10*(1), 1–15.

Wu, R., Ou, X., Tian, R., Zhang, J., Jin, H., Dong, M., Li, J. & Liu, L. (2018). Membrane destruction and phospholipid extraction by using two-dimensional MoS2 nanosheets. *Nanoscale*, *10*(43), 20162–20170.

Yang, K. S., Im, H., Hong, S., Pergolini, I., Del Castillo, A. F., Wang, R., Clardy, S., Huang, C. H., Pille, C., Ferrone, S., Yang, R., Castro, C. M., Lee, H., Del Castillo, C. F. & Weissleder, R. (2017). Multiparametric plasma EV profiling facilitates diagnosis of pancreatic malignancy. *Science Translational Medicine*, *9*(391).

Yang, Z., Atiyas, Y., Shen, H., Siedlik, M. J., Wu, J., Beard, K., Fonar, G., Dolle, J. P., Smith, D. H., Eberwine, J. H., Meaney, D. F. & Issadore, D. A. (2022). Ultrasensitive Single Extracellular Vesicle Detection Using High Throughput Droplet Digital Enzyme-Linked Immunosorbent Assay. *Nano Letters*, *22*(11), 4315–4324.

Ye, R., Song, W., Ou, X., Gu, Z. & Zhang, D. (2021). Membrane Insertion of MoS2 Nanosheets: Fresh vs. Aged. *Frontiers in Chemistry*, *9*, 499.

Zachariah, M. A., Oliveira-Costa, J. P., Carter, B. S., Stott, S. L. & Nahed, B. V. (2018). Blood-based biomarkers for the diagnosis and monitoring of gliomas. *Neuro-Oncology*, *20*(9), 1155–1161.

Zhang, K., Yue, Y., Wu, S., Liu, W., Shi, J. & Zhang, Z. (2019). Rapid Capture and Nondestructive Release of Extracellular Vesicles Using Aptamer-Based Magnetic Isolation. *ACS Sensors*, *4*(5), 1245–1251.

Zhang, P., Zhou, X., He, M., Shang, Y., Tetlow, A. L., Godwin, A. K. & Zeng, Y. (2019). Ultrasensitive detection of circulating exosomes with a 3D-nanopatterned microfluidic chip. *Nature Biomedical Engineering*, *3*(6), 438–451.

Zhao, Z., Yang, Y., Zeng, Y. & He, M. (2016). A microfluidic ExoSearch chip for multiplexed exosome detection towards blood-based ovarian cancer diagnosis. *Lab on a Chip*, *16*(3), 489–496.

Zhou, J., Wu, Z., Hu, J., Yang, D., Chen, X., Wang, Q., Liu, J., Dou, M., Peng, W., Wu, Y., Wang, W., Xie, C., Wang, M., Song, Y., Zeng, H. & Bai, C. (2020). High-throughput single-EV liquid biopsy: Rapid, simultaneous, and multiplexed detection of nucleic acids, proteins, and their combinations. *Science Advances*, *6*(47).

Zhou, Y. G., Mohamadi, R. M., Poudineh, M., Kermanshah, L., Ahmed, S., Safaei, T. S., Stojcic, J., Nam, R. K., Sargent, E. H. & Kelley, S. O. (2016). Interrogating Circulating Microsomes and Exosomes Using Metal Nanoparticles. *Small*, *12*(6), 727–732.

7 Bridging Chapters 6 and 8

In chapter VI we demonstrated an on-chip single EV isolation method using MoS_2 embedded plasmonic nanocavity array. The interaction of bilayer lipid of the EVs were studied theoretically and experimentally demonstrated a positive interaction between the two resulting in the entrapment of single EVs in the plasmonic nanocavities. By leveraging the plasmonic enhancement of the surface, we were able to provide electromagnetic (EM) field enhancement and record surface-enhanced Raman spectra of single EV resolution. Despite the promising results, there are still gaps in our understanding of the EM-field enhancement mechanisms at play in a monolayer MoS_2-embedded nanocavity. This prompted us to undertake further investigation in chapter VIII, where we delved into the material physics of the system.

In chapter VIII, we initially focused on studying the light-matter interactions between monolayer MoS_2 to shed new light on the mechanisms of EM-field enhancement in the MoS_2-embedded nanocavity system. By exploring these mechanisms, we aimed to better understand the underlying physical phenomena that enable the observed EM-field enhancement and ultimately improve the performance of our method for single EV isolation. Our findings demonstrated that the energy transfer, charge transfer, and photoluminescence enhancement resulting from the light-matter interaction between the MoS_2 layer and the plasmonic nanostructure participate in the SERS efficiency enhancement of a single EV.

We then used this device in *Chapter 6* to measure the extent of its potential in differentiating the fingerprint spectra of EVs in GBM paradigm. When interfaced with a convolutional neural network (CNN), single EV SERS showed an accuracy of 87% with which GBM patient samples were differentiated in 12 patient blood samples, on par with clinical pathology tests.

In *Chapter 8*, we discuss a study that builds upon the single EV SERS fingerprinting technology to explore the molecular changes that contribute to the cellular evolution of TMZ-naïve and -resistance xenograft models in a series of human glioma stem cells (GSCs) with mesenchymal molecular characteristics. The presence of these characteristic molecular traits was monitored in the presence of TMZ after 24 and 72 hours, demonstrating the set of molecular traits responsible for distinguishing the susceptible and resistant cells. The final aim is to use the single EV SERS interfaced with machine learning to identify the molecular traits that distinguish susceptible and resistant cells, and to quantify the SERS results of circulating EVs in the cerebrospinal fluid (CSF) and plasma of patients diagnosed with TMZ-resistant or -naïve GBM cancer.

8 Biomarker-Free Single Extracellular Vesicle SERS for Molecular Profiling of Resistance in Glioblastoma

Mahsa Jalali[1], Yao Lu[1], Laura Montermini[2], Walter Reisner[3], Janusz Rak[2], Sara Mahshid[1,4*]

[1] Department of Bioengineering, McGill University, Montreal, QC, Canada

[2] Research Institute of the McGill University Health Centre (RIMUHC), Montreal, Quebec, Canada

[3] Department of Physics, McGill University, Montreal, QC, Canada

[4]Department of Medicine, Division of Experimental Medicine, McGill University, Montreal, QC, Canada

Abstract

For cancers with low survival rates due to acquired therapy resistance, technologies monitoring of the molecular drift of cancer cells are key to improve outcomes. Extracellular vesicles (EVs) released by cancer cells carry molecular fingerprints of the underlying disease with considerable diagnostic potential but their application in complex cancers such as glioblastoma (GBM) poses multiple l challenges such as scarcity of tumour EVs in biofluids, their heterogeneity, and intrinsic complexity. Surface-enhanced Raman spectroscopy (SERS) produces a label-free spectroscopic fingerprint reflecting molecular composition of individual EVs and their populations. Using single EV (sEV) SERS, we have previously demonstrated the ability to detect crucial biomarkers of GBM progression. Here, we explored the SERS spectra reflective of molecular changes that contribute to the cellular responses to temozolomide (TMZ) chemotherapy, which is a cornerstone of the standard care in GBM patients and to which they inevitably develop resistance. In a series of human glioma stem cells (GSCs) with mesenchymal molecular characteristics we demonstrate SERS detectable changes associated with exposure to TMZ and loss of TMZ response due to specific molecular mechanisms such as expression of O6-methylguanine DNA methyltransferase (MGMT) or hypermutant phenotype. We also quantified the sEV SERS results of circulating EVs in the cerebrospinal fluid (CSF) and plasma of GBM patients with 96% accuracy on par with clinical pathology tests.

Keywords: Single Extracellular Vesicle (sEV), SERS, Molecular Subtypes, Glioblastoma, Temozolomide, Drug resistance

8.1 Introduction

High High grade brain tumours (HGBTs), such as glioblastoma (GBM) remain intractable, as they evolve rapidly confounding and outpacing standard diagnostic and therapeutic methods.(Wirsching et al., 2016) They are also relatively inaccessible to direct longitudinal molecular sampling (standard biopsy) due to risks and limitations associated with post-resection patient care.(Louis et al., 2016; Nawaz et al., 2014; P. Wu et al., 2019) Current GBM diagnostics consists of imaging and invasive tissue collection (at surgery or initial biopsy) unable to give a rapid, safe, sensitive and frequent access to information regarding disease progression and therapeutic responses.(Reifenberger et al., 2017) Indeed, the absence of alternative non-invasive diagnostic methods is among the major impediments in exploring new therapies in GBM.

The molecular makeup of HGBTs is reflected in the composition of cellular fragments, known as extracellular vesicles (EVs) which are released from tumour and host cells into all biofluids including cerebrospinal fluid (CSF) and blood of cancer patients.(Boriachek et al., 2018; Im et al., 2014; Mollaei et al., 2017; C.-Y. Wu et al., 2017; Zhou et al., 2016) EVs have recently attracted considerable interest as liquid biopsy analytes able to carry cancer-specific molecular signatures.(Al-Nedawi et al., 2008; Skog et al., 2008) Liquid biopsy represents an emerging paradigm across cancer spectrum (Ignatidis et al. 2021), including in GBM with the potential to assess cancer status rapidly and continually with minimal invasiveness and in a clinically actionable manner.(Preusser, 2014) In recent years, advances in liquid biopsy have enabled the extraction of useful information from tumor-derived material released into biofluids, with relatively low cost.(“Liquid Biopsy,” 2021) However, existing liquid biopsy platforms such as circulating tumour DNA (ctDNA) and tumor cells (CTCs), present significant numerical and biological disadvantages in GBM.(Keller & Pantel, 2019; Krol et al., 2018; Poudineh et al., 2018)

Moreover, while precision oncology based on molecular profiling of tumor biomarkers in tissues and biofluids holds great promise,(Choi et al., 2019) it has not yet impacted routine GBM care,(Siravegna et al., 2017; Zachariah et al., 2018) one obstacle being the low sensitivity of current assays. In spite of concerns as to low numbers of EVs that may enter general circulation from intracranial locations, a technology that would detect this signal with sufficient sensitivity and specificity would represent a promising platform for liquid biopsy applications in GBM.(Pan et al., 2021; Shao et al., 2012, 2015)

Indeed, while EVs could be sampled from blood for liquid biopsy applications, this is challenging as it is difficult to extract relevant information from myriads of EV subsets and their diverse molecular profiles that enter the circulation. At the same time the intrinsic complexity of EVs could be advantageous as a granular representation of their parental cellular populations, reflecting, like a hologram, their dynamic heterogeneity .(Zachariah et al., 2018) In the other words, the information contained in a population of individual EVs can capture the remarkable and clinically important traits reflective of cellular heterogeneity,(Al-Nedawi et al., 2008; Ramirez et al., 2018) and mutational as well as epigenetic diversity of driver events(Boriachek et al., 2018; Im et al., 2014; Mollaei et al., 2017; C.-Y. Wu et al., 2017) in HGBTs. Therein lies the need for a technology that can isolate and obtain a molecular fingerprint of single-EVs (sEV) yet possess sufficient throughput to ensure complete characterization of their landscapes informative as to tumor's dynamic state. In this regard, current approaches to analyse EVs either lack sufficient dimensionality(Cho et al., 2021; Dlugolecka et al., 2021; Ferguson et al., 2022; K. Lee et al., 2018; Yang et al., 2018) or sEV resolution.(Haldavnekar et al., 2022; C. Lee et al., 2015; Jongmin Park et al., 2021)

GSCs are also believed to drive inevitable recurrence of GBM which occurs post initial respite following surgical and cytoreductive treatment (TMZ and radiation). The dynamics this crucial phase of GBM progression, including longitudinal diagnostic tests detecting impending TMZ resistance are presently unavailable which impedes the design of suitable second line treatments. Notably, EVs carry signatures of GBM progression,(Lane et al., 2019) including hallmarks of TMZ resistance such as O^6-Methylguanine-DNA Methyltransferase (MGMT),and hypermutant phenotype {Garnier 2018; Daniel 2022}. The MGMT protein works by transferring the alkyl group from the damaged guanine to a cysteine residue on the protein itself. This process is referred to as suicide inactivation, as the MGMT protein becomes irreversibly damaged in the process. MGMT expression is normally silenced by promoter methylation in approximately 45% of GBM cases, a factor that renders these tumours uniquely sensitive to treatment with TMZ chemotherapy. However, MGMT may become re-expressed post chemotherapy, thereby obliterating its benefits on GBM relapse. Thus, distinguishing between patients who carry these molecular traits is of paramount importance. Access to the rich and diagnostically significant information contained in EVs is hampered by the limited sensitivity of currently available analytical methods.(Choi et al., 2019; Jongmin Park et al., 2021; Spinelli et al., 2018; Viehrig et al., 2018)

In this study, we used single EV Surface-enhanced Raman spectroscopy (sEV SERS) technology to identify the specific molecular traits that are correlated with different EV populations. SERS has shown potential to differentiate between biological blood samples collected from healthy and diseased donors of cancers.(Feng et al., 2017; Jaena Park et al., 2017; Shin, Oh, Hong, et al., 2020; Wang et al., 2019) Nevertheless, the bulk SERS-based techniques have not been investigated to resolve the changesin EVs indicative of TMZ resistance likely due to insufficient

field enhancement and inability to immobilize EVs in a diffraction-limited spot.(Fraire et al., 2019; Mahshid et al., 2015; Ruggeri et al., 2017; Stremersch et al., 2016; Wachsmann-Hogiu et al., 2019) Our present study offers promising solutions to this daunting problem.

8.2 Results

8.2.1 Design of single EV (sEV) SERS analysis

We devised a sEV SERS technique (sEV-SERS) to address the unresolved problem of label-free identification of the molecular patterns underlying. MGMT expression in glioma stem cells (GSCs; Figure 8-1a). We investigated the molecular changes and sEV SEES sign as accompanying the evolution of human glioma stem cells (GSCs) in the presence of TMZ resulting in drug resistance. Using machine learning, we formed a pipeline that connected the sEV SERS to an SVM algorithm as a pathway for classifying the expression of the molecular traits stratifying the identification of EVs as derived from drug susceptible or resistant cells and estimated their probabilities of detection in human CSF and plasma samples of GBM patients (Figure 8-1b).

SERS is a phenomenon that occurs when small objects are optically excited near an intense and sharp plasmon resonance frequency, resulting in an enhancement of the electromagnetic field surrounding them. To enhance the SERS enhancement factor for recording the signal from a single EV (Figure 8-1c), we designed a layered hybrid plasmonic surface using a monolayer of MoS_2, a semiconducting oxide layer and a plasmonic thin metallic film pierced with holes. MoS_2-plasmonic nanostructure light matter interaction can enhance SERS by several mechanisms (Figure 8-1d). First, energy transfer as MoS_2 can absorb light and transfer energy to the plasmonic nanostructures, leading to a stronger electromagnetic field around the nanostructures. This energy transfer can result in enhanced Raman signal intensity through SERS. Second, charge transfer

between hybrid plasmonic structure and biomolecule. This charge transfer can modify the electronic structure of MoS_2 and enhance the SERS signal of nearby molecules. Third, photoluminescence enhancement from the monolayer MoS_2 can also enhance the SERS signal. When excited by light, the electrons in MoS_2 can transfer energy to the plasmonic nanostructures, leading to a stronger electromagnetic field and higher SERS intensity. Overall, the combination of MoS_2 and plasmonic nanostructures can significantly enhance the SERS signal, making it a powerful tool for chemical sensing and surface analysis applications.

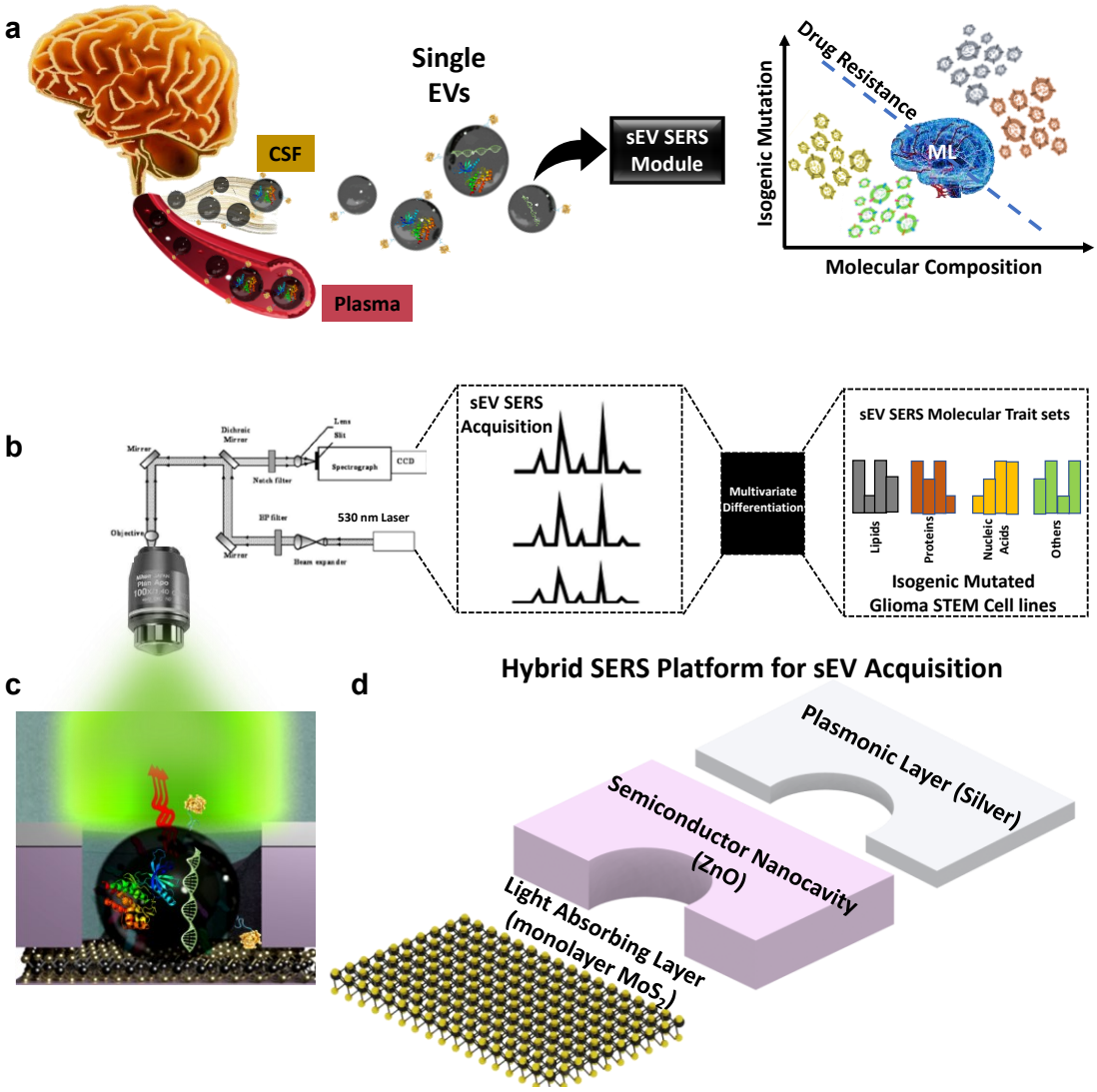

Figure 8-1. The concept and enhancement mechanisms in single EV SERS approach in liquid biopsy of GBM patients. (a) The concept of single EV (sEV) SERS to identify the underlying molecular traits in resistance genes according to the glioma stem cell EVs with molecular alterations. (b) Integration of SERS with SVM machine learning for a sample to answer pipeline. (c) Schematic illustrating the single EV in a layered plasmonic surface for SERS interrogation. (d) Schematic showing the layers used for the sEV-resolved SERS enhancement.

8.2.2 SERS Enhancement Mechanisms in Hybrid plasmonic platform

A combined bottom-up and top-down approach was used to develop the hybrid plasmonic nanocavity platform as an sEV SERS analyzer (Figure 8-2a). First, bottom-up chemical vapor deposition (CVD) technique was used to grow single crystalline monolayer MoS_2. The monolayer was produced through the CVD method by nucleation and growth from the vapour phase solidified on the substrate of choice (Figure 8-2c). Second, a top-down e-beam lithography technique was used to pattern silver plasmonic nanohole array in a 300 nm thick layer of negative photoresist (MaN-2300) via Reith equipment. Direct-write technology of electron-beam lithography was acquired to develop plasmonic nanostructures providing a high patterning resolution, placement accuracy and design degree of freedom. Third, a thin film of semiconducting Zinc oxide (ZnO) and silver (Ag, 10 nm) was deposited (via BJD 1600) on the developed chip as back-reflector and plasmonic layer, respectively (Figure 8-2b). The CMOS-compatible platform enables integration with most existing types of microfluidic devices.

The mechanism behind sEV SERS in our design can be attributed to three main methods: electromagnetic enhancement,(Shin et al., 2018) chemical enhancement,(Stiles et al., 2008) and photoluminescence from monolayer MoS_2(Jalali, Gao, et al., 2021; Sriram et al., 2020) (Figure 8-2d). Electromagnetic enhancement is the dominant factor, where the Raman signal is boosted by the interaction between the electric field of the scattered wave and the induced electric field at the metal/dielectric interface due to LSPR.(del Real Mata et al., 2022; Liu et al., 2020) To theoretically study the electric field of the pierced plasmonic layer, a series of simulations were performed via finite-difference time-domain (FDTD) module of Lumerical Solution (Figure 8-2e). A quantitative $\left|\frac{E}{E_0}\right|^2$ enhancement of ~2.7x 10^5 fold is theoretically calculated at the cavity edges of the hybrid

plasmonic platform. On the other hand, chemical enhancement occurs due to charge transfer through the metal/dielectric interface, which results in an electric field at the interface that enhances the intensity of the scattered beam.(Giannini et al., 2011; Shin, Oh, Kang, et al., 2020) The interaction between the electric field of the scattered photon and the interfacial electric field also plays a role in chemical enhancement. We benchmarked the hybrid plasmonic SERS response of the hybrid SERS platform using Rhodamine 6G (R6G) SERS marker (Figure8- 2f). Over 25 times enhancement in the SERS signal is quantified when comparing the patterned hybrid SERS platform with flat plasmonic layers. Additionally, the photoluminescence of MoS_2 can also contribute to the enhancement of the Raman signal.(Akselrod et al., 2015; B. Lee et al., 2015; Najmaei et al., 2014) The excitation of electrons in MoS_2 is capable of transferring energy to plasmonic nanostructures, resulting in a substantially amplified electromagnetic field that can further enhance the Raman signal. Therefore, the combination of photoluminescence of MoS_2 and plasmonic nanostructures can lead to a significant enhancement (Figure 8-2g) in the surface Raman spectroscopy enhancement factor, making it a powerful technique for surface analysis and sensing applications. In this specific case of R6G, where the MoS2 is integrated underneath the pierced ZnO/Ag layer, the SERS signal is observed to be over 2.25 times more intense compared to regions without MoS2.

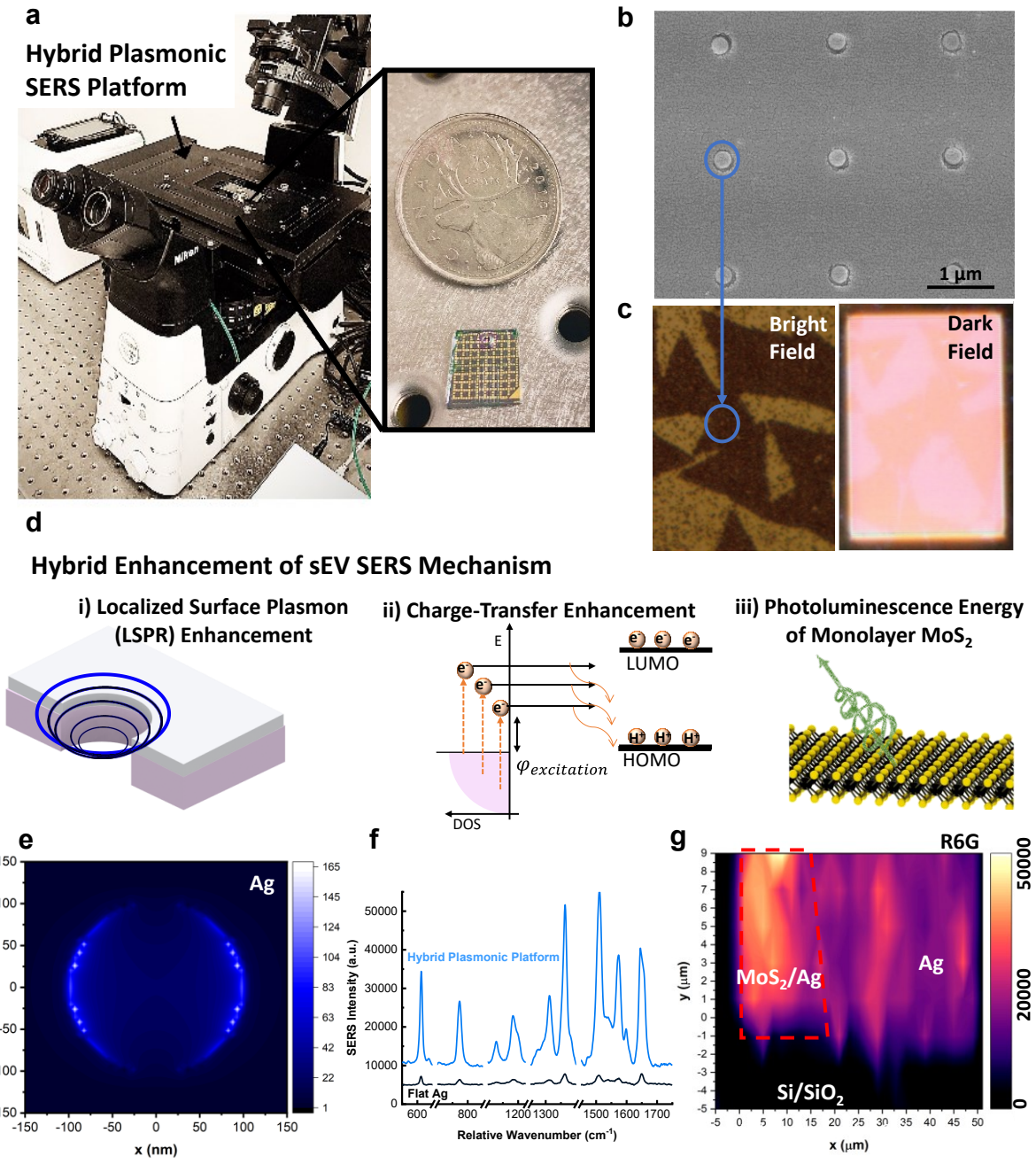

Figure 8-2. SERS performance mechanisms of hybrid plasmonic platform. (a) The e-beam patterned hybrid plasmonic platform enclosed in a channel made by PDMS to preserve the evaporation. (b) The SEM image of the hybrid platform and each layer. (c) The bright-field and dark-field micrograph of the monolayer MoS_2 demonstrating the photoluminescence of MoS_2 when hybridized with a patterned plasmonic Ag layer. (d) Representative mechanisms of SERS enhancement factor using the layered hybrid

plasmonic platform, LSPR, chemical charge transfer and light -mater interaction of the 2D monolayer. (e) The electric field distribution in 250 nm diameter nanocavities simulated using a *plane wave* light source. (f) The corresponding SERS intensity of the patterned *hybrid plasmonic platform* and the flat layers. (g) Spatial variation of SERS response over patterned *hybrid plasmonic platform* obtained from averaging the response from spectral peaks in the R6G spectra.

8.2.3 GSC sEV Isolation and Entrapment for sEV SERS

Glioma Glioma stem cells are known to be heterogeneous in terms of molecular characteristics, functional properties, genetic influences and treatment responses often evolving as a result of exposure to therapeutic intervention.(Garnier et al. 2018) These properties and changes can be modelled using patient derived GSC cultures and xenografts in immune deficient mice, including changing profiles of related EVs.(Jalali et al. 2023, Garnier et al., 2018) To assess the detectability of these changes using the sEV SERS platform , we isolated EVs from GSC1123 cells which are responsive to TMZ, but could acquire drug resistance following initially effective treatment in vivo. (Garnier et al. 2018)

In the present study we included the parental GSC1123 cells and a series of their isogenic variants sensitive or resistant to TMZ, the latter resulting from MGMT expression or other mechanisms (Figure 8-3a). Since the EV-nanocavity interaction that drives the uniform array loading is critical to optimal sEV SERS performance we assessed the size range of EVs of interest during their isolation. Thus, EVs were initially collected from conditioned media of cultured GSCs cells and passed through size exclusion chromatography (SEC) column followed scanning electron microscopy (SEM) imaging of different fractions. Indeed, fractions 7-12 demonstrated a wide size variation that can block the nanocavity surface. However, fraction 9 demonstrates was relatively homogeneous in size rendering it to be the most suitable EV analyte (Figure 8-3b). The

nanoparticle tracking analysis (NTA) of EVs from each GSC cell line demonstrated that fraction 9 has the highest population of EVs with a relatively narrow size profile in the range of 100 to 200 nm (Figure 8-3c). The high-magnification SEM image of sEV entrapped in the nanocavities for sEV SERS shows a high filling efficiency of 97% (Figure 8-3d).

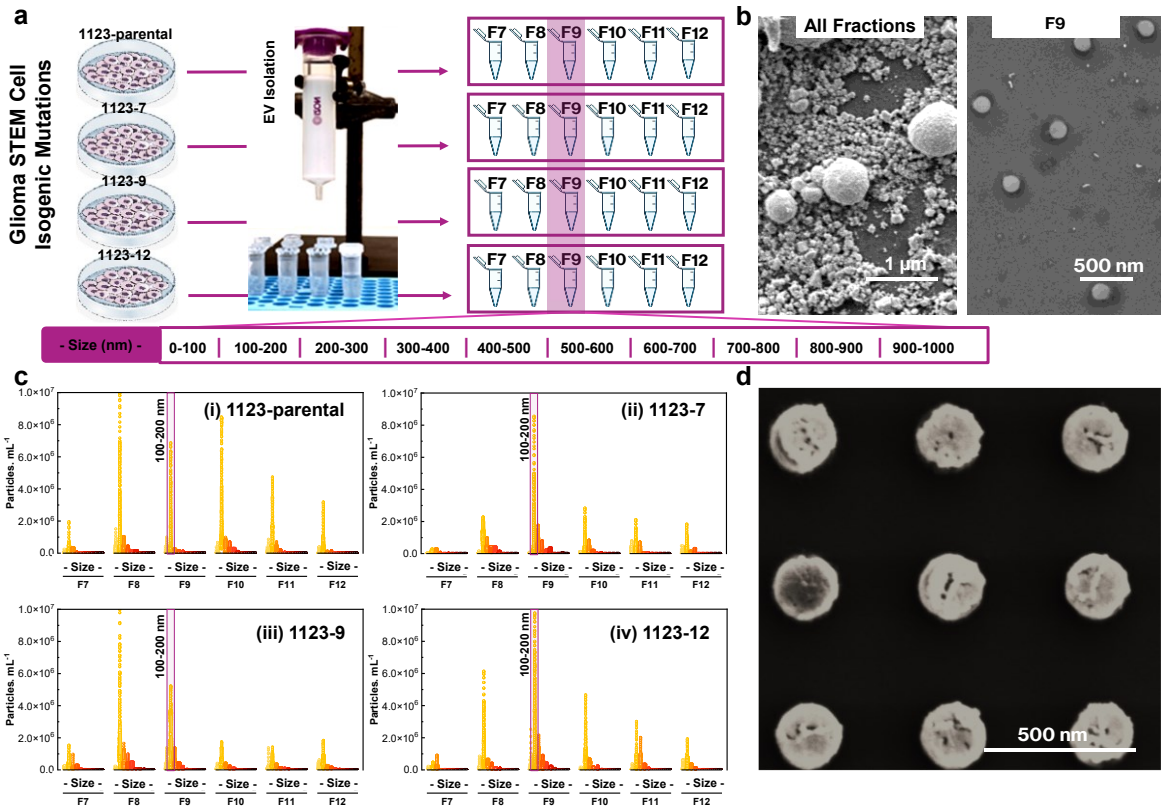

Figure 8-3. EVs isolation and entrapment in sEV SERS nanocavities. (a) Schematic illustrating the isolation of EVs from molecularly altered cell lines into different fractions to identify the best fit for the sEV SERS nanocavities entrapment. (b) The scanning electron micrograph of the size profile in EVs extracted from all fractions and specifically from fraction 9. (c) The nanoparticle tracking analysis of EVs from each GSC cell lines demonstrating that fraction 9 has the highest population of EVs in the size range of 100 to 200 nm. (d) High-magnification SEM image of sEV entrapped in the nanocavities for sEV SERS.

8.2.4 sEV-SERS Characterization of GSC EVs

We next tracked sEV responses to TMZ exposure to compare the respective sEV SERS spectra between control sEVs and those exposed to the drug or rendered resistant to TMZ in vivo,.(Garnier et al., 2018b) The latter was accomplished following establishment of xenografts of GSC1123 cells in immune deficient mice with or without exposure to TMZ. As described earlier {Garnier 2018} GSC 1123-initiated tumors were enzymatically dissociated and several GSC-like sphere forming cultures were established from individual lesions either therapy naïve and TMZ sensitive (1123-12) or recurring following treatment as TMZ-resistant tumours (1123-7, 1123-9). Among TMZ-resistant GSC lines GSC1123-9 cells acquired expression of MGMT which is functionally important for their phenotype while GSC1123-7 cells are TMZ-resistant due to hypermutant phenotype and in the absence of MGMT expression.

The sEV SERS spectra of EVs released byGSC1123 cells, demonstrated notable variation in the peak positions as well as peak intensities (Figure 4a). The variations in band position and relative intensities between the EVs of cancer cells are evident in 31 main regions, assigned to correlating molecular traits they represent (Table S1). The analysis of Raman spectra heat maps corresponding to the 31 benchmark peaks has revealed discernible differences in the biomolecular content of EVs from GSC1123-12 cells (TMZ naïve) relative to 1123 parental (xenograft naïve; Figure 4b). Furthermore, the null comparison of molecular traits demonstrates the significant variation between EVs released by these cells in 14 molecular traits (Figure 4c). Similarly, the heat map of the 31 benchmark Raman peaks variation in the biomolecular contents of TMZ-resistant 1123-7 and 1123-9 compared to 1123-parental is significant (Figure 4d,f). The null comparison of molecular traits demonstrates the significant variation between GSC parental EVs and those from TMZ-resistant GSC1123-7 and -9 cell lines in 14 molecular traits, mainly similar to the ones

underlying the differentiation of parental from GSC1123-12 cells (Figure 4e,g). In particular, 15 molecular traits were found to play important roles in differentiating GSC1123 sublines according to sEV SERS (Figure 4h), as summarized in Table 1. We hypothesize that the clue to find the underlying molecular traits to identify the TMZ-resistance in the patient liquid biopsy may lay within these 15 molecular traits.

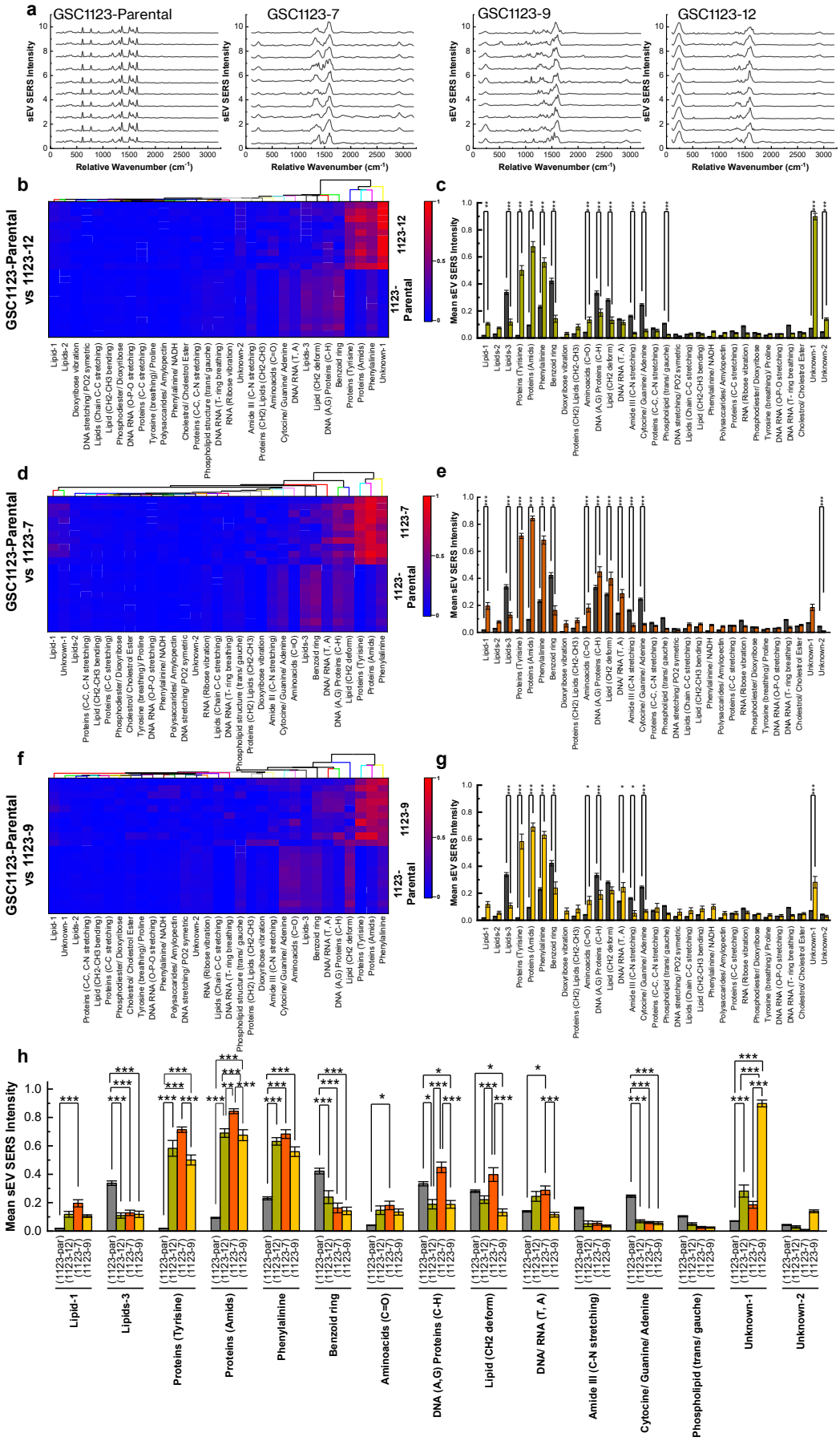
a
GSC1123-Parental
GSC1123-7
GSC1123-9
GSC1123-12
sEV SERS Intensity
Relative Wavenumber (cm-1)
b
GSC1123-Parental vs 1123-12
1123-12
1123-Parental
c
Mean sEV SERS Intensity
d
GSC1123-Parental vs 1123-7
1123-7
1123-Parental
e
f
GSC1123-Parental vs 1123-9
1123-9
1123-Parental
g
h
Mean sEV SERS Intensity
(1123-par)
(1123-12)
(1123-7)
(1123-9)
Lipid-1
Lipids-3
Proteins (Tyrisine)
Proteins (Amids)
Phenylalinine
Benzoid ring
Aminoacids (C=O)
DNA (A,G) Proteins (C-H)
Lipid (CH2 deform)
DNA/ RNA (T, A)
Amide III (C-N stretching)
Cytocine/ Guanine/ Adenine
Phospholipid (trans/ gauche)
Unknown-1
Unknown-2

Figure 8-4. The GSC EVs demonstrate distinct variation in signals between as a function of exposure to TMZ. (a) Raman spectra of GSC1123 EVs, derived from isogenic cell lines with different treatment histories. (b) Heat map of various Raman peaks demonstrate variation in the biomolecular contents of 1123-12 compared to 1123-parental counterpart, both TMZ-naive. (c) Null comparison of molecular traits demonstrates the significant variation between EVs from parental GSCs and EVs derived from xenograft-derived but TMZ-naïve GSC1123-12 cells. (d) Heat map of various Raman peaks demonstrate variation in the biomolecular contents of GSC1123-7 compared to GSC1123-parental counterpart. (e) Null comparison of molecular traits demonstrates the significant variation between GSC parental EVs and EVs from TMZ-resistant cells. (f) Heat map of Raman peaks demonstrate variation in the biomolecular contents of GSC1123-9 compared to their GSC1123-parental counterpart. (g) Null comparison of molecular traits demonstrates the significant variation between EVs from parental GSC1123 cells and TMZ-resistant and MGMT overexpressing GSC1123-9 cells. (h) Null comparison of the 15 molecular traits with different expressions in the sEV SERS signal of the molecularly altered GSCs, demonstrating the feasibility of using them for stratification.

Table 8-1. The 15 molecular traits demonstrating difference between TMZ-resistant and TMZ-naïve controlled cell types.

	Lipid-1	Lipids-3	Proteins (Tyrosine)	Proteins (Amides)	Phenylalanine	Benzoid ring	Aminoacids (C=O)	DNA (A, G)	Lipid (CH2 deform)	DNA/ RNA (T, A)	Amide III (C-N	Cytosine/	Phospholipid	Unknown-1	Unknown-2
123-12		**	**	**	**	**		**				**		**	

123-7	**	**	**	**	**	**	**	**	**	**	**	**	**	**	
123-9	*	**	**	**	**	**	**	**	**		**	**	**	**	**

8.2.5 Changes in sEV SERS profiles during the exposure of GSCs to TMZ chemotherapy in vitro

We have earlier observed that under therapeutic stress resulting from exposure to TMZ the numbers of EVs released by GSCs undergoes considerable changes both transient and constitutive. (Garnier et al. 2018) To investigate how the sEV-SERS fingerprint evolves in response under such conditions we used well controlled cell culture model where GSCs are cultured as tumour spheres in defined serum free medium into which they release EVs. We tracked sEV SERS responses to TMZ exposure in the case of parental GSC1123 cells, their TMZ-naïve isogenic GSC1123-12 counterparts as well as variants resistant to TMZ-mediated cytotoxicity either involving MGMT upregulation (GSC1123-9) or MGMT-unrelated mechanisms (GSC1123-7). The cells were treated with TMZ for 24 hr and 72 hr after which EVs were isolated and analysed (Figure 8-5a).

The multivariate principal component analysis (PCA) demonstrated a higher heterogeneity of EVs in the control (untreated) group. The EVs derived from TMZ-susceptible drug treated cells i.e. GSC1123 Parental (Figure 8-5b) and GSC1123-12, demonstrated much lower heterogeneity while having larger deviation compared to their control counterparts. In contrast, with a slightly differentiated distribution, similar heterogeneity was observed for TMZ resistant cells regardless of the type of resistance, i.e. in the case of MGMT- independent TMZ resistant GSC1123-7 and MGMT- dependent resistant cells GSC1123-9 (Figure 8-5c). From the heat map of the 31

benchmark Raman peaks variation in the biomolecular contents of each cell line and their TMZ-treated counterparts EVs is evident (Figure 8-5d-g). The null comparison of the 15 most pronounced molecular traits of EVs demonstrates the significant variation for each cell line both control and TMZ-treated for 72 hrs (Figure 8-5h). The molecular traits that show the most pronounced alterations after TMZ-treatment in the susceptible cell lines (i.e. GSC1123-parental and GSC1123-12), while not showing much difference after TMZ treatment, are phenylalanine and C-H2 deformation in lipids.

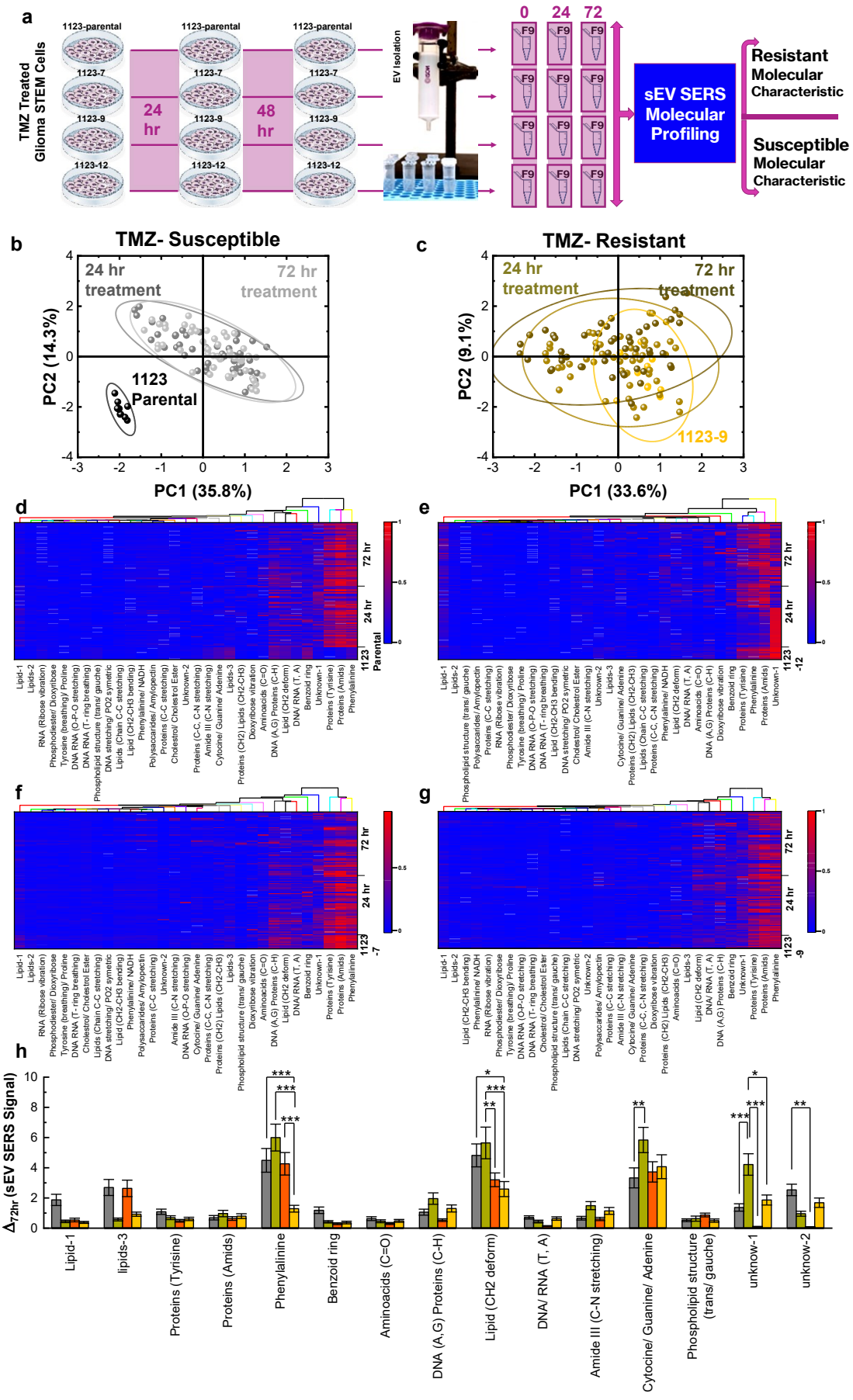
a
TMZ Treated Glioma STEM Cells
1123-parental
1123-7
1123-9
1123-12
24 hr
48 hr
EV Isolation
0
24
72
F9
sEV SERS Molecular Profiling
Resistant Molecular Characteristic
Susceptible Molecular Characteristic
b
TMZ- Susceptible
24 hr treatment
72 hr treatment
1123 Parental
PC2 (14.3%)
PC1 (35.8%)
c
TMZ- Resistant
24 hr treatment
72 hr treatment
1123-9
PC2 (9.1%)
PC1 (33.6%)
d
e
f
g
h
Δ72hr (sEV SERS Signal)
Lipid-1
lipids-3
Proteins (Tyrisine)
Proteins (Amids)
Phenylalinine
Benzoid ring
Aminoacids (C=O)
DNA (A,G) Proteins (C-H)
Lipid (CH2 deform)
DNA/ RNA (T, A)
Amide III (C-N stretching)
Cytocine/ Guanine/ Adenine
Phospholipid structure (trans/ gauche)
unknow-1
unknow-2

Figure 8-5. Differential sEV-SERS responses to TMZ-exposure of drug-sensitive and resistant isogenic GSCs. (a) Experimental design. PCA score plot differentiating TMZ-treated EVs from GSC1123 glioma stem cells (b) TMZ-susceptible GSC1123 Parental and (c) TMZ-resistant GSC1123-9. Heat map of various Raman peaks demonstrate variation in the biomolecular contents during 72 hours of TMZ treatment in (d) GSC1123-Parental cells, (e) GSC1123-12, (f) GSC1123-7, and (g) GSC1123-9. (h) Null comparison of the 15 molecular traits with different expressions in the sEV SERS signal of the molecularly altered GSCs after 72 hours treatment of TMZ, demonstrating the feasibility of changes in specific molecular traits after TMZ treatment for susceptible and resistant cells.

8.2.6 Differentiation of sEV-SERS profiles in CSF of susceptible and resistant GBM patients

Studies suggest that expression of the MGMT gene can confer resistance to TMZ chemotherapy in GBM patients, by allowing cancer cells to evade the effects of DNA-damaging effects of the drug. Therefore, patient stratification through sEV SERS-based liquid biopsy would be extremely valuable both at presentation and at the time of recurrence where predicting efficacy or failure of adjuvant treatment could have actionable consequences. To further explore this avenue, we developed a binary benchmark to predict the overall TMZ-resistance status (using GSC1123 cell line as a model) to determine whether a particular sEV SERS spectrum analyzed belongs to a “TMZ-resistant” or “TMZ-naive” state according to the 15 molecular characteristics that differentiate the resistant and susceptible cell lines. Initially, we studied the resistance state in the CSF samples derived from GBM patients whose lesions were determined to be MGMT positive, as a determinant of TMZ resistant phenotype (Figure 8-6a). The heat map generated from the 15 signature peaks utilized for differentiating the aforementioned model cell lines reveals variations in the composition of EVs comparable to those in CSF samples (Figure 8-6b). Each CSF sample

demonstrated a distinct pattern, suggesting that the presence of MGMT as a signature of TMZ resistance can be effectively stratified and quantified via sEV SERS profiles (Figure 8-6c).

Support Vector Machine (SVM) is a powerful tool to help identify SERS spectral features that distinguish between cell lines and molecular alterations from healthy controls, with potential applications for cancer diagnosis based on liquid biopsy.(Huang et al., 2018) To determine the probability of belonging to either resistant or susceptible groups, Mahalanobis distance was computed between each spectrum and the training set's resistant and susceptible spectra from cell lines, taking into account the standard deviations along different axes. Then, the probability was calculated based on the relative similarity of each spectrum according to comparing the distance ratio (Figure 8-6d). A low probability among spectra indicates a low likelihood of TMZ-resistant molecular traits in cancer (in the MGMT-negative sample), while a high probability implies a higher likelihood of TMZ-resistant molecular traits in cancer (in the MGMT-positive sample). A cut-off point was established at 0.25 to differentiate the signals bearing TMZ-resistant molecular traits (Figure 8-6e). The ROC curve demonstrated an area under the curve (AUC) of 0.92 (Figure 8-6f), with a high level of sensitivity (100%), and specificity (88%).

.

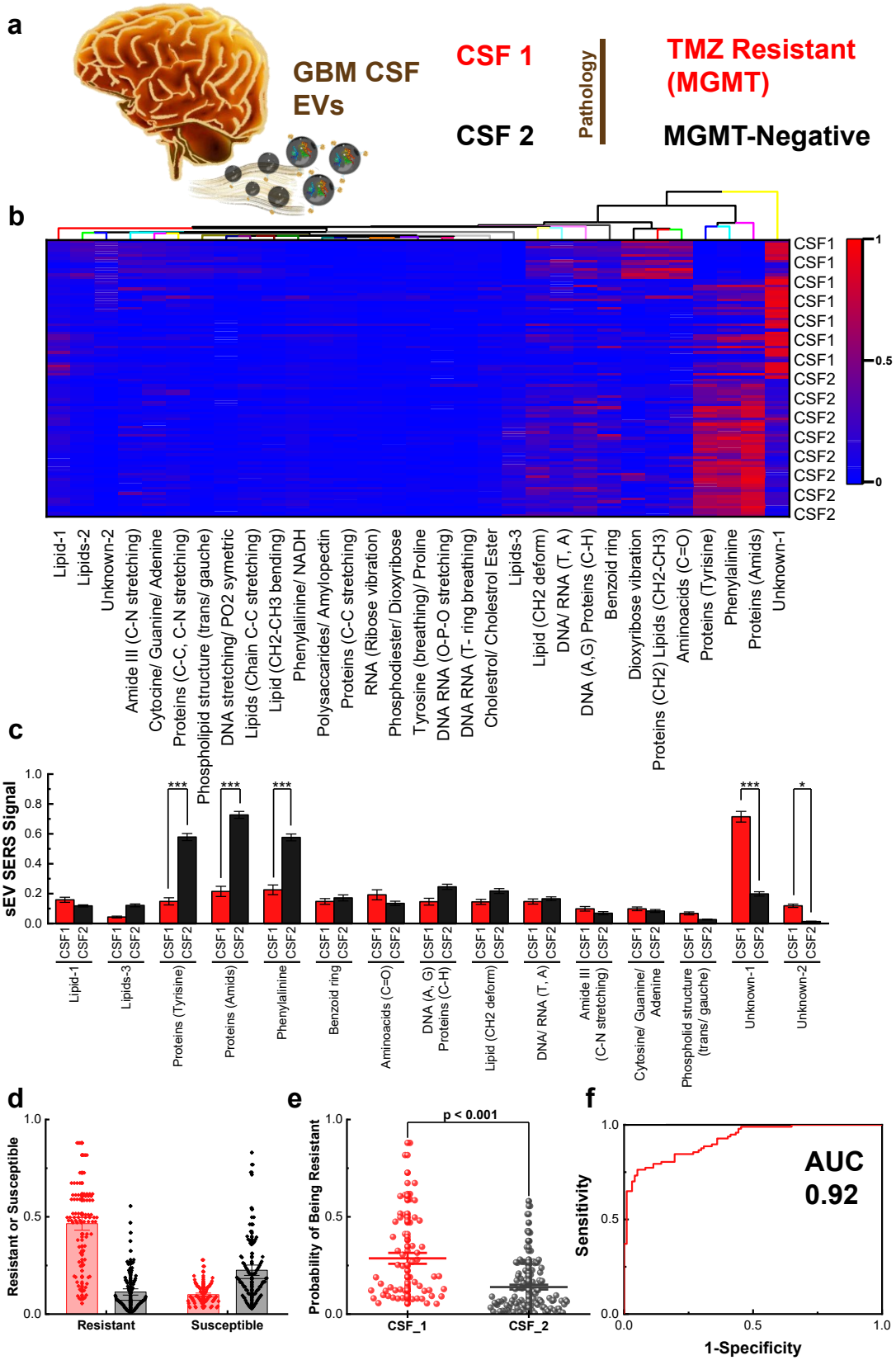
a
GBM CSF EVs
CSF 1
CSF 2
Pathology
TMZ Resistant (MGMT)
MGMT-Negative
b
CSF1
CSF2
Lipid-1
Lipids-2
Unknown-2
Amide III (C-N stretching)
Cytocine/ Guanine/ Adenine
Proteins (C-C, C-N stretching)
Phospholipid structure (trans/ gauche)
DNA stretching/ PO2 symetric
Lipids (Chain C-C stretching)
Lipid (CH2-CH3 bending)
Phenylalinine/ NADH
Polysaccarides/ Amylopectin
Proteins (C-C stretching)
RNA (Ribose vibration)
Phosphodiester/ Dioxyribose
Tyrosine (breathing)/ Proline
DNA RNA (O-P-O stretching)
DNA RNA (T- ring breathing)
Cholestrol/ Cholestrol Ester
Lipids-3
Lipid (CH2 deform)
DNA/ RNA (T, A)
DNA (A,G) Proteins (C-H)
Benzoid ring
Dioxyribose vibration
Proteins (CH2) Lipids (CH2-CH3)
Aminoacids (C=O)
Proteins (Tyrisine)
Phenylalinine
Proteins (Amids)
Unknown-1
c
sEV SERS Signal
Lipid-1
Lipids-3
Proteins (Tyrisine)
Proteins (Amids)
Phenylalinine
Benzoid ring
Aminoacids (C=O)
DNA (A, G) Proteins (C-H)
Lipid (CH2 deform)
DNA/ RNA (T, A)
Amide III (C-N stretching)
Cytosine/ Guanine/ Adenine
Phospholid structure (trans/ gauche)
Unknown-1
Unknown-2
d
Probability of Being Resistant or Susceptible
Resistant
Susceptible
e
Probability of Being Resistant
p < 0.001
CSF_1
CSF_2
f
Sensitivity
1-Specificity
AUC
0.92

Figure 8-6. Differential molecular traits of TMZ-susceptible and resistant phenotype based on sEV SERS profiles. (a) Schematic of the experimental design to identify the molecular traits underlying the MGMT-positive related resistance in the GBM patient using EVs from their CSF samples. (b) Heat map of various Raman peaks demonstrate variation in the biomolecular contents of CSF1 compared to CSF2 samples. (c) Null comparison of the 15 molecular traits with different expressions in the sEV SERS signal of the CSF derived EV samples, demonstrating the feasibility of sEV SERS in stratification. (d) The distribution of the probabilities of the sEV SERS spectra from CSF1 and CSF2 samples associated with their belonging to resistant and susceptible classes. (e) The one-way ANOVA comparison analysis of mean probabilities associated with the sEV SERS spectra. (f) The ROC curve of the SVM prediction of probabilities of sEV SERS spectra to belong to the right class resulted in an overall AUC of 0.92.

8.2.7 Performing sEV SERS Diagnosis for Traits of Drug Resistance in Human Blood Derived EVs

The outputs of the SVM model enabled us to determine an average relative similarity for each patient spectrum, based on Mahalanobis distance, to differentiate their probability of belonging to either non-cancer subset of samples, or cancer-related MGMT-Negative or MGMT-Positive groups (Figure 8-7a). The average probability value for each sample was calculated by taking in over 1200 sEV SERS spectra. High probability means high risk of molecular alterations related to MGMT prone TMZ resistance behavior in tumors. We benchmarked a cut-off probability value for tertiary classification of the dataset into MGMT related TMZ resistant, MGMT negative and non-cancer at 0.25 while considering MGMT-negative class as the threshold to predict a measure for the possibility of diagnosis with TMZ-resistance. According to this designation, all healthy samples belonged to naive class rather than the MGMT-Positive (TMZ-resistant) class

(Figure 8-7b). The *post hoc* comparisons demonstrated P-value below 0.001 for the probability of belonging to MGMT related TMZ-resistant class shows confidence in spectra being correctly classified based on the ensembled single EV spectra (Figure 8-7c). The ROC curve demonstrates the true positive rate as a function of the false positive rate (Figure 8-7d), to assess the overall dexterity of the true positive rate versus false negative rate of the sEV SERS prediction over clinical annotation resulted in an overall AUC of 0.96.

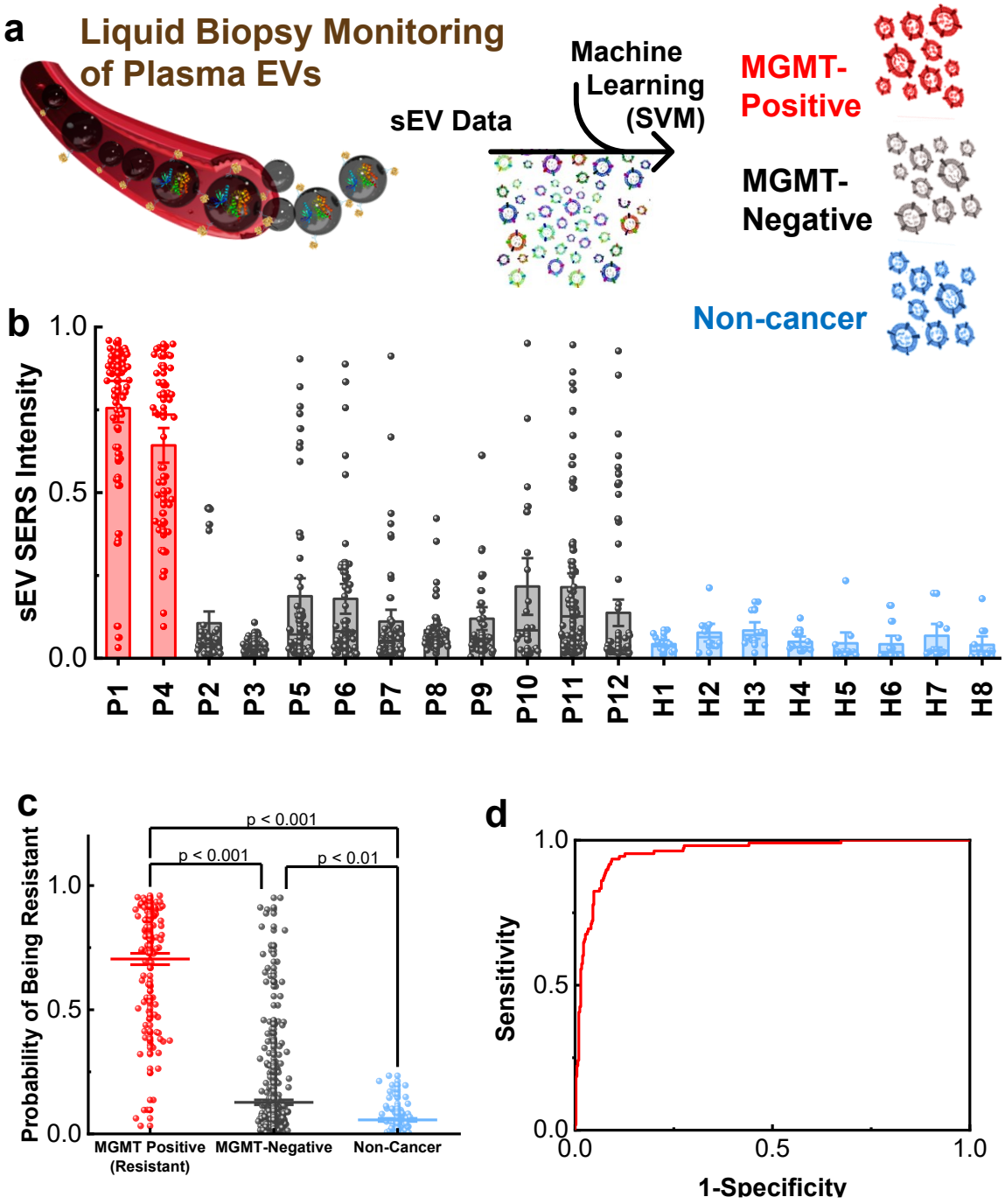

Figure 8-7. sEV SERS signals of blood samples of healthy subjects and glioblastoma patients with known state of MGMT expression as a marker of resistance to TMZ. a, Schematic showing sEV SERS classification of blood EVs into MGMT-positive (TMZ-resistant), MGMT-negative and non-cancer, according to the 15 molecular traits underlying the differentiation of TMZ-resistance in the controlled cell

line investigation. b, The distribution of the probabilities of the single EV spectra from MGMT-positive and MGMT-negative and non-cancer blood samples associated with their belonging to TMZ-resistant (MGMT-positive) class. c, The one-way ANOVA comparison analysis of mean probabilities associated with the single EV spectra. d, The ROC curve of the SVM prediction of probabilities of sEV spectra to belong to the right class according to pathology results, resulted in an overall AUC of 0.96.

Clinical annotations corresponding to patient MGMT mutation status. Plasma was obtained from 12 patients, clinically diagnosed with GBM while CSF was received from the first two patients. MGMT methylation status was determined by sequencing of the primary tumour.

CSF	Status	TMZ-resistant MGMT Status	Plasma	Status	TMZ-resistant MGMT Status	Plasma	Status
CSF 1	Glioblastoma	Resistant	P 1	Glioblastoma	Resistant	H 1	Healthy
CSF 2	Glioblastoma	Negative	P 2	Glioblastoma	Negative	H 2	Healthy
			P 3	Glioblastoma	ND	H 3	Healthy
			P 4	Glioblastoma	Resistant	H 4	Healthy
			P 5	Glioblastoma	Negative	H 5	Healthy
			P 6	Glioblastoma	Negative	H 6	Healthy
			P 7	Glioblastoma	Negative	H 7	Healthy
			P 8	Glioblastoma	Negative	H 8	Healthy
			P 9	Glioblastoma	Negative		
			P 10	Glioblastoma	Negative		
			P 11	Glioblastoma	ND		
			P 12	Glioblastoma	ND		

8.3 Conclusion

Our study suggests that sEV SERS spectra contain information that may be used to detect signatures of TMZ resistance in cellular supernatants and glioblastoma patients biofluids such as CSF and blood plasma. Healthcare providers currently use traditional characteristics, such as

tumor appearance, to diagnose tumor subtypes and determine treatment, often with few molecular markers in practical everyday use. This is in spite of enormous progress that has been achieved in molecular dissection of GBM and its microenvironment and largely due to barriers associated liquid biopsy approaches in this indication. We proposed to advance the sEV SERS technology for molecular profiling of single EVs to break the diagnostic and therapeutic gridlock in brain cancer by focusing on the sEV representation of the resistance to temozolomide (TMZ) chemotherapy underlying lethal recurrence of GBM. First, we focused on the SERS enhancement mechanisms of a designed hybrid MoS_2-plasmonic platform for single EV resolved spectra that is able to provide label-free molecular profiling of EVs subsets, which carry molecular fingerprints of underlying features.

We explored the molecular changes that contribute to the cellular evolution of xenograft models in a series of human glioma stem cells (GSCs) using sEV SERS technology. GSC 1123 parental cells and its naturally derived variants, including those that express MGMT, were used to identify the correlated molecular traits as compared with the parental cells. This observation demonstrated the set of molecular traits amenable to distinguish the susceptible and resistant cells. Finally, we demonstrated that via sEV SERS approach we can provide a way to investigate tumor heterogeneity and monitor molecular alterations in a statistical manner. As a result of stratified molecular changes that distinguish parental cells from their drug resistant variants, we quantified the sEV SERS profiles of circulating EVs in the blood of patients with GBM. The quantification of the underlying molecular traits demonstrated 96% accuracy on par with clinical pathology tests.

This approach represents a paradigm applicable to multiple indications. It has the potential to classify different molecular tumor subtypes based on spectroscopic fingerprints drawn from

single EVs spectra, which can be used as a form of liquid biopsy to determine the existence of molecular traits underlying drug resistance in tumors. The sEV SERS approach represents a promising avenue for the development of a non-invasive and label-free cancer monitoring tools that could significantly enhance the survival of patients with complex cancers, such as GBM. While there are still challenges to overcome, such as tumour EV scarcity, heterogeneity, and intrinsic complexity, which can hinder real-time monitoring of complex cancers, future studies are expected to enable clinical translation of our findings. Of particular significance is the validation of the accuracy and reproducibility of this technique across larger cohorts of patients.

8.4 Materials and Methods

Fabrication: A combined bottom-up and top-down approach was used to develop the single exosome analyzer nanoelectrodes. First, chemical vapor deposition (CVD) technique was used to grow single-crystalline monolayer MoS_2.(Jalali, Gao, et al., 2021) The monolayer was produced through CVD method by nucleation and growth from vapour phase solidified on the substrate of choice. Second, ebeam lithography (Raith e-line) was used to pattern the nanohole array in a 300 nm thick layer of negative photoresist (MaN-2300). Third, an 80 nm biocompatible ZnO layer and a 10-100 nm Ag layer were deposited (via BJD 1800) as back-reflector and plasmonic layer, respectively. Fourth, the plasmonic nanohole array was formed via lift-off. The CMOS-compatible platform enables integration with any existing type of microfluidic devices.

Characterization: The hybrid plasmonic platform was characterized with SEM (FEI Quanta 450 environmental scanning). The optical characterizations were performed via a Lambda750 NIR-UV-Visible equipment and a NanoSpec reflection spectro-microscopy. The workflow for EV

characterization using SEM is detailed below. The purified EVs suspended in PBS solution (100 µL, 1 mM) were left sitting on the recognition substrate for 2 min, followed by overnight incubation with glutaraldehyde 3% in sodium cacodylate (0.1 mM). Then, the EVs were immersed in ethyl alcohol (30–100% with 10 min immersion in each) for dehydration. Lastly, a critical point dryer (Leica Microsystems EM CPD030) was employed to substitute alcohol content with dry CO_2 with minimum damage to the EVs morphology.

Finite Difference Time-Domain: The electric-field distribution over the nanocavity array was modelled with the finite difference time domain (FDTD) module (v8.21.1781, Lumerical Solutions, Inc) using a plane wave and a laser excitation wavelength of 532 nm under a total-field scattered-field (TFSF) light source to resemble the Gaussian laser beam. The Ag/ZnO plasmonic layer was positioned above a monolayer MoS2-covered SiO_2 substrate to simulate the composition of hybrid plasmonic platform, and all the metallic materials were simulated based on Palik refractive indices, while the refractive index of the non-linear MoS_2 material was determined from previous work. The electromagnetic field enhancement factor, $EFEF$, scales with the 4th power of the electric field enhancement $E(\omega)/ E_0(\omega)$ according to the following equation: $EFEF = (|E(\omega)|/|E_0(\omega)|)^4$ Subsequent studies on the effect of the light source were carried out by simulating the reflectance spectra of nanocavities with varying cavity sizes under planewave illumination. The EM-field enhancement for a single nanocavity made of silver, gold, aluminum, was assessed with 2D contour plots to determine the optimal material.

Processing EV:

(i) Cell culture

Cells were cultured according to the provisions of the RIMUHC Biohazard Safety Certificate. Glioblastoma stem cells (GSCs) were cultured using sterile techniques and biosafety cabinets, as per institutional guidelines. The mesenchymal MES1123 sphere cultures were maintained in clusters using Dulbecco's modified Eagle's medium/F12 supplemented with B27 (2%), Glutamax (1%), epidermal growth factor (20 ng/mL), basic fibroblast growth factor (20 ng/mL), penicillin/streptomycin, and heparin (5 μg/mL).

(ii) TMZ treatment

For experimentation, 3×10^6 cells were plated in 15 mL of culture medium or medium containing 100 μM TMZ (S1237, Selleckchem) dissolved in dimethyl sulfoxide. The culture media were collected at 24 and 72 hours, and cell debris was removed by centrifugation at 400g for 20 minutes. The supernatant was filtered with a 0.2 mm syringe filter and concentrated using an Amicon Ultra-15 centrifugal Filter Unit with a 100,000 NMWL molecular cut-off to obtain a volume of 500 μL. The concentrate was loaded onto a qEV original SEC column followed by elution with phosphate-buffered saline. Five fractions of 500 μL each were collected after 2.5 mL of void volume.

(iii) Isolation of EVs from cell cultures

Optimized protocol was used to purify EVs from cancer cell growth media. This conditioned medium (CM) was collected from cells that had been grown for 72 hours in culture media containing 10% EV-depleted FBS. The CM was then centrifuged once at 400xg and filtered through a 0.2 μm pore-size filter. The resulting filtrate was concentrated to 500ul using an Amicon Ultra-15 Centrifugal Filter Unit with a 100,000 NMWL molecular cut-off. The concentrated media was further purified using a qEV single SEC column, with 500 μL of the sample loaded and 4 fractions of 500 μL of eluent collected after 2.5 mL of the initial eluent. The concentration and size distribution of EVs in the purified media were determined using the NanoSight NS500 instrument

and nanoparticle tracking analysis. Three 30-second recordings were obtained at 37ºC and processed using NTA software (version 3.0).

(iv) EV Isolation from CSF and blood

The CSF samples from the patient were first filtered through filters with a pore size of 0.2 µm. The filtered samples were then purified using a qEV single SEC column, where 500 µL of each sample was loaded, and 4 fractions of 500 µL of eluent were collected after 2.5 mL of the initial eluent.

To isolate EVs from patient blood samples, the samples were first centrifuged at 200xg for 20 minutes, and then the supernatants were further centrifuged at 1,000xg for 15 minutes. The resulting liquid phase was then subjected to another centrifugation step at 1,500xg for 20 minutes to remove platelets and obtain platelet-poor plasma (PPP), which was then passed through filters with a pore size of 0.2 µm. The EVs in the filtered PPP samples were then purified using a qEV single SEC column, where 500 µL of the sample was loaded, and 4 fractions of 500 µL of eluent were collected after 2.5 mL of the initial eluent.

(v) Nanoparticle tracking analysis (NTA)

NTA was performed on the cell culture media using a NanoSight NS300 system and the manufacturer's manual. Data acquisition and analysis were performed using the NanoSight Software NTA3.3.301. The samples were diluted 1:10 in PBS to a final volume of 0.5 mL, and their concentration was adjusted to obtain a range of 20–100 particles per frame. For each measurement, three consecutive 30-second videos were recorded at 37 °C and a syringe speed of 25 µL/s. Particles (extracellular vesicles) were detected using a 488 nm laser and a scientific CMOS camera.

Raman spectroscopy:

(i) Spectra Collection

The surface-enhanced Raman spectroscopy (SERS) and mapping SERS spectra were collected in back scattering geometry. This was done using an InVia Raman microscope equipped with a 532 nm HeNe laser delivering 15 mW of laser power. The laser was polarized along the x-axis direction. The biosamples were loaded onto a platform and mounted on a ProScan II motorized stage under the microscope. The laser was focused on the sample using a Leica 100x microscope objective, creating a spot of ~0.8 μm diameter. A thermoelectrically cooled charge coupled device (CCD) camera was used for detection. The spectrograph was calibrated using the Silicon substrate.

Single spectra were collected with an exposure time of 35 s at 0.5% of the laser intensity. Mapping was achieved by collecting spectra with steps of 1 μm, with an exposure time of 20 s for each spectrum. Spectra were obtained in the 100–3200 cm-1 region using the synchro mode of the instrument software WiRE 5.1. The dimensions of the map varied depending on the zone of interest investigated.

To measure Raman spectra and characterize the SERS signals, samples were nearly dried (0.5-10 μl). EVs were also isolated from human mesenchymal glioma stem cell lines GSC1123 and its isogenic molecular alteration subtypes (GSC1123-12, GSC1123-7, and GSC1123-9).

(ii) Data pre-processing and analysis

The software used for data pre-processing and analysis included Origin Pro 2021, ImageJ, and WiRE 5.1. Principal component analysis was performed using the spectroscopy v.1.2 App in OriginPro 2019. The pre-processing of SERS spectra involved four steps: i) identification and removal of cosmic rays, ii) baseline correction, iii) intensity vector-normalization based on Si peak, and iv) detection and removal of outliers. A linear baseline was automatically fit and subtracted

from each spectrum of the dataset for baseline correction. Outliers were identified by examining suspicious points on the PCA score maps and their corresponding spectra, and then individually examined before removal. PCA was used as a method to detect suspicious spectra and was sensitive to outliers.

(iii) PCA

PCA is a statistical technique used to simplify the information contained in a large number of spectra by reducing the number of variables. It does this by condensing the spectral information into fewer latent variables called principal components (PCs). In a Raman study, each spectrum can be described as a product between component concentrations and pure constituent spectra, but since the pure constituent spectra are often unknown, the latent spectra obtained from PCA are used instead. In this study, PCA was applied to pre-processed data, and the first three principal components (PC 1, PC 2, and PC 3) were considered for analysis, as they were interpretable in terms of the biochemical components of the EVs. The loadings and score maps for the principal components are difficult to interpret.

Machine Learning:

(i) SVM algorithm

A Support Vector Machine (SVM) is a classification ML algorithm that finds hyperplanes that best separate the input data points into different classes and is deemed suitable for processing high-dimensional datasets with a relatively small sample size. To find the optimal hyperparameters (C and the kernel) needed for our classification task, we used a Bayesian search, and a 5-fold cross

validation on the training set. C was explored from 10^{-6} to 100 using a log uniform distribution, and 2 different kernels, linear and radial basis function, were tested.

(ii) Signal preprocessing for SVM

The pre-processed spectra, as mentioned previously, were zeroed to eliminate peaks with less statistical significance and only the 15 pre-determined molecular traits were retained with defined ranges on the x-axis (wavelength), as they are regarded to encode the key information for differentiating among the 1123 cell line subtypes and render them either susceptible or resistant.

(iii) SVM- CSF study

The processed spectra, as described above, are fed into the model as inputs, and a subsequent prediction will be given for one of the predetermined classes that the spectrum most likely belongs to. The optimized model hyperparameters are as the following: C equals 0.47349443961872306, gamma equals 10^{-6} and a rbf kernel. The algorithm was trained on 70% of the cell line datasets with 1123-parental and 1123-12 grouped as naïve, while 1123-7 and 1123-9 were grouped as resistant. The 20% remaining data was used as testing sets, as detailed in Table S1.

(iv) SVM- blood plasma study

Following a similar workflow, the SVM model was tweaked by using all the 1123 cell lines, again with 1123-parental and 1123-12 grouped as naive while 1123-7 and 1123-9 grouped as resistant as the testing set. In addition, around 25% of the healthy control spectra were also included in the testing set through random selection. The remaining healthy controls and patient plasma samples were employed as testing sets, detailed in Table S1. The optimized hyperparameters were determined to be: C equals 18.913986216617698, gamma equals 0.2861262135851651 and a rbf kernel.

(vi) Nanoparticle tracking analysis (NTA)

Nanoparticle tracking analysis (NTA) was performed on the cell culture media using a NanoSight NS300 system and the manufacturer's manual. Data acquisition and analysis were performed using the NanoSight Software NTA3.3.301. The samples were diluted 1:10 in PBS to a final volume of 0.5 mL, and their concentration was adjusted to obtain a range of 20–100 particles per frame. For each measurement, three consecutive 30-second videos were recorded at 37 °C and a syringe speed of 25 μL/s. Particles (extracellular vesicles) were detected using a 488 nm laser and a scientific CMOS camera.

8.5 Authors Contributions

M.J. initiated the idea, design, and fabrication protocols, performed the physical characterizations, sample preparation, SERS data collection, FDTD modelling, data processing and analysis, designing the library for machine learning as well as writing the manuscript. Y.L. contributed to the SERS data collection, running machine learning algorithm and writing the supporting information. L.M. contributed in EVs sample preparation, purification, and NTA tests. K.P. provided patient samples and clinical annotations. J.R. provided the EV samples from GBM cell lines for the entire project, advice on the EV’s biological properties and response to TMZ, and contributed to the writing of the manuscript. S.M. supervised the project from the idea to development, contributed to the design of the figure sets and writing of the manuscript.

8.6 Acknowledgment

The authors thank the Faculty of Engineering at McGill University, the Canadian Cancer Society (255878 CCSRI), Natural Science and Engineering Research Council of Canada (NSERC, G247765), New Frontiers in Research Fund (250326), and Canada Foundation for Innovation (CFI,

G248924), for financial support. JR was supported by Foundation Grant from the Canadian Institutes of Health Research (CIHR), , McGill Interdisciplinary Initiative in Infection and Immunity (MI4) seed grant, Canadian Foundation for Innovation (CFI), NET program sponsored by Fondation Charles Bruneau (FCB) and Fondation CIBC, and Jack Cole Chair in Pediatric Hematology/Oncology. The authors acknowledge Nanotools-Microfab and the Facility for Electron Microscopy Research at McGill University, the Laboratoire de microfabrication (LMF) at Polytechnique, Montreal, and the research facilities of NanoQAM at the Université du Québec à Montréal. MJ appreciates McGill Engineering Award (MEDA) and Fonds du Recherche du Quebec (FRQnet) scholarships.

8.8 Reference

Akselrod, G. M., Ming, T., Argyropoulos, C., Hoang, T. B., Lin, Y., Ling, X., Smith, D. R., Kong, J. & Mikkelsen, M. H. (2015). Leveraging nanocavity harmonics for control of optical processes in 2d semiconductors. *Nano Letters*, *15*(5), 3578–

Al-Nedawi, K., Meehan, B., Micallef, J., Lhotak, V., May, L., Guha, A. & Rak, J. (2008). Intercellular transfer of the oncogenic receptor EGFRvIII by microvesicles derived from tumour cells. *Nature Cell Biology*, *10*(5), 619–624.

Boriachek, K., Islam, M. N., Möller, A., Salomon, C., Nguyen, N. T., Hossain, M. S. A., Yamauchi, Y. & Shiddiky, M. J. A. (2018). Biological Functions and Current Advances in Isolation and Detection Strategies for Exosome Nanovesicles. *Small*, *14*(6), 1–21.

Cho, S., Yi, J., Kwon, Y., Kang, H., Han, C. & Park, J. (2021). Multifluorescence Single Extracellular Vesicle Analysis by Time-Sequential Illumination and Tracking. *ACS Nano*, *15*(7), 11753–11761.

Choi, D., Montermini, L., Jeong, H., Sharma, S., Meehan, B. & Rak, J. (2019). Mapping Subpopulations of Cancer Cell-Derived Extracellular Vesicles and Particles by Nano-Flow Cytometry. *ACS Nano*, *13*(9), 10499–10511.

del Real Mata, C., Jeanne, O., Jalali, M., Lu, Y. & Mahshid, S. (2022). Nanostructured-Based Optical Readouts Interfaced with Machine Learning for Identification of Extracellular Vesicles. *Advanced Healthcare Materials*, 2202123.

Dlugolecka, M., Szymanski, J., Zareba, L., Homoncik, Z., Domagala-Kulawik, J., Polubiec-Kownacka, M. & Czystowska-Kuzmicz, M. (2021). Characterization of extracellular vesicles from bronchoalveolar lavage fluid and plasma of patients with lung lesions using fluorescence nanoparticle tracking analysis. *Cells*, *10*(12), 3473.

Feng, S., Zheng, Z., Xu, Y., Lin, J., Chen, G., Weng, C., Lin, D., Qiu, S., Cheng, M., Huang, Z., Wang, L., Chen, R., Xie, S. & Zeng, H. (2017). A noninvasive cancer detection strategy based on gold nanoparticle surface-enhanced raman spectroscopy of urinary modified nucleosides isolated by affinity chromatography. *Biosensors and Bioelectronics*, *91*, 616–622.

Ferguson, S., Yang, K. S., Zelga, P., Liss, A. S., Carlson, J. C. T., del Castillo, C. F. & Weissleder, R. (2022). Single-EV analysis (sEVA) of mutated proteins allows detection of stage 1 pancreatic cancer. *Science Advances*, *8*(16).

Fraire, J. C., Stremersch, S., Bouckaert, D., Monteyne, T., De Beer, T., Wuytens, P., De Rycke, R., Skirtach, A. G., Raemdonck, K., De Smedt, S. & Braeckmans, K. (2019). Improved Label-Free Identification of Individual Exosome-like Vesicles with Au@Ag Nanoparticles as SERS Substrate. *ACS Applied Materials and Interfaces*, *11*(43), 39424–39435.

Garnier, D., Meehan, B., Kislinger, T., Daniel, P., Sinha, A., Abdulkarim, B., Nakano, I. & Rak, J. (2018a). Divergent evolution of temozolomide resistance in glioblastoma stem cells is reflected in extracellular vesicles and coupled with radiosensitization. *Neuro-Oncology*, *20*(2), 236–248.

Garnier, D., Meehan, B., Kislinger, T., Daniel, P., Sinha, A., Abdulkarim, B., Nakano, I. & Rak,

J. (2018b). Divergent evolution of temozolomide resistance in glioblastoma stem cells is reflected in extracellular vesicles and coupled with radiosensitization. *Neuro-Oncology*, *20*(2), 236–248.

Giannini, V., Fernandez-Dominguez, A. I., Heck, S. C., Maier, S. A., Fernández-Domínguez, A. I., Heck, S. C. & Maier, S. A. (2011). Plasmonic nanoantennas: Fundamentals and their use in controlling the radiative properties of nanoemitters. *Chemical Reviews*, *111*(6), 3888–3912.

Haldavnekar, R., Venkatakrishnan, K. & Tan, B. (2022). Cancer Stem Cell Derived Extracellular Vesicles with Self-Functionalized 3D Nanosensor for Real-Time Cancer Diagnosis: Eliminating the Roadblocks in Liquid Biopsy. *ACS Nano*, *16*(8), 12226–12243.

Huang, S., Nianguang, C. A. I., Penzuti Pacheco, P., Narandes, S., Wang, Y. & Wayne, X. U. (2018). Applications of support vector machine (SVM) learning in cancer genomics. In *Cancer Genomics and Proteomics* (Vol. 15, Issue 1, pp. 41–51). International Institute of Anticancer Research.

Im, H., Shao, H., Park, Y. Il, Peterson, V. M., Castro, C. M., Weissleder, R. & Lee, H. (2014). Label-free detection and molecular profiling of exosomes with a nano-plasmonic sensor. *Nature Biotechnology*, *32*(5), 490–495.

Jalali, M., Gao, Z., Yu, Y., Siavash Moakhar, R., Ding, Y., Zhuang, M., Zhou, N., König, T., Fery, A., Mahshid, S. & Luo, Z. (2021). Synergistic enhancement of photoluminesent intensity in monolayer molybdenum disulfide embedded with plasmonic nanostructures for catalytic sensing. *2D Materials*, *8*(3), 035049.

Jalali, M., Isaac Hosseini, I., AbdelFatah, T., Montermini, L., Wachsmann Hogiu, S., Rak, J. & Mahshid, S. (2021). Plasmonic nanobowtiefluidic device for sensitive detection of glioma extracellular vesicles by Raman spectrometry. *Lab on a Chip*, *21*(5), 855–866.

Keller, L. & Pantel, K. (2019). Unravelling tumour heterogeneity by single-cell profiling of circulating tumour cells. In *Nature Reviews Cancer* (Vol. 19, Issue 10, pp. 553–567). Nature Publishing Group.

Krol, I., Castro-Giner, F., Maurer, M., Gkountela, S., Szczerba, B. M., Scherrer, R., Coleman, N., Carreira, S., Bachmann, F., Anderson, S., Engelhardt, M., Lane, H., Jeffry Evans, T. R., Plummer, R., Kristeleit, R., Lopez, J. & Aceto, N. (2018). Detection of circulating tumour cell clusters in human glioblastoma. *British Journal of Cancer*, *119*(4), 487–491.

Lane, R., Simon, T., Vintu, M., Solkin, B., Koch, B., Stewart, N., Benstead-Hume, G., Pearl, F. M. G., Critchley, G., Stebbing, J. & Giamas, G. (2019). Cell-derived extracellular vesicles can be used as a biomarker reservoir for glioblastoma tumor subtyping. *Communications Biology*, *2*(1), 1–12.

Lee, B., Park, J., Han, G. H., Ee, H.-S., Naylor, C. H., Liu, W., Johnson, A. T. C. & Agarwal, R. (2015). Fano Resonance and Spectrally Modified Photoluminescence Enhancement in Monolayer MoS_2 Integrated with Plasmonic Nanoantenna Array. *Nano Letters*, *15*(5), 3646–3653.

Lee, C., Carney, R. P., Hazari, S., Smith, Z. J., Knudson, A., Robertson, C. S., Lam, K. S. & Wachsmann-Hogiu, S. (2015). 3D plasmonic nanobowl platform for the study of exosomes

in solution. *Nanoscale*, *7*(20), 9290–9297.

Lee, K., Fraser, K., Ghaddar, B., Yang, K., Kim, E., Balaj, L., Chiocca, E. A., Breakefield, X. O., Lee, H. & Weissleder, R. (2018). Multiplexed Profiling of Single Extracellular Vesicles. *ACS Nano*, *12*(1), 494–503.

Liquid biopsy. (2021). *Nature Biotechnology*, *39*(2), 154.

Liu, J., Jalali, M., Mahshid, S. & Wachsmann-Hogiu, S. (2020). Are plasmonic optical biosensors ready for use in point-of-need applications? In *Analyst* (Vol. 145, Issue 2, pp. 364–384). Royal Society of Chemistry.

Louis, D. N., Perry, A., Reifenberger, G., Deimling, A. Von, Figarella, D., Webster, B., Hiroko, K. C., Wiestler, O. D., Kleihues, P. & Ellison, D. W. (2016). The 2016 World Health Organization Classification of Tumors of the Central Nervous System : a summary. *Acta Neuropathologica*, *131*(6), 803–820.

Mahshid, S., Ahamed, M. J., Berard, D., Amin, S., Sladek, R., Leslie, S. R. & Reisner, W. (2015). Development of a platform for single cell genomics using convex lens-induced confinement. *Lab Chip*, *15*(14), 3013–3020.

Mollaei, H., Safaralizadeh, R. & Pouladi, N. (2017). A brief review of exosomes and their roles in cancer. *Meta Gene*, *11*, 70–74.

Najmaei, S., Mlayah, A., Arbouet, A., Girard, C., Leotin, J. & Lou, J. (2014). Plasmonic pumping of excitonic photoluminescence in hybrid MoS2-Au nanostructures. *ACS Nano*, *8*(12), 12682–12689.

Nawaz, M., Fatima, F., Zanetti, B. R. & Martins, I. D. L. (2014). *Microvesicles in Gliomas and Medulloblastomas : An Overview*. *February*.

Pan, S., Zhang, Y., Natalia, A., Lim, C. Z. J., Ho, N. R. Y., Chowbay, B., Loh, T. P., Tam, J. K. C. & Shao, H. (2021). Extracellular vesicle drug occupancy enables real-time monitoring of targeted cancer therapy. *Nature Nanotechnology*, *16*(6), 734–742.

Park, Jaena, Hwang, M., Choi, B., Jeong, H., Jung, J. H., Kim, H. K., Hong, S., Park, J. H. & Choi, Y. (2017). Exosome Classification by Pattern Analysis of Surface-Enhanced Raman Spectroscopy Data for Lung Cancer Diagnosis. *Analytical Chemistry*, *89*(12), 6695–6701.

Park, Jongmin, Park, J. S., Huang, C. H., Jo, A., Cook, K., Wang, R., Lin, H. Y., Van Deun, J., Li, H., Min, J., Wang, L., Yoon, G., Carter, B. S., Balaj, L., Choi, G. S., Castro, C. M., Weissleder, R. & Lee, H. (2021). An integrated magneto-electrochemical device for the rapid profiling of tumour extracellular vesicles from blood plasma. *Nature Biomedical Engineering*, *5*(7), 678–689.

Poudineh, M., Sargent, E. H., Pantel, K. & Kelley, S. O. (2018). Profiling circulating tumour cells and other biomarkers of invasive cancers. In *Nature Biomedical Engineering* (Vol. 2, Issue 2, pp. 72–84). Nature Publishing Group.

Preusser, M. (2014). Neuro-oncology: A step towards clinical blood biomarkers of glioblastoma. In *Nature Reviews Neurology* (Vol. 10, Issue 12, pp. 681–682). Nature Publishing Group.

Ramirez, M. I., Amorim, M. G., Gadelha, C., Milic, I., Welsh, J. A., Freitas, V. M., Nawaz, M., Akbar, N., Couch, Y., Makin, L., Cooke, F., Vettore, A. L., Batista, P. X., Freezor, R., Pezuk, J. A., Rosa-Fernandes, L., Carreira, A. C. O., Devitt, A., Jacobs, L., … Dias-Neto, E. (2018). Technical challenges of working with extracellular vesicles. In *Nanoscale* (Vol. 10, Issue 3, pp. 881–906). Royal Society of Chemistry.

Reifenberger, G., Wirsching, H. G., Knobbe-Thomsen, C. B. & Weller, M. (2017). Advances in the molecular genetics of gliomas-implications for classification and therapy. In *Nature Reviews Clinical Oncology* (Vol. 14, Issue 7, pp. 434–452). Nature Publishing Group.

Ruggeri, F., Zosel, F., Mutter, N., Rozycka, M., Wojtas, M., Ozyhar, A., Schuler, B. & Krishnan, M. (2017). Single-molecule electrometry. *Nature Nanotechnology*, *12*(5), 488–495.

Shao, H., Chung, J., Balaj, L., Charest, A., Bigner, D. D., Carter, B. S., Hochberg, F. H., Breakefield, X. O., Weissleder, R. & Lee, H. (2012). Protein typing of circulating microvesicles allows real-time monitoring of glioblastoma therapy. *Nature Medicine*, *18*(12), 1835–1840.

Shao, H., Chung, J., Lee, K., Balaj, L., Min, C., Carter, B. S., Hochberg, F. H., Breakefield, X. O., Lee, H. & Weissleder, R. (2015). Chip-based analysis of exosomal mRNA mediating drug resistance in glioblastoma. *Nature Communications*, *6*(1), 1–9.

Shin, H., Jeong, H., Park, J., Hong, S. & Choi, Y. (2018). Correlation between Cancerous Exosomes and Protein Markers Based on Surface-Enhanced Raman Spectroscopy (SERS) and Principal Component Analysis (PCA) [Research-article]. *ACS Sensors*, *3*, 2637–2643.

Shin, H., Oh, S., Hong, S., Kang, M., Kang, D., Ji, Y. G., Choi, B. H., Kang, K. W., Jeong, H., Park, Y., Kim, H. K. & Choi, Y. (2020). Early-Stage Lung Cancer Diagnosis by Deep Learning-Based Spectroscopic Analysis of Circulating Exosomes. *ACS Nano*, *14*(5), 5435–5444.

Shin, H., Oh, S., Kang, D. & Choi, Y. (2020). Protein Quantification and Imaging by Surface-Enhanced Raman Spectroscopy and Similarity Analysis. *Advanced Science*, *7*(11), 1903638.

Siravegna, G., Marsoni, S., Siena, S. & Bardelli, A. (2017). Integrating liquid biopsies into the management of cancer. In *Nature Reviews Clinical Oncology* (Vol. 14, Issue 9, pp. 531–548). Nature Publishing Group.

Spinelli, C., Montermini, L., Meehan, B., Brisson, A. R., Tan, S., Choi, D., Nakano, I. & Rak, J. (2018). Molecular subtypes and differentiation programmes of glioma stem cells as determinants of extracellular vesicle profiles and endothelial cell-stimulating activities. *Journal of Extracellular Vesicles*, *7*(1).

Sriram, P., Manikandan, A., Chuang, F. C. & Chueh, Y. L. (2020). Hybridizing Plasmonic Materials with 2D-Transition Metal Dichalcogenides toward Functional Applications. In *Small* (Vol. 16, Issue 15, p. 1904271). Wiley-VCH Verlag.

Stiles, P. L., Dieringer, J. A., Shah, N. C. & Van Duyne, R. P. (2008). Surface-enhanced Raman spectroscopy. In *Annual Review of Analytical Chemistry* (Vol. 1, Issue 1, pp. 601–626). Annual Reviews.

Stremersch, S., Marro, M., Pinchasik, B. El, Baatsen, P., Hendrix, A., De Smedt, S. C., Loza-

Alvarez, P., Skirtach, A. G., Raemdonck, K. & Braeckmans, K. (2016). Identification of individual exosome-like vesicles by surface enhanced raman spectroscopy. *Small*, *12*(24), 3292–3301.

Viehrig, M., Thilsted, A. H., Matteucci, M., Wu, K., Catak, D., Schmidt, M. S., Zórzór, K. & Boisen, A. (2018). *Injection-Molded Microfluidic Device for SERS Sensing Using Embedded Au-Capped Polymer Nanocones*.

Wachsmann-Hogiu, S., Smith, Z. J. & Kahraman, M. (2019). Editorial: Plasmonic Technologies for Bioanalytical Applications. In *Frontiers in Chemistry* (Vol. 7, p. 865). Frontiers Media S.A.

Wang, J., Koo, K. M., Wang, Y. & Trau, M. (2019). Engineering State-of-the-Art Plasmonic Nanomaterials for SERS-Based Clinical Liquid Biopsy Applications. *Advanced Science*, *6*(23).

Wirsching, H. G., Galanis, E. & Weller, M. (2016). Glioblastoma. In *Handbook of Clinical Neurology* (Vol. 134, pp. 381–397). Elsevier.

Wu, C.-Y., Du, S.-L., Zhang, J., Liang, A.-L. & Liu, Y.-J. (2017). Exosomes and breast cancer: a comprehensive review of novel therapeutic strategies from diagnosis to treatment. *Cancer Gene Therapy*, *24*(1), 6–12.

Wu, P., Cai, J., Chen, Q., Han, B., Meng, X., Li, Y., Li, Z., Wang, R., Lin, L., Duan, C., Kang, C. & Jiang, C. (2019). Lnc-TALC promotes O 6 -methylguanine-DNA methyltransferase expression via regulating the c-Met pathway by competitively binding with miR-20b-3p. *Nature Communications*, *10*(1), 1–15.

Yang, Y., Shen, G., Wang, H., Li, H., Zhang, T., Tao, N., Ding, X. & Yu, H. (2018). Interferometric plasmonic imaging and detection of single exosomes. *Proceedings of the National Academy of Sciences of the United States of America*, *115*(41), 10275–10280.

Zachariah, M. A., Oliveira-Costa, J. P., Carter, B. S., Stott, S. L. & Nahed, B. V. (2018). Blood-based biomarkers for the diagnosis and monitoring of gliomas. *Neuro-Oncology*, *20*(9), 1155–1161.

Zhou, Y. G., Mohamadi, R. M., Poudineh, M., Kermanshah, L., Ahmed, S., Safaei, T. S., Stojcic, J., Nam, R. K., Sargent, E. H. & Kelley, S. O. (2016). Interrogating Circulating Microsomes and Exosomes Using Metal Nanoparticles. *Small*, *12*(6), 727–732.

9 Comprehensive Discussions, Conclusions and Future Directions

9.1 Thesis Findings

The thesis demonstrates the successful development and implementation of a microchip utilizing a hybrid nanocavity plasmonic surface for capturing the Raman spectra of individual extracellular vesicles (EVs). This breakthrough technology showcases the potential of single EV surface-enhanced Raman scattering (SERS) interrogation as a powerful tool for molecular profiling and characterization of EVs. Furthermore, the thesis presents a detailed exploration of the SERS spectra, which reflect molecular changes contributing to cellular responses to temozolomide (TMZ) chemotherapy—a crucial component of standard care for glioblastoma (GBM) patients. Through experiments conducted on human glioma stem cells (GSCs) with mesenchymal molecular characteristics, the study demonstrates the detection of SERS-detectable changes associated with TMZ exposure and the loss of TMZ response due to specific molecular mechanisms such as the expression of O^6-methylguanine DNA methyltransferase (MGMT) or the presence of a hypermutant phenotype. Additionally, the thesis addresses the quantification of SERS results obtained from circulating extracellular vesicles (EVs) present in the cerebrospinal fluid (CSF) and plasma of GBM patients. The remarkable accuracy of 96% achieved in comparison to clinical pathology tests highlights the diagnostic value and clinical potential of utilizing SERS analysis of circulating EVs.

The scientific development achieved through my Ph.D. studies holds impact in multiple aspects. Firstly, the development of the microchip-based technology for single EV Raman interrogation provides a potentially precise platform for label free EV analysis, enabling advancements in the fields of diagnostics, disease monitoring, and personalized medicine. Secondly, the investigation of SERS spectra and their correlation with molecular changes in

response to TMZ chemotherapy contributes to a deeper understanding of the cellular mechanisms involved in drug resistance and treatment response in GBM. This knowledge may assist the future development of more effective therapeutic strategies and targeted interventions. Lastly, the quantification and accurate analysis of SERS results obtained from circulating EVs offer a non-invasive and reliable approach for assessing treatment responses and disease progression in GBM patients. This has significant implications for clinical practice, providing clinicians with valuable information to inform treatment decisions and monitor patient outcomes. The detail of the findings in each chapter is discussed in the following.

In chapter 1, the objectives, motivations, and aims of the thesis project are introduced, along with a technical background on the design and development of hybrid nanoplasmonic arrays.

Chapter 2 presents a comprehensive literature review of state-of-the-art plasmonic arrays utilized for optical sensing of EVs as potential cancer liquid biopsy biomarkers. Different nanoarrays used for entrapment enhancement, investigating cancer status via biorecognition dependent methods such as SPR and fluorescent microscopy, and label-free methods such as SERS are reviewed. Furthermore, clinical validation studies using nanoarrays along with analysis tools are highlighted.

Bridging Chapter 3 outlines the design and evaluation of the convex plasmonic nanoarray microchip, with a focus on enhanced optical and electrical properties, as well as surface chemistry, to improve the efficiency of SERS. The material purity and optical properties of the systems were also characterized. Initially, low-cost patterning techniques were used to develop on-chip optical sensing platforms. However, due to the limitations of bulk analysis in profiling molecular traits in EVs harboring genomic molecular alterations, precision lithography techniques were used,

enabling single EV resolution. The chapter also includes an overview of the attempts to develop on-chip plasmonic nanostructured platforms with enhanced light-matter interaction properties, although not necessarily suitable for optical investigation of EVs.

In chapter 4, we demonstrated the differentiation of EVs released by different cancer cells, glioblastoma (GBM) based on their SERS molecular profiling using a plasmonic nanobowtie array embedded in a fluidic device. With assisted properties laid by a fluidic sample delivery system, we were able to record and discern the SERS fingerprint of EVs from non-cancerous glial cells (NHA) and two sub-populations of the glioma EVs (i.e. U87 and U373). The fabless nanopatterned structure of nanobowties (convex) with sharp apex and narrow gaps served as a SERS platform with enhanced electromagnetic field at the apex. In manuscript and supporting theoretical and experimental information we characterized different properties of the nanobowtie platform in terms of surface morphology, optical characteristics and simulated physical behavior. Our studies revealed that narrow gaps of nanobowtie structure comprises strong electromagnetic field (theoretical EFEF of 9.0×10^5). The assembly of such signals is the initial step in building a comprehensive library of data that can ultimately inform clinicians as to diversity and relevant traits of cancer cells. The SERS signals from two sub-populations of the glioblastomas cells was documented in the manuscript with complete multivariate principal component analysis.

However, as discussed in the bridging chapter 5, using a convex nanosurface microfluidic does not allow for single EV SERS interrogation. Therefore, to achieve the capacity of recording single EV Raman fingerprint we aimed to design, fabricate and validate a microchip based on a hybrid nanocavity plasmonic surface in the following chapter.

In chapter 6, initially demonstrated the potential of single EV SERS for differentiation of the EVs derived from molecularly altered cancer cell lines (GBM) and compile their spectra as a reference library. Next, we showed the potential of the single EV SERS approach in a translational setting to stratify the mutational epigenetic molecular traits in the circulating EVs from the patient plasma samples. To enable sensitive single EV SERS molecular profiling, we designed a plasmonic nanocavity array embedded with monolayer single crystalline MoS_2 for interrogation of clinically important molecular traits reflective of cellular heterogeneity, and mutational and epigenetic driver events in hard to access tumor cancers (Glioblastoma). A silver thin film pierced with nanocavity array was used as plasmonic active surface propelling enhanced SERS signal from EVs biocargo entrapped in the nanocavities with similar size and geometry. The zinc oxide material was used as spacer (and back reflector) of the plasmonic substrate to have the interior walls of the nanocavities biocompatible all the while providing the high refractive index material as back-reflector for enhanced plasmonic effect from silver thin-film. A large area single crystalline, monolayer MoS_2 hybridized with plasmonic silver nanocavities was used for single EV entrapment and amplified SERS profiling.

In this chapter, we focused on the differentiation of EVs derived from GBM patient plasma samples from non-cancer ones according to signatures of glioblastoma paradigmatic molecular subtypes, including the mutant oncogenic variant of epidermal growth factor receptor (EGFR), known as EGFRvIII, as well as O^6-Methylguanine-DNA Methyltransferase (MGMT). We validated the accuracy of plasmonic 2D-3D nanostructured micro-chip using glioma cells harbouring the key mutant oncogenic variants for diagnosis via multivariate analysis methods and machine learning algorithms. We were able to enhance the accuracy with which the micro-chip distinguishes the molecular alteration traits in single EVs which enabled the recognition of EV

subsets in the parental population with a detection limit of 1.23%. Finally, we analysed the composition of putative glioblastoma mutations in 12 established patient models and differentiate tumour EVs from largely platelet-derived particles in GBM patient blood samples with an accuracy of 87%.

In Chapter 7, we provide a rationale for extending the single extracellular vesicle (EV) study and elaborate on our decision to integrate this analytical platform for tracking epigenetic changes that underlie chemotherapy resistance in GBM. We postulated that conducting a thorough investigation into the potential of single EV SERS fingerprint spectra, which provide insights into molecular changes associated with cellular responses to temozolomide (TMZ) chemotherapy, could offer valuable contributions to the field of EVs liquid biopsy and therapeutic research.

Chapter 8 covers a study that uses single EV SERS fingerprinting technology to investigate the molecular changes that contribute to the cellular evolution of TMZ-naïve and -resistance xenograft models in human glioma stem cells with mesenchymal molecular characteristics. The study monitored the presence of these characteristic molecular traits in the presence of TMZ after 24 and 72 hours to identify the set of molecular traits that distinguish susceptible and resistant cells. The ultimate goal of the study is to employ the single EV SERS in conjunction with machine learning to detect the molecular traits that differentiate susceptible and resistant cells. Additionally, the study seeks to quantify the SERS findings of circulating EVs in the cerebrospinal fluid and plasma of patients diagnosed with TMZ-resistant or -naïve GBM cancer.

Chapter 9 discusses the thesis findings and highlights the future outlook. It is my hope that the technologies and concepts shared in this dissertation will enable researchers to access critically important information on the status of molecular alterations in the tumors, all the while, inspire

them to develop better, more accurate on-chip systems of molecular recognition for point-of-care diagnostic systems.

9.2 Discussion and Conclusion

Cancer is a significant cause of mortality globally, with a high financial burden on the healthcare industry with a cost crossing over 26 billion in Canada alone. The lack of deep knowledge about the progression of cancer is a major problem, and 77% of the mortality cases, although differs depending on the type and stage of the cancer, are due to chemotherapy-resistant mutations. Lethal brain cancers, such as GBM, have the highest mortality rates even after therapy, with a median survival time of 15 months after diagnosis. Non-invasive liquid biopsies provide a promising avenue for providing real-time insights into the molecular characteristics of diseases, including drug resistance and targets, without invasive procedures.

Tumor-derived extracellular vesicles (EVs) represent unique liquid biopsy platforms, owing to their crucial biological roles in intercellular tumor communication and their ability to serve as natural carriers of oncogenic mutations and biological information. However, standard molecular analyses of bulk EVs face numerous challenges related to preparation, high background noise from normal signals, and diagnostic signal averaging, which restrict multiplexing opportunities and obscure the molecular signatures of tumor heterogeneity. Therefore, there is an urgent need for a diagnostic tool that can selectively isolate single nucleic acid-carrying exosomes and enable high-throughput, comprehensive analysis of nucleic acid contents and multiple cancer markers.

This study aimed to design label-free, on-chip platforms using hybrid plasmonic nanoarrays, for the identification of molecular characteristics in single EVs as potential biomarkers for cancer liquid biopsy. The development, customization, and characterization of on-chip plasmonic nanoconfined frameworks promoted with 2D material with positive interaction with

bilayer lipid for label-free single EV entrapment. We used monolayer MoS_2 to introduce positive attraction between the bottom of the nanocavities and the bilayer lipid of the EVs, led to 97% filling of the nanocavities with single EVs. The unique properties of the layered oxide/metal layers in the confined plasmonic nanocavity spaces, provide amplified electromagnetic field enhancement (6.4×10^5), enabling the detection and molecular profiling of heterogeneous EVs. Surface-enhanced approaches, such as surface-enhanced Raman spectroscopy (SERS), were employed to investigate molecular alterations in heterogeneous circulating EVs as alternative cancer biomarkers, leveraging the plasmonic effect of the ordered array of nanostructured surfaces to achieve enhanced optical signal transduction.

We used the single EV molecular fingerprint profiling in the paradigm of glioblastoma (GBM) brain cancer. The hybrid plasmonic microchips for the label-free isolation and confinement of EVs, with a field enhancement sufficient to obtain sensitive signal resolution. demonstrated a detection limit of 1.23% for EVs from variant cells suspended in a wild-type EV population. This allows for processing blood samples where the GBM biomarkers are diluted to 3-10%. The single EV molecular fingerprint profiling was then used to differentiate EVs derived from different non-cancer and cancer cells were differentiated via single EV molecular fingerprinting profiling with 91% accuracy. The circulating EVs derived from blood samples of healthy individuals and cancer patients were investigated using multivariate analysis and machine learning as a tool with more than 87% accuracy to record changes in the single EV spectral fingerprint.

The single EV SERS technology was used then to investigate molecular changes that contribute to the cellular evolution of xenograft models in human glioma stem cells (GSCs) and identified molecular traits that distinguish susceptible and resistant cells. This study demonstrated

the potential of sEV SERS profiles to stratify the circulating EVs from drug resistant GBM patients,with 91% accuracy compared with hich is on par with clinical pathology tests.

The results demonstrate the potential of using single EV SERS fingerprinting for the diagnosis and monitoring of cancer progression, especially for high-risk individuals and patients under therapy for monitoring the development of resistance. This approach offers a non-invasive and cost-effective way to monitor cancer progression and treatment response with high accuracy and sensitivity. This approach has the potential to classify different molecular tumor subtypes based on spectroscopic fingerprints drawn from single EVs spectra, which can be used as a form of liquid biopsy to determine the existence of molecular traits underlying drug resistance in tumors. The sEV SERS approach represents a promising avenue for the development of a non-invasive and label-free cancer monitoring tool that could significantly enhance the survival of patients with complex cancers, such as GBM. However, there are still challenges to overcome, such as tumor EV scarcity, heterogeneity, and intrinsic complexity, which can hinder real-time monitoring of complex cancers. Future studies are expected to validate the accuracy and reproducibility of this technique across larger cohorts of patients.

In conclusion, this dissertation presents an innovative and effective approach for the identification of molecular characteristics in single extracellular vesicles as potential biomarkers for cancer liquid biopsy. The on-chip hybrid plasmonic cavity array promoted with 2D material provide a label-free isolation and confinement of EVs, enabling sensitive signal resolution. The single EV SERS fingerprinting method, combined with machine learning, offers a non-invasive and cost-effective approach for the diagnosis and monitoring of cancer progression, especially for high-risk individuals and patients under therapy for monitoring the development of resistance. This

approach offers a promising avenue for providing real-time insights into the molecular characteristics of diseases, including drug resistance and targets, without invasive procedures, and has the potential to significantly improve cancer diagnosis and treatment.

9.3 Future Outlook

In the realm of precision medicine and liquid biopsy the identification of molecular traits of cancer cells is crucial diagnostically (disease type) and therapeutically (targeted therapy options, companion diagnostics). From a technology development standpoint, the interdisciplinary nature of this work is likely to attract a broad audience in the fields of bioengineering, glioma, cancer, diagnostics, and encourage innovative applications of the bioengineering solutions proposed to address important medical questions. In particular, the technology developed in this PhD project provides an enhanced readout of molecular traits such as genomic information, as SERS provides a distinguished fingerprint from enclosed bio-cargo of EVs.

From *diagnosis* point of view, invasive cancers are highly heterogeneous, difficult to detect early and exhibits resistance to therapy due to cellular diversity that is presently extremely difficult to grasp, with no real time solutions. The development of non-invasive liquid biopsy technologies based on decoded SERS signals of EVs bio-cargo is a groundbreaking achievement in cancer research. The potential for these technologies to offer risk-free, real-time glimpses into the molecular hallmarks of invasive cancers such as pediatric, leukemia, and hepatoma is truly remarkable. With this new approach, it will be possible to treat each patient individually based on the biologically malignant state of their tumor.

The single EV SERS approach requires no surface markers for EVs isolation, offers label-free sensing, high throughput, and quantitative analysis of EVs. Therefore, the potential for this

technology to be customizable for investigating the stratification of molecular traits in other invasive cancers, as well as other diseases with circulating EVs as their biomarkers, is very exciting.

The comparison-driven analytical approaches used in this thesis for the classifying of single EV SERS provide a coherent and reproducible pipeline based on distinguishable SERS signals as a fingerprint library for known data to stratify the blind samples accordingly. Therefore, this pipeline withstands the potential to offer customizable analytical readout to investigate stratification of molecular traits not only in other invasive cancers but also in other diseases with circulating EVs as their biomarkers.

From *Therapeutic* point of view, the effectiveness of drugs in patients with metabolic diseases such as cancer is an important goal in healthcare. The development of non-invasive liquid biopsies offers a promising avenue for obtaining rapid, risk-free, and real-time insights into the molecular hallmarks of diseases such as cancer, including drug resistance and targets. The non-invasive optical molecular profiling of extracellular vesicles (EVs) is a significant step towards the development of new therapies where decoded surface-enhanced Raman scattering (SERS) signals of EVs could serve as a measure of therapeutic response.

As a preliminary study, the occupancy of Temozolomide (TMZ) was tested on susceptible cell lines and those bearing O^6-Methylguanine-DNA Methyltransferase (MGMT), a marker of resistance to this chemotherapy drug. The stratification of the effectiveness of TMZ on the susceptible and resistant cells, along with the ability to stratify resistant markers such as MGMT in patient-derived EV samples, opens potential windows for real-time monitoring of the effect of the chemotherapeutic drug occupancy in patients. This technology provides a powerful tool for

identifying drug-resistant tumor cells and monitoring the efficacy of chemotherapy treatment, which can ultimately improve patient outcomes.

From the *materials and manufacturing* point of view, the development of customizable label-free methods for simultaneous isolation and surface-enhanced optical detection of nanoscale analytes based on their physicochemical interaction with functional materials holds immense value. The results obtained from this PhD research project on different hybrid plasmonic nanostructured frameworks promoted with monolayer materials, provide a suitable grid for customization of these frameworks for other types of bioanalytes of interest, depending on their surface chemistry, size, and spatial geometry.

Unlike the liquid phase SERS nanotags, the on-chip patterning methods investigated in this project (entailing fabless colloidal self-assembly monolayer nanoparticle lithography and ebeam lithography) offer easy integrability sample delivery microfluidic systems which allows for easy sample delivery and confined space for high throughput testing. The ease of integration with different substrates and optoelectronic devices provides ample opportunities for future investigation of these platforms in other settings such as field effect transistors (FETs).

The development of these customizable label-free methods for simultaneous isolation and surface-enhanced optical detection of nanoscale analytes has the potential to revolutionize the field of molecular profiling and detection. By enabling highly sensitive and specific detection of a wide range of bioanalytes, these platforms could have significant implications for diagnostic and therapeutic applications. Moreover, the easy integrability with various microfluidic systems and substrates could facilitate the adoption of these platforms in various research and clinical settings.

Overall, this research has demonstrated the immense potential of nanoscale manufacturing and patterning techniques for developing innovative and efficient biosensing platforms.

10 References

AbdelFatah, T., Jalali, M. & Mahshid, S. (2018). A nanofilter for fluidic devices by pillar- assisted self-assembly microparticles. *Biomicrofluidics*, *12*, 064103. https://doi.org/10.1063/1.5048623

Akselrod, G. M., Ming, T., Argyropoulos, C., Hoang, T. B., Lin, Y., Ling, X., Smith, D. R., Kong, J. & Mikkelsen, M. H. (2015). Leveraging nanocavity harmonics for control of optical processes in 2d semiconductors. *Nano Letters*, *15*(5), 3578–3584. https://doi.org/10.1021/acs.nanolett.5b01062

Al-Nedawi, K., Meehan, B., Micallef, J., Lhotak, V., May, L., Guha, A. & Rak, J. (2008a). Intercellular transfer of the oncogenic receptor EGFRvIII by microvesicles derived from tumour cells. *Nature Cell Biology*, *10*(5), 619–624. https://doi.org/10.1038/ncb1725

Al-Nedawi, K., Meehan, B., Micallef, J., Lhotak, V., May, L., Guha, A. & Rak, J. (2008b). Intercellular transfer of the oncogenic receptor EGFRvIII by microvesicles derived from tumour cells. *Nature Cell Biology*, *10*(5), 619–624. https://doi.org/10.1038/ncb1725

Ali, H., Harting, R., de Vries, R., Ali, M., Wurdinger, T. & Best, M. G. (2021). Blood-Based Biomarkers for Glioma in the Context of Gliomagenesis: A Systematic Review. In *Frontiers in Oncology* (Vol. 11, p. 2134). Frontiers Media S.A. https://doi.org/10.3389/fonc.2021.665235

Anker, J. N., Hall, W. P., Lyandres, O., Shah, N. C., Zhao, J., Duyne, R. P. V. A. N. & Un, N. (2008). *B i osens i ng w i th plasmon i c nanosensors*. *7*(June), 8–10.

Arraud, N., Linares, R., Tan, S., Gounou, C., Pasquet, J. M., Mornet, S. & Brisson, A. R. (2014). Extracellular vesicles from blood plasma: Determination of their morphology, size, phenotype and concentration. *Journal of Thrombosis and Haemostasis*, *12*(5), 614–627. https://doi.org/10.1111/jth.12554

Ashcroft, N. W.; Mermin, N. D. (1968). Solid state physics. *Vacuum*, *18*(9), 525. https://doi.org/10.1016/0042-207x(68)90868-3

Avella-Oliver, M., Puchades, R., Wachsmann-Hogiu, S. & Maquieira, A. (2017). Label-free SERS analysis of proteins and exosomes with large-scale substrates from recordable compact disks. *Sensors and Actuators, B: Chemical*, *252*, 657–662. https://doi.org/10.1016/j.snb.2017.06.058

Bagshaw, C R & Cherny, D. (2006). *Blinking fluorophores : what do they tell us about protein dynamics ?* 979–982.

Bagshaw, Clive R, Conibear, P. B., Le, L. & Bagshaw, C. R. (2000). *Single-Molecule Enzymology : Critical Aspects Exemplified by Myosin ATPase Activity*. *1*, 271–277.

Bai, S., Serien, D., Hu, A. & Sugioka, K. (2018a). 3D Microfluidic Surface-Enhanced Raman Spectroscopy (SERS) Chips Fabricated by All-Femtosecond-Laser-Processing for Real-Time Sensing of Toxic Substances. *Advanced Functional Materials*, *28*(23), 1706262. https://doi.org/10.1002/adfm.201706262

Bai, S., Serien, D., Hu, A. & Sugioka, K. (2018b). 3D Microfluidic Surface-Enhanced Raman Spectroscopy (SERS) Chips Fabricated by All-Femtosecond-Laser-Processing for Real-Time Sensing of Toxic Substances. *Advanced Functional Materials*, *28*(23), 1706262. https://doi.org/10.1002/adfm.201706262

Bai, Y., Lu, Y., Wang, K., Cheng, Z., Qu, Y., Qiu, S., Zhou, L., Wu, Z., Liu, H., Zhao, J. & Mao, H. (2019). Rapid Isolation and Multiplexed Detection of Exosome Tumor Markers Via Queued Beads Combined with Quantum Dots in a Microarray. *Nano-Micro Letters*, *11*(1), 1–11. https://doi.org/10.1007/s40820-019-0285-x

Bardelli, A. & Pantel, K. (2017). Liquid Biopsies, What We Do Not Know (Yet). In *Cancer Cell* (Vol. 31, Issue 2, pp. 172–179). Cell Press. https://doi.org/10.1016/j.ccell.2017.01.002

Biagioni, P., Huang, J., Hecht, B., Decker, M., Staude, I., Lindquist, N. C., Nagpal, P. & Mcpeak, K. M. (2013). *Optical nanoantennas*. https://doi.org/10.3367/UFNe.0183.201306a.0561

Biswas, D., Ganeshalingam, J. & Wan, J. C. M. (2020). The future of liquid biopsy. In *The Lancet Oncology* (Vol. 21, Issue 12, p. 550). https://doi.org/10.1016/S1470-2045(20)30687-2

Bo, X., Zhou, M. & Guo, L. (2017). Biosensors and Bioelectronics Electrochemical sensors and biosensors based on less aggregated graphene. *Biosensors and Bioelectronic*, *89*, 167–186. https://doi.org/10.1016/j.bios.2016.05.002

Bohren, C. F. (1983). Absorption and scattering of light by small particles. In *Absorption and scattering of light by small particles*. WILEY-VCH Verlag. https://doi.org/10.1088/0031-9112/35/3/025

Bolotin, K. I., Sikes, K. J., Jiang, Z., Klima, M., Fudenberg, G., Hone, J., Kim, P. & Stormer, H. L. (2008). Ultrahigh electron mobility in suspended graphene. *Solid State Communications*, *146*(9–10), 351–355. https://doi.org/10.1016/j.ssc.2008.02.024

Bonyár, A., Csarnovics, I., Veres, M., Himics, L., Csik, A., Kámán, J., Balázs, L. & Kökényesi, S. (2018). Investigation of the performance of thermally generated gold nanoislands for LSPR and SERS applications. *Sensors and Actuators, B: Chemical*, *255*, 433–439. https://doi.org/10.1016/j.snb.2017.08.063

Boriachek, K., Islam, M. N., Möller, A., Salomon, C., Nguyen, N. T., Hossain, M. S. A., Yamauchi, Y. & Shiddiky, M. J. A. (2018). Biological Functions and Current Advances in Isolation and Detection Strategies for Exosome Nanovesicles. *Small*, *14*(6), 1–21. https://doi.org/10.1002/smll.201702153

Boulesbaa, A., Babicheva, V. E., Wang, K., Kravchenko, I. I., Lin, M.-W., Mahjouri-Samani, M., Jacobs, C. B., Puretzky, A. A., Xiao, K., Ivanov, I., Rouleau, C. M. & Geohegan, D. B. (2016). Ultrafast Dynamics of Metal Plasmons Induced by 2D Semiconductor Excitons in Hybrid Nanostructure Arrays. *ACS Photonics*, acsphotonics.6b00618. https://doi.org/10.1021/acsphotonics.6b00618

Bradbury, S. and Evennett, P. (1996). *Fluorescence microscopy, Contrast Techniques in Light Microscopy.,*. BIOS Scientific Publishers, Ltd.,.

Brenner, H. (1961). The slow motion of a sphere through a viscous fluid towards a plane surface. *Chemical Engineering Science*, *16*(3–4), 242–251. https://doi.org/10.1016/0009-2509(61)80035-3

Broekman, M. L., Maas, S. L. N., Abels, E. R., Mempel, T. R., Krichevsky, A. M. & Breakefield, X. O. (2018). Multidimensional communication in the microenvirons of glioblastoma. *Nature Reviews Neurology*, *14*(8), 482–495. https://doi.org/10.1038/s41582-018-0025-8

Butler, H. J., Ashton, L., Bird, B., Cinque, G., Curtis, K., Dorney, J., Esmonde-White, K., Fullwood, N. J., Gardner, B., Martin-Hirsch, P. L., Walsh, M. J., McAinsh, M. R., Stone, N. & Martin, F. L. (2016).

Using Raman spectroscopy to characterize biological materials. *Nature Protocols*, *11*(4), 664–687. https://doi.org/10.1038/nprot.2016.036

Cai, W., Zhu, Y., Li, X., Piner, R. D. & Ruoff, R. S. (2009). Large area few-layer graphene/graphite films as transparent thin conducting electrodes. *Applied Physics Letters*, *95*(12). https://doi.org/10.1063/1.3220807

Carmicheal, J., Hayashi, C., Huang, X., Liu, L., Lu, Y., Krasnoslobodtsev, A., Lushnikov, A., Kshirsagar, P. G., Patel, A., Jain, M., Lyubchenko, Y. L., Lu, Y., Batra, S. K. & Kaur, S. (2019). Label-free characterization of exosome via surface enhanced Raman spectroscopy for the early detection of pancreatic cancer. *Nanomedicine: Nanotechnology, Biology, and Medicine*, *16*, 88–96. https://doi.org/10.1016/j.nano.2018.11.008

Chaffer, C. L. & Weinberg, R. A. (2011). A perspective on cancer cell metastasis. In *Science* (Vol. 331, Issue 6024, pp. 1559–1564). American Association for the Advancement of Science. https://doi.org/10.1126/science.1203543

Chen, C., Zong, S., Liu, Y., Wang, Z., Zhang, Y., Chen, B. & Cui, Y. (2019a). Profiling of Exosomal Biomarkers for Accurate Cancer Identification: Combining DNA-PAINT with Machine- Learning-Based Classification. *Small*, *15*(43), 1901014. https://doi.org/10.1002/smll.201901014

Chen, C., Zong, S., Liu, Y., Wang, Z., Zhang, Y., Chen, B. & Cui, Y. (2019b). Profiling of Exosomal Biomarkers for Accurate Cancer Identification: Combining DNA-PAINT with Machine- Learning-Based Classification. *Small*, *15*(43), 1901014. https://doi.org/10.1002/smll.201901014

Chen, Jing, Ge, J., Zhang, L., Li, Z., Li, J., Sun, Y. & Qu, L. (2016). Reduced graphene oxide nanosheets functionalized with poly(styrene sulfonate) as a peroxidase mimetic in a colorimetric assay for ascorbic acid. *Microchimica Acta*, *183*(6), 1847–1853. https://doi.org/10.1007/s00604-016-1826-3

Chen, Juhong, Jackson, A. A., Rotello, V. M. & Nugen, S. R. (2016). Colorimetric Detection of Escherichia coli Based on the Enzyme-Induced Metallization of Gold Nanorods. *Small*, *12*(18), 2469–2475. https://doi.org/10.1002/smll.201503682

Chen, W., Li, J., Wei, X., Fan, Y., Qian, H., Li, S., Xiang, Y. & Ding, S. (2020). Surface plasmon resonance biosensor using hydrogel-AuNP supramolecular spheres for determination of prostate cancer-derived exosomes. *Microchimica Acta*, *187*(11), 1–10. https://doi.org/10.1007/s00604-020-04573-4

Chen, W. Y., Chang, H. Y., Lu, J. K., Huang, Y. C., Harroun, S. G., Tseng, Y. T., Li, Y. J., Huang, C. C. & Chang, H. T. (2015). Self-Assembly of Antimicrobial Peptides on Gold Nanodots: Against Multidrug-Resistant Bacteria and Wound-Healing Application. *Advanced Functional Materials*, *25*(46), 7189–7199. https://doi.org/10.1002/adfm.201503248

Chhowalla, M., Shin, H. S., Eda, G., Li, L.-J., Loh, K. P. & Zhang, H. (2013). The chemistry of two-dimensional layered transition metal dichalcogenide nanosheets. *Nature Chemistry*, *5*(4), 263–275. https://doi.org/10.1038/nchem.1589

Chien, F.-C., Kuo, C. W., Yang, Z.-H., Chueh, D.-Y. & Chen, P. (2011). Exploring the Formation of Focal Adhesions on Patterned Surfaces Using Super-Resolution Imaging. *Small*, *7*(20), 2906–2913. https://doi.org/10.1002/smll.201100753

Chin, L. K., Son, T., Hong, J. S., Liu, A. Q., Skog, J., Castro, C. M., Weissleder, R., Lee, H. & Im, H.

(2020). Plasmonic sensors for extracellular vesicle analysis: From scientific development to translational research. In *ACS Nano* (Vol. 14, Issue 11, pp. 14528–14548). American Chemical Society. https://doi.org/10.1021/acsnano.0c07581

Cho, K., Min, M., Kim, T. Y., Jeong, H., Pak, J., Kim, J. K., Jang, J., Yun, S. J., Lee, Y. H., Hong, W. K. & Lee, T. (2015). Electrical and Optical Characterization of MoS2 with Sulfur Vacancy Passivation by Treatment with Alkanethiol Molecules. *ACS Nano*, *9*(8), 8044–8053. https://doi.org/10.1021/acsnano.5b04400

Cho, S., Yi, J., Kwon, Y., Kang, H., Han, C. & Park, J. (2021). Multifluorescence Single Extracellular Vesicle Analysis by Time-Sequential Illumination and Tracking. *ACS Nano*, *15*(7), 11753–11761. https://doi.org/10.1021/acsnano.1c02556

Choi, D., Montermini, L., Jeong, H., Sharma, S., Meehan, B. & Rak, J. (2019). Mapping Subpopulations of Cancer Cell-Derived Extracellular Vesicles and Particles by Nano-Flow Cytometry. *ACS Nano*, *13*(9), 10499–10511. https://doi.org/10.1021/acsnano.9b04480

Choi, D., Montermini, L., Kim, D. K., Meehan, B., Roth, F. P. & Rak, J. (2018). The impact of oncogenic egfrviii on the proteome of extracellular vesicles released from glioblastoma cells. *Molecular and Cellular Proteomics*, *17*(10), 1948–1964. https://doi.org/10.1074/mcp.RA118.000644

Choi, D., Spinelli, C., Montermini, L. & Rak, J. (2019). Oncogenic Regulation of Extracellular Vesicle Proteome and Heterogeneity. In *Proteomics* (Vol. 19, Issues 1–2, p. 1800169). https://doi.org/10.1002/pmic.201800169

Contreras-Naranjo, J. C., Wu, H. J. & Ugaz, V. M. (2017). Microfluidics for exosome isolation and analysis: Enabling liquid biopsy for personalized medicine. In *Lab on a Chip* (Vol. 17, Issue 21, pp. 3558–3577). Royal Society of Chemistry. https://doi.org/10.1039/c7lc00592j

Couch, Y., Buzàs, E. I., Vizio, D. Di, Gho, Y. S., Harrison, P., Hill, A. F., Lötvall, J., Raposo, G., Stahl, P. D., Théry, C., Witwer, K. W. & Carter, D. R. F. (2021). A brief history of nearly EV-erything – The rise and rise of extracellular vesicles. In *Journal of Extracellular Vesicles* (Vol. 10, Issue 14, p. e12144). John Wiley & Sons, Ltd. https://doi.org/10.1002/jev2.12144

De Abajo, F. J. G. (2007). Colloquium: Light scattering by particle and hole arrays. *Reviews of Modern Physics*, *79*(4), 1267–1290. https://doi.org/10.1103/RevModPhys.79.1267

De Maesschalck, R., Jouan-Rimbaud, D. & Massart, D. L. (2000). The Mahalanobis distance. *Chemometrics and Intelligent Laboratory Systems*, *50*(1), 1–18. https://doi.org/10.1016/S0169-7439(99)00047-7

Di Noto, G., Bugatti, A., Zendrini, A., Mazzoldi, E. L., Montanelli, A., Caimi, L., Rusnati, M., Ricotta, D. & Bergese, P. (2016). Merging colloidal nanoplasmonics and surface plasmon resonance spectroscopy for enhanced profiling of multiple myeloma-derived exosomes. *Biosensors and Bioelectronics*, *77*, 518–524. https://doi.org/10.1016/j.bios.2015.09.061

Diem, M., Romeo, M., Boydston-White, S., Miljković, M. & Matthäus, C. (2004). A decade of vibrational micro-spectroscopy of human cells and tissue (1994-2004). *Analyst*, *129*(10), 880–885. https://doi.org/10.1039/b408952a

Ding, Y., Zhou, N., Gan, L., Yan, X., Wu, R., Abidi, I. H., Waleed, A., Pan, J., Ou, X., Zhang, Q., Zhuang,

M., Wang, P., Pan, X., Fan, Z., Zhai, T. & Luo, Z. (2018). Stacking-mode confined growth of 2H-MoTe2/MoS2 bilayer heterostructures for UV–vis–IR photodetectors. *Nano Energy*, *49*, 200–208. https://doi.org/10.1016/j.nanoen.2018.04.055

Dittrich, P. S. & Manz, A. (2006). Lab-on-a-chip: Microfluidics in drug discovery. *Nature Reviews Drug Discovery*, *5*(3), 210–218. https://doi.org/10.1038/nrd1985

Dodson, S., Haggui, M., Bachelot, R., Plain, J., Li, S. & Xiong, Q. (2013). Optimizing electromagnetic hotspots in plasmonic bowtie nanoantennae. *Journal of Physical Chemistry Letters*, *4*(3), 496–501. https://doi.org/10.1021/jz302018x

Dong, J., Chen, J. F., Smalley, M., Zhao, M., Ke, Z., Zhu, Y. & Tseng, H. R. (2020). Nanostructured Substrates for Detection and Characterization of Circulating Rare Cells: From Materials Research to Clinical Applications. In *Advanced Materials* (Vol. 32, Issue 1, p. 1903663). John Wiley & Sons, Ltd. https://doi.org/10.1002/adma.201903663

Dong, J., Zhang, R. Y., Sun, N., Hu, J., Smalley, M. D., Zhou, A., Hua, Y., Rothermich, W., Chen, M., Chen, J., Ye, J., Teng, P. C., Qi, D., Toretsky, J. A., Tomlinson, J. S., Li, M., Weiss, P. S., Jonas, S. J., Federman, N., … Zhu, Y. (2020). Coupling Nanostructured Microchips with Covalent Chemistry Enables Purification of Sarcoma-Derived Extracellular Vesicles for Downstream Functional Studies. *Advanced Functional Materials*, *30*(49). https://doi.org/10.1002/adfm.202003237

Dong, J., Zhang, R. Y., Sun, N., Smalley, M., Wu, Z., Zhou, A., Chou, S. J., Jan, Y. J., Yang, P., Bao, L., Qi, D., Tang, X., Tseng, P., Hua, Y., Xu, D., Kao, R., Meng, M., Zheng, X., Liu, Y., … Zhu, Y. (2019). Bio-Inspired NanoVilli Chips for Enhanced Capture of Tumor-Derived Extracellular Vesicles: Toward Non-Invasive Detection of Gene Alterations in Non-Small Cell Lung Cancer. *ACS Applied Materials and Interfaces*, *11*(15), 13973–13983. https://doi.org/10.1021/acsami.9b01406

Dong, S., Wang, Y., Liu, Z., Zhang, W., Yi, K., Zhang, X., Zhang, X., Jiang, C., Yang, S., Wang, F. & Xiao, X. (2020). Beehive-Inspired Macroporous SERS Probe for Cancer Detection through Capturing and Analyzing Exosomes in Plasma. *ACS Applied Materials and Interfaces*, *12*(4), 5136–5146. https://doi.org/10.1021/acsami.9b21333

Dong, X., Chi, J., Zheng, L., Ma, B., Li, Z., Wang, S., Zhao, C. & Liu, H. (2019). Efficient isolation and sensitive quantification of extracellular vesicles based on an integrated ExoID-Chip using photonic crystals. *Lab on a Chip*, *19*(17), 2897–2904. https://doi.org/10.1039/c9lc00445a

Du, K., Zhu, Y., Xu, H. & Yang, X. (2011). Multifunctional magnetic nanoparticles: Synthesis modification and biomedical applications. *Progress in Chemistry*, *23*(11).

Eda, G. & Maier, S. A. (2013). Two-dimensional crystals: Managing light for optoelectronics. *ACS Nano*, *7*(7), 5660–5665. https://doi.org/10.1021/nn403159y

Elbourne, A., Crawford, R. J. & Ivanova, E. P. (2017). Nano-structured antimicrobial surfaces: From nature to synthetic analogues. *Journal of Colloid and Interface Science*, *508*, 603–616. https://doi.org/10.1016/j.jcis.2017.07.021

Fan, M., Wang, P., Escobedo, C., Sinton, D. & Brolo, A. G. (2012). Surface-enhanced Raman scattering (SERS) optrodes for multiplexed on-chip sensing of nile blue A and oxazine 720. *Lab on a Chip*, *12*(8), 1554–1560. https://doi.org/10.1039/c2lc20648j

Fan, X., White, I. M., Shopova, S. I., Zhu, H., Suter, J. D. & Sun, Y. (2008). Sensitive optical biosensors for unlabeled targets: A review. *Analytica Chimica Acta*, *620*(1–2), 8–26. https://doi.org/10.1016/j.aca.2008.05.022

Faried, M., Suga, K., Okamoto, Y., Shameli, K., Miyake, M. & Umakoshi, H. (2019). Membrane Surface-Enhanced Raman Spectroscopy for Cholesterol-Modified Lipid Systems: Effect of Gold Nanoparticle Size. *ACS Omega*, *4*(9), 13687–13695. https://doi.org/10.1021/acsomega.9b01073

Feng, S., Zheng, Z., Xu, Y., Lin, J., Chen, G., Weng, C., Lin, D., Qiu, S., Cheng, M., Huang, Z., Wang, L., Chen, R., Xie, S. & Zeng, H. (2017). A noninvasive cancer detection strategy based on gold nanoparticle surface-enhanced raman spectroscopy of urinary modified nucleosides isolated by affinity chromatography. *Biosensors and Bioelectronics*, *91*, 616–622. https://doi.org/10.1016/j.bios.2017.01.006

Feng, X., Tang, Q., Zhou, J., Fang, J., Ding, P., Sun, L. & Shi, L. (2013). Novel mixed-solvothermal synthesis of MoS2 nanosheets with controllable morphologies. *Crystal Research and Technology*, *48*(6), 363–368. https://doi.org/10.1002/crat.201300003

Ferguson, S., Yang, K. S., Zelga, P., Liss, A. S., Carlson, J. C. T., del Castillo, C. F. & Weissleder, R. (2022). Single-EV analysis (sEVA) of mutated proteins allows detection of stage 1 pancreatic cancer. *Science Advances*, *8*(16). https://doi.org/10.1126/sciadv.abm3453

Ferhan, A. R., Jackman, J. A., Park, J. H. & Cho, N. J. (2018). Nanoplasmonic sensors for detecting circulating cancer biomarkers. In *Advanced Drug Delivery Reviews* (Vol. 125, pp. 48–77). Elsevier. https://doi.org/10.1016/j.addr.2017.12.004

Fontaine, N., Picard-Lafond, A., Asselin, J. & Boudreau, D. (2020). Thinking outside the shell: Novel sensors designed from plasmon-enhanced fluorescent concentric nanoparticles. In *Analyst* (Vol. 145, Issue 18, pp. 5965–5980). Royal Society of Chemistry. https://doi.org/10.1039/d0an01092h

Fort, E. & Grésillon, S. (2008a). Surface enhanced fluorescence. *Journal of Physics D: Applied Physics*, *41*(1), 013001. https://doi.org/10.1088/0022-3727/41/1/013001

Fort, E. & Grésillon, S. (2008b). Surface enhanced fluorescence. *Journal of Physics D: Applied Physics*, *41*(1), 013001. https://doi.org/10.1088/0022-3727/41/1/013001

Foudeh, A. M., Fatanat Didar, T., Veres, T. & Tabrizian, M. (2012). Microfluidic designs and techniques using lab-on-a-chip devices for pathogen detection for point-of-care diagnostics. *Lab on a Chip*, *12*(18), 3249. https://doi.org/10.1039/c2lc40630f

Fraire, J. C., Stremersch, S., Bouckaert, D., Monteyne, T., De Beer, T., Wuytens, P., De Rycke, R., Skirtach, A. G., Raemdonck, K., De Smedt, S. & Braeckmans, K. (2019). Improved Label-Free Identification of Individual Exosome-like Vesicles with Au@Ag Nanoparticles as SERS Substrate. *ACS Applied Materials and Interfaces*, *11*(43), 39424–39435. https://doi.org/10.1021/acsami.9b11473

Fraser, K., Jo, A., Giedt, J., Vinegoni, C., Yang, K. S., Peruzzi, P., Chiocca, E. A., Breakefield, X. O., Lee, H. & Weissleder, R. (2019a). Characterization of single microvesicles in plasma from glioblastoma patients. *Neuro-Oncology*, *21*(5), 606–615. https://doi.org/10.1093/neuonc/noy187

Fraser, K., Jo, A., Giedt, J., Vinegoni, C., Yang, K. S., Peruzzi, P., Chiocca, E. A., Breakefield, X. O., Lee, H. & Weissleder, R. (2019b). Characterization of single microvesicles in plasma from glioblastoma

patients. *Neuro-Oncology*, *21*(5), 606–615. https://doi.org/10.1093/neuonc/noy187

Fromm, D. P., Sundaramurthy, A., James Schuck, P., Kino, G. & Moerner, W. E. (2004). Gap-dependent optical coupling of single "bowtie" nanoantennas resonant in the visible. *Nano Letters*, *4*(5), 957–961. https://doi.org/10.1021/nl049951r

Galarreta, B. C., Tabatabaei, M., Guieu, V., Peyrin, E. & Lagugné-Labarthet, F. (2013). Microfluidic channel with embedded SERS 2D platform for the aptamer detection of ochratoxin A. *Analytical and Bioanalytical Chemistry*, *405*(5), 1613–1621. https://doi.org/10.1007/s00216-012-6557-7

Gale, J. D., Geim, A. K., Novoselov, K. S., Castro Neto, A. H., Peres, N. M. R., Novoselov, K. S., Geim, A. K., Tuckerman, M. E., Tomadin, A., Loya, A., Stair, J. L., Ren, G., Geim, A. K., Novoselov, K. S., Geim A. K., Novoselov K. S., Dewapriya, M. A. N., Barker, J. a., Henderson, D., … Vozmediano, M. A. H. (2012). The rise of graphene. *Reviews of Modern Physics*, *58*(1), 710–734. https://doi.org/10.1016/j.jmps.2010.02.008

Gan, T. & Hu, S. (2011). Electrochemical sensors based on graphene materials. *Microchimica Acta*, *175*(1–2), 1–19. https://doi.org/10.1007/s00604-011-0639-7

Gao, F., Cai, X., Wang, X., Gao, C., Liu, S., Gao, F. & Wang, Q. (2013). Highly sensitive and selective detection of dopamine in the presence of ascorbic acid at graphene oxide modified electrode. *Sensors and Actuators, B: Chemical*, *186*, 380–387. https://doi.org/10.1016/j.snb.2013.06.020

Garnier, D., Meehan, B., Kislinger, T., Daniel, P., Sinha, A., Abdulkarim, B., Nakano, I. & Rak, J. (2018a). Divergent evolution of temozolomide resistance in glioblastoma stem cells is reflected in extracellular vesicles and coupled with radiosensitization. *Neuro-Oncology*, *20*(2), 236–248. https://doi.org/10.1093/neuonc/nox142

Garnier, D., Meehan, B., Kislinger, T., Daniel, P., Sinha, A., Abdulkarim, B., Nakano, I. & Rak, J. (2018b). Divergent evolution of temozolomide resistance in glioblastoma stem cells is reflected in extracellular vesicles and coupled with radiosensitization. *Neuro-Oncology*, *20*(2), 236–248. https://doi.org/10.1093/neuonc/nox142

Garnier, D., Meehan, B., Kislinger, T., Daniel, P., Sinha, A., Abdulkarim, B., Nakano, I. & Rak, J. (2018c). Divergent evolution of temozolomide resistance in glioblastoma stem cells is reflected in extracellular vesicles and coupled with radiosensitization. *Neuro-Oncology*, *20*(2), 236–248. https://doi.org/10.1093/neuonc/nox142

Geim, A. K. & Novoselov, K. S. (2009). The rise of graphene. In *Nanoscience and Technology: A Collection of Reviews from Nature Journals* (pp. 11–19). World Scientific Publishing Co. https://doi.org/10.1142/9789814287005_0002

Gerkman, M. A., Lee, J. K., Li, X., Zhang, Q., Windley, M., Fonseca, M. V., Lu, Y., Warner, J. H. & Han, G. G. D. (2019). Direct Imaging of Individual Molecular Binding to Clean Nanopore Edges in 2D Monolayer MoS $_2$. *ACS Nano*, acsnano.9b06061. https://doi.org/10.1021/acsnano.9b06061

Giannini, V., Fernandez-Dominguez, A. I., Heck, S. C., Maier, S. A., Fernández-Domínguez, A. I., Heck, S. C. & Maier, S. A. (2011). Plasmonic nanoantennas: Fundamentals and their use in controlling the radiative properties of nanoemitters. *Chemical Reviews*, *111*(6), 3888–3912. https://doi.org/10.1021/cr1002672

Gittens, R. A., Olivares-navarrete, R., Cheng, A., Anderson, D. M., Mclachlan, T., Stephan, I., Geis-gerstorfer, J., Sandhage, K. H., Fedorov, A. G., Rupp, F., Boyan, B. D., Tannenbaum, R. & Schwartz, Z. (2013). Acta Biomaterialia The roles of titanium surface micro / nanotopography and wettability on the differential response of human osteoblast lineage cells. *Acta Biomaterialia*, *9*(4), 6268–6277. https://doi.org/10.1016/j.actbio.2012.12.002

Grasso, L., Wyss, R., Weidenauer, L., Thampi, A., Demurtas, D., Prudent, M., Lion, N. & Vogel, H. (2015). Molecular screening of cancer-derived exosomes by surface plasmon resonance spectroscopy. *Analytical and Bioanalytical Chemistry*, *407*(18), 5425–5432. https://doi.org/10.1007/s00216-015-8711-5

Gregory, Kalyuzhny; Gregory, Kalyuzhny; Marie Anne, S. I. & Rubinstein. (2002). T-SPR measurements for monitoring adsorption on ultrathin Gold Island Films. *Business*, *17*, 3849–3857.

Gu, Z., Chen, S. H., Ding, Z., Song, W., Wei, W., Liu, S., Ma, G. & Zhou, R. (2019). The molecular mechanism of robust macrophage immune responses induced by PEGylated molybdenum disulfide. *Nanoscale*, *11*(46), 22293–22304. https://doi.org/10.1039/C9NR04358F

Gu, Z., Plant, L. D., Meng, X. Y., Perez-Aguilar, J. M., Wang, Z., Dong, M., Logothetis, D. E. & Zhou, R. (2018). Exploring the Nanotoxicology of MoS2: A Study on the Interaction of MoS2 Nanoflakes and K+ Channels. *ACS Nano*, *12*(1), 705–717. https://doi.org/10.1021/acsnano.7b07871

Han, S., Xu, Y., Sun, J., Liu, Y., Zhao, Y., Tao, W. & Chai, R. (2020). Isolation and analysis of extracellular vesicles in a Morpho butterfly wing-integrated microvortex biochip. *Biosensors and Bioelectronics*, *154*, 112073. https://doi.org/10.1016/j.bios.2020.112073

Hanash, S. M., Baik, C. S. & Kallioniemi, O. (2011). Emerging molecular biomarkers-blood-based strategies to detect and monitor cancer. In *Nature Reviews Clinical Oncology* (Vol. 8, Issue 3, pp. 142–150). Nature Publishing Group. https://doi.org/10.1038/nrclinonc.2010.220

Happel, J. & Brenner, H. (1973). *Low Reynolds number hydrodynamics.* (Vol. 1). Springer Netherlands. https://doi.org/10.1016/0009-2509(66)85045-5

Harris, L. G., Meredith, D. O., Eschbach, L. & Richards, R. G. (2007). Staphylococcus aureus adhesion to standard micro-rough and electropolished implant materials. *Journal of Materials Science: Materials in Medicine*, *18*(6), 1151–1156. https://doi.org/10.1007/s10856-007-0143-0

Hartjes, T. A., Mytnyk, S., Jenster, G. W., van Steijn, V. & van Royen, M. E. (2019). Extracellular vesicle quantification and characterization: Common methods and emerging approaches. In *Bioengineering* (Vol. 6, Issue 1, p. 7). Multidisciplinary Digital Publishing Institute. https://doi.org/10.3390/bioengineering6010007

Hatab, N. A., Hsueh, C. H., Gaddis, A. L., Retterer, S. T., Li, J. H., Eres, G., Zhang, Z. & Gu, B. (2010a). Free-standing optical gold bowtie nanoantenna with variable gap size for enhanced Raman spectroscopy. *Nano Letters*, *10*(12), 4952–4955. https://doi.org/10.1021/nl102963g

Hatab, N. A., Hsueh, C. H., Gaddis, A. L., Retterer, S. T., Li, J. H., Eres, G., Zhang, Z. & Gu, B. (2010b). Free-standing optical gold bowtie nanoantenna with variable gap size for enhanced Raman spectroscopy. *Nano Letters*, *10*(12), 4952–4955. https://doi.org/10.1021/nl102963g

He, K., Zhang, X., Ren, S. & Sun, J. (2016). Deep residual learning for image recognition. *Proceedings of*

the IEEE Computer Society Conference on Computer Vision and Pattern Recognition, *2016-Decem*, 770–778. https://doi.org/10.1109/CVPR.2016.90

He, M., Crow, J., Roth, M., Zeng, Y. & Godwin, A. K. (2014). Integrated immunoisolation and protein analysis of circulating exosomes using microfluidic technology. *Lab on a Chip*, *14*(19), 3773–3780. https://doi.org/10.1039/c4lc00662c

Henkel, T., Popp, J. & März, A. (2010). SERS and Microfluidics. In *Surface Enhanced Raman Spectroscopy: Analytical, Biophysical and Life Science Applications* (pp. 173–190). Wiley-VCH Verlag GmbH & Co. KGaA. https://doi.org/10.1002/9783527632756.ch8

Hisey, C. L., Dorayappan, K. D. P., Cohn, D. E., Selvendiran, K. & Hansford, D. J. (2018). Microfluidic affinity separation chip for selective capture and release of label-free ovarian cancer exosomes. *Lab on a Chip*, *18*(20), 3144–3153. https://doi.org/10.1039/c8lc00834e

Ho, C. S., Jean, N., Hogan, C. A., Blackmon, L., Jeffrey, S. S., Holodniy, M., Banaei, N., Saleh, A. A. E., Ermon, S. & Dionne, J. (2019). Rapid identification of pathogenic bacteria using Raman spectroscopy and deep learning. *Nature Communications*, *10*(1), 1–8. https://doi.org/10.1038/s41467-019-12898-9

Hoi, S.-K., Chen, X., Kumar, V. S., Homhuan, S., Sow, C.-H. & Bettiol, A. A. (2011). A Microfluidic Chip with Integrated Colloidal Crystal for Online Optical Analysis. *Advanced Functional Materials*, *21*(15), 2847–2853. https://doi.org/10.1002/adfm.201002632

Hosseini, I. I., Liu, Z., Capaldi, X., Abdelfatah, T., Montermini, L., Rak, J., Reisner, W. & Mahshid, S. (2021). Nanofluidics for Simultaneous Size and Charge Profiling of Extracellular Vesicles. *Nano Letters*, *21*(12), 4895–4902. https://doi.org/10.1021/acs.nanolett.0c02558

Hu, M., Chen, J., Li, Z.-Y., Au, L., Hartland, G. V., Li, X., Marquez, M. & Xia, Y. (2006). Gold nanostructures: engineering their plasmonic properties for biomedical applications. *Chemical Society Reviews*, *35*(11), 1084. https://doi.org/10.1039/b517615h

Huang, H. K., Cheng, H. W., Liao, C. C., Lin, S. J., Chen, Y. Z., Wang, J. K., Wang, Y. L. & Huang, N. T. (2020). Bacteria encapsulation and rapid antibiotic susceptibility test using a microfluidic microwell device integrating surface-enhanced Raman scattering. *Lab on a Chip*, *20*(14), 2520–2528. https://doi.org/10.1039/d0lc00425a

Huang, J., Dong, Z., Li, Y., Li, J., Tang, W., Yang, H., Wang, J., Bao, Y., Jin, J. & Li, R. (2013). MoS2nanosheet functionalized with Cu nanoparticles and its application for glucose detection. *Materials Research Bulletin*, *48*(11), 4544–4547. https://doi.org/10.1016/j.materresbull.2013.07.060

Im, H., Shao, H., Park, Y. Il, Peterson, V. M., Castro, C. M., Weissleder, R. & Lee, H. (2014a). Label-free detection and molecular profiling of exosomes with a nano-plasmonic sensor. *Nature Biotechnology*, *32*(5), 490–495. https://doi.org/10.1038/nbt.2886

Im, H., Shao, H., Park, Y. Il, Peterson, V. M., Castro, C. M., Weissleder, R. & Lee, H. (2014b). Label-free detection and molecular profiling of exosomes with a nano-plasmonic sensor. *Nature Biotechnology*, *32*(5), 490–495. https://doi.org/10.1038/nbt.2886

Imanbekova, M., Suarasan, S., Lu, Y., Jurchuk, S. & Wachsmann-Hogiu, S. (2022). Recent advances in optical label-free characterization of extracellular vesicles. In *Nanophotonics* (Vol. 11, Issue 12, pp. 2827–2863). De Gruyter Open Ltd. https://doi.org/10.1515/nanoph-2022-0057

Imanbekova, M., Suarasan, S., Rojalin, T., Mizenko, R. R., Hilt, S., Mathur, M., Lepine, P., Nicouleau, M., Mohamed, N.-V. V., Durcan, T. M., Carney, R. P., Voss, J. C. & Wachsmann-Hogiu, S. (2021). Identification of amyloid beta in small extracellular vesicles *via* Raman spectroscopy. *Nanoscale Advances*, *3*(14), 4119–4132. https://doi.org/10.1039/D1NA00330E

Issadore, D., Chung, H. J., Chung, J., Budin, G., Weissleder, R. & Lee, H. (2013). μHall chip for sensitive detection of bacteria. *Advanced Healthcare Materials*, *2*(9), 1224–1228. https://doi.org/10.1002/adhm.201200380

Jain, P. K., Lee, K. S., El-Sayed, I. H. & El-Sayed, M. A. (2006). Calculated absorption and scattering properties of gold nanoparticles of different size, shape, and composition: Applications in biological imaging and biomedicine. *Journal of Physical Chemistry B*, *110*(14), 7238–7248. https://doi.org/10.1021/jp057170o

Jalali, M., AbdelFatah, T., Mahshid, S. S., Labib, M. & Mahshid, S. (2018). Hierarchical 3D Nanostructured Microfluidic Device for Sensitive Detection of Pathogenic Bacteria. *Small*, *1801893*, 1–15. https://doi.org/10.1002/smll.201801893

Jalali, M., Filine, E., Dalfen, S. & Mahshid, S. (2020). Microscale reactor embedded with Graphene/hierarchical gold nanostructures for electrochemical sensing: application to the determination of dopamine. *Microchimica Acta*, *187*(1), 90. https://doi.org/10.1007/s00604-019-4059-4

Jalali, M., Gao, Z., Yu, Y., Siavash Moakhar, R., Ding, Y., Zhuang, M., Zhou, N., König, T., Fery, A., Mahshid, S. & Luo, Z. (2021). Synergistic enhancement of photoluminesent intensity in monolayer molybdenum disulfide embedded with plasmonic nanostructures for catalytic sensing. *2D Materials*, *8*(3), 035049. https://doi.org/10.1088/2053-1583/ac040e

Jalali, M., Isaac Hosseini, I., AbdelFatah, T., Montermini, L., Wachsmann Hogiu, S., Rak, J. & Mahshid, S. (2021). Plasmonic nanobowtiefluidic device for sensitive detection of glioma extracellular vesicles by Raman spectrometry. *Lab on a Chip*, *21*(5), 855–866. https://doi.org/10.1039/d0lc00957a

Jalali, M., Moakhar, R. S., Abdelfattah, T., Filine, E., Mahshid, S. S. & Mahshid, S. (2020). Nanopattern-Assisted Direct Growth of Peony-like 3D MoS2/Au Composite for Nonenzymatic Photoelectrochemical Sensing. *ACS Applied Materials and Interfaces*, *12*(6), 7411–7422. https://doi.org/10.1021/acsami.9b17449

Johnstone, I. B. (1983). Comparative effects of phenylbutazone, naproxen and flunixin meglumine on equine platelet aggregation and platelet factor 3 availability in vitro. *Canadian Journal of Comparative Medicine*, *47*(2), 172–179. /pmc/articles/PMC1235914/?report=abstract

Kang, Y. T., Purcell, E., Palacios-Rolston, C., Lo, T. W., Ramnath, N., Jolly, S. & Nagrath, S. (2019). Isolation and Profiling of Circulating Tumor-Associated Exosomes Using Extracellular Vesicular Lipid–Protein Binding Affinity Based Microfluidic Device. *Small*, *15*(47), 1903600. https://doi.org/10.1002/smll.201903600

Kaufman, L., Cooper, T. T., Wallace, G. Q., Hawke, D. C., Betts, D., Hess, D. A. & Lagugné-Labarthet, F. (2019). Trapping and SERS identification of extracellular vesicles using nanohole arrays. In T. Vo-Dinh, H.-P. A. Ho & K. Ray (Eds.), *Plasmonics in Biology and Medicine XVI* (Vol. 10894, p. 10). SPIE. https://doi.org/10.1117/12.2506633

Kim, G., Vinerean, H. & Gaitas, A. (2017). A Novel Pathogen Capturing Device for Removal and Detection. *Scientific Reports*, *7*(1), 1–11. https://doi.org/10.1038/s41598-017-05854-4

Kingma, D. P. & Ba, J. L. (2015, December 22). Adam: A method for stochastic optimization. *3rd International Conference on Learning Representations, ICLR 2015 - Conference Track Proceedings*. https://arxiv.org/abs/1412.6980v9

Knudson, A., Hazari, S., Carney, R. P., Robertson, C. S., Lam, K. S., Wachsmann-Hogiu, S., Lee, C. & Smith, Z. J. (2015). 3D plasmonic nanobowl platform for the study of exosomes in solution. *Nanoscale*, *7*(20), 9290–9297. https://doi.org/10.1039/c5nr01333j

Ko, J., Bhagwat, N., Yee, S. S., Ortiz, N., Sahmoud, A., Black, T., Aiello, N. M., McKenzie, L., O'Hara, M., Redlinger, C., Romeo, J., Carpenter, E. L., Stanger, B. Z. & Issadore, D. (2017). Combining Machine Learning and Nanofluidic Technology to Diagnose Pancreatic Cancer Using Exosomes. *ACS Nano*, *11*(11), 11182–11193. https://doi.org/10.1021/acsnano.7b05503

Laing, S., Jamieson, L. E., Faulds, K. & Graham, D. (2017). Surface-enhanced Raman spectroscopy for in vivo biosensing. In *Nature Reviews Chemistry* (Vol. 1). https://doi.org/10.1038/s41570-017-0060

Lakowicz, J. R. (2006). Plasmonics in biology and plasmon-controlled fluorescence. In *Plasmonics* (Vol. 1, Issue 1, pp. 5–33). https://doi.org/10.1007/s11468-005-9002-3

Lane, R., Simon, T., Vintu, M., Solkin, B., Koch, B., Stewart, N., Benstead-Hume, G., Pearl, F. M. G., Critchley, G., Stebbing, J. & Giamas, G. (2019). Cell-derived extracellular vesicles can be used as a biomarker reservoir for glioblastoma tumor subtyping. *Communications Biology*, *2*(1), 1–12. https://doi.org/10.1038/s42003-019-0560-x

Lao, Z., Zheng, Y., Dai, Y., Hu, Y., Ni, J., Ji, S., Cai, Z., Smith, Z. J., Li, J., Zhang, L., Wu, D. & Chu, J. (2020). Nanogap Plasmonic Structures Fabricated by Switchable Capillary-Force Driven Self-Assembly for Localized Sensing of Anticancer Medicines with Microfluidic SERS. *Advanced Functional Materials*, *30*(15), 1909467. https://doi.org/10.1002/adfm.201909467

Le Ru, E. C., Blackie, E., Meyer, M. & Etchegoint, P. G. (2007). Surface enhanced raman scattering enhancement factors: A comprehensive study. *Journal of Physical Chemistry C*, *111*(37), 13794–13803. https://doi.org/10.1021/jp0687908

Lee, C., Carney, R., Lam, K. & Chan, J. W. (2017). SERS analysis of selectively captured exosomes using an integrin-specific peptide ligand. *Journal of Raman Spectroscopy*, *48*(12), 1771–1776. https://doi.org/10.1002/jrs.5234

Lee, C., Carney, R. P., Hazari, S., Smith, Z. J., Knudson, A., Robertson, C. S., Lam, K. S. & Wachsmann-Hogiu, S. (2015). 3D plasmonic nanobowl platform for the study of exosomes in solution. *Nanoscale*, *7*(20), 9290–9297. https://doi.org/10.1039/c5nr01333j

Lee, K., Fraser, K., Ghaddar, B., Yang, K., Kim, E., Balaj, L., Chiocca, E. A., Breakefield, X. O., Lee, H. & Weissleder, R. (2018a). Multiplexed Profiling of Single Extracellular Vesicles. *ACS Nano*, *12*(1), 494–503. https://doi.org/10.1021/acsnano.7b07060

Lee, K., Fraser, K., Ghaddar, B., Yang, K., Kim, E., Balaj, L., Chiocca, E. A., Breakefield, X. O., Lee, H. & Weissleder, R. (2018b). Multiplexed Profiling of Single Extracellular Vesicles. *ACS Nano*, *12*(1), 494–503. https://doi.org/10.1021/acsnano.7b07060

Li, M., Cushing, S. K. & Wu, N. (2015). Plasmon-enhanced optical sensors: A review. In *Analyst* (Vol. 140, Issue 2, pp. 386–406). The Royal Society of Chemistry. https://doi.org/10.1039/c4an01079e

Li, S. J., He, J. Z., Zhang, M. J., Zhang, R. X., Lv, X. L., Li, S. H. & Pang, H. (2013). Electrochemical detection of dopamine using water-soluble sulfonated graphene. *Electrochimica Acta*, *102*, 58–65. https://doi.org/10.1016/j.electacta.2013.03.176

Li, W., Wang, H., Zhao, Z., Gao, H., Liu, C., Zhu, L., Wang, C. & Yang, Y. (2019). Emerging Nanotechnologies for Liquid Biopsy: The Detection of Circulating Tumor Cells and Extracellular Vesicles. In *Advanced Materials* (Vol. 31, Issue 45, p. 1805344). John Wiley & Sons, Ltd. https://doi.org/10.1002/adma.201805344

Li, X., Corbett, A. L., Taatizadeh, E., Tasnim, N., Little, J. P., Garnis, C., Daugaard, M., Guns, E., Hoorfar, M. & Li, I. T. S. (2019). Challenges and opportunities in exosome research—Perspectives from biology, engineering, and cancer therapy. *APL Bioengineering*, *3*(1), 011503. https://doi.org/10.1063/1.5087122

Liang, K., Li, Z., Luo, Y., Zhang, Q., Yin, F., Xu, L., Chen, H. & Wang, H. (2020). Intelligent Nanocomposites with Intrinsic Blood–Brain-Barrier Crossing Ability Designed for Highly Specific MR Imaging and Sonodynamic Therapy of Glioblastoma. *Small*, *16*(8), 1906985. https://doi.org/10.1002/smll.201906985

Liang, Y., Lehrich, B. M., Zheng, S. & Lu, M. (2021). Emerging methods in biomarker identification for extracellular vesicle-based liquid biopsy. In *Journal of Extracellular Vesicles* (Vol. 10, Issue 7, p. e12090). John Wiley & Sons, Ltd. https://doi.org/10.1002/jev2.12090

Lin, B., Lei, Y., Wang, J., Zhu, L., Wu, Y., Zhang, H., Wu, L., Zhang, P. & Yang, C. (2021). Microfluidic-Based Exosome Analysis for Liquid Biopsy. In *Small Methods* (Vol. 5, Issue 3, p. 2001131). John Wiley & Sons, Ltd. https://doi.org/10.1002/smtd.202001131

Link, S. & El-Sayed, M. A. (1999a). Size and Temperature Dependence of the Plasmon Absorption of Colloidal Gold Nanoparticles. *The Journal of Physical Chemistry B*, *103*(21), 4212–4217. https://doi.org/10.1021/jp984796o

Link, S. & El-Sayed, M. A. (1999b). Spectral Properties and Relaxation Dynamics of Surface Plasmon Electronic Oscillations in Gold and Silver Nanodots and Nanorods. *The Journal of Physical Chemistry B*, *103*(40), 8410–8426. https://doi.org/10.1021/jp9917648

Liquid biopsy. (2021). *Nature Biotechnology*, *39*(2), 154. https://doi.org/10.1038/s41587-021-00829-3

Liu, C., Zeng, X., An, Z., Yang, Y., Eisenbaum, M., Gu, X., Jornet, J. M., Dy, G. K., Reid, M. E., Gan, Q. & Wu, Y. (2018). Sensitive Detection of Exosomal Proteins via a Compact Surface Plasmon Resonance Biosensor for Cancer Diagnosis. *ACS Sensors*, *3*(8), 1471–1479. https://doi.org/10.1021/acssensors.8b00230

Liu, Jiangang, Cai, C., Wang, Y., Liu, Y., Huang, L., Tian, T., Yao, Y., Wei, J., Chen, R., Zhang, K., Liu, B. & Qian, K. (2020). A Biomimetic Plasmonic Nanoreactor for Reliable Metabolite Detection. *Advanced Science*, *1903730*. https://doi.org/10.1002/advs.201903730

Liu, Juanjuan, Jalali, M., Mahshid, S. & Wachsmann-Hogiu, S. (2020a). Are plasmonic optical biosensors ready for use in point-of-need applications? In *Analyst* (Vol. 145, Issue 2, pp. 364–384). Royal Society

of Chemistry. https://doi.org/10.1039/c9an02149c

Liu, Juanjuan, Jalali, M., Mahshid, S. & Wachsmann-Hogiu, S. (2020b). Are plasmonic optical biosensors ready for use in point-of-need applications? In *Analyst* (Vol. 145, Issue 2, pp. 364–384). Royal Society of Chemistry. https://doi.org/10.1039/c9an02149c

Liu, L., Chen, S., Xue, Z., Zhang, Z., Qiao, X., Nie, Z., Han, D., Wang, J. & Wang, T. (2018). Bacterial capture efficiency in fluid bloodstream improved by bendable nanowires. *Nature Communications*, *9*(1), 1–9. https://doi.org/10.1038/s41467-018-02879-9

Liu, W., Lee, B., Naylor, C. H., Ee, H. S., Park, J., Johnson, A. T. C. & Agarwal, R. (2016). Strong Exciton-Plasmon Coupling in MoS2 Coupled with Plasmonic Lattice. *Nano Letters*, *16*(2), 1262–1269. https://doi.org/10.1021/acs.nanolett.5b04588

Liu, Y., Dong, X. & Chen, P. (2012). Biological and chemical sensors based on graphene materials. *Chemical Society Reviews*, *41*(6), 2283–2307. https://doi.org/10.1039/c1cs15270j

Lo, T. W., Zhu, Z., Purcell, E., Watza, D., Wang, J., Kang, Y. T., Jolly, S., Nagrath, D. & Nagrath, S. (2020). Microfluidic device for high-throughput affinity-based isolation of extracellular vesicles. *Lab on a Chip*, *20*(10), 1762–1770. https://doi.org/10.1039/c9lc01190k

Lodewijks, K., Ryken, J., Van Roy, W., Borghs, G., Lagae, L. & Van Dorpe, P. (2013). Tuning the Fano Resonance Between Localized and Propagating Surface Plasmon Resonances for Refractive Index Sensing Applications. *Plasmonics*, *8*(3), 1379–1385. https://doi.org/10.1007/s11468-013-9549-3

Louis, D. N., Perry, A., Reifenberger, G., Deimling, A. Von, Figarella, D., Webster, B., Hiroko, K. C., Wiestler, O. D., Kleihues, P. & Ellison, D. W. (2016). The 2016 World Health Organization Classification of Tumors of the Central Nervous System : a summary. *Acta Neuropathologica*, *131*(6), 803–820. https://doi.org/10.1007/s00401-016-1545-1

Lv, X., Geng, Z., Su, Y., Fan, Z., Wang, S., Fang, W. & Chen, H. (2019). Label-Free Exosome Detection Based on a Low-Cost Plasmonic Biosensor Array Integrated with Microfluidics. *Langmuir*, *35*(30), 9816–9824. https://doi.org/10.1021/acs.langmuir.9b01237

Mader, S. & Pantel, K. (2017). Liquid biopsy: Current status and future perspectives. In *Oncology Research and Treatment* (Vol. 40, Issues 7–8, pp. 404–408). S. Karger AG. https://doi.org/10.1159/000478018

Mahshid, S., Ahamed, M. J., Berard, D., Amin, S., Sladek, R., Leslie, S. R. & Reisner, W. (2015). Development of a platform for single cell genomics using convex lens-induced confinement. *Lab Chip*, *15*(14), 3013–3020. https://doi.org/10.1039/C5LC00492F

Maier, S. A. (2004). Fundamentals and Applications Plasmonics : Fundamentals and Applications. In *Physics* (Vol. 677, Issue 1). Springer US. https://doi.org/10.1007/0-387-37825-1/COVER

Massad-Ivanir, N., Shtenberg, C., Zeidman, T. & Segal, E. (2010). Construction and characterization of porous SiO2/ hydrogel hybrids as optical biosensors for rapid detection of bacteria. *Advanced Functional Materials*, *20*(14), 2269–2277. https://doi.org/10.1002/adfm.201000406

Mateo, J., McKay, R., Abida, W., Aggarwal, R., Alumkal, J., Alva, A., Feng, F., Gao, X., Graff, J., Hussain, M., Karzai, F., Montgomery, B., Oh, W., Patel, V., Rathkopf, D., Rettig, M., Schultz, N., Smith, M., Solit, D., … Beltran, H. (2020). Accelerating precision medicine in metastatic prostate cancer. *Nature*

Cancer, *1*(11), 1041–1053. https://doi.org/10.1038/s43018-020-00141-0

McClain, M. A., Culbertson, C. T., Jacobson, S. C. & Ramsey, J. M. (2001). Flow cytometry of Escherichia coli on microfluidic devices. *Analytical Chemistry*, *73*(21), 5334–5338. https://doi.org/10.1021/ac010504v

Menon, P. S., Gan, S. M., Mohamad, N. R., Jamil, N. A., Tarumaraja, K. A., Razak, N. R., Bakar, A. A. A., Mukhtar, W. M., Murat, N. F., Mohamed, R., Khairulazdan, N. B. & Said, F. A. (2019, July 1). Kretschmann based surface plasmon resonance for sensing in visible region. *2019 IEEE 9th International Nanoelectronics Conferences, INEC 2019*. https://doi.org/10.1109/INEC.2019.8853847

Min, L., Wang, B., Bao, H., Li, X., Zhao, L., Meng, J. & Wang, S. (2021). Advanced Nanotechnologies for Extracellular Vesicle-Based Liquid Biopsy. In *Advanced Science* (Vol. 8, Issue 20, p. 2102789). John Wiley & Sons, Ltd. https://doi.org/10.1002/advs.202102789

Miyazaki, C. M., Shimizu, F. M. & Ferreira, M. (2017). Surface Plasmon Resonance (SPR) for Sensors and Biosensors. In *Nanocharacterization Techniques* (pp. 183–200). William Andrew Publishing. https://doi.org/10.1016/B978-0-323-49778-7.00006-0

Mollaei, H., Safaralizadeh, R. & Pouladi, N. (2017). A brief review of exosomes and their roles in cancer. *Meta Gene*, *11*, 70–74. https://doi.org/10.1016/j.mgene.2016.11.010

Mubeen, S., Lee, J., Singh, N., Krämer, S., Stucky, G. D. & Moskovits, M. (2013). An autonomous photosynthetic device in which all charge carriers derive from surface plasmons. *Nature Nanotechnology*, *8*(4), 247–251. https://doi.org/10.1038/nnano.2013.18

Mustafa, F., Hassan, R. Y. A. & Andreescu, S. (2017). Multifunctional nanotechnology-enabled sensors for rapid capture and detection of pathogens. *Sensors (Switzerland)*, *17*(9). https://doi.org/10.3390/s17092121

Nawaz, M., Fatima, F., Zanetti, B. R. & Martins, I. D. L. (2014). *Microvesicles in Gliomas and Medulloblastomas : An Overview*. *February*. https://doi.org/10.4236/jct.2014.52023

Nguyen, H. H., Park, J., Kang, S. & Kim, M. (2015). Surface plasmon resonance: A versatile technique for biosensor applications. In *Sensors (Switzerland)* (Vol. 15, Issue 5, pp. 10481–10510). Multidisciplinary Digital Publishing Institute (MDPI). https://doi.org/10.3390/s150510481

Notingher, I., Verrier, S., Haque, S., Polak, J. M. & Hench, L. L. (2003). Spectroscopic study of human lung epithelial cells (A549) in culture: Living cells versus dead cells. *Biopolymers - Biospectroscopy Section*, *72*(4), 230–240. https://doi.org/10.1002/bip.10378

Novoselov, K. S., Jiang, D., Schedin, F., Booth, T. J., Khotkevich, V. V., Morozov, S. V. & Geim, A. K. (2005). Two-dimensional atomic crystals. *Proceedings of the National Academy of Sciences of the United States of America*, *102*(30), 10451–10453. https://doi.org/10.1073/pnas.0502848102

Pan, S., Zhang, Y., Natalia, A., Lim, C. Z. J., Ho, N. R. Y., Chowbay, B., Loh, T. P., Tam, J. K. C. & Shao, H. (2021). Extracellular vesicle drug occupancy enables real-time monitoring of targeted cancer therapy. *Nature Nanotechnology*, *16*(6), 734–742. https://doi.org/10.1038/s41565-021-00872-w

Pang, Y., Wang, C., Lu, L., Wang, C., Sun, Z. & Xiao, R. (2019). Dual-SERS biosensor for one-step detection of microRNAs in exosome and residual plasma of blood samples for diagnosing pancreatic

cancer. *Biosensors and Bioelectronic*, *130*(November 2018), 204–213. https://doi.org/10.1016/j.bios.2019.01.039

Pantel, K. & Alix-Panabières, C. (2016). Liquid biopsy: Potential and challenges. In *Molecular Oncology* (Vol. 10, Issue 3, pp. 371–373). Wiley-Blackwell. https://doi.org/10.1016/j.molonc.2016.01.009

Park, Jaena, Hwang, M., Choi, B., Jeong, H., Jung, J. H., Kim, H. K., Hong, S., Park, J. H. & Choi, Y. (2017). Exosome Classification by Pattern Analysis of Surface-Enhanced Raman Spectroscopy Data for Lung Cancer Diagnosis. *Analytical Chemistry*, *89*(12), 6695–6701. https://doi.org/10.1021/acs.analchem.7b00911

Park, Jongmin, Park, J. S., Huang, C. H., Jo, A., Cook, K., Wang, R., Lin, H. Y., Van Deun, J., Li, H., Min, J., Wang, L., Yoon, G., Carter, B. S., Balaj, L., Choi, G. S., Castro, C. M., Weissleder, R. & Lee, H. (2021). An integrated magneto-electrochemical device for the rapid profiling of tumour extracellular vesicles from blood plasma. *Nature Biomedical Engineering*, *5*(7), 678–689. https://doi.org/10.1038/s41551-021-00752-7

Patel, A. P., Tirosh, I., Trombetta, J. J., Shalek, A. K., Gillespie, S. M., Wakimoto, H., Cahill, D. P., Nahed, B. V., Curry, W. T., Martuza, R. L., Louis, D. N., Rozenblatt-Rosen, O., Suvà, M. L., Regev, A. & Bernstein, B. E. (2014). Single-cell RNA-seq highlights intratumoral heterogeneity in primary glioblastoma. *Science*, *344*(6190), 1396–1401. https://doi.org/10.1126/science.1254257

Pereiro, I., Bendali, A., Tabnaoui, S., Alexandre, L., Srbova, J., Bilkova, Z., Deegan, S., Joshi, L., Viovy, J.-L., Malaquin, L., Dupuy, B. & Descroix, S. (2017). A new microfluidic approach for the one-step capture, amplification and label-free quantification of bacteria from raw samples. *Chem. Sci.*, *8*(2), 1329–1336. https://doi.org/10.1039/C6SC03880H

Piccart-Gebhart, M. J., Procter, M., Leyland-Jones, B., Goldhirsch, A., Untch, M., Smith, I., Gianni, L., Baselga, J., Bell, R., Jackisch, C., Cameron, D., Dowsett, M., Barrios, C. H., Steger, G., Huang, C.-S., Andersson, M., Inbar, M., Lichinitser, M., Láng, I., … Gelber, R. D. (2005). Trastuzumab after Adjuvant Chemotherapy in HER2-Positive Breast Cancer. *New England Journal of Medicine*, *353*(16), 1659–1672. https://doi.org/10.1056/nejmoa052306

Pilot, R., Signorini, R., Durante, C., Orian, L., Bhamidipati, M. & Fabris, L. (2019). A review on surface-enhanced Raman scattering. *Biosensors*, *9*(2). https://doi.org/10.3390/bios9020057

Platt, J. & others. (1999). Probabilistic outputs for support vector machines and comparisons to regularized likelihood methods. *Advances in Large Margin Classifiers*, *10*(3), 61–74. https://www.researchgate.net/profile/John-Platt-2/publication/2594015_Probabilistic_Outputs_for_Support_Vector_Machines_and_Comparisons_to_Regularized_Likelihood_Methods/links/004635154cff5262d6000000/Probabilistic-Outputs-for-Support-Vector-Machines-and-

Plebanek, M. P., Angeloni, N. L., Vinokour, E., Li, J., Henkin, A., Martinez-Marin, D., Filleur, S., Bhowmick, R., Henkin, J., Miller, S. D., Ifergan, I., Lee, Y., Osman, I., Thaxton, C. S. & Volpert, O. V. (2017). Pre-metastatic cancer exosomes induce immune surveillance by patrolling monocytes at the metastatic niche. *Nature Communications*, *8*(1), 1–12. https://doi.org/10.1038/s41467-017-01433-3

Plowman, B. J., Abdelhamid, M. E., Ippolito, S. J., Bansal, V., Bhargava, S. K. & O'Mullane, A. P. (2014). Electrocatalytic and SERS activity of Pt rich Pt-Pb nanostructures formed via the utilisation of in-situ

underpotential deposition of lead. *Journal of Solid State Electrochemistry*, *18*(12), 3345–3357. https://doi.org/10.1007/s10008-014-2622-9

Potyrailo, R. & Naik, R. R. (n.d.). *Bionanomaterials and Bioinspired Nanostructures for Selective Vapor Sensing*. https://doi.org/10.1146/annurev-matsci-071312-121710

Premasiri, W. R., Moir, D. T., Klempner, M. S., Krieger, N., Jones, G. & Ziegler, L. D. (2005). Characterization of the Surface Enhanced Raman Scattering (SERS) of bacteria. *Journal of Physical Chemistry B*, *109*(1), 312–320. https://doi.org/10.1021/jp040442n

Preusser, M. (2014). Neuro-oncology: A step towards clinical blood biomarkers of glioblastoma. In *Nature Reviews Neurology* (Vol. 10, Issue 12, pp. 681–682). Nature Publishing Group. https://doi.org/10.1038/nrneurol.2014.208

Pucci, F., Garris, C., Lai, C. P., Newton, A., Pfirschke, C., Engblom, C., Alvarez, D., Sprachman, M., Evavold, C., Magnuson, A., Von Andrian, U. H., Glatz, K., Breakefield, X. O., Mempel, T. R., Weissleder, R. & Pittet, M. J. (2016). SCS macrophages suppress melanoma by restricting tumor-derived vesicle-B cell interactions. *Science*, *352*(6282), 242–246. https://doi.org/10.1126/science.aaf1328

Putz, U., Howitt, J., Doan, A., Goh, C. P., Low, L. H., Silke, J. & Tan, S. S. (2012). The tumor suppressor PTEN is exported in exosomes and has phosphatase activity in recipient cells. *Science Signaling*, *5*(243). https://doi.org/10.1126/scisignal.2003084

Raether, H. (1988). *Surface plasmons on gratings* (pp. 91–116). Springer, Berlin, Heidelberg. https://doi.org/10.1007/bfb0048323

Rak, J. (2013). Extracellular vesicles - biomarkers and effectors of the cellular interactome in cancer. In *Frontiers in Pharmacology: Vol. 4 MAR* (p. 21). Frontiers. https://doi.org/10.3389/fphar.2013.00021

Raman, C. V. & Krishnan, K. S. (1928). A new type of secondary radiation [11]. In *Nature* (Vol. 121, Issue 3048, pp. 501–502). https://doi.org/10.1038/121501c0

Ramirez, M. I., Amorim, M. G., Gadelha, C., Milic, I., Welsh, J. A., Freitas, V. M., Nawaz, M., Akbar, N., Couch, Y., Makin, L., Cooke, F., Vettore, A. L., Batista, P. X., Freezor, R., Pezuk, J. A., Rosa-Fernandes, L., Carreira, A. C. O., Devitt, A., Jacobs, L., … Dias-Neto, E. (2018a). Technical challenges of working with extracellular vesicles. In *Nanoscale* (Vol. 10, Issue 3, pp. 881–906). Royal Society of Chemistry. https://doi.org/10.1039/c7nr08360b

Ramirez, M. I., Amorim, M. G., Gadelha, C., Milic, I., Welsh, J. A., Freitas, V. M., Nawaz, M., Akbar, N., Couch, Y., Makin, L., Cooke, F., Vettore, A. L., Batista, P. X., Freezor, R., Pezuk, J. A., Rosa-Fernandes, L., Carreira, A. C. O., Devitt, A., Jacobs, L., … Dias-Neto, E. (2018b). Technical challenges of working with extracellular vesicles. In *Nanoscale* (Vol. 10, Issue 3, pp. 881–906). Royal Society of Chemistry. https://doi.org/10.1039/c7nr08360b

Raposo, G., Nijman, H. W., Stoorvogel, ~willem, Leijendekker, R., Harding, C. V., Melief, C. J. M. & Geuze, H. J. (1996). B lymphocytes secrete antigen-presenting vesicles. *Journal of Experimental Medicine*, *183*(3), 1161–1172. https://doi.org/10.1084/jem.183.3.1161

Reifenberger, G., Wirsching, H. G., Knobbe-Thomsen, C. B. & Weller, M. (2017a). Advances in the molecular genetics of gliomas-implications for classification and therapy. In *Nature Reviews Clinical*

Oncology (Vol. 14, Issue 7, pp. 434–452). Nature Publishing Group. https://doi.org/10.1038/nrclinonc.2016.204

Reifenberger, G., Wirsching, H. G., Knobbe-Thomsen, C. B. & Weller, M. (2017b). Advances in the molecular genetics of gliomas-implications for classification and therapy. In *Nature Reviews Clinical Oncology* (Vol. 14, Issue 7, pp. 434–452). Nature Publishing Group. https://doi.org/10.1038/nrclinonc.2016.204

Robersona, C. D., Ataya, S., Gercel-Taylora, C. & Taylora, D. D. (2010). Tumor-derived exosomes as mediators of disease and potential diagnostic biomarkers. *Cancer Biomarkers*, *8*(4–5), 281–291. https://doi.org/10.3233/CBM-2011-0211

Rojalin, T., Koster, H. J., Liu, J., Mizenko, R. R., Tran, D., Wachsmann-Hogiu, S. & Carney, R. P. (2020a). Hybrid Nanoplasmonic Porous Biomaterial Scaffold for Liquid Biopsy Diagnostics Using Extracellular Vesicles. *ACS Sensors*, *5*(9), 2820–2833. https://doi.org/10.1021/acssensors.0c00953

Rojalin, T., Koster, H. J., Liu, J., Mizenko, R. R., Tran, D., Wachsmann-Hogiu, S. & Carney, R. P. (2020b). Hybrid Nanoplasmonic Porous Biomaterial Scaffold for Liquid Biopsy Diagnostics Using Extracellular Vesicles. *ACS Sensors*, *5*(9), 2820–2833. https://doi.org/10.1021/acssensors.0c00953

Rojalin, T., Phong, B., Koster, H. & Carney, R. P. (2019). Nanoplasmonic approaches for sensitive detection and molecular characterization of extracellular vesicles. In *Frontiers in Chemistry* (Vol. 7, Issue APR, p. 279). Frontiers Media S.A. https://doi.org/10.3389/fchem.2019.00279

Rose, M., Korenblit, Y., Kockrick, E., Borchardt, L., Oschatz, M., Kaskel, S. & Yushin, G. (2011). *Hierarchical Micro- and Mesoporous Carbide-Derived Carbon as a High-Performance Electrode Material in Supercapacitors*. *8*, 1108–1117. https://doi.org/10.1002/smll.201001898

Ruggeri, F. & Krishnan, M. (2018). Entropic Trapping of a Singly Charged Molecule in Solution. *Nano Letters*, *18*(6), 3773–3779. https://doi.org/10.1021/acs.nanolett.8b01011

Rupert, D. L. M., Lässer, C., Eldh, M., Block, S., Zhdanov, V. P., Lotvall, J. O., Bally, M. & Höök, F. (2014). Determination of exosome concentration in solution using surface plasmon resonance spectroscopy. *Analytical Chemistry*, *86*(12), 5929–5936. https://doi.org/10.1021/ac500931f

S Rickard, J. J., Di-Pietro, V., Smith, D. D. J., Davies, D. J., Belli, A. & Goldberg Oppenheimer, P. (2020). *Rapid optofluidic detection of biomarkers for traumatic brain injury via surface-enhanced Raman spectroscopy*. *4*(6), 610–623. https://doi.org/10.1038/s41551-019-0510-4

Saha, K., Agasti, S. S., Kim, C., Li, X. & Rotello, V. M. (2012). Gold nanoparticles in chemical and biological sensing. *Chemical Reviews*, *112*(5), 2739–2779. https://doi.org/10.1021/cr2001178

Sassa, F., Biswas, G. C. & Suzuki, H. (2020). Microfabricated electrochemical sensing devices. In *Lab on a Chip* (Vol. 20, Issue 8, pp. 1358–1389). Royal Society of Chemistry. https://doi.org/10.1039/c9lc01112a

Schuller, J. A., Barnard, E. S., Cai, W., Jun, Y. C., White, J. S. & Brongersma, M. L. (2010). Plasmonics for extreme light concentration and manipulation. *Nature Materials*, *9*(3), 193–204. https://doi.org/10.1038/nmat2630

Schuster, J., Cichos, F. & Von Borczyskowski, C. (2005). Influence of self-trapped states on the

fluorescence intermittency of single molecules. *Applied Physics Letters*, *87*(5), 1–4. https://doi.org/10.1063/1.2006217

Sevim, S., Franco, C., Chen, X., Sorrenti, A., Rodríguez-San-Miguel, D., Pané, S., deMello, A. J. & Puigmartí-Luis, J. (2020). SERS Barcode Libraries: A Microfluidic Approach. *Advanced Science*, 1903172. https://doi.org/10.1002/advs.201903172

Shao, H., Chung, J., Balaj, L., Charest, A., Bigner, D. D., Carter, B. S., Hochberg, F. H., Breakefield, X. O., Weissleder, R. & Lee, H. (2012a). Protein typing of circulating microvesicles allows real-time monitoring of glioblastoma therapy. *Nature Medicine*, *18*. https://doi.org/10.1038/nm.2994

Shao, H., Chung, J., Balaj, L., Charest, A., Bigner, D. D., Carter, B. S., Hochberg, F. H., Breakefield, X. O., Weissleder, R. & Lee, H. (2012b). Protein typing of circulating microvesicles allows real-time monitoring of glioblastoma therapy. *Nature Medicine*, *18*(12), 1835–1840. https://doi.org/10.1038/nm.2994

Shao, H., Chung, J., Lee, K., Balaj, L., Min, C., Carter, B. S., Hochberg, F. H., Breakefield, X. O., Lee, H. & Weissleder, R. (2015). Chip-based analysis of exosomal mRNA mediating drug resistance in glioblastoma. *Nature Communications*, *6*(1), 1–9. https://doi.org/10.1038/ncomms7999

Shao, H., Im, H., Castro, C. M., Breakefield, X., Weissleder, R. & Lee, H. (2018a). New Technologies for Analysis of Extracellular Vesicles. In *Chemical Reviews* (Vol. 118, Issue 4, pp. 1917–1950). American Chemical Society. https://doi.org/10.1021/acs.chemrev.7b00534

Shao, H., Im, H., Castro, C. M., Breakefield, X., Weissleder, R. & Lee, H. (2018b). New Technologies for Analysis of Extracellular Vesicles. In *Chemical Reviews* (Vol. 118, Issue 4, pp. 1917–1950). American Chemical Society. https://doi.org/10.1021/acs.chemrev.7b00534

Sheng, Y., Jiang, S., Yang, C., Liu, M., Liu, A., Zhang, C., Li, Z., Huo, Y., Wang, M. & Man, B. (2017). Three-dimensional nanoporous MoS 2 framework decorated with Au nanoparticles for surface-enhanced Raman scattering. *Chemical Physics Letters*, *682*, 64–70. https://doi.org/10.1016/j.cplett.2017.05.069

Shin, H., Jeong, H., Park, J., Hong, S. & Choi, Y. (2018a). Correlation between Cancerous Exosomes and Protein Markers Based on Surface-Enhanced Raman Spectroscopy (SERS) and Principal Component Analysis (PCA) [Research-article]. *ACS Sensors*, *3*, 2637–2643. https://doi.org/10.1021/acssensors.8b01047

Shin, H., Jeong, H., Park, J., Hong, S. & Choi, Y. (2018b). Correlation between Cancerous Exosomes and Protein Markers Based on Surface-Enhanced Raman Spectroscopy (SERS) and Principal Component Analysis (PCA) [Research-article]. *ACS Sensors*, *3*(12), 2637–2643. https://doi.org/10.1021/acssensors.8b01047

Shin, H., Oh, S., Hong, S., Kang, M., Kang, D., Ji, Y. G., Choi, B. H., Choi, B. H., Kang, K. W., Jeong, H., Park, Y., Hong, S., Kim, H. K., Kim, H. K., Choi, Y., Choi, Y., Choi, Y. & Choi, Y. (2020). Early-Stage Lung Cancer Diagnosis by Deep Learning-Based Spectroscopic Analysis of Circulating Exosomes. *ACS Nano*, *14*(5), 5435–5444. https://doi.org/10.1021/acsnano.9b09119

Shin, H., Oh, S., Hong, S., Kang, M., Kang, D., Ji, Y. G., Choi, B. H., Kang, K. W., Jeong, H., Park, Y., Kim, H. K. & Choi, Y. (2020a). Early-Stage Lung Cancer Diagnosis by Deep Learning-Based Spectroscopic Analysis of Circulating Exosomes. *ACS Nano*, *14*(5), 5435–5444.

https://doi.org/10.1021/acsnano.9b09119

Shin, H., Oh, S., Hong, S., Kang, M., Kang, D., Ji, Y. G., Choi, B. H., Kang, K. W., Jeong, H., Park, Y., Kim, H. K. & Choi, Y. (2020b). Early-Stage Lung Cancer Diagnosis by Deep Learning-Based Spectroscopic Analysis of Circulating Exosomes. *ACS Nano*, *14*(5), 5435–5444. https://doi.org/10.1021/acsnano.9b09119

Shin, H., Oh, S., Kang, D. & Choi, Y. (2020). Protein Quantification and Imaging by Surface-Enhanced Raman Spectroscopy and Similarity Analysis. *Advanced Science*, *1903638*, 1–9. https://doi.org/10.1002/advs.201903638

Siavash Moakhar, R., Abdelfatah, T., Sanati, A., Jalali, M., Flynn, S. E., Mahshid, S. S. & Mahshid, S. (2020). A Nanostructured Gold/Graphene Microfluidic Device for Direct and Plasmonic-Assisted Impedimetric Detection of Bacteria. *ACS Applied Materials and Interfaces*, *12*(20), 23298–23310. https://doi.org/10.1021/acsami.0c02654

Siegel, J., Lyutakov, O., Rybka, V., Kolská, Z. & Švorčík, V. (2011). Properties of gold nanostructures sputtered on glass. *Nanoscale Research Letters*, *6*(1), 1–9. https://doi.org/10.1186/1556-276X-6-96

Sina, A. A. I., Vaidyanathan, R., Dey, S., Carrascosa, L. G., Shiddiky, M. J. A. & Trau, M. (2016). Real time and label free profiling of clinically relevant exosomes. *Scientific Reports*, *6*(1), 1–9. https://doi.org/10.1038/srep30460

Sina, A. A. I., Vaidyanathan, R., Wuethrich, A., Carrascosa, L. G. & Trau, M. (2019). Label-free detection of exosomes using a surface plasmon resonance biosensor. *Analytical and Bioanalytical Chemistry*, *411*(7), 1311–1318. https://doi.org/10.1007/s00216-019-01608-5

Siravegna, G., Marsoni, S., Siena, S. & Bardelli, A. (2017). Integrating liquid biopsies into the management of cancer. In *Nature Reviews Clinical Oncology* (Vol. 14, Issue 9, pp. 531–548). Nature Publishing Group. https://doi.org/10.1038/nrclinonc.2017.14

Skotland, T., Hessvik, N. P., Sandvig, K. & Llorente, A. (2019). Exosomal lipid composition and the role of ether lipids and phosphoinositides in exosome biology. *Journal of Lipid Research*, *60*(1), 9–18. https://doi.org/10.1194/JLR.R084343

So, H. M., Park, D. W., Jeon, E. K., Kim, Y. H., Kim, B. S., Lee, C. K., Choi, S. Y., Kim, S. C., Chang, H. & Lee, J. O. (2008). Detection and titer estimation of Escherichia coli using aptamer-functionalized single-walled carbon-nanotube field-effect transistors. *Small*, *4*(2), 197–201. https://doi.org/10.1002/smll.200700664

Soleymani, L., Fang, Z., Sargent, E. H. & Kelley, S. O. (2009). Programming the detection limits of biosensors through controlled nanostructuring. *Nature Nanotechnology*, *4*(12), 844–848. https://doi.org/10.1038/nnano.2009.276

Spinelli, C., Montermini, L., Meehan, B., Brisson, A. R., Tan, S., Choi, D., Nakano, I. & Rak, J. (2018). Molecular subtypes and differentiation programmes of glioma stem cells as determinants of extracellular vesicle profiles and endothelial cell-stimulating activities. *Journal of Extracellular Vesicles*, *7*(1). https://doi.org/10.1080/20013078.2018.1490144

Stahl, S. M. (1977). The Human Platelet: A Diagnostic and Research Tool for the Study of Biogenic Amines in Psychiatric and Neurologic Disorders. *Archives of General Psychiatry*, *34*(5), 509–516.

https://doi.org/10.1001/archpsyc.1977.01770170019001

Stiles, P. L., Dieringer, J. A., Shah, N. C. & Van Duyne, R. P. (2008). Surface-enhanced Raman spectroscopy. In *Annual Review of Analytical Chemistry* (Vol. 1, Issue 1, pp. 601–626). Annual Reviews. https://doi.org/10.1146/annurev.anchem.1.031207.112814

Stiles, W. B., Barkham, M., Mellor-Clark, J. & Connell, J. (2008). Effectiveness of cognitive-behavioural, person-centred, and psychodynamic therapies in UK primary-care routine practice: Replication in a larger sample. *Psychological Medicine*, *38*(5), 677–688. https://doi.org/10.1017/S0033291707001511

Stremersch, S., Marro, M., Pinchasik, B. El, Baatsen, P., Hendrix, A., De Smedt, S. C., Loza-Alvarez, P., Skirtach, A. G., Raemdonck, K. & Braeckmans, K. (2016). Identification of individual exosome-like vesicles by surface enhanced raman spectroscopy. *Small*, *12*(24), 3292–3301. https://doi.org/10.1002/smll.201600393

Stremersch, S., Marro, M., Pinchasik, B. El, Baatsen, P., Hendrix, A., De Smedt, S. C., Loza-alvarez, P., Skirtach, A. G., Raemdonck, K., Braeckmans, K., Smedt, S. C. De, Loza-alvarez, P., Skirtach, A. G., Raemdonck, K., Braeckmans, K., De Smedt, S. C., Loza-alvarez, P., Skirtach, A. G., Raemdonck, K., … Braeckmans, K. (2016). Identification of individual exosome-like vesicles by surface enhanced raman spectroscopy. *Small*, *12*(24), 3292–3301. https://doi.org/10.1002/smll.201600393

Suga, K., Otsuka, Y., Okamoto, Y. & Umakoshi, H. (2018). Gel-Phase-like Ordered Membrane Properties Observed in Dispersed Oleic Acid/1-Oleoylglycerol Self-Assemblies: Systematic Characterization Using Raman Spectroscopy and a Laurdan Fluorescent Probe. *Langmuir*, *34*(5), 2081–2088. https://doi.org/10.1021/acs.langmuir.7b04044

Svedendahl, M., Chen, S., Dmitriev, A. & Ka, M. (2009). *Refractometric Sensing Using Propagating versus Localized Surface Plasmons : A Direct Comparison*.

Takeuchi, T., Mori, K., Sunayama, H., Takano, E., Kitayama, Y., Shimizu, T., Hirose, Y., Inubushi, S., Sasaki, R. & Tanino, H. (2020). Antibody-Conjugated Signaling Nanocavities Fabricated by Dynamic Molding for Detecting Cancers Using Small Extracellular Vesicle Markers from Tears. *Journal of the American Chemical Society*, *142*(14), 6617–6624. https://doi.org/10.1021/jacs.9b13874

Tantussi, F., Messina, G. C., Capozza, R., Dipalo, M. & Lovato, L. (2018). Long-Range Capture and Delivery of Water-Dispersed Nano-Objects by Microbubbles Generated on 3D Plasmonic Surfaces. *ACS Nano*, *12*, 4116–4122. https://doi.org/10.1021/acsnano.7b07893

Tantussi, F., Messina, G. C., Capozza, R., Dipalo, M., Lovato, L. & Angelis, F. De. (2018). Long-Range Capture and Delivery of Water-Dispersed Nano-objects by Microbubbles Generated on 3D Plasmonic Surfaces [Research-article]. *ACS Nano*, *12*, 4116–4122. https://doi.org/10.1021/acsnano.7b07893

Tantussi, F., Messina, G. C., Capozza, R., Dipalo, M., Lovato, L. & De Angelis, F. (2018). Long-Range Capture and Delivery of Water-Dispersed Nano-objects by Microbubbles Generated on 3D Plasmonic Surfaces. *ACS Nano*, *12*(5), 4116–4122. https://doi.org/10.1021/acsnano.7b07893

Thakur, A., Qiu, G., NG, S. P., Guan, J., Yue, J., Lee, Y. & Wu, C. M. L. (2017). Direct detection of two different tumor-derived extracellular vesicles by SAM-AuNIs LSPR biosensor. *Biosensors and Bioelectronics*, *94*, 400–407. https://doi.org/10.1016/j.bios.2017.03.036

The, K., He, I. & Bang, B. (2002). *Nanomaterial advantage*. *419*(October).

Thuenauer, R., Juhasz, K., Mayr, R., Frühwirth, T., Lipp, A. M., Balogi, Z. & Sonnleitner, A. (2011). A PDMS-based biochip with integrated sub-micrometre position control for TIRF microscopy of the apical cell membrane. *Lab on a Chip*, *11*(18), 3064–3071. https://doi.org/10.1039/c1lc20458k

Tian, F., Zhang, S., Liu, C., Han, Z., Liu, Y., Deng, J., Li, Y., Wu, X., Cai, L., Qin, L., Chen, Q., Yuan, Y., Liu, Y., Cong, Y., Ding, B., Jiang, Z. & Sun, J. (2021). Protein analysis of extracellular vesicles to monitor and predict therapeutic response in metastatic breast cancer. *Nature Communications*, *12*(1), 1–13. https://doi.org/10.1038/s41467-021-22913-7

Toma, M., Loget, G. & Corn, R. M. (2013). Fabrication of broadband antireflective plasmonic gold nanocone arrays on flexible polymer films. *Nano Letters*, *13*(12), 6164–6169. https://doi.org/10.1021/nl403496a

Trams, E. G., Lauter, C. J., Norman Salem, J. & Heine, U. (1981). Exfoliation of membrane ecto-enzymes in the form of micro-vesicles. *BBA - Biomembranes*, *645*(1), 63–70. https://doi.org/10.1016/0005-2736(81)90512-5

Tran, T. T., Wang, D., Xu, Z. Q., Yang, A., Toth, M., Odom, T. W. & Aharonovich, I. (2017). Deterministic Coupling of Quantum Emitters in 2D Materials to Plasmonic Nanocavity Arrays. *Nano Letters*, *17*(4), 2634–2639. https://doi.org/10.1021/acs.nanolett.7b00444

Tran, T. T., Zachreson, C., Berhane, A. M., Bray, K., Sandstrom, R. G., Li, L. H., Taniguchi, T., Watanabe, K., Aharonovich, I. & Toth, M. (2016). Quantum Emission from Defects in Single-Crystalline Hexagonal Boron Nitride. *Physical Review Applied*, *5*(3), 2–6. https://doi.org/10.1103/PhysRevApplied.5.034005

Tripathy, A., Sen, P., Su, B. & Briscoe, W. H. (2017). Natural and bioinspired nanostructured bactericidal surfaces. *Advances in Colloid and Interface Science*, *248*, 85–104. https://doi.org/10.1016/j.cis.2017.07.030

Tsai, S. S. H., Wexler, J. S., Wan, J. & Stone, H. A. (2013). Microfluidic ultralow interfacial tensiometry with magnetic particles. *Lab on a Chip*, *13*(1), 119–125. https://doi.org/10.1039/c2lc40797c

Uno, S., Kamiya, M., Yoshihara, T., Sugawara, K., Okabe, K., Tarhan, M. C., Fujita, H., Funatsu, T., Okada, Y. & Tobita, S. (2014). super-resolution imaging. *Nature Chemistry*, *6*(8), 681–689. https://doi.org/10.1038/nchem.2002

van Niel, G., Carter, D. R. F., Clayton, A., Lambert, D. W., Raposo, G. & Vader, P. (2022). Challenges and directions in studying cell–cell communication by extracellular vesicles. *Nature Reviews Molecular Cell Biology*, *23*(5), 369–382. https://doi.org/10.1038/s41580-022-00460-3

Váradi, L., Luo, J. L., Hibbs, D. E., Perry, J. D., Anderson, R. J., Orenga, S. & Groundwater, P. W. (2017). Methods for the detection and identification of pathogenic bacteria: past, present, and future. *Chem. Soc. Rev.*, *46*(16), 4818–4832. https://doi.org/10.1039/C6CS00693K

Viehrig, M., Thilsted, A. H., Matteucci, M., Wu, K., Catak, D., Schmidt, M. S., Zórzór, K. & Boisen, A. (2018). *Injection-Molded Microfluidic Device for SERS Sensing Using Embedded Au-Capped Polymer Nanocones*. https://doi.org/10.1021/acsami.8b13424

Vietmeyer, F., Volkan-Kacso, S., Frantsuzov, P., Kuno, M. & Janko, B. (2011). Understanding fluorescence blinking is the first path to an imaging solution. *Laser Focus World*, *47*(2), 45-+.

Vinita, Nirala, N. R. & Prakash, R. (2018). One step synthesis of AuNPs@MoS2-QDs composite as a robust peroxidase- mimetic for instant unaided eye detection of glucose in serum, saliva and tear. *Sensors and Actuators, B: Chemical*, *263*, 109–119. https://doi.org/10.1016/j.snb.2018.02.085

Walter, A., März, A., Schumacher, W., Rösch, P. & Popp, J. (2011). Towards a fast, high specific and reliable discrimination of bacteria on strain level by means of SERS in a microfluidic device. *Lab on a Chip*, *11*(6), 1013–1021. https://doi.org/10.1039/c0lc00536c

Wang, Jing, Kao, Y. C., Zhou, Q., Wuethrich, A., Stark, M. S., Schaider, H., Soyer, H. P., Lin, L. L. & Trau, M. (2021). An Integrated Microfluidic-SERS Platform Enables Sensitive Phenotyping of Serum Extracellular Vesicles in Early Stage Melanomas. *Advanced Functional Materials*, 2010296. https://doi.org/10.1002/adfm.202010296

Wang, Jing, Koo, K. M., Wang, Y. & Trau, M. (2019). Engineering State-of-the-Art Plasmonic Nanomaterials for SERS-Based Clinical Liquid Biopsy Applications. *Advanced Science*, *6*(23). https://doi.org/10.1002/advs.201900730

Wang, Joseph. (2005). *Nanomaterial-based electrochemical biosensors*. *i*, 421–426. https://doi.org/10.1039/b414248a

Wang, Kaikai & He, J. (2018). One-Pot Fabrication of Antireflective/Antibacterial Dual-Function Ag NP-Containing Mesoporous Silica Thin Films. *ACS Applied Materials and Interfaces*, *10*(13), 11189–11196. https://doi.org/10.1021/acsami.8b00192

Wang, Kaiqiang, Pu, H. & Sun, D. W. (2018). Emerging Spectroscopic and Spectral Imaging Techniques for the Rapid Detection of Microorganisms: An Overview. *Comprehensive Reviews in Food Science and Food Safety*, *17*(2), 256–273. https://doi.org/10.1111/1541-4337.12323

Wang, Kaizhe, Zhou, L., Li, J., Liu, W., Wei, Y., Guo, Z., Fan, C., Hu, J., Li, B. & Wang, L. (2020). Label-Free and Three-Dimensional Visualization Reveals the Dynamics of Plasma Membrane-Derived Extracellular Vesicles. *Nano Letters*, *20*(9), 6313–6319. https://doi.org/10.1021/acs.nanolett.0c01735

Wang, L., Ng, R. J. H., Safari Dinachali, S., Jalali, M., Yu, Y. & Yang, J. K. W. (2016). Large Area Plasmonic Color Palettes with Expanded Gamut Using Colloidal Self-Assembly. *ACS Photonics*, *3*(4), 627–633. https://doi.org/10.1021/acsphotonics.5b00725

Wang, P., Xia, M., Liang, O., Sun, K., Cipriano, A. F., Schroeder, T., Liu, H. & Xie, Y. H. (2015). Label-Free SERS Selective Detection of Dopamine and Serotonin Using Graphene-Au Nanopyramid Heterostructure. *Analytical Chemistry*, *87*(20), 10255–10261. https://doi.org/10.1021/acs.analchem.5b01560

Wang, Q. H., Kalantar-Zadeh, K., Kis, A., Coleman, J. N. & Strano, M. S. (2012). Electronics and optoelectronics of two-dimensional transition metal dichalcogenides. *Nature Nanotechnology*, *7*(11), 699–712. https://doi.org/10.1038/nnano.2012.193

Wang, Y., Li, Q., Shi, H., Tang, K., Qiao, L., Yu, G., Ding, C. & Yu, S. (2020). Microfluidic Raman biochip detection of exosomes: A promising tool for prostate cancer diagnosis. *Lab on a Chip*, *20*(24), 4632–4637. https://doi.org/10.1039/d0lc00677g

Wang, Zhaoyin & Dai, Z. (2015). Carbon nanomaterial-based electrochemical biosensors: An overview. *Nanoscale*, *7*(15), 6420–6431. https://doi.org/10.1039/c5nr00585j

Wang, Zongxing, Wu, H. J., Fine, D., Schmulen, J., Hu, Y., Godin, B., Zhang, J. X. J. & Liu, X. (2013). Ciliated micropillars for the microfluidic-based isolation of nanoscale lipid vesicles. *Lab on a Chip*, *13*(15), 2879–2882. https://doi.org/10.1039/c3lc41343h

Wells, S. M., Retterer, S. D., Oran, J. M. & Sepaniak, M. J. (2009). Controllable nanofabrication of aggregate-like nanoparticle substrates and evaluation for surface-enhanced Raman spectroscopy. *ACS Nano*, *3*(12), 3845–3853. https://doi.org/10.1021/nn9010939

Weng, Z., Zong, S., Wang, Y., Li, N., Li, L., Lu, J., Wang, Z., Chen, B. & Cui, Y. (2018). Screening and multiple detection of cancer exosomes using an SERS-based method. *Nanoscale*, *10*(19), 9053–9062. https://doi.org/10.1039/c7nr09162a

Whitesides, G. M. (2003). The "right" size in nanobiotechnology. In *Nature Biotechnology* (Vol. 21, Issue 10, pp. 1161–1165). Nature Publishing Group. https://doi.org/10.1038/nbt872

Wirsching, H. G., Galanis, E. & Weller, M. (2016). Glioblastoma. In *Handbook of Clinical Neurology* (Vol. 134, pp. 381–397). Elsevier. https://doi.org/10.1016/B978-0-12-802997-8.00023-2

Wolf, P. (1967). The nature and significance of platelet products in human plasma. *British Journal of Haematology*, *13*(3), 269–288. https://doi.org/10.1111/j.1365-2141.1967.tb08741.x

Wong, I. Y., Bhatia, S. N. & Toner, M. (2013). Nanotechnology: Emerging tools for biology and medicine. In *Genes and Development* (Vol. 27, Issue 22, pp. 2397–2408). Cold Spring Harbor Laboratory Press. https://doi.org/10.1101/gad.226837.113

Wu, C.-Y., Du, S.-L., Zhang, J., Liang, A.-L. & Liu, Y.-J. (2017). Exosomes and breast cancer: a comprehensive review of novel therapeutic strategies from diagnosis to treatment. *Cancer Gene Therapy*, *24*(1), 6–12. https://doi.org/10.1038/cgt.2016.69

Wu, P., Cai, J., Chen, Q., Han, B., Meng, X., Li, Y., Li, Z., Wang, R., Lin, L., Duan, C., Kang, C. & Jiang, C. (2019). Lnc-TALC promotes O 6 -methylguanine-DNA methyltransferase expression via regulating the c-Met pathway by competitively binding with miR-20b-3p. *Nature Communications*, *10*(1), 1–15. https://doi.org/10.1038/s41467-019-10025-2

Wu, Rongrong, Ou, X., Tian, R., Zhang, J., Jin, H., Dong, M., Li, J. & Liu, L. (2018). Membrane destruction and phospholipid extraction by using two-dimensional MoS2 nanosheets. *Nanoscale*, *10*(43), 20162–20170. https://doi.org/10.1039/c8nr04207a

Wu, Runrun, Ma, Y., Pan, J., Lee, S. H., Liu, J., Zhu, H., Gu, R., Shea, K. J. & Pan, G. (2018a). Efficient capture, rapid killing and ultrasensitive detection of bacteria by a nano-decorated multi-functional electrode sensor. *Biosensors and Bioelectronics*, *101*(September 2017), 52–59. https://doi.org/10.1016/j.bios.2017.10.003

Wu, Runrun, Ma, Y., Pan, J., Lee, S. H., Liu, J., Zhu, H., Gu, R., Shea, K. J. & Pan, G. (2018b). Efficient capture, rapid killing and ultrasensitive detection of bacteria by a nano-decorated multi-functional electrode sensor. *Biosensors and Bioelectronics*, *101*(August 2017), 52–59. https://doi.org/10.1016/j.bios.2017.10.003

Wu, Runrun, Zhang, H., Pan, J., Zhu, H., Ma, Y., Cui, W., Santos, H. A. & Pan, G. (2016). Spatio-Design of Multidimensional Prickly Zn-Doped CuO Nanoparticle for Efficient Bacterial Killing. *Advanced Materials Interfaces*, *3*(18), 1–11. https://doi.org/10.1002/admi.201600472

Xi, Z. Y., Xu, Y. Y., Zhu, L. P., Wang, Y. & Zhu, B. K. (2009). A facile method of surface modification for hydrophobic polymer membranes based on the adhesive behavior of poly(DOPA) and poly(dopamine). *Journal of Membrane Science*, *327*(1–2), 244–253. https://doi.org/10.1016/j.memsci.2008.11.037

Xie, Y., Rufo, J., Zhong, R., Rich, J., Li, P., Leong, K. W. & Huang, T. J. (2020). Microfluidic Isolation and Enrichment of Nanoparticles. In *ACS Nano* (Vol. 14, Issue 12, pp. 16220–16240). American Chemical Society. https://doi.org/10.1021/acsnano.0c06336

Yan, Z., Dutta, S., Liu, Z., Yu, X., Mesgarzadeh, N., Ji, F., Bitan, G. & Xie, Y. H. (2019). A Label-free platform for identification of exosomes from different sources. *ACS Sensors*, *4*(2), 488–497. https://doi.org/10.1021/acssensors.8b01564

Yáñez-Mó, M., Siljander, P. R. M., Andreu, Z., Zavec, A. B., Borràs, F. E., Buzas, E. I., Buzas, K., Casal, E., Cappello, F., Carvalho, J., Colás, E., Cordeiro-Da Silva, A., Fais, S., Falcon-Perez, J. M., Ghobrial, I. M., Giebel, B., Gimona, M., Graner, M., Gursel, I., … De Wever, O. (2015). Biological properties of extracellular vesicles and their physiological functions. In *Journal of Extracellular Vesicles* (Vol. 4, Issue 2015, pp. 1–60). Co-Action Publishing. https://doi.org/10.3402/jev.v4.27066

Yang, J., Shen, H., Zhang, X., Tao, Y., Xiang, H. & Xie, G. (2016). A novel platform for high sensitivity determination of PbP2a based on gold nanoparticles composited graphitized mesoporous carbon and doxorubicin loaded hollow gold nanospheres. *Biosensors and Bioelectronics*, *77*, 1119–1125. https://doi.org/10.1016/j.bios.2015.11.009

Yang, K. S., Im, H., Hong, S., Pergolini, I., Del Castillo, A. F., Wang, R., Clardy, S., Huang, C. H., Pille, C., Ferrone, S., Yang, R., Castro, C. M., Lee, H., Del Castillo, C. F. & Weissleder, R. (2017a). Multiparametric plasma EV profiling facilitates diagnosis of pancreatic malignancy. *Science Translational Medicine*, *9*(391). https://doi.org/10.1126/scitranslmed.aal3226

Yang, K. S., Im, H., Hong, S., Pergolini, I., Del Castillo, A. F., Wang, R., Clardy, S., Huang, C. H., Pille, C., Ferrone, S., Yang, R., Castro, C. M., Lee, H., Del Castillo, C. F. & Weissleder, R. (2017b). Multiparametric plasma EV profiling facilitates diagnosis of pancreatic malignancy. *Science Translational Medicine*, *9*(391). https://doi.org/10.1126/scitranslmed.aal3226

Yang, K. S., Im, H., Hong, S., Pergolini, I., Del Castillo, A. F., Wang, R., Clardy, S., Huang, C. H., Pille, C., Ferrone, S., Yang, R., Castro, C. M., Lee, H., Del Castillo, C. F. & Weissleder, R. (2017c). Multiparametric plasma EV profiling facilitates diagnosis of pancreatic malignancy. *Science Translational Medicine*, *9*(391). https://doi.org/10.1126/scitranslmed.aal3226

Yang, Ye, Ma, L., Cheng, C., Deng, Y., Huang, J., Fan, X., Nie, C., Zhao, W. & Zhao, C. (2018). Nonchemotherapic and Robust Dual-Responsive Nanoagents with On-Demand Bacterial Trapping, Ablation, and Release for Efficient Wound Disinfection. *Advanced Functional Materials*, *1705708*, 1705708. https://doi.org/10.1002/adfm.201705708

Yang, Yuting, Shen, G., Wang, H., Li, H., Zhang, T., Tao, N., Ding, X. & Yu, H. (2018). Interferometric plasmonic imaging and detection of single exosomes. *Proceedings of the National Academy of Sciences of the United States of America*, *115*(41), 10275–10280. https://doi.org/10.1073/pnas.1804548115

Yang, Z., Atiyas, Y., Shen, H., Siedlik, M. J., Wu, J., Beard, K., Fonar, G., Dolle, J. P., Smith, D. H., Eberwine, J. H., Meaney, D. F. & Issadore, D. A. (2022). Ultrasensitive Single Extracellular Vesicle

Detection Using High Throughput Droplet Digital Enzyme-Linked Immunosorbent Assay. *Nano Letters*, *22*(11), 4315–4324. https://doi.org/10.1021/acs.nanolett.2c00274

Yeo, L. Y., Chang, H. C., Chan, P. P. Y. & Friend, J. R. (2011). Microfluidic devices for bioapplications. *Small*, *7*(1), 12–48. https://doi.org/10.1002/smll.201000946

Yeow, E. K. L., Melnikov, S. M., Bell, T. D. M., De Schryver, F. C. & Hofkens, J. (2006). Characterizing the fluorescence intermittency and photobleaching kinetics of dye molecules immobilized on a glass surface. *Journal of Physical Chemistry A*, *110*(5), 1726–1734. https://doi.org/10.1021/jp055496r

Yokoi, A. & Ochiya, T. (2021). Exosomes and extracellular vesicles: Rethinking the essential values in cancer biology. *Seminars in Cancer Biology*, *74*, 79–91. https://doi.org/10.1016/j.semcancer.2021.03.032

Yu, J. L., May, L., Lhotak, V., Shahrzad, S., Shirasawa, S., Weitz, J. I., Coomber, B. L., Mackman, N. & Rak, J. W. (2005). Oncogenic events regulate tissue factor expression in colorectal cancer cells: Implications for tumor progression and angiogenesis. *Blood*, *105*(4), 1734–1741. https://doi.org/10.1182/blood-2004-05-2042

Yu, M., Hou, Y., Song, R., Xu, X. & Yao, S. (2018). Tunable Confinement for Bridging Single-Cell Manipulation and Single-Molecule DNA Linearization. *Small*, *1800229*, 1–8. https://doi.org/10.1002/smll.201800229

Yu, P., Wang, C., Zhou, J., Jiang, L., Xue, J. & Li, W. (2016). Influence of Surface Properties on Adhesion Forces and Attachment of Streptococcus mutans to Zirconia In Vitro. *BioMed Research International*, *2016*. https://doi.org/10.1155/2016/8901253

Yu, X., Xia, Y., Tang, Y., Zhang, W. L., Yeh, Y. T., Lu, H. & Zheng, S. Y. (2017). A Nanostructured Microfluidic Immunoassay Platform for Highly Sensitive Infectious Pathogen Detection. *Small*, *13*(24), 1–12. https://doi.org/10.1002/smll.201700425

Zachariah, M. A., Oliveira-Costa, J. P., Carter, B. S., Stott, S. L. & Nahed, B. V. (2018). Blood-based biomarkers for the diagnosis and monitoring of gliomas. *Neuro-Oncology*, *20*(9), 1155–1161. https://doi.org/10.1093/neuonc/noy074

Zhang, L., Luan, B. & Zhou, R. (2019). Parameterization of Molybdenum Disulfide Interacting with Water Using the Free Energy Perturbation Method. *Journal of Physical Chemistry B*, *123*(34), 7243–7252. https://doi.org/10.1021/acs.jpcb.9b02797

Zhang, Peng, Crow, J., Lella, D., Zhou, X., Samuel, G., Godwin, A. K. & Zeng, Y. (2018). Ultrasensitive quantification of tumor mRNAs in extracellular vesicles with an integrated microfluidic digital analysis chip. *Lab on a Chip*, *18*(24), 3790–3801. https://doi.org/10.1039/c8lc01071d

Zhang, Peng, He, M. & Zeng, Y. (2016a). Ultrasensitive microfluidic analysis of circulating exosomes using a nanostructured graphene oxide/polydopamine coating. *Lab on a Chip*, *16*(16), 3033–3042. https://doi.org/10.1039/c6lc00279j

Zhang, Peng, He, M. & Zeng, Y. (2016b). Ultrasensitive microfluidic analysis of circulating exosomes using a nanostructured graphene oxide/polydopamine coating. *Lab on a Chip*, *16*(16), 3033–3042. https://doi.org/10.1039/c6lc00279j

Zhang, Peng, He, M. & Zeng, Y. (2016c). Ultrasensitive microfluidic analysis of circulating exosomes using a nanostructured graphene oxide/polydopamine coating. *Lab on a Chip*, *16*(16), 3033–3042. https://doi.org/10.1039/c6lc00279j

Zhang, Peng, Wu, X., Gardashova, G., Yang, Y., Zhang, Y., Xu, L. & Zeng, Y. (2020). Molecular and functional extracellular vesicle analysis using nanopatterned microchips monitors tumor progression and metastasis. *Science Translational Medicine*, *12*(547), 2878. https://doi.org/10.1126/scitranslmed.aaz2878

Zhang, Peng, Zhou, X., He, M., Shang, Y., Tetlow, A. L., Godwin, A. K. & Zeng, Y. (2019a). Ultrasensitive detection of circulating exosomes with a 3D-nanopatterned microfluidic chip. *Nature Biomedical Engineering*, *3*(6), 438–451. https://doi.org/10.1038/s41551-019-0356-9

Zhang, Peng, Zhou, X., He, M., Shang, Y., Tetlow, A. L., Godwin, A. K. & Zeng, Y. (2019b). Ultrasensitive detection of circulating exosomes with a 3D-nanopatterned microfluidic chip. *Nature Biomedical Engineering*, *3*(6), 438–451. https://doi.org/10.1038/s41551-019-0356-9

Zhang, Peng, Zhou, X. & Zeng, Y. (2019). Multiplexed immunophenotyping of circulating exosomes on nano-engineered ExoProfile chip towards early diagnosis of cancer. *Chemical Science*, *10*(21), 5495–5504. https://doi.org/10.1039/c9sc00961b

Zhang, Pengchao, Chen, L., Xu, T., Liu, H., Liu, X., Meng, J., Yang, G., Jiang, L. & Wang, S. (2013). Programmable fractal nanostructured interfaces for specific recognition and electrochemical release of cancer cells. *Advanced Materials*, *25*(26), 3566–3570. https://doi.org/10.1002/adma.201300888

Zhang, Q., Jeppesen, D. K., Higginbotham, J. N., Graves-Deal, R., Trinh, V. Q., Ramirez, M. A., Sohn, Y., Neininger, A. C., Taneja, N., McKinley, E. T., Niitsu, H., Cao, Z., Evans, R., Glass, S. E., Ray, K. C., Fissell, W. H., Hill, S., Rose, K. L., Huh, W. J., … Coffey, R. J. (2021). Supermeres are functional extracellular nanoparticles replete with disease biomarkers and therapeutic targets. *Nature Cell Biology*, *23*(12), 1240–1254. https://doi.org/10.1038/s41556-021-00805-8

Zhang, W., Jiang, L., Diefenbach, R. J., Campbell, D. H., Walsh, B. J., Packer, N. H. & Wang, Y. (2020). Enabling Sensitive Phenotypic Profiling of Cancer-Derived Small Extracellular Vesicles Using Surface-Enhanced Raman Spectroscopy Nanotags. *ACS Sensors*, *5*(3), 764–771. https://doi.org/10.1021/acssensors.9b02377

Zhang, X., Huang, X., Xue, M., Ye, X., Lei, W., Tang, H. & Li, C. (2015). Hydrothermal synthesis and characterization of 3D flower-like MoS2 microspheres. *Materials Letters*, *148*, 67–70. https://doi.org/10.1016/j.matlet.2015.02.027

Zhao, C., Ge, Z. & Yang, C. (2017). Microfluidic techniques for analytes concentration. *Micromachines*, *8*(1), 1–33. https://doi.org/10.3390/mi8010028

Zhao, G., Li, X., Huang, M., Zhen, Z., Zhong, Y., Chen, Q., Zhao, X., He, Y., Hu, R., Yang, T., Zhang, R., Li, C., Kong, J., Xu, J. Bin, Ruoff, R. S. & Zhu, H. (2017). The physics and chemistry of graphene-on-surfaces. *Chemical Society Reviews*, *46*(15), 4417–4449. https://doi.org/10.1039/c7cs00256d

Zhao, Z., Yang, Y., Zeng, Y. & He, M. (2016). A microfluidic ExoSearch chip for multiplexed exosome detection towards blood-based ovarian cancer diagnosis. *Lab on a Chip*, *16*(3), 489–496. https://doi.org/10.1039/c5lc01117e

Zhou, T., Liu, Z., Wu, Y., Deng, Y., Liu, Y. & Liu, G. (2013). Hydrodynamic particle focusing design using fluid-particle interaction. *Biomicrofluidics*, *7*(5), 054104. https://doi.org/10.1063/1.4821170

Zhou, X., Ravichandran, G. C., Zhang, P., Yang, Y. & Zeng, Y. (2019). A microfluidic alternating-pull-push active digitization method for sample-loss-free digital PCR. *Lab on a Chip*, *19*(24), 4104–4116. https://doi.org/10.1039/c9lc00932a

Zhou, Y. G., Mohamadi, R. M., Poudineh, M., Kermanshah, L., Ahmed, S., Safaei, T. S., Stojcic, J., Nam, R. K., Sargent, E. H. & Kelley, S. O. (2016). Interrogating Circulating Microsomes and Exosomes Using Metal Nanoparticles. *Small*, *12*(6), 727–732. https://doi.org/10.1002/smll.201502365

Zhu, S., Li, H., Yang, M. & Pang, S. W. (2018). Highly sensitive detection of exosomes by 3D plasmonic photonic crystal biosensor. *Nanoscale*, *10*(42), 19927–19936. https://doi.org/10.1039/c8nr07051b

Zhu, Y., Murali, S., Cai, W., Li, X., Suk, J. W., Potts, J. R. & Ruoff, R. S. (2010). Graphene and graphene oxide: Synthesis, properties, and applications. *Advanced Materials*, *22*(35), 3906–3924. https://doi.org/10.1002/adma.201001068

Zitvogel, L., Regnault, A., Lozier, A., Wolfers, J., Flament, C., Tenza, D., Ricciardi-Castagnoli, P., Raposo, G. & Amigorena, S. (1998). Eradication of established murine tumors using a novel cell-free vaccine: Dendritic cell-derived exosomes. *Nature Medicine*, *4*(5), 594–600. https://doi.org/10.1038/nm0598-594

Zou, S. & Schatz, G. C. (2004). Narrow plasmonic/photonic extinction and scattering line shapes for one and two dimensional silver nanoparticle arrays. *Journal of Chemical Physics*, *121*(24), 12606–12612. https://doi.org/10.1063/1.1826036